Investigating the Dark Sector of the Universe using Cosmological Observables

by

Lindsay Forestell

B.Sc., The University of Alberta, 2014

A THESIS SUBMITTED IN PARTIAL FULFILLMENT
OF THE REQUIREMENTS FOR THE DEGREE OF

Doctor of Philosophy

in

THE FACULTY OF GRADUATE AND POSTDOCTORAL STUDIES
(Physics)

The University of British Columbia
(Vancouver)

August 2019

The following individuals certify that they have read, and recommend to the Faculty of Graduate and Postdoctoral Studies for acceptance, the thesis entitled:

Investigating the Dark Sector of the Universe using Cosmological Observables

submitted by **Lindsay Forestell** in partial fulfillment of the requirements for the degree of **Doctor of Philosophy** in **Physics**.

Examining Committee:

Kris Sigurdson, Physics
Co-Supervisor

David Morrissey, Physics
Co-Supervisor

Mark Van Raamsdonk, Physics
University Examiner

Mark Thachuk, Chemistry
University Examiner

Heather Logan, Physics
External Examiner

Additional Supervisory Committee Members:

Gary Hinshaw, Physics
Supervisory Committee Member

Jeremy Heyl, Physics
Supervisory Committee Member

Alison Lister, Physics
Supervisory Committee Member

Abstract

Although the Standard Model of particle physics has been a phenomenal success in modelling known particles and predicting new, theoretically founded particles, it is known to be incomplete. And while the Standard Model of cosmology has been a phenomenal success in modelling the evolution of the Universe, it too has open questions that remain unresolved. In this thesis, we aim to address properties of new physics models that are being developed that aim to answer these questions. In particular, we wish to focus on and examine in detail the connection between the dark sector of the Universe and the visible sector. In examining this connection, we may use cosmological observables to place strict limits on new theories that go beyond the Standard Model.

In the first part of this thesis we will address the flow of energy from the visible sector to the hidden via a phenomenon known as freeze-in. Here, we explore the effects that early-time, ultraviolet energy transfer may have on the infrared, late-time evolution of a dark matter candidate. We use a simplified hidden-sector model to highlight the notion that operators that are typically considered early may have relevant late-time effects.

Following this, we consider the reverse energy flow, and consider how dark-sector energy injection via decays of electromagnetic radiation may affect the products of Big Bang Nucleosynthesis. In this section, we focus on arbitrary light particle (< 100 MeV) decays, and identify how direct and indirect alteration of the light element abundances can be constrained using the measured values today. Direct alteration is caused by photodissociation, while indirect effects are felt through changes in the radiation energy density.

Finally, we consider a full and rich dark sector, consisting of a non-Abelian SU(3) gauge force. This new gauge field presents itself as glueballs after a confining transition. We study the effects of this confining transition, as well as the subsequent dynamic evolution of the spectrum of glueballs produced. In the final chapter, we examine how decays to Standard Model particles via higher-dimensional, non-renormalizable operators can place stringent limits on the parameter space of this gauge force.

Lay Summary

While science has made incredible discoveries throughout the ages, the Universe is still a vast, incredible mystery. A large portion of the Universe is considered to be 'dark matter,' a new type of matter that does not have an explanation within our current particle models, but seems to be required by our most up-to-date cosmological models. Beyond dark matter, we have puzzles in our particle models that hint at the need for new unknown particles to create consistent explanations within all our theories.

This thesis aims to explore the relationship between cosmological and particle models, and how new physics may connect the two. We examine methods for creating dark matter, how destroying it might affect the world around us, and how it might behave in different physical scenarios. In doing so, we hope to shed new light on some of the problems that face the physics community today.

Preface

Parts II, III, and IV of this thesis are based on published (and peer-reviewed) work in collaboration with others, while parts I and V are original to this thesis.

Part II is based on L. Forestell and D. E. Morrissey, *Infrared Effects of Ultraviolet Operators on Dark Matter Freeze-In*, [arXiv:1811.08905] [1]. I participated in constructing the models to study, and was responsible for the numerical calculations carried out, as well as some of the analytic calculations. David Morrissey, the supervisory author on this work also provided analytic estimates, as well as providing self-interaction constraints. Both authors contributed to the composition of the manuscript.

Part III is based on L. Forestell, D. E. Morrissey, and G. White, *Limits from BBN on Light Electromagnetic Decays*, JHEP, **1901**, (2018), 074, [arXiv:1809.01179] [2]. The supervisory author, David Morrissey, provided photon spectrums, while Graham White and I provided numerical and analytic estimates of the effects on Big Bang Nucleosynthesis. I also provided the numerical and analytic inputs for section 4.4.1, and provided the constraint estimates shown in Figures 4.11. An expanded section on N_{eff} effects is included as well. David Morrissey wrote the initial draft of the manuscripts, while all authors contributed and edited.

Part IV is based on two papers: L. Forestell, D. E. Morrissey, and K. Sigurdson, *Non-Abelian Dark Forces and the Relic Densities of Dark Glueballs*, Phys. Rev. D, **95**, (2016), 015032, [arXiv:1605.08048] [3] and L. Forestell, D. E. Morrissey, and K. Sigurdson, *Cosmological Bounds on Non-Abelian Dark Forces*, Phys. Rev. D, **97**, (2018), 075029, [arXiv:1710.06447] [4] I was responsible for the majority of numerical results throughout both manuscripts. David Morrissey and Kris Sigurdson were the supervisory authors. We jointly composed and edited these manuscripts.

Table of Contents

List of Tables

List of Figures

Glossary

ACT Atacama Cosmology Telescope

BBN Big Bang Nucleosynthesis

BSM Beyond the Standard Model

CMB Cosmic Microwave Background

CKM Cabibbo-Kobayashi-Maskawa

CP charge-conjugation parity

CS Compton scattering

DLA damped Lyman-α

DM dark matter

EM electromagnetic

EWSB electroweak symmetry breaking

EW electroweak

EFT effective field theory

FI freeze-in

FIMP feebly-interacting massive particle

FRW Friedmann-Robertson-Walker

FSR final state radiation

GB glueball

GUT Grand Unified Theory

IC inverse Compton

IGM inter-galactic medium

IR infrared

ΛCDM Λ cold dark matter

LHC Large Hadron Collider

LSND Liquid Scintillator Neutrino Detector

LSP lightest super-partner

NGB Nambu-Goldstone Boson

PCN pair creation on nuclei

PMNS Pontecorvo-Maki-Nakagawa-Sakata

PP photon photon scattering

QCD Quantum Chromodynamics

QED Quantum Electrodynamics

QFT quantum field theory

RG renormalization group

SIMP self-interacting massive particle

SM Standard Model

SPT South Pole Telescope

SSB spontaneous symmetry breaking

SUSY supersymmetry

UV ultraviolet

vev vacuum expectation value

WIMP weakly-interacting massive particle

4P photon photon pair production

Acknowledgments

This thesis would not have been possible without the support of a large group of mentors, collaborators, friends, family, and financial supporters. Here I wish to acknowledge and thank those who made this all possible.

First I would like to thank the Natural Science and Engineering Research Council of Canada, as well as the University of British Columbia and TRIUMF for the financial support, without which none of this would have been possible.

Next, I would like to thank everyone who I was able to collaborate with to write interesting papers, troubleshoot various technical malfunctions, and listen to and improve various presentations over the years. In particular, the theory group at TRIUMF has been a great support. I am grateful to everyone who has come and gone over the years, including Mirko Miorelli the ever patient office-mate and Graham White for the helpful discussions.

I am also grateful to my doctoral committee, Jeremy Heyl, Alison Lister, Gary Hinshaw, Kris Sigurdson, and David Morrissey, for the insightful and thought-provoking questions and feedback over the past few years.

Most importantly, I need to thank my supervisors Kris Sigurdson and David Morrissey for guiding me over the last five years. To Kris, I thank you for stimulating discussions and always pushing the bounds on the vast world of theoretical physics. To David, I thank you for always having an open door and supporting, encouraging words whenever I felt uncertain along this path.

Finally, to my friends and family, especially my parents. I could not have done this without you. You have kept me rooted and sane when the Universe threatened to steal me away for good! I would not be here without the incredible support, helping hands, listening ears, and encouraging words from all of you.

Thank you, everyone.

To Emily, Bentley, Lachlan, Jack, and Everett. You guys have inspired me to see the world in an entirely new, open and curious light. Thank you for being you, and for being a joy in my life.

To Aron, thank you for being there every day, good and bad, always encouraging me in my drive to complete this goal. Your support and love have meant the world to me, and have made this entirely possible.

Part I

Introduction

Chapter 1

The Standard Model

1.1 Introduction

The Standard Model (SM) of particle physics is one of the most successful physical theories of modern physics, successfully explaining the strong, weak and electromagnetic forces. It has been tested, successfully predicting new particles such as the Higgs Boson and the massive electroweak gauge bosons [13–15]. Although we have successfully built, used and tested this powerful model, there are still some key problems that we wish to address. Doing so inevitably require introducing new physics. However, well motivated physics models need to do more than just answer the question they were proposed to solve. They must also pass tests in the rest of the physics realms as well. In particular, new models must not contradict currently known and well understood effects. In this thesis, we aim to study exactly how new physics may interact with old, from a variety of angles. In order to do this, we must first understand how our successful models work.

In this chapter we will build up the Standard Model, focusing on three key pieces that build the fundamental Lagrangian:

$$\mathscr{L} = \mathscr{L}_{Gauge} + \mathscr{L}_{Higgs} + \mathscr{L}_{Yukawa} \tag{1.1}$$

where each piece of this Lagrangian will be explained in detail in this chapter. Following this, we will address some problems that have arisen that the SM cannot solve, and give common solutions that incorporate new physics. Reviews of quantum field theory (QFT) and the SM can be found in Refs. [16–20].

Throughout this thesis, unless stated otherwise we will use natural units, where $\hbar = c = k_B = 1$, and typically use units of GeV as our natural energy unit.

1.2 The Standard Model

1.2.1 Gauge Symmetries

In this section, we wish to explicitly define $\mathscr{L}_{gauge}$, the portion of the Standard Model that describes the interactions between fermions via gauge forces. This will rely heavily on group theory and Lie algebras, for which good references can be found at [21, 22], while gauge field theories can be found in Ref. [23].

All of the known particles can be well defined by the SM, a theoretical description of the Strong, Weak, and Electromagnetic forces. These forces define the interactions that exist between different particles, and are explicitly identified in nature by a gauge symmetry of the form:

$$SU(3)_C \times SU(2)_L \times U(1)_Y \tag{1.2}$$

The first term, $SU(3)_C$, corresponds to Quantum Chromodynamics (QCD), the fundamental description of the strong force. This covers the interactions of quarks and gluons (or bound states of quarks and gluons, hadrons, at low energy). The next two terms, $SU(2)_L \times U(1)_Y$, together form electroweak (EW) theory, which as we shall see can be broken down to the Weak force and the electromagnetic (EM) force (or in QFT terms, the EM force is often described by Quantum Electrodynamics (QED)) separately after the symmetry is explicitly broken. The EM force will independently preserve a new $U(1)_{EM}$ symmetry, with the group charge corresponding to the physical charge of particles that we see (eg. Q = -1 for electrons). The Weak force remains responsible for events such as β decay of a nucleus, and is the only explicit connection between neutrinos and other particles in the SM.

In the modern view of particle physics, we take as our starting point that any particles that are charged under these gauge groups must be invariant under local gauge transformations of the form:

$$U_r = e^{i\alpha^a t_r^a} \tag{1.3}$$

where $\alpha^a = \alpha^a(x)$ has local spatial dependence, and t_r^a correspond to the Hermitian generators of the Lie algebra in question. Some examples of such generators include the Pauli matrices for $SU(2)$, where they are typically normalized as $t_r^a = \frac{1}{2}\sigma^a$:

$$\sigma_1 = \begin{pmatrix} 0 & 1 \\ 1 & 0 \end{pmatrix} \qquad \sigma_2 = \begin{pmatrix} 0 & -i \\ i & 0 \end{pmatrix} \qquad \sigma_3 = \begin{pmatrix} 1 & 0 \\ 0 & -1 \end{pmatrix} \tag{1.4}$$

or the Gell-Mann matrices for $SU(3)$, with normalization $t_r^a = \frac{1}{2}\lambda^a$:

$$\lambda_1 = \begin{pmatrix} 0 & 1 & 0 \\ 1 & 0 & 0 \\ 0 & 0 & 0 \end{pmatrix} \quad \lambda_2 = \begin{pmatrix} 0 & -i & 0 \\ i & 0 & 0 \\ 0 & 0 & 0 \end{pmatrix} \quad \lambda_3 = \begin{pmatrix} 1 & 0 & 0 \\ 0 & -1 & 0 \\ 0 & 0 & 0 \end{pmatrix}$$

$$\lambda_4 = \begin{pmatrix} 0 & 0 & 1 \\ 0 & 0 & 0 \\ 1 & 0 & 0 \end{pmatrix} \quad \lambda_5 = \begin{pmatrix} 0 & 0 & -i \\ 0 & 0 & 0 \\ i & 0 & 0 \end{pmatrix} \tag{1.5}$$

$$\lambda_6 = \begin{pmatrix} 0 & 0 & 0 \\ 0 & 0 & 1 \\ 0 & 1 & 0 \end{pmatrix} \quad \lambda_7 = \begin{pmatrix} 0 & 0 & 0 \\ 0 & 0 & -i \\ 0 & i & 0 \end{pmatrix} \quad \lambda_8 = \frac{1}{\sqrt{3}} \begin{pmatrix} 1 & 0 & 0 \\ 0 & 1 & 0 \\ 0 & 0 & -2 \end{pmatrix}$$

Under these transformations, fermions will transform as $\psi \to U_r \psi$ and $\bar{\psi} \to \bar{\psi} U_r^\dagger$. Here we use the standard definitions, $\bar{\psi} = i\sigma^2 \psi^*$ and σ^2 is the Pauli matrix. Note that here we refer to ψ ($\bar{\psi}$) as left (right)-handed Weyl spinors [24, 25]. To get the more familiar 4-component Dirac spinors, we require two 2-component Weyl spinors:

$$\Psi_D = \begin{pmatrix} \psi \\ \bar{\chi} \end{pmatrix}, \tag{1.6}$$

while the Pauli matrices (including $\sigma^0 = \mathbb{I}_2$) can be promoted to the more familiar gamma matrices using:

$$\gamma^\mu = \begin{pmatrix} 0 & \sigma^\mu \\ \bar{\sigma}^\mu & 0 \end{pmatrix} \tag{1.7}$$

where $\bar{\sigma} = (\mathbb{I}_2, -\vec{\sigma})$ and for the special case of Majorana fermions, $\bar{\chi} = \bar{\psi}$. Although we are typically only interested in the 4-component Dirac notation for the spinors, it is instructive to use the chiral Weyl-spinors here to explicitly identify the left and right-handed dependencies within the SM. If we now wish to apply this transformation to a canonical kinetic term for a fermion, we will immediately run into problems:

$$\psi^\dagger i\bar{\sigma}^\mu \partial_\mu \psi \to \psi^\dagger i\bar{\sigma}^\mu \partial_\mu \psi + \psi^\dagger i\bar{\sigma}^\mu U_r^\dagger (\partial_\mu U_r)\psi \tag{1.8}$$

which is not invariant under the transformation. However, we can remedy this by introducing a vector field, A_μ, and promote it to a matrix via the specific representation we are interested in: $A_{r\mu} = A_\mu^a t_r^a$. If we allow A_μ to transform under the adjoint representation of the group:

$$A_{r\mu} \to U_r A_{r\mu} U_r^\dagger + \frac{1}{ig} U_r (\partial_\mu U_r^\dagger) \tag{1.9}$$

We can then show that:

$$(igA_{r\mu} + \partial_\mu)\psi \to U_r(igA_{r\mu} + \partial_\mu)\psi \tag{1.10}$$

So, if we promote our derivatives to covariant derivatives,

$$D_\mu = igA^a_\mu t^a_r + \partial_\mu \tag{1.11}$$

then the kinetic terms will remain invariant under the gauge transformation:

$$\psi^\dagger i\bar{\sigma}^\mu D_\mu \psi \to \psi^\dagger i\bar{\sigma}^\mu D_\mu \psi \tag{1.12}$$

and so we see that adding an interaction with a vector field, and simultaneously transforming both fields will preserve the symmetry. Thus, gauge vector interactions with any particles charged under that specific gauge are necessary to preserve our gauge symmetries.

Now that we have introduced the gauge vector field, we must also define its own kinetic term. To be gauge invariant, this can be done using:

$$F_{\mu\nu} = \partial_\mu A_\nu - \partial_\nu A_\mu - gf^{abc}A^b_\mu A^c_\nu \tag{1.13}$$

where f^{abc} are the structure constants for the group representation. Finally, we write the kinetic term as:

$$\mathscr{L} \supset -\frac{1}{4}F^a_{\mu\nu}F^{a\,\mu\nu} \tag{1.14}$$

Here it is important to note that for Abelian gauge groups, such as $U(1)$, the structure constants are all zero, and so there will be no gauge boson self-interactions. However, non-Abelian gauge groups will have non-zero structure constants, leading to the possibility of interesting self-interacting effects. These self-interactions for a particular non-Abelian extension to the SM are explored in much more detail in Part IV.

In the Standard Model, we thus have to introduce three sets of gauge vector bosons, one for each gauge symmetry. For $SU(3)_C$, this will be the gluons, G^a_μ, where a runs from 1 to 8.[1] We also have 3 Weak bosons, W^a_μ for the $SU(2)_L$ group, and finally B_μ for the $U(1)_Y$ hypercharge group. To be concrete, we can explicitly express all the vector gauge bosons in terms of their gauge representations, as shown in Table 1.1. It is important to note that all of these vectors must necessarily be massless, as a vector gauge term ($\sim -m^2A^\mu A_\mu$) would violate gauge-invariance. We will see where the masses for the observed vector bosons come from in the next section.

Of course, these vectors need something to interact with: these are the fermions of the Standard Model. They will transform as $\psi_{ij} \to U_C U_L U_Y \psi_{ij}$, where i and j represent the $SU(3) \times SU(2)$ representations for that particular state. The fermions can be broken up into two subgroups: quarks, which have

[1] Note that because we only experimentally see the strong force at short ranges, we expect there to be no color neutral gluon which would mediate a long range force, thus we postulate that the strong force is SU(3) instead of U(3), which would have 9 generators.

Vector Gauge Boson	$SU(3)_C$	$SU(2)_L$	$U(1)_Y$
G^a_μ	**8**	**1**	0
W^a_μ	**1**	**3**	0
B_μ	**1**	**1**	0

Table 1.1: Vector gauge bosons and their gauge charges.

$SU(3)_C$ charge, and leptons, which only have $SU(2)_L \times U(1)_Y$. Both quarks and leptons come in three generations, with each copy being identical except for the masses of the quarks and leptons involved. Like the gauge bosons, we can explicitly write out the gauge charges of every fermion in the Standard Model, which we show in Table 1.2.

Note again that here we have used 2-component Weyl spinors to represent the fermions. In reality, four-component Dirac spinors represent the physical fields, which are simply the sum of the two Weyl spinors: $\psi_D = \binom{\psi_L}{\psi_R}$. However, it is enlightening to write it this way as it emphasizes the chiral nature of the EW gauge force. Only the left-handed fermions are charged under $SU(2)_L$, while the right-handed fermions are singlets, causing the EW force to be maximally parity violating. Because of this, we cannot explicitly write out a mass term, and these fermions must necessarily be massless to preserve gauge invariance. Not only that, but in the SM there is no right-handed neutrino at all, and as we shall see, this means that in the SM, the neutrinos should necessarily all have zero mass. This is not the case, and hints at problems with our model of physics. Nonetheless, armed with these gauge charges, we can now write down the gauge portion of the SM Lagrangian:

$$\mathscr{L}_{gauge} = \quad -\tfrac{1}{4} G^{a\,\mu\nu} G^a_{\mu\nu} - \tfrac{1}{4} W^{a\,\mu\nu} W^a_{\mu\nu} - \tfrac{1}{4} B^{\mu\nu} B_{\mu\nu} + \sum_\psi \bar{\psi} i \bar{\sigma}^\mu D_\mu \psi \tag{1.15}$$

where the vector kinetic terms are defined in Eq. (1.13), $\psi \in \{Q_L, u_R, d_R, L_L, e_R\}$ and covariant derivatives are defined in Eq. (1.11) (where the correct representation must be used for each fermion, noting that t^a_r=0 under the trivial representation). For the SM, the covariant derivatives are explicitly given by:

$$D_\mu = \partial_\mu + i g_s t^a_{r_c} G^a_\mu + i g t^p_{r_L} W^p_\mu + i g' Y B_\mu \tag{1.16}$$

where g_s, g, and g' are the Strong, Weak, and hypercharge (Y) couplings. $t^a_{r_c}$ corresponds to the generators of the fundamental representation of $SU(3)$, which are given by the Gell-Mann matrices in Eq. (1.5), while $t^a_{r_L}$ are the generators of $SU(2)$, given by the Pauli matrices in Eq. (1.4). Y represents the hypercharge, the charge of the field under $U(1)_Y$.

So we see that, if the SM consisted solely of fermions charged under the SM gauge symmetries, and their corresponding vector gauge bosons, we could entirely fix the Lagrangian, but we would necessarily require massless particles. This is not the case, and so we must introduce a new mechanism to provide mass for the particles. This will be discussed in the next section.

Fermion	$SU(3)_C$	$SU(2)_L$	$U(1)_Y$
$Q_L = \begin{pmatrix} u_L \\ d_L \end{pmatrix}$	**3**	**2**	$+1/6$
u_R	**3**	**1**	$+2/3$
d_R	**3**	**1**	$-1/3$
$L_L = \begin{pmatrix} \nu_L \\ e_L \end{pmatrix}$	**1**	**2**	$-1/2$
e_R	**1**	**1**	-1

Table 1.2: Fermions of the SM and their gauge charges. The top group corresponds to quarks, while the bottom group corresponds to leptons.

Higgs	$SU(3)_C$	$SU(2)_L$	$U(1)_Y$
H	**1**	**2**	$+1/2$

Table 1.3: Higgs Boson and its gauge charges.

1.2.2 Spontaneous Symmetry Breaking

Under the SM symmetries $SU(3)_C \times SU(2)_L \times U(1)_Y$, all of the vector gauge bosons must necessarily be massless. Furthermore, the chiral nature of the EW symmetry, $SU(2)_L \times U(1)_Y$, necessarily requires that the SM fermions must also be massless. However, this does not agree with what we see in nature, and we need some new mechanism to match observations. In particular, the $W^{\pm}$ and Z bosons of the Weak force have masses of $\sim$80 GeV and 91 GeV, respectively, while every fermion mass has been measured to be non-zero as well.[2] Although these two mechanisms are distinct, it turns out that we can reconcile both cases with a single new field. This is the Englert-Brout-Higgs-Guralnik-Hagen-Kibble mechanism, which gives rise to the more commonly named Higgs Boson [27–29] through spontaneous symmetry breaking (SSB). The next two pieces of the SM Lagrangian are thus $\mathscr{L}_{Higgs}$ and $\mathscr{L}_{Yukawa}$, which provide the Higgs connection to both the weak vector bosons as well as (most of) the fermions. Here we will show that these are both necessary to give mass to the rest of the SM.

To provide masses, we need to spontaneously break the EW gauge symmetries. We do this by introducing a new complex scalar Higgs field, H, that is a doublet under Weak isospin:

$$H = \begin{pmatrix} \phi^+ \\ \phi^0 \end{pmatrix} \tag{1.17}$$

This will be the final field of the SM, and we write down its gauge representation in Table 1.3.

Because this field is charged under $SU(2)_L \times U(1)_Y$, it must include a covariant derivative within the kinetic term:

$$\mathscr{L}_{Higgs} \supset |D_\mu H|^2 = \left| \left(\partial_\mu + ig\frac{\sigma^p}{2}W_\mu^p + ig'\frac{1}{2}B_\mu \right) H \right|^2 \tag{1.18}$$

[2]For up-to-date measurements of all of these masses, you can see, for example, Ref. [26]

We also include here the symmetry breaking scalar potential:

$$\mathscr{L}_{Higgs} \supset -\left(-\mu^2|H|^2 + \frac{\lambda^2}{2}|H|^4\right) \tag{1.19}$$

This potential has a minima that is not at zero, but rather at $v/\sqrt{2} = \mu/\lambda$ (where v = 246 GeV has been normalized to match standard convention). We can expand around this minima to define excitations of the Higgs field out of this minima. However, because the Higgs is a complex scalar, we can rotate this v by any phase and still be at the minima. Choosing a specific minima will force us to spontaneously break our symmetries. To be concrete, we choose a gauge to work in (which can always be done by applying an $SU(2)_L \times U(1)_Y$ rotation), and define the Higgs vacuum state to be:

$$\langle H \rangle = \begin{pmatrix} 0 \\ v/\sqrt{2} \end{pmatrix} \tag{1.20}$$

where v is chosen by construction to be real and positive. Working in this gauge, and expanding H as

$$H = \begin{pmatrix} 0 \\ (v+h(x))/\sqrt{2} \end{pmatrix} \tag{1.21}$$

we can show that this vacuum state is trivially invariant under $SU(3)_C$. Because it is an eigenstate of weak isospin, it is also invariant under an abelian subgroup of $SU(2)_L \times U(1)_Y = U(1)_{EM}$, which has charge Q = $t^3 + Y$, where t^3 is the third component of the weak isospin. We know that for each group generator that does not leave the vacuum state invariant, we expect a Nambu-Goldstone Boson (NGB) [30–32]. In EW theory, there are 3 such generators. These modes would remain massless. However, what actually happens is that the NGB modes of H become the longitudinal polarizations of the now-massive gauge bosons. We can look at this by explicitly counting degrees of freedom. The original Higgs field had 4 degrees of freedom (being a complex doublet). After symmetry breaking, we have chosen a gauge in which it will have 1 degree of freedom, h. The other 3 degrees of freedom are 'eaten' by 3 of the weak isospin bosons, giving them mass (and going from 2 massless, independent polarizations to 3 massive, independent polarizations), leaving the fourth massless. These will, after diagonalization of the mass matrices, become the $W^{\pm}$ and Z modes of the weak theory, while the massless state becomes the photon. These will be explicitly shown in the next section.

As we mentioned above, the Higgs is again used to generate the masses of the fermions. This is also done through the broken symmetry of the Higgs field, but arises due to Yukawa connections between the Higgs and the fermions, rather than the covariant derivative of the vector bosons. In the unbroken phase, it is possible to write down gauge invariant operators involving the Higgs field and the fermions as Yukawa interactions:

$$\mathscr{L}_{Yukawa} = -Y_u \bar{Q}_L \tilde{H} u_R - Y_d \bar{Q}_L H d_R - Y_e \bar{L}_L H e_R + h.c. \tag{1.22}$$

where $\tilde{H} = i\sigma^2 H^*$ and Y_i are general 3x3 matrices that allow the generations of different quarks and leptons to mix. These are the most general interactions we can write down that obey the combined EW

gauge group $SU(2)_L \times U(1)_Y$. After electroweak symmetry breaking (EWSB), H will be replaced by Eq. (1.21) in the unitary gauge, which leads to terms of the form $\sim v\bar{f}_L f_R$, which correspond to mass terms for the fermions. Note that there is no equivalent $-Y_\nu \bar{L}_L \tilde{H} \nu_R$ term, as there are no right-handed neutrinos in the Standard Model. This is ultimately the reason that neutrinos do not have mass in the SM.

Now that we have all of the pieces required for the SM as laid out in Eq. (1.1), let us put this all together (in the broken phase) to see exactly what the physical world (nearly[3]) looks like today.

1.2.3 The Physical Standard Model

Let us now write down the physically observed fields of the Standard Models, and the values of their couplings and masses. An extensive review of this, as well as up-to-date values for all masses and couplings quoted here, can be found in Ref. [26], and references therein. We will begin with determining the appropriate combinations of fields that have physical masses, before commenting on the effects of confinement on fields that have SU(3) charges.

Fundamental Fields

We begin with the simplest portion, the mass of the Higgs boson. If we expand around our chosen vacuum state, we find that the scalar potential in Eq. (1.19) reduces to:

$$\mathscr{L}_{Higgs} \sim -v^2\lambda^2 h^2 + (\text{self couplings}) \tag{1.23}$$

and so we identify the mass of the Higgs boson as

$$m_H = \sqrt{2}\lambda v\,. \tag{1.24}$$

This has been experimentally measured to be $m_H = 125.18 \pm 0.16$ GeV. The vacuum expectation value (vev) (v) for the Higgs is constrained to be $v \sim 246$ GeV, which implies that the self-coupling value, λ must be $\sim$0.13.

Next, we consider the gauge bosons in the broken phase. Although Eq. (1.18) will also contain Higgs-gauge boson interactions in the broken phase, we again focus on the v^2 terms that will contribute to the mass matrix. Writing this out, we find:

$$|D_\mu H|^2 = \frac{1}{2}\frac{g^2v^2}{4}\left(W_\mu^{1\,2} + W_\mu^{2\,2}\right) + \frac{1}{2}\frac{v^2}{4}\left(g'B_\mu - gW_\mu^3\right)^2 + (\text{Higgs-gauge boson couplings}) \tag{1.25}$$

[3] As we will show in a later section, there are problems with the Standard Model that still need to be explained. We have hinted at this already with the fact that neutrinos do not have mass in the SM, and yet they do in reality.

which gives us the mass matrix

$$M = \frac{v^2}{4}\begin{pmatrix} g^2 & 0 & 0 & 0 \\ 0 & g^2 & 0 & 0 \\ 0 & 0 & g^2 & -gg' \\ 0 & 0 & -gg' & g'^2 \end{pmatrix} \tag{1.26}$$

Diagonalizing this, and re-arranging the $W^{1,2}$ bosons into two with orthogonal states that have charge ± 1 in the $U(1)_{EM}$ gauge, we find:

$$W^{\pm}_{\mu} = \frac{1}{\sqrt{2}}(W^1_{\mu} \mp iW^2_{\mu}) \tag{1.27}$$

with mass

$$M^2_W = \frac{1}{4}g^2v^2 \, . \tag{1.28}$$

This has been measured to be 80.379 ± 0.012 GeV. The W^3 and B bosons mix according to:

$$\begin{pmatrix} Z_{\mu} \\ A_{\mu} \end{pmatrix} = \begin{pmatrix} c_W & -s_W \\ s_W & c_W \end{pmatrix}\begin{pmatrix} W^3_{\mu} \\ B_{\mu} \end{pmatrix} \tag{1.29}$$

where c_W (s_W) are the cosine (sine) of the Weinberg angle (or weak mixing angle, θ_W), defined by

$$s_W = \sin(\theta_W) = \frac{g'}{\sqrt{g^2 + g'^2}} \tag{1.30}$$

Measurements of the Weinberg angle give $s_W = 0.23120 \pm 0.00015$. In this basis, the mass matrix is now diagonal, with a massless photon (A_{μ}), and the Z boson has mass:

$$M^2_Z = \left(\frac{g^2 + g'^2}{2}\right)v^2 \tag{1.31}$$

The Z mass has been measured as $M_Z = 91.1876 \pm 0.0021$ GeV. Thus, the symmetry breaking energy scale set by v also sets the scale for the masses of the weak bosons. Because of this, we consider energies $\mathcal{O}(100 \text{ GeV})$ to be at the weak scale.

We complete our physical SM model by looking at the Yukawa terms in Eq. (1.22). When H is replaced by its vev, we find:

$$\mathscr{L}_{Yukawa} = -\frac{v}{\sqrt{2}}Y_u\bar{u}_L u_R - \frac{v}{\sqrt{2}}Y_d\bar{d}_L d_R - \frac{v}{\sqrt{2}}Y_e\bar{e}_L e_R + h.c. \tag{1.32}$$

To get the physical mass eigenstates, we need to diagonalize the mixing matrices, $Y_{u,d,e}$. This can be

done by choosing a unitary transform for each left or right handed fermion, V_L^f and V_R^f, such that

$$M_{diag}^f = \frac{v}{\sqrt{2}} V_L^f Y_f V_R^{f\dagger} \ , \tag{1.33}$$

and sending each fermion to:

$$f_L \to V_L^f f_L, \quad f_R \to V_R^f f_R \ . \tag{1.34}$$

When we do this, we are choosing a new basis that corresponds to the physical mass eigenstates of the quarks and leptons, where the coupling between the fermion and the Higgs is explicitly realized as:

$$y_f = \sqrt{2}\frac{m_f}{v} \tag{1.35}$$

This is of course allowed, and if we apply these transformations to the rest of the SM Lagrangian, it turns out that nearly all of the gauge interactions will be invariant under these rotations as well. However, the charged-current interactions of the quarks via the $W^\pm$ gauge-bosons will not be invariant. This is equivalent to the Yukawa couplings breaking an $(SU(3))^3$ global symmetry under rotations of Q_L, u_R, and d_R between the different generations. Thus, by choosing to diagonalize the masses of the up and down quarks, we are forced to include a mixing matrix elsewhere. This shows up in the charged current interaction, which mixes up and down quarks as:

$$\mathscr{L}_{CC} = -\frac{g}{\sqrt{2}}(\bar{u}_L, \bar{c}_L, \bar{t}_L)\bar{\sigma}^\mu W_\mu^\pm V_{CKM} \begin{pmatrix} d_L \\ s_L \\ b_L \end{pmatrix} + h.c. \tag{1.36}$$

where u, c, t correspond to the three 'up' generations of quarks, and d, s, b correspond to the 'down' generations. $V_{CKM} = V_L^{u\dagger} V_L^d$ is the Cabibbo-Kobayashi-Maskawa (CKM) matrix [33, 34]. This is a unitary matrix, characterized by three mixing angles and one charge-conjugation parity (CP) violating phase.[4] Note that, because we have no neutrino masses, we do not have this difficulty in the lepton sector, as we can always choose a neutrino mixing matrix $V_L^\nu = V_L^e$.

Confinement

Although we can now define all the fundamental particles, and their masses, in the Standard Model, we cannot quite explain the particles that we physically observe at lower energies. Mesons and baryons, for example, are confined states of 2 and 3 quarks, respectively. These are the physical fields that we observe at low energies, but they do not correspond directly to fundamental fields in the Lagrangian. We wish to briefly describe this phenomena here in the context of QCD, but we will make use of confinement in Part IV.

[4] It is interesting to note that the CP violating phase only arises due to the fact that there are 3 generations of quarks. With only 2, we can always define a real unitary matrix via a clever choice of field redefinitions that will rotate the CP violating phase away.

To understand why quarks and gluons exist in bound states, we must first look at how the strong coupling, g_s, depends on the energy that we are concerned with. This can be done by solving the renormalization group (RG) equations that link the coupling at one momentum scale, μ, to another. For a non-Abelian gauge theory, the RG equation becomes [16]:

$$\frac{dg}{dt} := \beta(t) = -\frac{b}{(4\pi)^3} g^3 \tag{1.37}$$

where g is the running coupling, $t = ln(\mu/\mu_0)$, and b is given by:

$$b = \frac{11}{3} C_2(A) - \sum_{r,f} \frac{2}{3} T_2(r) - \sum_{r',c} \frac{1}{3} T_2(r') \tag{1.38}$$

Where $C_2(A)$ is the Casimir of the adjoint (N for SU(N)) and $T_2(r)$ is the trace invariant of the representation (1/2 for the fundamental representation). The first (second) sum over r (r') runs over all 2-component fermions (complex scalars) in the theory with masses below the scale of interest. For $SU(3)_C$, which has 6 fermion flavours (12 2-component fermions), and no complex scalars, this reduces to:

$$b_{QCD} = 7 \tag{1.39}$$

for energies above the top quark mass. Solving the RG equation leaves us with the unusual running of the QCD coupling strength:

$$\alpha_s(\mu) = \frac{g_s^2(\mu)}{4\pi} = \frac{\alpha_s(\mu_0)}{1 + \frac{b_{QCD}}{2\pi} \alpha_s(\mu_0) \log\left(\frac{\mu}{\mu_0}\right)} \tag{1.40}$$

Because b_{QCD} is positive, the coupling strength actually decreases as the energy increases. This is known as asymptotic freedom. On the other end, as our energy scales decrease, we approach non-perturbativity as $\alpha_s \to 4\pi$. This occurs at the scale $\mu \equiv \Lambda_{QCD} \sim 214$MeV. Above this scale, QCD can be treated perturbatively, with free quarks and gluons. Below this, however, the strong force becomes non-perturbative and other methods, such as Lattice QCD, must be used [35, 36].

We can still make qualitative statements about the low energy theory based on confinement and global symmetries. Quarks and gluons become strongly-coupled at low energy, or equivalently, large distance. If we consider a $q\bar{q}$ pair, we can imagine attempting to pull these apart. Eventually the pair will be separated enough that the energy stored in the gluon flux tube will be large enough that it becomes energetically favourable to break the tube and nucleate a new quark pair from the vacuum (as long as the quark masses are below the confinement scale). This will be a new meson state, and signals that confinement is preferred to free states at low energies. However, these confined states are not fundamental, and thus not well defined by the QCD Lagrangian. In principle, the QCD Lagrangian should be able to calculate these states and their interactions, but it is unclear how to do so as it is highly non-perturbative. To describe these states, we would like to have an effective field theory (EFT) for

QCD at low energies.

One such approach is to write down an EFT that contains the dynamical fields of interest, together with all possible operators consistent with the underlying symmetries of QCD. This is known as chiral perturbation theory, and provides an excellent starting point for an EFT of QCD [37]. The underlying idea is that there is an $SU(2)_L \times SU(2)_R \times U(1)_V \times U(1)_A$ symmetry associated with the QCD Lagrangian in the massless phase when considering only up (u) and down (d) quarks. This corresponds to SU(2) transformations of the isospin doublets $\binom{u_L}{d_L}$ and $\binom{u_R}{d_R}$, as well as Baryon number conservation via the vector current ($U(1)_V$) and a symmetry associated with the axial vector current ($U(1)_A$). All of these but $U(1)_A$ have cancellations in their anomalies, and so $SU(2)_L \times SU(2)_R \times U(1)_V$ is a good global symmetry that should be obeyed in the low energy limit.

One further useful feature of QCD comes from the quark condensate vacuum state:

$$\langle \bar{q}_R q_L \rangle \neq 0 \tag{1.41}$$

This expectation value does not respect the global symmetry defined above, and thus we can expect to find NGBs of a spontaneously broken symmetry. Here, the full global symmetry is broken down to a subgroup $SU(2)_V \times U(1)_V$, where $SU(2)_V$ is the subgroup corresponding to transformations that affect left and right-handed states in the same way. Thus, we start with (3+3+1=7) generators of the full global symmetry, broken down to (3+1=4) generators that leave the vacuum state invariant. Thus we expect to see 3 NGBs; we can associate these with the lightest meson states, the pions: π^0, $\pi^{\pm}$. Although the NGBs should be massless, in the full QCD theory the quark states are not massless. This explicitly breaks the global symmetry above, and so the pions actually correspond to pseudo-Goldstone bosons within chiral field theory. This is in fact why this EFT is termed chiral perturbation theory; breaking the global chiral symmetry plays a large role in the creation of our new bound states.

This can be extended formally to include other meson states, all the quark flavours (that fall below the confinement scale), as well as the full baryon spectrum. Bound states of gluons are even predicted to exist, in the form of glueballs [5, 6].[5] Thus we have both chiral field theory and Lattice QCD methods to attempt to understand not only the fundamental fields of the SM, but the physically observed fields as well.

Now we have all the pieces of the physical Standard Model, where everything can be neatly expressed in terms of their gauge-boson couplings (g_s, g, g' and their RG evolutions) and representations, Higgs potential couplings (v, λ), and the Yukawa couplings (y_i, which if diagonalized, lead to the CKM matrix terms as well). With all this in hand, we can move on to problems with the Standard Model that motivate our search for new physics beyond.

[5] We will explicitly study a non-Abelian gauge theory in Part IV that looks at realizations of glueballs and their effects in the early Universe.

1.3 Problems with the Standard Model

Despite overwhelming evidence that the Standard Model does an exceptional job of modeling fundamental physics, it is known to be incomplete. There are many problems in particle physics that cannot be explained by the chosen gauge symmetries, generations of fermions, and the presence of a light Higgs. In this section we will lay out some of the most prominent problems with the SM today, in the hopes to motivate searches for physics beyond it (also known as BSM physics). Here, we will focus on concrete problems arising directly from the Standard Model. In a future section, we will extend our motivations for BSM physics by identifying problems that arise due to our coupling of knowledge of both the SM and cosmology (such as, for example, the need for dark matter and even more CP violation than that present in the CKM matrix). Good references addressing and providing overviews of some of these problems can be found at [20, 38, 39].

Neutrino Masses

As we have hinted at already, one problem with the SM is the lack of neutrino masses. Under the SM, right-handed neutrinos do not exist, and so we cannot produce neutrino masses via the Higgs mechanism. However, the discovery of oscillations between neutrino flavours from atmospheric neutrinos [40], as well as solar neutrinos [41] necessitates that at least two of the neutrino species must have mass. Qualitatively, this can be seen by the argument that a truly massless particle must travel at the speed of light, and by construction will thus not feel the passage of time. If that were the case, oscillations (which happen over large distances or equivalently timescales) would be impossible. This can be worked out quantitatively as well. In a simplified 2-state neutrino model, with flavour eigenstates $|\nu_{e,\mu}\rangle$ and mass eigenstates $|\nu_{1,2}\rangle$, the probability of arriving in the same flavour state as the initial is [42]:

$$P_{ee} = 1 - \sin^2(2\theta)\sin^2\left(\frac{\Delta m^2 L}{4E}\right) \tag{1.42}$$

where Δm^2 is the neutrino mass difference, L the distance travelled, E the neutrino energy, and θ the mixing parameter that mixes flavour and mass states. For three generations of neutrinos, similar arguments will apply, although we must use a mixing matrix similar to the CKM matrix in the quark sector. For leptons, this is known as the Pontecorvo-Maki-Nakagawa-Sakata (PMNS) matrix [43, 44].

Thus the observation of oscillations provides concrete evidence for at least some of the SM neutrinos to have mass, which necessitates BSM physics. The easiest solution is to allow for the existence of three right-handed neutrinos that are gauge singlets. This would allow for Yukawa couplings to the Higgs and thus give mass to the neutrinos. However, the extreme difference in masses between neutrinos (which, from cosmological observations must be less than an eV [45]) and charged leptons is enough to question if there is some other mechanism providing neutrino masses.[6] One other popular solution is the (Type I) see-saw mechanism [46]. In this model, the new neutrinos, N, being gauge singlets, are given Majorana

[6]The top quark to electron mass ratio is $\sim 10^5$, while the electron to neutrino mass ratio is at least the same order of magnitude. Although these are not dissimilar, it will still be satisfying to identify some mechanism for the mass hierarchies.

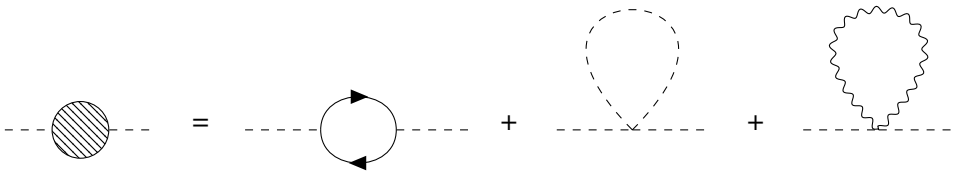

Figure 1.1: Feynman diagrams contributing to the one-loop corrections to the Higgs mass in the SM. From left to right, these include fermion loops (particularly the top), Higgs self-couplings, and massive gauge boson loops. All three diagrams are quadratically divergent.

masses at a scale M_N:

$$\mathscr{L} \supset -\frac{1}{2}\bar{N_R}M_N N_R \tag{1.43}$$

When combined with the Yukawa masses of Eq. (1.35), this results in a mass matrix of the form:

$$M_\nu = \begin{pmatrix} 0 & y_\nu v/\sqrt{2} \\ y_\nu v/\sqrt{2} & M_N \end{pmatrix} \tag{1.44}$$

If the scale at which the new physics is present is much larger than the Yukawa coupling and Higgs vev, $M_N >> y_\nu v/\sqrt{2}$, then the left and right handed neutrino masses essentially decouple:

$$m_{\nu,L} \sim \frac{y_\nu v}{\sqrt{2}M_N}, \qquad m_{\nu,R} \sim M_N \tag{1.45}$$

and we are left with our three SM neutrinos that naturally have small masses, suppressed by v/M_N, as well as three (mostly singlet) heavy neutrino states. These are effectively *sterile* neutrinos, as the singlet states are extraordinarily hard to detect. Although new neutrinos have not yet been discovered, there have been hints of a fourth neutrino at experiments such as Liquid Scintillator Neutrino Detector (LSND) and MiniBoone [47, 48], and as such models that explain the neutrino masses and add new neutrino-like states are well motivated to study and understand.

Hierarchy Problem

As we have now seen, new physics at higher scales is well motivated. An elegant solution to the neutrino mass problem relies on heavy sterile neutrinos. Many other models, such as Grand Unified Theories (GUTs) and quantum gravity also point to natural energy scales much higher than the EW scale.[7] However, introducing new energy scales above the EW scales leads to a new problem. One of the most interesting problems with the SM is this hierarchy problem, and the desire for a *natural* model of physics.

In particular, when computing quantum corrections to the Higgs mass, diagrams of the form shown

[7] GUTs typically require energy scales around 10^{14} GeV, while quantum theories of gravity are naturally expected at the Planck Mass, $M_{PL} \sim 10^{19}$ GeV.

in Fig. 1.1 must be considered. In all three cases, the superficial degrees of divergence of the loop integrals are D = (power of p in numerator)-(power of p in denominator) = 2, which naively leads to quadratic divergences [16].[8] For example, the first diagram corresponding to a loop from the top quark will have a loop integral contribution of the form:

$$\text{loop integral} \propto \int d^4p \frac{\gamma^\mu p_\mu + m}{p^2 - m^2} \frac{\gamma^\mu p'_\mu + m}{p'^2 - m^2} \propto p^2 \ , \tag{1.46}$$

where p and p' correspond to the internal propagator momenta of the top quark, and m its mass. This will naively lead to a quadratic divergence in the integral if we integrate over all possible momenta. In this case, all the naive expectations align with reality, and contributions to the Higgs mass are of the form:

$$\delta m_H^2 \sim \frac{\Lambda^2}{32\pi^2}\left[-6y_t^2 + \frac{1}{4}(9g^2 - 3g'^2) + 6\lambda\right] \tag{1.47}$$

where the loops have been regularized using a momentum cut-off at Λ. If Λ is much larger than the weak scale, where the Higgs and weak boson masses appear, then in order to realize a physical Higgs mass of $m_H = 125$ GeV we would require a very fine tuned value of the bare Higgs mass to nearly exactly cancel any large contributions from new physics at scale Λ. For example, new physics is almost certainly expected to arise at the Planck scale, where quantum gravity is expected to emerge. With $\Lambda = M_{PL} \sim 10^{19} GeV$, then $m_{H,bare}$ must be chosen with a precision of one part in 10^{32}. This fine-tuning is the hierarchy problem, as there is naively no reason for these parameters to show such remarkable cancellations.

We might worry that these quadratic divergences are simply a relic of using a cut-off regulator, and they should disappear when renormalizing the theory to remove UV divergences. However, it is more appropriate to understand Λ as a new physical scale corresponding to the mass of the new heavy particle, and the corrections that appear in Eq. (1.47) can be considered as finite contributions from heavy particles (such as the top and gauge bosons) that are proportional to the scale of new physics. For example, integrating out the massive sterile neutrinos of the previous section leaves a non-renormalizable operator in the SM EFT that will necessarily include corrections of the form of Eq. (1.47), with $\Lambda \sim M_N$. Thus, the hierarchy problem is truly a problem that the SM Higgs is sensitive to new scales - if there is no new UV physics there is no hierarchy problem. But as UV physics is well motivated, this problem is a fundamental one that many physicists have attempted to explain.

It is also interesting to note that this problem is unique to elementary scalars, and does not arise when we consider either fermions or gauge bosons. If we pose the exact same problem but consider

[8] Note that sometimes the superficial degrees of divergence do not lead to the correct UV divergent behavior. This is the case, for example, with the photon self-energy correction, which naively expects a quadratic divergence but is only logarithmic. Symmetries in the theory (such as the gauge symmetry which leads to the Ward Identity [49]) can reduce the number of degrees of freedom, changing the UV behavior. Nevertheless, it is still a good reference point to understand where in our theories these divergences may arise.

corrections to the fermion mass, these corrections will scale as:

$$m_f \propto m_f \log\left(\frac{\Lambda}{m_f}\right) \tag{1.48}$$

which is a far slower divergence, and protects the masses of the fermions (and gauge bosons) from the divergence we see in scalars. This arises due to the fact that there is an approximate symmetry in the chiral theory. If $m_f \to 0$, this symmetry becomes exact, which serves to suppress large corrections to the masses.

Many solutions to the hierarchy problem have been proposed. One possible option is that this is not a problem at all, and we simply require fine-tuning for life to exist. This anthropic argument is unsatisfying to many, as it is still possible to create 'habitable Universes' for Higgs masses that are much larger [50]. More popular solutions have included supersymmetry (SUSY) and Higgs extension models. In supersymmetry, (a good primer for which can be found in Ref. [51]), the Poincaré symmetries of space-time are extended to include particles of different spins. In doing this, an entire complement of new particles to the SM are predicted, with every elementary SM particle gaining a superpartner with spin differing by half.[9] This cleanly solves the hierarchy problem, as the superpartners will contribute to the quadratic divergence of the Higgs with the same couplings (modulo their broken masses) but opposite signs as their SM counterparts. As long as SUSY is broken softly, this leads to $\delta m_H^2 \sim m_{soft}^2$, and so new superpartners near the TeV range would help to explain the hierarchy problem.

With no hint yet of such physics at the Large Hadron Collider (LHC) experiments, other solutions to the hierarchy problem are also gaining interest. Most of these involve changing the elementary nature of the Higgs in some way. These are collectively known as Composite Higgs models, including Little Higgs, Twin Higgs, Technicolor, and more [52–57]. In these models, the common motivation is that the Higgs is no longer an elementary scalar, but rather a composite bound state of some more fundamental objects. In these cases the Higgs is then an NGB of an underlying global symmetry, G. To allow the Higgs a quadratic mass term, the underlying symmetry must not be exact, but rather an approximate symmetry. In this way, G is explicitly broken, making Higgs a pseudo-Nambu-Goldstone-Boson. The underlying shift-symmetry associated with NGBs allows for m_H to naturally be small, providing another solution to the hierarchy problem.

Strong CP Problem

The last major issue that we will comment on here is the strong CP problem [58–61]. When we wrote down the gauge boson kinetic terms for the SM Lagrangian in Eq. (1.14), we ignored a number of possible gauge invariant operators. We could also have included terms of the form:

$$\mathscr{L} \supset -\left(\frac{\theta_{QCD}}{32\pi^2} G_{\mu\nu}\tilde{G}^{\mu\nu} + \frac{\theta_L}{32\pi^2} W_{\mu\nu}\tilde{W}^{\mu\nu} + \frac{\theta_Y}{32\pi^2} B_{\mu\nu}\tilde{B}^{\mu\nu}\right) \tag{1.49}$$

[9] In standard SUSY models, the masses of the superpartners are predicted to be identical to their counterparts. As we have not discovered any such particles, if SUSY exists, it must be a spontaneously broken form to lift the mass degeneracies.

where $\tilde{G}_{\mu\nu} = \varepsilon_{\mu\nu\alpha\beta}G^{\alpha\beta}/2$ is the dual field strength tensor. It can be shown that these terms are equivalent to total derivatives of the fundamental fields. These would then vanish in the action as boundary terms if the fields have non-trivial windings. This is true for Abelian fields (and so we do not worry about θ_Y), but the theta terms cannot be removed for non-Abelian theories. While θ_L can be removed by transformations in lepton number (L) and baryon number (B) [62], the term cannot be removed from QCD, and so we should include its effects when considering standard physics models. Even if we were to naively set $\theta_{QCD} = 0$, rotations of the quark fields to try to produce diagonal mass matrices results in a re-introduction of the theta term, and so it would appear to be the case that we should naturally expect some non-zero value of the phase.

However, there is an important effect that is predicted if this term exists. In particular, CP violating couplings of pions to neutrons are expected, that give rise to a calculable neutron electric dipole moment [63]. This is calculated to be:

$$d_N \sim 5.2 \times 10^{-16}\theta \text{ cm} \tag{1.50}$$

Current limits on the (non)-existence of such a dipole moment imply extremely small values for $\theta < 5 \times 10^{-11}$ [64]. Understanding why this value is so small is the strong CP problem.

The most popular solution to this is the axion, a new particle that arises in the Peccei-Quinn theory [65]. In this theory, an extra $U(1)$ symmetry is added to the Standard Model in such a way so as to balance the problematic term. Spontaneous breaking of this symmetry, together with explicit breaking associated with low-energy QCD effects lead to a pseudo-NGB. This new particle is the axion, a pseudoscalar field, a, that couples to the SM as:

$$\mathscr{L} \supset -\frac{g_s^2}{32\pi^2}\frac{a}{f_a}G\tilde{G}\,, \tag{1.51}$$

with a potential:

$$V(a) \sim m_a^2 f_a^2 \left(1 - \cos(\bar{\theta} + a/f_a)\right) \tag{1.52}$$

where $\bar{\theta}$ corresponds to the value of θ_{QCD} chosen by nature, which is arbitrarily expected to be non-zero. After SSB, the axion gains a vacuum expectation value that exactly cancels off $\bar{\theta}$, thus completely eliminating the strong CP problem. Other solutions to the strong CP problem involve invoking discrete symmetries instead of the continuous U(1) Peccei-Quinn symmetry. Invoking a P symmetry at high energies between left-handed SM particles and right-handed mirror particles will eliminate the theta term, once again solving the CP problem [66].

These are only a few of the problems associated with the SM, (with some more to be discussed later in the context of cosmology) but already we can see that there are plenty of well motivated reasons to search for new physics. However, when doing so, we need to remember that any new physics models must remain consistent with the rest of our understanding of how the Universe appears to work and interact with itself. Of interest to us will be how new physics may interact with the SM in the early

Universe, and so next we will provide a short overview of useful cosmological theory.

Chapter 2

Cosmology and Dark Matter

2.1 Introduction

While the SM of particle physics has done a remarkable job on small scales, predicting new particles and explaining their interactions, the 'Standard Model' of cosmology has been doing the same thing on larger scales, successfully modelling the evolution and expansion of the observable Universe. This model has successfully predicted the Cosmic Microwave Background (CMB) power spectrum [67], as well as the abundances of light elements created during Big Bang Nucleosynthesis (BBN) [68, 69]. However, just like the SM, there are problems that cannot be solved in cosmology with only the known particles, and so we must once again turn to new physics to attempt to explain the unexplainable.

In this chapter, we will build up a working knowledge of the cosmology needed to incorporate new physics into the early Universe. Some good reviews and texts for the following discussion can be found at Refs. [70–72]. This will include looking at how we currently understand the expansion of the Universe is driven, as well as a detailed look into the thermodynamics of the early Universe. Following this, we will address problems that cannot be explained by our current models. We will focus on dark matter (DM) and dark sectors, as this is the frontier where particle physics directly coincides with cosmology, and understanding how dark sectors interact with the SM will be the main focus of this thesis. In particular, in this chapter we will address how DM (and other new particles that may be relevant in the early Universe) can leave an observable imprint that can be used to constrain new physics.

Through this chapter, we will be using the mostly negative convention for the metric: $\eta_{\mu,\nu}$ = diag(1,-1,-1,-1). Also note that we will use the reduced Planck mass, $M_{PL} = \frac{1}{\sqrt{8\pi G}}$ whenever it is referenced.

2.2 The ΛCDM Model

We begin our survey of the 'Standard Model' of cosmology by considering the expansion of the Universe. On large scales, all astrophysical evidence points towards the idea that the observable Universe is homogeneous and isotropic. The most general metric ($g_{\mu\nu}$) that satisfies these conditions is the

Friedmann-Robertson-Walker (FRW) metric, which can be written in the form:

$$ds^2 = dt^2 - a^2(t)\left(\frac{dr^2}{1-kr^2} + r^2 d\theta^2 + r^2 \sin^2\theta d\phi^2\right) = g_{\mu\nu}dx^\mu dx^\nu \tag{2.1}$$

where $(t,\ r,\ \theta,\ \phi)$ are comoving coordinates, $a(t)$ is the scale factor, and k = -1, 0, 1 correspond to spaces of negative, zero, or positive spatial curvature, respectively. When k = 0 (as is suggested from many large scale observations), r is the standard radial comoving coordinate. In flat space, then, we can find physical distances between objects by simply scaling the comoving distances:

$$\vec{x}_{physical} = a(t)\vec{x}_{comoving} \tag{2.2}$$

It is standard to assume that the present-day scale factor, $a(t_0)$ = 1. Often, distances to astrophysical objects are quoted in terms of redshift, z, instead of the scale factor. This is a direct measurement of how much a wavelength of light has stretched before reaching us: $\lambda_0 = (1+z)\lambda_i$. These are related by:

$$z(t) = \frac{a(t_0)}{a(t)} - 1 \tag{2.3}$$

Thus, in order to study the evolution of the Universe we simply need to understand how the scale factor changes with time. To do this, we solve the Einstein equations:

$$G_{\mu\nu} \equiv R_{\mu\nu} - \frac{1}{2}g_{\mu\nu}R = 8\pi G T_{\mu\nu} \tag{2.4}$$

where $G_{\mu\nu}$ is the Einstein tensor, $R_{\mu\nu}$ the Ricci tensor (which depends on the metric and its derivatives), R the Ricci Scalar = $g_{\mu\nu}R^{\mu\nu}$, G the Gravitational constant, and $T_{\mu\nu}$ the stress-energy tensor describing all the fields and energy that are present. For simplicity (and to match the symmetries, isotropy, and homogeneity of the metric), we consider perfect fluids as the source of all energy. In this case, the stress-energy tensor can be written in terms of the energy density, ρ, and pressure, p, of the fluid, as:

$$T_{\mu\nu} = \begin{pmatrix} \rho & 0 & 0 & 0 \\ 0 & -p & 0 & 0 \\ 0 & 0 & -p & 0 \\ 0 & 0 & 0 & -p \end{pmatrix} \tag{2.5}$$

When we impose conservation of the stress-energy tensor (under vanishing covariant derivative, $\nabla_\mu T^{\mu\nu}$=0), we find the first law of thermodynamics in an expanding Universe:

$$\frac{\partial\rho}{\partial t} + \frac{\dot{a}}{a}(3\rho + 3p) = 0 \tag{2.6}$$

where dots are used to denote time derivatives. If we take this stress-energy tensor, together with the FRW metric, we find, for the time-time component of Einstein's equations, the Friedmann equation:

$$\left(\frac{\dot{a}}{a}\right)^2 + \frac{k}{a^2} = \frac{8\pi G}{3}\rho \tag{2.7}$$

This is usually written in terms of the Hubble rate, $H = \dot{a}/a$ and a critical energy density, $\rho_C = 3M_{PL}^2 H^2$ such that we find:

$$\frac{\rho}{\rho_C} = 1 + \frac{k}{H^2 a^2} \ , \tag{2.8}$$

or equivalently, in dimensionless form:

$$\Omega = 1 - \Omega_k \tag{2.9}$$

where Ω gives the dimensionless fractional energy density with respect to the critical, and $\Omega_k = -\frac{k}{H^2 a^2}$. In a closed Universe, k = +1 and $\Omega > 1$. If the Universe is open, k = -1 and $\Omega < 1$. Finally, a flat Universe will find that the total energy density will exactly match the critical density, and so the curvature must vanish. Experimentally, there is a growing amount of evidence that supports this scenario, and so from here on we will consider a flat Universe only, and explicitly set k = 0.

The spatial components of the Einstein equations can similarly be used to determine the second Friedmann equation. When taken together with Eq. (2.6), this is typically written as an equation governing the acceleration of the scale factor:

$$\frac{\ddot{a}}{a} = -\frac{4\pi G}{3}(\rho + 3p) \ . \tag{2.10}$$

Let us now explain why the standard cosmological model of expansion is called ΛCDM. To take the Friedmann equations any further, we require knowledge of the type of fluid that is driving expansion. This can be done using the equation of state,

$$p = w\rho \tag{2.11}$$

where w parametrizes the type of fluid present. The three main parametrizations that we will consider are w = 1/3 (radiation), 0 (matter), and -1 (vacuum energy, or a cosmological constant, Λ). Using the Friedmann equations, we can show that the evolution of the energy densities must be:

$$\rho \propto a^{-3(1+w)} \tag{2.12}$$

This makes intuitive sense: matter scales like a^{-3}, which is equivalent to the volume of space expanding, as expected. Radiation scales like a^{-4}, which has the volume of space expanding, plus an additional factor for the redshifting of each wavelength. Finally, the cosmological constant does not scale, but remains constant as the Universe expands. We can take it a step further to determine how the scale

factor must change with time given a particular equation of state as well:

$$a(t) \propto \begin{cases} t^{2/3(1+w)} & w > -1 \\ e^{H_0 t} & w = -1 \end{cases} \tag{2.13}$$

Because the energy densities scale at different rates, we can define unique Cosmological epochs within which different types of energy density are dominant. Early in the history of the Universe, when $a << a(t_0)$, radiation energy density will be the dominant form. As the Universe continues to expand, eventually we will reach the matter dominated era, signalled by the time of matter-radiation equality:

$$\frac{\rho_{r,0}}{a^4} = \frac{\rho_{m,0}}{a^3} \tag{2.14}$$

This can be solved for the cross-over scale factor, $a_{eq} = \Omega_r/\Omega_m$, where it is more standard to work using the dimensionless energy fractions, $\Omega_x = \rho_x/\rho_C$.

After a period of matter domination, the Universe will eventually be dominated by the cosmological constant term, provided by Λ. When we are within each epoch, it is fairly numerically safe to solve the Friedmann equations using only one of the three types of energy densities. If we are crossing over multiple epochs, however, it is best to use the full equation for the Hubble rate, which is best expressed as:

$$H^2 = H_0^2 \left(\frac{\Omega_{r,0}}{a^4} + \frac{\Omega_{m,0}}{a^3} + \Omega_\Lambda \right) \tag{2.15}$$

where H_0 is the present Hubble rate, and $\Omega_0 = \Omega_{r,0} + \Omega_{m,0} + \Omega_\Lambda$ is the present day (dimensionless) energy density. Typically, H_0 is parametrized in terms of a dimensionless number, h, as well, and is historically given as $H_0 = 100\ h$ km/s/Mpc. The current observational limits on the above values are given by the latest CMB results from the Planck telescope, together with lensing reconstruction and baryonic acoustic oscillation (BAO) results [67]:

$$\begin{aligned} h &= 0.6766 \pm 0.0042 \\ \Omega_m &= 0.3111 \pm 0.0056 \\ \Omega_\Lambda &= 0.6889 \pm 0.0056 \end{aligned} \tag{2.16}$$

and Ω_r is negligible today. These are enough to fully inform the evolution of the Universe. Thus, the Λ comes from the cosmological constant, and CDM comes from the cold dark matter (that we will delve into in a future section) that makes up the dominant portion of the matter density of the Universe (although Ω_m still accounts for the baryonic portion as well). Together these make up effectively all of the energy density in the Universe today.

2.3 Thermal Evolution

2.3.1 Thermodynamics

With our understanding of how the Universe evolves in hand, we can now turn to thermodynamics to understand how evolution will move forward for species that are in thermal equilibrium. Before discussing the early Universe and the radiation-dominated phase, we first review some basic thermodynamics.

In order to track the evolution of a species i, we will wish to know the number density n_i, energy density, ρ_i, and pressure, p_i. For a given gas of particles with g_i internal degrees of freedom, this only depends on the phase space distribution $f_i(p)$:

$$n_i = \frac{g_i}{(2\pi)^3}\int f_i(\vec{p})d^3p \tag{2.17}$$

$$\rho_i = \frac{g_i}{(2\pi)^3}\int E(\vec{p})f_i(\vec{p})d^3p \tag{2.18}$$

$$p_i = \frac{g_i}{(2\pi)^3}\int \frac{|\vec{p}|^2}{3E}f_i(\vec{p})d^3p \tag{2.19}$$

where $E^2 = |\vec{p}|^2 + m^2$. In kinetic equilibrium, we can identify the phase space occupancy by the Fermi-Dirac or Bose-Einstein distribution:

$$f_i(\vec{p}) = \frac{1}{e^{(E_i-\mu_i)/T_i} \pm 1} \tag{2.20}$$

where +1 pertains to fermions, -1 to bosons, and μ_i is the chemical potential of the species. Furthermore, if we have chemical equilibrium as well as kinetic, then the chemical potential of each species can be related to those it interacts with. For example, for an interaction of the form:

$$i + j \leftrightarrow k + l \ , \tag{2.21}$$

we must have:

$$\mu_i + \mu_j = \mu_k + \mu_l \ . \tag{2.22}$$

In the relativistic limit, these equations can be solved exactly for both sets of statistics, giving:

$$n_i^{(0)} = \left[\frac{3}{4}\right]\frac{\zeta(3)}{\pi^2}g_i T_i^3 \tag{2.23}$$

$$\rho_i^{(0)} = \left[\frac{7}{8}\right]\frac{\pi^2}{30}g_i T_i^4 \tag{2.24}$$

$$p_i^{(0)} = \frac{\rho_i^{(0)}}{3} \tag{2.25}$$

where the factor in square brackets [] must be included for Fermi statistics. Shown here are the limits where $\mu = 0$ (which will often be referred to as the equilibrium value). In the non-relativistic limit, both

sets of statistics reduce to the same form:

$$n_i^{(0)} = g_i \left(\frac{m_i T_i}{2\pi}\right)^{3/2} e^{-m_i/T_i} \tag{2.26}$$

$$\rho_i^{(0)} = m_i n_i \tag{2.27}$$

$$p_i^{(0)} = n_i T_i \sim 0 \tag{2.28}$$

If we wish to relate these solutions back to the full solution including the chemical potential, we can neglect quantum statistics, and approximate the phase space distribution by the Maxwell-Boltzmann distribution ($f \sim exp(-(E_i - \mu_i)/T_i)$). This is typically reasonable for $T < m/3$ [73]. The full number density, for example, would then be given as $n_i = e^{\mu_i/T_i} n_i^{(0)}$.

We can see parametrically that, due to the Boltzmann suppression of non-relativistic species, the number and energy densities for relativistic species is typically much larger. As such, it is a good approximation to treat the entire energy density as a relativistic bath of particles, and essentially ignore any particle whose temperature has dropped below its mass. In this way, we can rewrite the entire radiation energy density as:

$$\rho_r = \frac{\pi^2}{30} g_* T^4 \tag{2.29}$$

where we assume that T is the photon bath temperature, and the effective massless degrees of freedom is a sum over all relativistic ($T_i > m_i$) species:

$$g_* = \sum_{bosons} g_i \left(\frac{T_i}{T}\right)^4 + \frac{7}{8} \sum_{fermions} g_i \left(\frac{T_i}{T}\right)^4 \tag{2.30}$$

In reality, the drops in g_* are not quite this discrete, as the change from relativistic to non-relativistic is a smooth process. The full evolution of $g_*(T)$ as a function of temperature in $SU(3)_C \times SU(2)_L \times U(1)_Y$ is shown in Fig. 2.1.

Using Eq. (2.29) as the entire energy density in the early Universe, we can then write down an explicit form for the Hubble rate we started with in Eq. (2.7):

$$H = \sqrt{\frac{g_* \pi^2}{90}} \frac{T^2}{M_{PL}} \tag{2.31}$$

Furthermore, we can show that the temperature will scale as $1/a$ (up to slight variations as g_* drops). As we will often be concerned with changes that are occuring during the radiation epoch, these relations will prove to be useful when we wish to solve for the number density evolution of interacting particles.

The final piece of thermodynamics that we will need to introduce is the idea of entropy. In an expanding Universe, the second law of thermodynamics can be written as:

$$T dS = d(\rho V) + p dV - \mu d(nV) \geq 0 \tag{2.32}$$

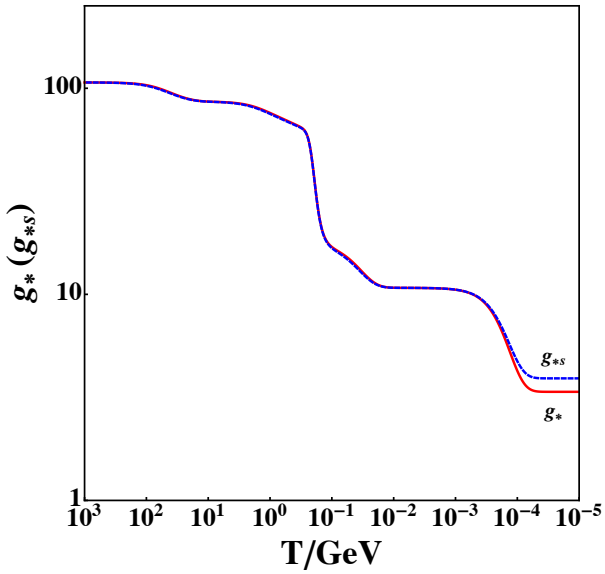

Figure 2.1: Evolution of the relativistic degrees of freedom, g_* and g_{*s} as a function of temperature in the SM.

where S is the entropy, and V is the volume of the region in question. In an expanding Universe, such that Eq. 2.6 describes conservation of energy and the vast majority of the energy density is in thermal equilibrium, we can actually take this inequality to be exact, and thus have an adiabatically expanding Universe such that $dS = 0$. If we take this together with the first law of thermodynamics given in Eq. (2.6), it is possible to define an entropy density, $s = S/a^3$ as:

$$s = \frac{\rho + p - \mu n}{T} \tag{2.33}$$

In standard cosmology in the early Universe, we only need to consider radiation energy density, as it will be much larger than contributions from any other sources.[1] In that case, the entropy density can then be written as:

$$s = \frac{2\pi^2}{45} g_{*s} T^3 \tag{2.34}$$

Here, we have introduced a new effective degree of freedom, g_{*s}:

$$g_{*s} = \sum_{bosons} g_i \left(\frac{T_i}{T}\right)^3 + \frac{7}{8} \sum_{fermions} g_i \left(\frac{T_i}{T}\right)^3 \tag{2.35}$$

At the hottest temperatures, this will map directly onto g_*, as all SM particles are in thermal equilibrium and share a common temperature. However, as particles cool and decouple from the photon bath so that $T_i \neq T$, this will deviate from g_*. Both degrees of freedom are shown in Fig. 2.1. As we will discuss in

[1] We keep the full entropy density here as reference, however, as it will prove to be useful in Part IV, where we will need to consider entropy conservation in a sector entirely dominated by out of equilibrium, non-relativistic particles

a future section, the main reason for the deviation is the decoupling of neutrinos at $T \sim$MeV, at which point they are no longer heated by further photon interactions, such as the decoupling of electron and positron annihilations.

Conservation of S implies that $s \propto a^{-3}$, and that $g_{*s}T^3a^3$ remains constant as the Universe expands. Thus, in periods when g_{*s} is constant (or varying slowly), $T \propto 1/a$, as we predicted before. The evolution of s with a^{-3} also helps us define a useful quantity that will be used throughout later chapters. For a particle that is no longer interacting with the thermal bath such that the total number of particles has stopped changing, it is straightforward to see that the quantity:

$$Y_i \equiv \frac{n_i}{s} \tag{2.36}$$

will remain constant. This is known as the yield for species i. Thus, if we can determine $n(T)$ at the last point of interaction, we can determine the density we would expect to see today, which can be used to make predictions and provide constraints based on observations of the Universe as we view it today:

$$n_0 = n_i \frac{s_0}{s_i} \tag{2.37}$$

where s_0 is the current entropy density, given by the temperature of photons today, $T = 2.7255 \pm 0.0006$K [74], such that $s_0 \sim 3000$ cm^{-3}.

We now have enough understanding of the thermodynamics of the early Universe to move onto particle interactions, which will be governed by Boltzmann equations.

2.3.2 Boltzmann Equations

As particles are interacting and maintaining thermal equilibrium, their number densities naturally become suppressed as the Universe expands. When the equilibriating reactions responsible for particle interactions drop below the Hubble rate, departures from thermodynamic equilibrium will occur. This departure from equilibrium can be described as a modification in the phase space distribution, f_i, of a species. The modification of the distribution for a single species is governed by the Boltzmann equation:

$$\hat{\mathbf{L}}[f] = \mathbf{C}[f] \tag{2.38}$$

where $\hat{\mathbf{L}}$ is the Liouville operator, and $\mathbf{C}$ the collision operator. For a spatially homogeneous and isotropic distribution (such that $f(p_\mu, x_\mu) = f(|\vec{p}|, t)$) in the FRW metric, the Liouville operator is:[2]

$$\hat{\mathbf{L}} = \frac{\partial}{\partial t} - Hp\frac{\partial}{\partial p} \tag{2.39}$$

where p corresponds to the usual magnitude of the momentum 3-vector. If we integrate both sides of Eq. (2.38) by d^3p, and include the appropriate normalizing constants, this can be transformed to a

[2]Note that we should actually take derivatives with respect to the affine parameter [71, 72]. However, we can adjust our definition of the collision operator to account for the extra factor of E that this would involve.

Boltzmann equation for the number density:[3]

$$\frac{\partial n}{\partial t} + 3Hn = \int g \frac{d^3p}{(2\pi)^3} \mathbf{C}[f] = \tilde{\mathbf{C}}[f] \tag{2.40}$$

Integrals over higher moments can be taken as well to get Boltzmann equations for the energy density, pressure, etc. In general, the collisional term will be a complex expression, involving the matrix element associated with the forward and reverse reactions, as well as the phase space distributions of each species. However, for $2 \to 2$ interactions of the form in Eq. (2.21), the equation can be vastly simplified. We present this case here, although we will be interested in generalizations of this in later chapters (for example, we will consider particles starting out of equilibrium in Part II, and $3 \to 2$ interactions in Part IV). We begin by writing down a general collision equation for the $2 \to 2$ reaction, where we are interested in the evolution of species i:

$$\begin{aligned} \mathbf{C}[f] = \frac{1}{2E_i} \frac{1}{S} \int d\Pi_j d\Pi_k d\Pi_l (2\pi)^4 \delta^{(4)}(p_i + p_j - p_k - p_l) \\ \times \{ |\mathscr{M}|^2_{kl \to ij} f_k f_l (1 \pm f_i)(1 \pm f_j) \\ - |\mathscr{M}|^2_{ij \to kl} f_i f_j (1 \pm f_k)(1 \pm f_l) \} \end{aligned} \tag{2.41}$$

where E_i is the energy of particle i, $|\mathscr{M}|_{ij \to kl}$ is the standard unpolarized amplitude, obtained with the usual Feynman rules, and we average over initial and sum over final spins. S is a symmetry factor that accounts for identical particles in the initial or final state. $d\Pi_i$ corresponds to the differential Lorentz-invariant phase space:

$$d\Pi_j = g_i \frac{d^3 p_i}{(2\pi)^3 2E_i} \tag{2.42}$$

The $1 \pm f_i$ terms correspond to Bose enhancement and Pauli blocking factors. Reversibility and unitarity of the interaction will imply that $|\mathscr{M}|_{ij \to kl} = |\mathscr{M}|_{kl \to ij} \equiv |\mathscr{M}|$. For many cases of interest, we will typically consider systems at temperatures smaller than $E_i - \mu$. In this regime, we can make a further approximation that the quantum statistics can be ignored. In particular, we can ignore the Bose enhancement and Pauli blocking factors, and further replace the equilibrium distributions by $f_{i,eq}(E) \to e^{\mu_i/T} e^{-E_i/T}$.

Making these adjustments, we can write our modified collision operator $\tilde{\mathbf{C}}$ as:

$$\tilde{\mathbf{C}}[f] = \int d\Pi_i d\Pi_j d\Pi_k d\Pi_l (2\pi)^4 \delta^{(4)}(p_i + p_j - p_k - p_l) \frac{1}{S} |\mathscr{M}|^2 (f_k f_l - f_i f_j) \tag{2.43}$$

To proceed further, we need to make some assumptions about the form of the phase space distributions. In most cases, we will be interested in particles annihilating into SM particles, or particles coupled tightly to the plasma, such that kinetic and chemical equilibrium are immediately obtained. Thus, we can replace $f_k f_l \to f_{k,eq} f_{l,eq}$. Furthermore, detailed balance allows us to replace these with the initial

[3] Strictly speaking, the term Boltzmann equation only applies to Eq. 2.38, but this terminology is widely accepted in the cosmological community.

state distributions: $f_{k,eq}f_{l,eq} = f_{i,eq}f_{j,eq} \sim e^{-(E_i+E_j)/T}$.[4] Because of this, we can do the final state phase space integrals independent of their distributions, and replace them with the cross section corresponding to the interaction:

$$\sigma v = \frac{1}{4E_iE_j}\int d\Pi_k d\Pi_l (2\pi)^4 \delta^{(4)}(p_i + p_j - p_k - p_l)\frac{1}{S}|\mathscr{M}|^2 \tag{2.44}$$

where v is the Møller velocity:

$$v = \frac{\sqrt{(p_i \cdot p_j)^2 - m_i^2 m_j^2}}{E_iE_j} \tag{2.45}$$

Using all of this, we can write a simple version of the collision operator

$$\tilde{\mathbf{C}}[f] = \langle\sigma v\rangle(n_i^{(0)}n_j^{(0)} - n_i n_j) \tag{2.46}$$

where $n_i^{(0)} = n_i(\mu = 0)$ as defined in Eq. (2.17) and we have taken the thermal average of the cross section:

$$\langle\sigma v\rangle = \frac{1}{n_i^{(0)}n_j^{(0)}}\int g_i \frac{d^3p_i}{(2\pi)^3} g_j \frac{d^3p_j}{(2\pi)^3} f_{i,eq}f_{j,eq}\sigma v \tag{2.47}$$

Using the thermal average here allows us to use truncation schemes for the cross-section. For small temperatures, and thus low relative velocities, we can compute σv in the center of mass frame, and then expand in terms of the relative velocity, v. Most interactions will have an s-wave term that is velocity independent. Then, $\langle\sigma v\rangle \sim \sigma_0$. If a symmetry forbids the lowest angular momentum term, then the p-wave cross section will become relevant: $\langle\sigma v\rangle \sim \sigma_1 T/m$. In general, we can use:

$$\langle\sigma v\rangle \sim \sigma_n \left(\frac{m}{T}\right)^{-n} \tag{2.48}$$

where σ_n will be constant, and n corresponds to the lowest allowed angular momentum state. n = 0 for s-wave, 1 for p-wave, and so on to higher angular momentum states. Putting everything together, this gives us the basic Boltzmann equation for a $2 \to 2$ interaction in the early Universe:

$$\frac{\partial n_i}{\partial t} + 3Hn_i = -\langle\sigma v\rangle(n_i n_j - n_i^{(0)}n_j^{(0)}) \tag{2.49}$$

We will make use of this equation when we discuss DM in section 2.5, and similar modified versions throughout later sections.

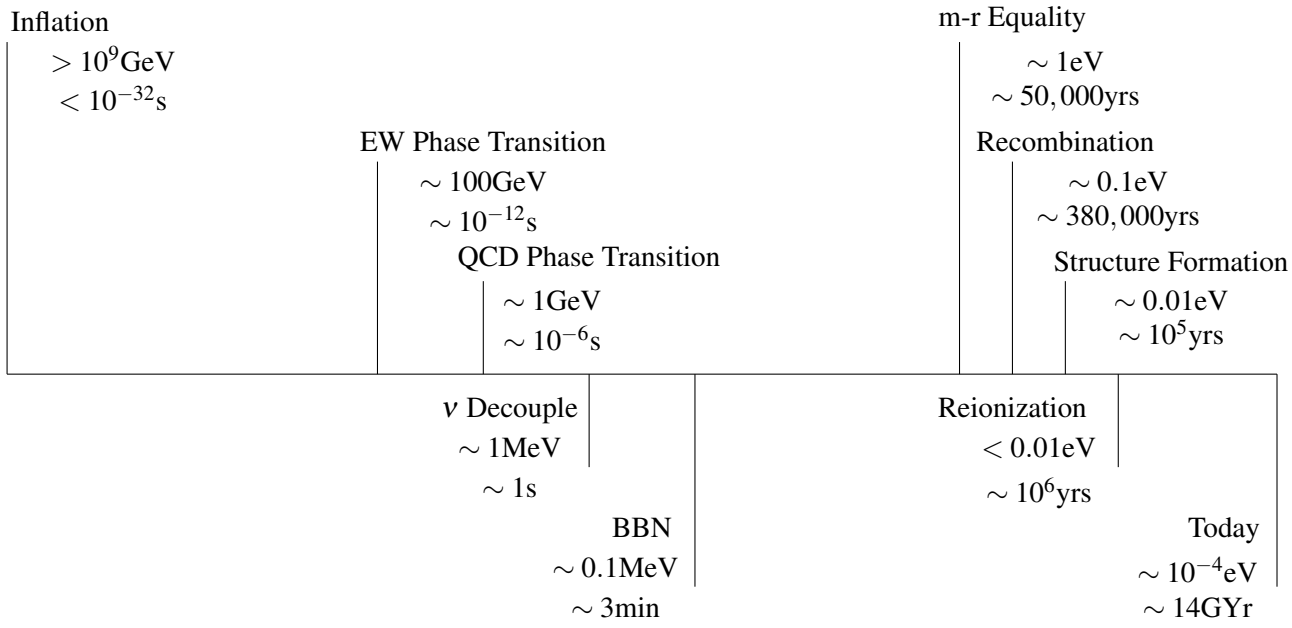

Figure 2.2: Brief timeline of the evolution of the Universe. Note that inflation could in principle happen at much lower energies.

2.4 The Universe Timeline

Now that we have tools to describe particle interactions and the evolution of the Universe, we wish to reconstruct the thermal history of the Universe. In doing so, we will highlight key problems that we do not yet fully understand, as well as epochs in our history that lead to key pieces of observational evidence that can be used to constrain new physics. A brief outline is given in Fig. 2.2 as reference. Note that in this upcoming section, we will simply assume that there is some form of dark matter making up the primary abundance of matter. In a future section we will discuss this puzzling detail that is necessary for standard Big Bang cosmology in more detail.

The Early Unknown

Above temperatures around ~ 5MeV, not much is known experimentally about what were the exact conditions of the early Universe. However, well-founded theories typically extend to energies much higher than this, often involving multiple different phase transitions early on. For example, our current vacuum state is well described by $SU(3)_C \times U(1)_{em}$, which is the unbroken remnant of $SU(3)_C \times SU(2)_L \times U(1)_Y$. It is expected that we would have gone through a phase-transition at temperatures around 100 GeV, at which point the Higgs potential would be spontaneously broken and all relevant particles would gain mass. There is also an expected QCD phase transition at around 1 GeV (the scale of non-perturbativity in QCD, Λ_{QCD}), above which quarks and gluons would be free, but below we expect the usual bound states of baryons and mesons.

[4]This is typically always true, as scattering processes that enforce kinetic equilibrium will stay relevant for longer than those that enforce chemical equilibrium.

However, even before this, we expect a phase transition corresponding to a period of inflation. In order to postulate the existence of a spatially flat, homogeneous and isotropic metric, a period of cosmic inflation is almost a requirement [75]. This epoch can solve many different problems in cosmology, including the flatness and horizon problems. However, to do so we must postulate the existence of some new scalar field to drive inflation.[5]

To see how inflation could occur, we can consider a scalar field with a symmetry breaking potential similar to the Higgs,

$$V(\phi) = \frac{1}{4}\lambda\phi^4 - \frac{1}{2}\mu^2\phi^2 + V(0) \tag{2.50}$$

Although this has a vacuum expectation value at $\langle\phi\rangle = \mu\sqrt{\lambda}$, at finite temperatures there are radiative corrections of the form $T^2\phi^2$. These would restore the symmetry, and $\langle\phi\rangle \to 0$. As the Universe cools, the symmetry would be broken either through a first order phase transition (and the field would tunnel through a barrier), or via a second order transition (and the field can transform smoothly from the local to global minima). In either case, the field can slowly transform from the false vacuum to the true vacuum if the properties of the potential are appropriate. As the field 'slow rolls' from the false vacuum to the true vacuum, it will be dominated by the constant energy density of the potential, $V(0)$. This can be large enough to overcome the energy density of any radiation present, and so dominate the energy density of the Universe. As we saw in Eq. (2.13), a constant energy density leads to exponentially driven expansion of the scale factor.

During this exponential expansion, many desired effects will happen. First, the observed isotropy and homogeneity of the Universe would be fixed, as one small causally connected region would be blown up, and the entire visible Universe would have been in thermal contact early on. This solves the horizon problem, as evolving backwards from our current point would imply that the Universe we see today would never have been causally connected, without this period of inflation. Furthermore, we can also solve the flatness problem. This is best seen by looking at the evolution of the net energy density:

$$1 - \Omega = \frac{a^2(1-\Omega_0)}{\Omega_r + \Omega_m a + \Omega_\Lambda a^4} \tag{2.51}$$

Before Ω_Λ came to be relevant, $1-\Omega$ was always increasing. However, current measurements of Ω_0 imply that the Universe is still incredibly flat, and so the initial curvature must have been fine-tuned to 1 part in 10^{60} to see the flatness we do today [77]. However, having an early period of inflation drives the flatness to zero automatically, thus bypassing the fine-tuned flatness problem altogether.

Once inflation has finished, the inflaton field can transfer its energy density to the visible, radiative sector through a process termed reheating. As the scalar field reaches the global minima of its potential, it will oscillate around this point. The kinetic energy associated with these oscillations will be transferred via decays to SM (or hidden sector) coupled particles. When the SM has had enough energy transferred

[5]For some time, it was thought that perhaps the Higgs field itself could drive inflation, but after the discover of the Higgs boson at its observed mass and self-interaction values, this is no longer considered to be the case, as it would require an extremely large coupling in $|H|^2R$. So the question of what new field is required is still open [76].

and rethermalized, we can continue with the standard hot big bang model, where radiation energy will dominate. In future sections, we will often refer to a period of reheating as an initial condition for the models we consider, but will not attempt to model the UV physics that would be required to describe how the reheating came to occur.

After this period of inflation, there is a new puzzle we must address: baryogenesis. This is the cosmological problem associated with the observed baryon asymmetry in the Universe. From our perspective, anti-matter appears to be extremely rare, only seemingly detected in accelerators or cosmic rays. In both cases, the presence of anti-matter is expected to be a result of collisions of high-energy matter, and not a primordial source. Understanding why there are more baryons than anti-baryons today is a puzzle that has not yet been explained by the SM or cosmology. Explicitly, we are trying to understand why the parameter:

$$\eta = \frac{n_b - n_{\bar{b}}}{n_\gamma} = (6.09 \pm 0.06) \times 10^{-10} \tag{2.52}$$

is close to, but not exactly zero [9, 75]. [6] Typically, we cannot even use inflation as a source of the asymmetry: any initial fluctuations in the baryon symmetry are diluted by the expansion of the Universe, while entropy is being produced, implying we would expect a symmetric Universe directly after inflation. Thus, we need a mechanism by which we can dynamically produce the asymmetry. To do so, one must postulate three conditions for baryogenesis: violation of Baryon number, B, violation of C (charge conjugation) and CP (charge conjugation-parity), and a departure from thermal equilibrium. These are known as the Sakharov conditions for baryogenesis [78], and are necessary to produce an asymmetry. Baryon number must be violated so that an asymmetry can be produced from a symmetric state. C and CP must be violated so that baryons will be produced preferentially over antibaryons. Finally, the process must occur out of equilibrium, so that the reverse process does not have the same rate.

Although all three of these conditions are met in the Standard Model, they are not strong enough to explain the entirety of the asymmetry that we see today. As such, some new physics must be incorporated to explain our observations. One such solution arises in the see-saw mechanism we considered earlier in the context of neutrino masses. In this context, an asymmetry in leptons (aptly named leptogenesis [79]) due to decays of the heavy right-handed neutrino is transferred to the baryon sector through SM sphalerons, which conserve B-L [70]. There have been many other models of baryogenesis proposed [80], all of which must invoke some new physics at scales above ~ 5 MeV. However, once we reach 5 MeV, we can take this asymmetry as a given parameter in our models, and continue the evolution with this asymmetry in mind.

[6] It is actually better to use the entropy instead of photon number density in the ratio, such that the whole ratio is actually conserved as particles become non-relativistic and freeze-out of the relativistic energy density. This is given by $n_b/s = \eta/7.04$ today.

Neutrinos Decouple

Now that the Universe has cooled to a few MeV, we can start making concrete predictions based on the interactions of the SM. One of the first important things that will happen is the decoupling of neutrinos from the rest of the visible sector. At hot enough temperatures, neutrinos are kept in equilibrium through weak interactions such as $\bar{\nu}\nu \leftrightarrow e^+e^-$ and $\nu e \leftrightarrow \nu e$. If we compare the interaction rates to the Hubble rate, we find:

$$\frac{\Gamma}{H} = \frac{n\langle\sigma v\rangle}{H} \simeq \frac{G_F^2 T^5}{T^2/M_{PL}} \simeq \left(\frac{T}{\text{MeV}}\right)^3 \tag{2.53}$$

where G_F is the Fermi constant describing weak interactions, and factors that are of order unity have been left out. At temperatures above an MeV, the interaction rates are strong enough to drive the neutrinos into thermal contact with the plasma. Below this, however, the Hubble rate is such that the Universe expands faster than the neutrinos can interact, freezing them out of thermal contact. After this point, the neutrino temperature will scale as $1/a$, independent of anything occurring in the photon plasma. This is the first of many times we will consider ratios of interaction rates to the Hubble rate, a useful tool in understanding the parametrics of the early Universe.

Shortly after neutrinos freeze-out, the temperature drops below the mass of electrons, and the entropy that was in $e^\pm$ pairs will be transferred to photons, but not neutrinos. We can estimate the effect this will have on the temperature of photons by counting relativistic degrees of freedom before and after $e^\pm$ annihilations. Directly before, we have photons (g=2), $e^\pm$ pairs (g=4), and neutrinos (g=6), and everything shares the same temperature. However, directly after, the $e^\pm$ pairs will no longer contribute, and the photon temperature will be raised above the neutrinos as they gain the electron entropy. By equating the entropy density before and after the electron annihilations, we can find that the ratio of temperatures between photons and neutrinos must be:

$$\frac{T}{T_\nu} = \left(\frac{11}{4}\right)^{1/3} \simeq 1.40 \tag{2.54}$$

We make use of this temperature ratio when considering the effects of new physics on BBN, the next step in the evolution of the Universe.

Big Bang Nucleosynthesis

After neutrinos have decoupled, the next major step in the evolution of the Universe comes from the creation of light elements during Big Bang Nucleosynthesis (BBN). These elements include D, ^{3}He, ^{4}He, and ^{7}Li. This takes place primarily at temperatures just below an MeV, when the Universe has cooled enough to allow for reactions involving heavier elements to proceed.

The main output of BBN is the relic abundance of ^{4}He, which can be estimated extremely simply by considering the parametric evolution of all the reactions involved [81]. There are three main phases typically considered in BBN: the freeze-out of neutrons, the Deuterium bottleneck, and the nuclear reactions that drive BBN. Before the onset of BBN, neutrons and protons are in equilibrium, due to

weak interactions of the form $n + e^+ \leftrightarrow p + \bar{\nu}_e$ and $n + \nu_e \leftrightarrow p + e^-$. Because the abundances are driven to equilibrium, the ratio of neutrons to protons will simply be given by:

$$\frac{n}{p}\Big|_{eq} = e^{-\Delta m/T} \tag{2.55}$$

where $\Delta m = m_n - m_p = 1.293$ MeV is the neutron-proton mass difference. Similar to neutrinos, the weak interactions keeping this abundance in equilibrium will freeze-out around 1 MeV, which leads to a freeze-out ratio of $\sim 1/6$. This sets the amount of neutrons that are initially available to take part in the creation of heavier elements. However, because neutrons decay ($n \to p + e^- + \bar{\nu}_e$), there will be slightly fewer available at the onset of BBN. This reduces the freeze-out ratio from $\sim 1/6$ to $\sim 1/7$. The main reason for the delay is the Deuterium bottleneck; many of the interactions that occur during the creation of light elements involve Deuterium. For example, the first link in the nucleosynthesis chain is $p + n \to d + \gamma$. It is also required for the production of ^{3}He (D+D$\to^3$ He$+n$), as well as ^{4}He (D+T$\to^4$ He$+n$). Because the ratio of baryons to photons is so small, the temperature must cool well below the binding energy of Deuterium ($E_B = 2.2$ MeV) before the Deuterium destruction rate falls below the production rate. Thus, BBN is delayed until $\eta^{-1} e^{-E_B/T} \sim 1$. This is at approximately 0.1 MeV.

Once we have passed this bottleneck, all nuclear reactions proceed fairly quickly. To a good approximation, nearly all of the neutrons present at this point will end up in ^{4}He, the most stable light element. Thus the primordial mass fraction of Helium, $Y_p \equiv \rho_{He}/\rho_b$ can be estimated by:

$$Y_p = \frac{2\frac{n}{p}}{1 + \frac{n}{p}} \sim 0.25 \tag{2.56}$$

This turns out to be a remarkably good estimate of the full numerical solution. The numerical results will also estimate the final yields of D and ^{3}He to $\sim 10^{-5}$ relative to H, while ^{7}Li is reduced further to $\sim 10^{-10}$ H. These can be compared to the present day observations of the abundances of these isotopes.

Deuterium is measured using absorption lines of distant quasars through damped Lyman-α (DLA) systems that have low metallicities [82]. These are good sites as they have high column densities of neutral gas, which implies a good optical depth for many of the Lyman series. Low metallicity is also useful as there will be negligible D astration from sources such as dust within the region [83, 84]. Researchers have also studied whether deuterium is formed in appreciable amounts, such as via stellar processes [85, 86], and found that deuterium is essentially not created, but only destroyed, and thus only monotonically decreases over time. Thus, any measurement of D made today will be a lower bound on the D present at BBN. That is:

$$\left(\frac{\mathrm{D}}{\mathrm{H}}\right)_{DLA} \leq \left(\frac{\mathrm{D}}{\mathrm{H}}\right)_{p} \tag{2.57}$$

One group (Cooke), continually updates their result every time a new observation for a Ly-α system is completed that matches their selection criteria [87–91]. Their most recent observation/analysis, [91]

uses results from 7 systems, and is:

$$\left(\frac{\mathrm{D}}{\mathrm{H}}\right)_p = (2.527 \pm 0.030) \times 10^{-5} \tag{2.58}$$

Another group has also recently completed an analysis of 13 systems, with a slightly smaller uncertainty [92]:

$$\left(\frac{\mathrm{D}}{\mathrm{H}}\right)_p = (2.545 \pm 0.025) \times 10^{-5} \tag{2.59}$$

If we take the weighted average of these two analyses, we get:

$$\left(\frac{\mathrm{D}}{\mathrm{H}}\right)_p = (2.538 \pm 0.019) \times 10^{-5} \tag{2.60}$$

The consensus on the Helium-3 values are much more vague, as it is a much more difficult isotope to track. Unlike when searching for D, which uses absorption lines, ^{3}He is observed in emissions from regions of ionized gas (HII regions) [93]. Thus far, only successful searches have been done within the galaxy, specifically in planetary nebulas, HII regions, and within the solar system. There is also a secondary issue that does not arise with D: stellar processes are more than happy to create helium in low mass stars, or destroy it in high mass stars. As such, it is hard to decipher the true primordial amount, and thus searches are typically done in locations that have not been too disturbed by galactic/stellar processes (such as protosolar clouds).

However, Kawasaki ([94]) and Sigl ([95]) both point out that helium cannot be used to overproduce D, and so, even though ^{3}He is much more sensitive to its surroundings, the ratio ^{3}He/D should always monotonically increase, and so you should be able to get upper bounds on the primordial abundance from regions where both He and D are measured. It also appears to be the case that the quantity (D + ^{3}He)/H is stable through galactic evolution [96], and so measuring this, together with D/H can give ratios such as ^{3}He/H and ^{3}He/D.

Some of the most recent observations are from Bania [97], who measure the upper limit on the abundance from planetary neblua:

$$\frac{^3\mathrm{He}}{\mathrm{H}} = (1.1 \pm 0.2) \times 10^{-5} \tag{2.61}$$

Mahaffy provide results from the Galileo probe that measured the ratio of He isotopes in Jupiter's atmosphere [98]:

$$\frac{^3\mathrm{He}}{^4\mathrm{He}} = (1.66 \pm 0.06) \times 10^{-4}\ , \tag{2.62}$$

and Geiss provide results from protosolar clouds [96]:

$$\frac{\mathrm{D}+^3\mathrm{He}}{\mathrm{H}} = (3.63 \pm 0.35) \times 10^{-5} \; . \tag{2.63}$$

Note that if we use the results from Eqs. (2.58) and (2.63), we get:

$$\frac{^3\mathrm{He}}{\mathrm{H}} = (1.10 \pm 0.35) \times 10^{-5} \tag{2.64}$$

Which agrees with the results from Eq. (2.61). We can also combine the Eqs. (2.58) and (2.63) to arrive at:

$$\frac{^3\mathrm{He}}{\mathrm{D}} < 0.44 \pm 0.14 \tag{2.65}$$

Note that this is much lower than the value cited in Kawasaki [94]: this is because they don't use the observed value of D/H from Cooke, but rather those from Geiss. Using this, you arrive at:

$$\frac{^3\mathrm{He}}{\mathrm{D}} < 0.83 \pm 0.27 \tag{2.66}$$

Like ^{3}He, ^{4}He measurements are coming from ionization regions such as HII, the sun, planetary nebulas, and regions within the galactic disk [99]. Again, they look for regions that have low metallicity so that the region is relatively unaffected by stellar processes, giving the best indication of the initial primordial abundance. Although the fit is done by determining the abundance vs. metallicity and then extrapolating to low metallicity [100, 101], having as much data as possibile at low metallicities is the current observational goal.

There appear to be three current measurements of Y_p, the helium fraction. The first is from the group that did the actual observations [102], who update their old measurement by incorporating both optical and IR measurements of the helium emission lines to help constrain the density by breaking a degeneracy in the parameter space with temperature. They have 45 low metallicity HII regions from 'primitive galaxies.' The Izotov group determines:

$$Y_p = 0.2551 \pm 0.0022 \tag{2.67}$$

Two other groups have used the data from the observations. The first is Aver [101], who use updated emissivities from Porter [103] to arrive at:

$$Y_p = 0.2449 \pm 0.0040 \tag{2.68}$$

And the second is Peimber [104], who also use the updated emissivities, and arrive at:

$$Y_p = 0.2446 \pm 0.0029 \tag{2.69}$$

Note that Eqs. (2.68) and (2.69) agree with each other, but not with (2.67). This appears to be due to the methods used, and selection criteria used for including/discarding various sources from the data set. The consensus seems to be that the Aver and Peimber results are most reliable [67]. The combined result from both of these analysis is:

$$Y_p = 0.2447 \pm 0.0023 \tag{2.70}$$

Finally, there is a puzzle associated with the abundance of Lithium. The best systems for observation of the Lithium abundance are metal-poor stars in the spheroid of the Galaxy [105]. Here, observations have shown that Lithium does not appear to vary significantly with low metallicity [106]. However, systematics and uncertainties in different measurement techniques have led to a host of different measurements for the observed abundance of Lithium [107–109]. Furthermore, in some very metal poor stars, Lithium is not even detected at all [110, 111]. Thus best estimates appear to come from the mid-range metallicities, with a value of:

$$\frac{\mathrm{Li}}{\mathrm{H}} = (1.6 \pm 0.3) \times 10^{-10} \tag{2.71}$$

taken as the safest estimate [111]. However, while observations of Helium and Deuterium are in agreement with BBN predictions, the measurement of Lithium is not, leading to the Lithium puzzle. BBN predictions tend to overpredict the amount of Lithium that should be produced compared to observations. However, there is much more uncertainty on the observational abundance and its relation to the primordial abundance, due to the possibility of both creating and destroying Lithium in different astrophysical environments. Although we do not attempt to resolve this puzzle here, it is worth noting as it could be incorporated into future works, and is often considered as a possible source of new physics.

Because the predictions of BBN agree so well with the primordial abundances inferred from present day observations, any new physics that may be present at this time is highly constricted [112]. Indirect alterations to the radiation energy density (typically denoted through the parameter N_{eff}, the number of effective degrees of freedom in the neutrino sector) will alter when neutrons freeze-out, which in turn alter the final amount available to produce ^{4}He. Furthermore, direct dissociation of the elements can occur via the decay or annihilation of new particles during or following BBN.

If the energy is injected via hadronic channels, it is possible to affect both the process of BBN as well as the outputs. For short lifetimes ($\tau < 10^4 s$), hadronic decays will produce partons that will hadronize into stable particles (such as pions and nucleons) that will directly alter the final abundances. Long-lived partons may interact with background nuclei, and charged current interactions with pions can alter the neutron-proton ratio, all of which will alter the final abundances of light elements. However, more stringent constraints can be placed on decays after the production of ^{4}He. Once ^{4}He has been produced, hadrodissociation can occur, breaking up the light elements. Energetic nucleons can also cause spallation processes on Helium, once again reducing its abundance and interfering with present day observations.

Energy can also be injected via electromagnetic channels as well (or into the EM channels via sec-

ondary EM showers produced by hadronic decays). In this case, photodissociation of the light elements can take place. However, these tend to occur at later lifetimes, as high energy decays can efficiently scatter off the background photons, dissipating the energy that could be used for photodissociation. It is only when energies drop below a critical energy:

$$E_c = \frac{m_e^2}{22T} \sim 2 \text{ MeV} \left(\frac{6 \text{ keV}}{T} \right) \tag{2.72}$$

that photodissociation typically begins to take place [7]. This tells the temperature (and equivalently, the time), at which electromagnetic decays become important. In particular, we can equate the binding energies of the light elements with the critical energies to find the relevant temperatures [112]:

$$T_{ph} \simeq \begin{cases} 7 \text{ keV} & {}^7\text{Be} + \gamma \rightarrow {}^3\text{He} + {}^4\text{He} \qquad E_b = 1.59 \text{ MeV} \\ 5 \text{ keV} & \text{D} + \gamma \rightarrow n + p \qquad\qquad\quad E_b = 2.22 \text{ MeV} \\ 0.6 \text{ keV} & {}^4\text{He} + \gamma \rightarrow {}^3\text{He} + n \qquad\quad E_b \sim 20 \text{ MeV} \end{cases} \tag{2.73}$$

As the temperature drops below each of these scales, the light element begins to be destroyed, which highly constrains the presence of any new particles decaying at these temperatures. Note that as the temperature falls below 0.6 keV, photodisintegration of ^{4}He actually implies net production of D and ^{3}He as well. We can make use of this to constrain new physics, and will use the remarkable accuracy of BBN and the primordial abundances of the light elements in future chapters.

Matter-Radiation Equality

Once the light element abundances have been formed, the Universe continues to evolve relatively uninterrupted. At some point, the Hubble expansion rate has caused the scale factor to reach a point at which matter and radiation contribute equally to the radiation density. If we ignore any contributions to matter except for the baryon component, we would find that this occurs at a redshift of z$\sim$550, which will have consequences for structure formation [113].

However, we expect there to be a large dark matter component to the matter density today (in fact, this is one of the reasons why). If we plug the observed densities today into Eq. (2.14), we find that the actual epoch of matter-radiation equality physically corresponds to a scale factor of $a \sim 2 \times 10^{-4}$, or a redshift of $z \sim 3600$. This is when the Universe is $\sim$ 50,000 years old. After this occurs, matter will be the dominant energy form, and the expansion speed will actually increase relative to the radiation dominated epoch, with scale factor increasing like $t^{2/3}$ instead of $t^{1/2}$. At this point, dark matter overdensities, which have already formed out of primordial fluctuations, will begin the slow push to nonlinear growth that will signal the true start of structure formation.

Recombination and the CMB

As the Universe continues to expand, the photon-baryon plasma is initially tightly coupled, as Compton scattering of free electrons efficiently thermalizes photons to the baryonic matter. However, as the

temperature cools below the ionization energy of Hydrogen, neutral atoms form and photons no longer have anything to scatter with. This point of recombination is the 'last scattering' surface for photons, after which they free-stream towards us. This occurs at temperatures of about 0.1 eV, or 380,000 years (or a redshift of 1100) into the evolution of the Universe.

Because photons free-stream from this point on, they give us a unique snapshot of what the Universe looked like when it was still relatively young. Careful study of this epoch can give us a rich and detailed account of the parameters that make up the standard model of cosmology. Light from this time is known as the Cosmic Microwave Background (CMB), and its spectral form is a main supporting pillar of the hot Big Bang model for the Universe. In particular, we can use the CMB to study the evolution of density perturbations that would eventually give rise to the structure (galaxies, clusters, etc) that we see today. A good review can be found at Ref. [114], while a more up-to-date review, with current parameter values, can be found at Ref. [26].

Although the physics that must be incorporated to completely model the shape of the CMB spectrum is complicated, we can explain qualitatively the main features that we expect to see. These can be explained by the evolution of two different types of length scales (or equivalently, the Fourier modes, described by wavenumber, k): those that were in causal contact at the time of last scattering, and those that were not. Because the over-densities at this point are still small ($\mathcal{O}(10^{-5})$), they can be modelled as linear perturbations, and thus the separate modes will evolve independently. These length scales can be directly related to angular distances on the sky: smaller causally connected regions (larger k) map directly onto smaller angular distances.

With this in mind, we can lay out the main features of the CMB spectrum:

- The 'monopole' of the CMB. This corresponds to the overarching blackbody spectrum and associated temperature that is predicted for an isotropic and homogeneous fluid. Because inflation (or something like it) provided a causally connected surface that later rapidly expanded out of contact, it is expected that the temperature of the CMB should be uniform in all directions. Indeed, the fact that we observe such a uniform backbody is a strong motivation for inflation.[7]

- The 'dipole' of the CMB. This is another large, overarching feature due to Doppler boosting of the underlying spectrum caused by the motion of the Earth relative to the isotropic background. This is not a 'primordial' feature of the CMB, but rather an effect that must be removed to see the true underlying anisotropies.

- CMB anisotropies. As we mentioned already, the seeds of density perturbations that eventually give rise to structures should also be present in the CMB. These density perturbations would, for example, arise naturally as quantum fluctuations in the gravitational potential during inflation. These lead to four main features in the anisotropies of the CMB:

    1. The Sachs-Wolfe plateau. For modes that were not yet back in causal contact at the time of recombination, the spectra should be a direct measure of the primordial density fluctuations,

[7] Late decays of non standard particles could distort the near perfect blackbody frequency spectrum of the CMB. We discuss the possible effects of such decays in Parts III and IV.

as only gravity is able to affect these modes. By this point, the density fluctuations in matter are closely following these initial perturbations, and so the large scale anisotropies in the temperature of CMB photons should follow the over-densities present in matter. As the Universe is matter dominated at the time of recombination, the gravitational potential is constant, and so there should be a plateau in the power spectrum as all different scales crossing into causal contact see the same potential [71]. Interestingly enough, although at the time of recombination, the over-densities would correspond to hotter, denser regions, the photons that reach us have actually redshifted (to climb out of the gravitational wells), and so we see these as colder regions in the CMB at large scales.

2. The Integrated Sachs-Wolfe (ISW) rise. At the largest scales, we expect a deviation from the primordial fluctuations due to the presence of the cosmological constant, Λ. This is due to the change in the comoving distance that must be considered when modes come into causal contact closer to the time of dark energy dominating the energy density. Thus, the largest scales are slightly raised above the Sachs-Wolfe plateau.

3. Acoustic Peaks. For small scales that are back in causal contact before recombination, the photons were tightly coupled to the electrons present in the plasma. As a result of this coupling, the photon-baryon plasma can effectively be treated as a driven harmonic oscillator, with sound speed $c_s \sim 1/\sqrt{3}$, driven by the perturbations of the gravitational potential. As such, the photons and baryons will oscillate around the over-densities, causing the photon temperature spectrum to fluctuate accordingly. At the time of recombination, the phases of the oscillations are frozen in, which become projected onto the sky today as peaks and troughs in the temperature power spectrum. The locations of the peak will vary with the sound speed (which depends on the baryon abundance), and the strength of each peak depends on the baryon abundance as well. Thus, the size and location of these peaks tells us unique information about the baryon density instead of the entire matter density. This is a strong piece of evidence for dark matter as well, as it is indicative of the baryon density being much smaller than the net matter density required to explain the Universe as we see it today.

4. Silk Damping. Because the photon-electron plasma coupling is not perfect, there will be some diffusion associated with the coupling. In particular, it takes time for the ionization fraction of electrons to be reduced to zero, and so the last scattering surface will actually have some thickness associated with it. Any modes that are shorter than this scale will have their anisotropies washed out, and the peaks in the oscillations are damped.

Taken together, these peaks and plateaus provide a strong theoretical prediction for the CMB that has been tested extensively over the years, from the COBE satellite, to WMAP, to the third generation CMB telescope Planck [115–117]. In this era of precision cosmology, the CMB continues to agree remarkably well with predictions, and stands as a true pillar of cosmology. Because of the remarkable agreement between the CMB and the standard model of cosmology, any new physics that we might introduce must

not interfere too much with this spectrum. For example, increasing the amount of radiation energy in the early Universe (through the parameter N_{eff}, the effective degrees of freedom in the neutrino sector) will delay the onset of matter-radiation equality, damping the peaks in the CMB anisotropy oscillations. We will use the stringent behaviour of the CMB to place limits on new models in future chapters.

Structure Formation

Following the formation of the CMB, matter over-densities will continue to evolve. During the radiation dominated epoch, these perturbations will be partially damped by pressure waves in the radiative bath. However, as the over-dense regions grow large enough, they overcome the radiative effects, growing logarithmically with the scale factor during this epoch [71]. After matter-radiation equality, the over-densities continue to grow, but now linearly with scale factor. For density modes that have only just recently entered into the cosmic horizon, the growth will be slightly altered due to the presence of the cosmological constant. In a low mass-density Universe, the growth of over-densities is reduced to:

$$\frac{d\ \ln\delta}{d\ \ln a} \sim \Omega_m^{\gamma} \tag{2.74}$$

where δ is the matter over-density, and the gamma parameter is $\sim$0.55, independent of vacuum density [118]. Thus, perturbations grow fastest during matter dominated epochs. This is strong evidence for dark matter being 'cold.' If dark matter was hot, or relativistic, for a long enough time, it would take longer for the Universe to reach matter-radiation equality, thus delaying the start of structure formation, at which point we would not expect to see the structures that we do today. This actually implies a lower bound on the mass of thermal dark matter [119]:

$$m_X \gtrsim \text{keV} \tag{2.75}$$

Eventually, these densities will grow non-linear, and the full structure of the Universe will begin to be realized. The earliest stars will form, expected to be extremely large and bright Population III stars [120, 121]. The furthest galaxy yet recorded has been at a redshift of $z \sim 11$ [122], signalling the onset of structure formation at around 10^{5-6}yrs.

Reionization

After the earliest stars and galaxies have formed, the Universe may go through a period of reionization. In this epoch, the non-thermal light from stars, quasars, early supernovae, etc., will travel through neutral Hydrogen that has not collapsed yet, partially reionizing the matter. This reionization shows up in the CMB today as an increase in the damping of small scale anisotropies and peaks. The presence of this astrophysical effect shows up in the measurement of the reionization optical depth from CMB data, which is taken as a fundamental parameter that must be measured. The optical depth, τ is a measure of the mean free path of photons between now and reionization, and causes the amplitude of the anisotropy peaks to be damped by $e^{-2\tau}$ [123].

This can be used as a useful tool if we wish to constrain new physics. Any new particles that inject energy into the inter-galactic medium (IGM) during the cosmic 'dark ages,' while photons are free-streaming and the ionization fraction is low can alter the reionization optical depth, which in turn would appear in the temperature spectrum of the CMB. This can occur if particles decay or annihilate to SM particles during this epoch. Although the effect may persist throughout the cosmic dark ages, ionization of the IGM has the strongest effect on the CMB if energy injections actually occur near recombination, ionizing neutral hydrogen and broadening the last scattering surface. As the CMB is so well measured and understood, this can place strong constraints on the types of new physics that may be allowed.

The Present Day

After reionization, we finally arrive at the present day. At this point, structure formation has successfully built up a vast network of galaxies, galactic clusters, filaments, and voids to create the enchanting Universe that we live in. As recently as redshifts of $z \sim 0.3$, the Universe is expected to have become dominated by the cosmological constant, Λ. During this current epoch, there are a variety of different methods that may be used to constrain new physics, as we can physically look out and search for signals that are being created today. These include looking at gamma ray bursts from high density regions, searches for weakly-interacting massive particles (WIMPs) in various experimental setups, and even more recently using gravitational waves to limit new models. Thus we have now seen the evolution of the Universe, and have seen many different tools that we can use to constrain new physics. In the bulk of this work, we will focus on constraints that pertain to BBN and the CMB, although when applicable we will consider others as well. In particular we are interested in how new physics in a dark sector will interact with the rest of the SM. This dark sector may contain DM, which we will discuss in more detail now.

2.5 Dark Matter

Over the last few decades, evidence for the existence of some source of non-luminous matter has become overwhelming. We discuss here the evidence for such dark matter, as well as possible candidates and their production mechanisms. Excellent references and reviews can be found at [124–127].

2.5.1 Evidence

Evidence for dark matter began to amass as early as the 1930s. Some of the earliest and most convincing evidence comes from the velocity dispersion of galaxies. This was first observed in the Coma cluster, which had galactic velocities within the cluster not supported by the amount of luminous matter alone [128]. This was further reinforced by the measurement of galactic rotation curves [129–131]. We may consider a single object that is orbiting at some radius, r, from the center of a galaxy. Assuming spherical symmetry and a stable Keplerian orbit, the velocity of this satellite should be:

$$v(r) = \sqrt{\frac{GM(r)}{r}} \tag{2.76}$$

where M is the amount of mass inside the orbit. Observations of spiral galaxies indicate that most of the luminous matter lies within the central bulge, and so, if this makes up the bulk of matter, velocities should be $\propto 1/\sqrt{r}$. However, galactic rotation curve observations show that the velocity is roughly constant at large r, implying that $M \propto r$ in this region, or $\rho \propto r^{-2}$. This cannot be explained by the visible matter alone, and so the standard adopted theory is that of a spherical dark matter halo, within which the baryonic matter of stars, dust, and gas is embedded.

The dark matter distribution of galaxies, clusters, and even larger scales can also be mapped using gravitational lensing. This technique uses background galaxies to map the density of matter by correlating distortions in their images to the amount of matter present in the foreground. One of the most famous examples of this is the Bullet Cluster, which is the remnants of the collision of two clusters in recent (cosmological) times [132]. The result of the collision was the collapse of baryonic matter as particles interacted and dissipated kinetic energy as they fell into the gravitational well. This can be measured directly using x-ray emissions from the hot gases. However, when gravitational lensing is used, the map clearly shows that the bulk of matter associated with the cluster is separate from the visible matter, having not felt the strong dissipative effects associated with the baryons.[8]

These astrophysical observations are supported by many other independent sources of proof. Most of these we have discussed already in Section 2.4, and come from a larger cosmological scale. For example, BBN and the CMB together put strict constraints on the overall abundance of baryons that can be present to produce both the abundance of light elements we see today, and the peaks of the oscillations in the CMB temperature anisotropies. However, the CMB also needs a specific overall matter density so that the correct scales are sub-horizon at the time of recombination, to match the observed patterns we see today. Between these two values, we can place stringent limits on both matter densities [67]:

$$\Omega_c h^2 = 0.1198 \pm 0.0012 \tag{2.77}$$

$$\Omega_b h^2 = 0.02233 \pm 0.00015 \tag{2.78}$$

where Ω_b is the baryon abundance and Ω_c is the excess abundance required by cold dark matter. This implies that we need 5-6 times more dark matter than we have baryons, a ratio that is in agreement with the amount required by velocity dispersions in galaxies. This is also in agreement with structure formation arguments for dark matter. The presence of early universe galaxies is only possible if non-linearities have had time to grow before the redshift of galactic observations. Because we know from the CMB that the density perturbations were still very linear at the time of recombination, there needs to be an extended period of time between then and galactic formation in which matter over-densities can grow faster. Because these over-densities grow linearly (vs logarithmically) during matter dominated epochs, and cold dark matter would push the matter dominated epoch back further, the presence of such old galaxies is once again compelling evidence for cold dark matter.

While there is extremely compelling evidence for the existence of DM on scales the size of galaxies

[8] In fact, this is strong evidence that dark matter can only be weakly self-interacting, otherwise the dark matter would not have remained separated as the clusters collided. This can be used to place limits on the mass and self-interactions of dark matter candidates, as we shall consider in later chapters.

and larger, there are still some troubling conflicts between astrophysical observations and simulations on smaller scales. These challenges to the DM hypothesis include the missing satellite problem, cusp-vs-core, diversity, and the 'too-big-to-fail' ([133, 134]) problem. In the missing satellite scenario, N-body simulations of DM in galaxies tend to predict far more substructure and satellite/sub-haloes than what we actually observe [135]. Similarly, these same simulations often predict 'cuspy' profiles for the dark matter, with the density scaling like 1/r near the core of galaxies. However, galactic observations include many cored inner profiles, with densities nearly constant over the core [136]. This ties into the diversity problem, which implies that there should be remarkably little scatter in density profiles for a given halo mass. In nature, this does not seem to be evident, as there seems to be a large scatter in the profiles of observed galaxies [137]. Finally, the 'too-big-to-fail' problem is that the largest sub-haloes of the Milky Way should be dense enough to host star formation and their own observable galaxies, but this is not observed [138]. All of these issues stem from the overabundance of substructure in dark matter structure simulations. There is ongoing work to try to solve these issues: these include incorporating baryons or self-interactions of dark matter into the simulations [137, 139, 140].

2.5.2 Candidates and their Production Mechanisms

In order to have a candidate for dark matter, it must satisfy multiple conditions. It must be stable on cosmological timescales, have extremely weak EM interactions, and have the correct relic abundance. There are many such candidates to be found in BSM models, including those models which we have already discussed when attempting to solve other problems in the SM. For example, the axion, originally postulated to solve the strong CP problem, may produce DM via the oscillation of the axion field around its minima. These coherent oscillations redshift the same way as matter, and could have the correct relic abundance if the free parameters of the model are tuned appropriately [125, 141]. Supersymmetry, proposed to solve the hierarchy problem, may also produce dark matter candidates, if there is an exact R-parity that forces the lightest super-partner (LSP) to be stable [142]. Little Higgs models also produce viable DM candidates if a T-parity is imposed, such that the lightest T-odd particle is stable [125]. Finally, sterile neutrinos (proposed both to give mass to SM neutrinos and perhaps solve the baryon asymmetry) could also be DM candidates, with the added bonus that light sterile neutrinos could make up a small portion of warm dark matter that could help to alleviate the core-vs-cusp problem [143, 144].

To address the question of whether or not these (and many other) candidates have the correct relic yield, we must consider the various production mechanisms. These fall into two broad categories: thermal and non-thermal production.

Thermal Production

In thermal production of dark matter, the new BSM candidate is in thermal equilibrium with the SM at high temperatures. This is the standard WIMP scenario, which has very weak couplings to the SM, but large enough to equilibriate at high temperatures. WIMPs will typically have interactions of the form $\chi\chi \leftrightarrow SM\ SM$, where χ is the DM candidate. As the temperature cools, the reaction rates keeping this equilibrium will fall below the Hubble rate, causing the particle to freeze-out of equilibrium, at which

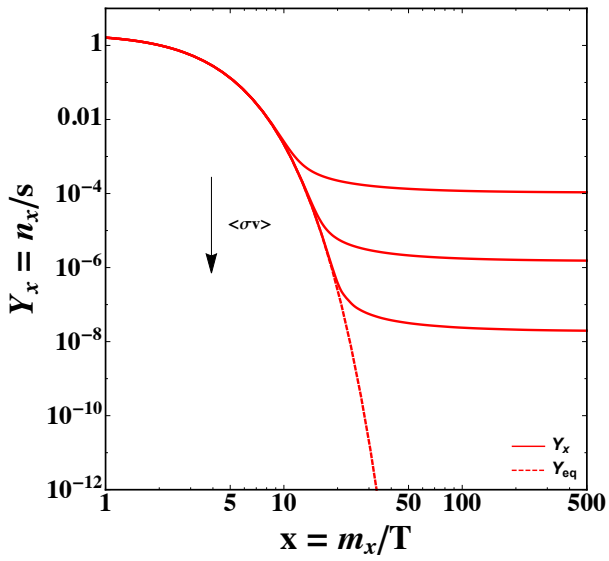

Figure 2.3: Generic freeze-out of a WIMP, the most commonly considered production mechanism for dark matter. Going to lower branches is equivalent to moving to larger cross-sections.

point it will evolve independently with constant yield, as defined in Eq. (2.36). The numerical solution for such a yield is shown in Fig. 2.3. This constant yield can be estimated semi-analytically in the case of WIMPs. We can begin at Eq. (2.49), where the standard lore is to use the relic yield, Y_x, instead of particle number, and an inverse temperature ($x = m_x/T$), where m_x is the DM candidate mass, instead of time, as the evolution variable. Recast in these variables, the freeze-out interaction Boltzmann equation becomes:

$$\frac{dY_x}{dx} = -\frac{xs}{H(m_x)}\langle\sigma v\rangle(Y_x^2 - Y_x^{(0)^2}) \tag{2.79}$$

We can estimate the temperature at which the particle freezes out by equating its interaction rate to the Hubble rate:

$$H \simeq \langle\sigma v\rangle n_x^{(0)} \tag{2.80}$$

where we can use the equilibrium number density as an approximate solution before freeze-out. Solving this equation for an arbitrary partial wave (Eq. (2.48)) in the cross-section, we find the approximate freeze-out temperature [70]:

$$x_{fo} \simeq \ln\left[\sqrt{\frac{90}{8\pi^3}}\frac{g_x}{g_*^{1/2}} m_x M_{PL}\sigma_n\right] - (n+1)\ln\left(\ln\left[\sqrt{\frac{90}{8\pi^3}}\frac{g_x}{g_*^{1/2}} m_x M_{PL}\sigma_n\right]\right) \tag{2.81}$$

where n is the power of the temperature in the partial-wave being considered and g_x the degrees of freedom of the DM particle. This corresponds to $x_{fo} \sim 20$ for a large range of masses, as there is only a logarithmic dependence on the parameters involved. Following freeze-out, the yield will stop following

equilibrium, and Eq. (2.79) can be solved exactly, as $Y_x \gg Y_x^{(0)}$. Doing this results in an approximate solution for the final yield of:

$$Y_\infty \sim \frac{45}{2\pi\sqrt{90}} \frac{g_*^{1/2}}{g_{*s}} \frac{n+1}{M_{PL} m_x \sigma_n} x_{fo}^{n+1} \tag{2.82}$$

or in dimensionless units (for n=1):

$$\Omega_x h^2 = m_x Y_x \frac{s_0}{\rho_C} \sim 0.1 \left(\frac{3 \times 10^{-26} cm^3/s}{\langle \sigma v \rangle} \right) \left(\frac{x_{fo}}{20} \right) \tag{2.83}$$

A new particle with weak-scale couplings, such that

$$\langle \sigma v \rangle \sim \frac{g^4}{(4\pi)^2} \frac{1}{m_x^2} \sim 10^{-23} cm^3/s \left(\frac{100 \text{ GeV}}{m_x} \right)^2 \tag{2.84}$$

has nearly the exact cross-section required for the correct relic abundance for masses at the weak scale.[9] This is known as the WIMP miracle, and has driven the search for WIMP-like DM for many years.

Although many thermal interactions will follow this approximate form, there are some deviations that must also be considered. These become important when the DM candidate is interacting with other states present in the plasma at the time of decoupling. These effects include coannihilations, in which a species with a similar mass efficiently depletes the DM density, and resonant enhancements if the mass of the DM particle is close to that of a mediator [145]. Sommerfeld enhancement due to the presence of a light boson mediator will also cause changes to the present day cross-section (relative to the cross-section at freeze-out), which has significant implications when constructing detectors [146].

Finally, another thermal method to produce dark matter may be through a $3 \leftrightarrow 2$ self-interaction of the DM candidate [147]. If kinetic equilibrium with the visible sector is maintained, these so-called self-interacting massive particles (SIMPs) require large self-interactions in order to deplete the yield to an acceptable level. We consider a variation of this production mechanism in Part IV, in which we do not require thermalization with the visible sector, but make use of this self-interacting number changing interaction to set the relic abundance in a disconnected dark sector.

Non-Thermal Production

Dark matter can also be produced via non-thermal mechanisms, in which the thermally averaged cross-section connecting the SM to DM is not the main contributing factor. As we briefly discussed above, axions are a classic example of a non-thermal dark matter candidate, as it is simply the coherent oscillations of the axion field that contribute to dark matter, and not the axion itself.

Another non-thermal production mechanism includes gravitational production of WIMPZillas, superheavy DM states [148]. These are produced similarly to the inflationary generation of gravitational

[9] Although there are a few orders of magnitude difference between the cross section required to get the correct relic density and the naive weak-scale estimate, the fact that these two values are still so close is the true miracle. There are many sources of uncertainties, such as the true coupling values, form of the cross section, current Hubble rate, etc., that could easily push this closer to the desired value.

perturbations that seed the formation of large scale structure. Effectively, for very large masses, a very small number of particles must be produced. This is done via the decay of the inflaton, which effectively reheats the SM sector, which in turn can produce a very small amount of the WIMPZilla candidate. This is a specific case of a more general class of massive particle decays in the early Universe. If the original massive particle has very weak couplings to the SM, it may freeze-out of equilibrium very early with a large relic abundance. This could lead to an early period of matter domination, which could have interesting implications for the evolution of structure in the Universe. When the massive particle decays, the Universe goes through a (possibly secondary) period of reheating, as the massive particle transfers all of its energy to radiative energy density. This could partially transfer energy to 'superWIMPs' at the same time, leading to a non-thermal production of the DM candidate [149, 150].

There is also the possibility that dark matter is set by an asymmetry in the dark sector, similar to the unknown mechanism producing the baryon abundance [151]. This would require that the DM particle, ψ, have a distinct antiparticle, with which it could efficiently annihilate. If these annihilations are strong enough (typically much stronger than WIMP interactions), the symmetric densities will be washed out, leaving behind the asymmetric abundance of only ψ particles. This would have the unfortunate side-effect of being very difficult to detect today, as there would no longer be any annihilations occurring. However, it does have an appealing symmetry, in that the asymmetry setting the dark matter abundance could also, in principle, be setting the baryonic abundance. This could happen if dark matter has a conserved charge related to baryon number. In this case, we get a nice relationship between the mass of dark matter and baryonic matter. As there is $\sim$5 times more dark matter than baryonic, then we would expect the masses to be $\sim$5 times higher as well.

Finally, there is the possibility of freeze-in (FI) of dark matter. This corresponds to the production of DM through a thermal scattering off SM particles that was too feeble to ever thermalize the two sectors [152], but strong enough to allow some energy-leakage into the hidden sector. Freeze-in can occur if two conditions are met: the dark matter particle starts with a negligible density, $n_x \ll n_x^{(0)}$, and the particle interacts weakly with the SM so that thermodynamic equilibrium is never attained. When renormalizable operators govern the interaction, this is typically called feebly-interacting massive particle (FIMP) dark matter, as the coupling strengths must be much smaller than even a standard WIMP scenario. An excellent review of FIMPs can be found at Ref. [153]. Although renormalizable operators have been well studied, less emphasis has been placed on non-renormalizable operators [154]. We study effects associated with this explicit scenario in Part II.

2.5.3 Observational Status

Now that we have built up models to explain the nature of dark matter (and other phenomena), we can attempt to observe this new physics. Within the context of dark matter, this is typically done in three different ways: through direct detection, indirect detection, and collider searches, depicted schematically in Fig. 2.4. Direct detection attempts to measure the small recoil energy of a nucleus in underground detectors that have scattered off the ambient dark matter present that makes up the galactic halo. These have been mostly aimed at the detection of WIMP DM, as the thermal annihilation cross-section that

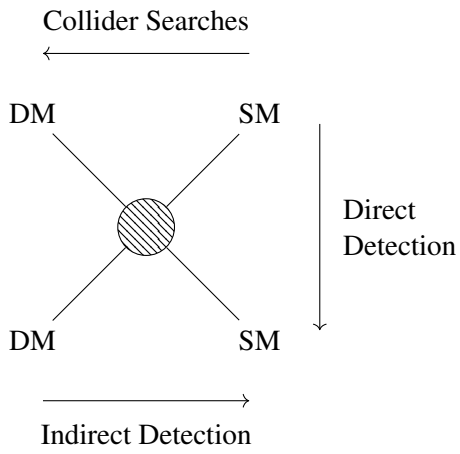

Figure 2.4: Three fundamental methods to detect dark matter.

gives rise to the relic yield should also give rise to nucleon scattering interactions today. Although there have been some hints at detections (see for example, [155, 156]), there have mostly been null results. An excellent review of the current status of direct detection experiments can be found in Ref. [26]. Although direct detection WIMP searches have historically focused on the mass range 1-1000 GeV, more recent electron scattering experiments have aimed to explore the low mass regime [157], while the upper bound has been reconsidered in multi-scatter models [158].

While direct detection considers the scattering cross-section, indirect detection looks explicitly for the flux of final stable particles produced by annihilations and decays of dark matter. Gamma-ray observations of dwarf galaxies and the Galactic center, which should have high densities of dark matter, provide robust limits on the cross-sections and masses of dark matter that could be present. Although there have been some reported excesses (such as the Galactic center excess [159], the 3.5 keV line in clusters [160], an antiproton excess [161], and a positron excess [162]), it is not clear yet whether these excesses are BSM in nature, or if they can be explained by more natural astrophysical sources. A review of the current status of indirect detection experiments and limits can be found in Ref. [163].

A more direct way to attempt to see dark matter is at colliders, where we do not rely on the ambient presence of dark matter on galactic scales, but rather attempt to produce it via the collision of SM particles. There has been a great deal of work in constraining dark matter in this way, with more null results complementing the direct detection searches [164–166].

The majority of these DM searches hinge upon having a strong enough interaction in Fig. 2.4 for a detection to occur. This has lead to the search being mostly focused on WIMPs, as they have the most appealing interactions to search for today. The lack of evidence for WIMP DM thus far has lead to growing interest in the non-thermal production mechanisms listed above. With the lack of WIMP DM, we have also had many null results in the search for physics to explain any of the other current problems in the SM. Because of this, combined with an unprecedented era of precision Cosmology, we have begun to place more indirect constraints on new physics using all of the different Universal epochs we discussed above. These constraints are complementary to those provided by direct detection and

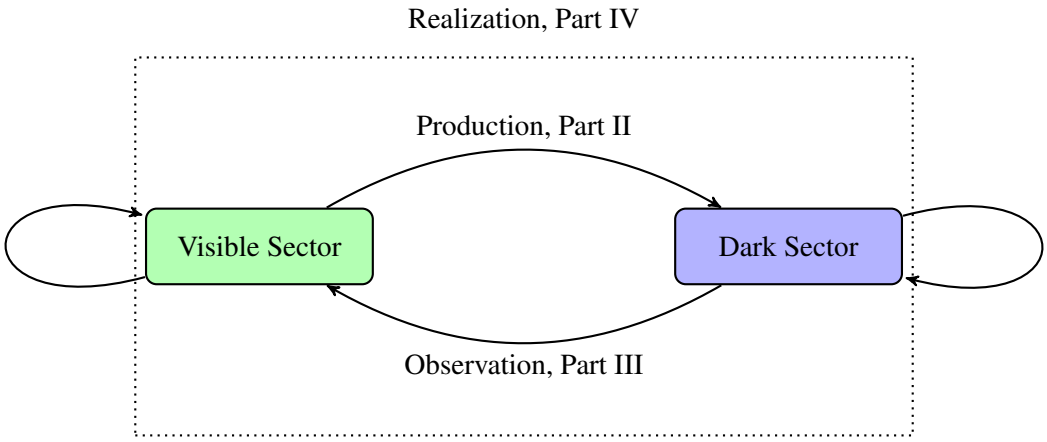

Figure 2.5: Visualization of the connections possible between the visible and dark sectors.

colliders, and provide invaluable information as we attempt to narrow down the possibilities for new physics in our Universe.

2.6 Beyond the Standard Models

Now that we have built up a solid foundation of well understood physics, between the Standard Model of particle physics and the Standard Model of cosmology, we wish to learn how new physics will interact with these models. As we have seen, there are problems that cannot be explained by the SM, including the nature of DM, the hierarchy problem, and more. This has motivated many different possible extensions, with each problem spawning a plethora of unique solutions. However, well motivated physics models need to do more than just answer the questions they were proposed to solve. In particular, new models must not contradict currently known and well understood effects in other areas. In this thesis, we study exactly how new physics may interact with old, from a variety of angles. Concretely, we shall focus on dark (or hidden) sectors, that may contain dark matter, decaying dark particles, or more. These dark sectors may have weak, feeble, or non-existent interactions with the SM. The very nature of these feeble interactions suggest that we must move beyond the conventional collider searches, and so we approach this problem using cosmological observables as our basis for constraining new physics. As we are now in an era of unprecedented precision cosmology, these observables will prove to be invaluable tools moving forward.

This is depicted schematically in Fig. 2.5. Within each sector, there will be interactions between all the particles present, while at the same time energy may flow between the two sectors during different eras of the Universe, complicating the responses. In this thesis, we look to break this down, and focus on different components of these interactions in specific, realized scenarios. In Part II, we will start with the transfer of energy from the visible to the dark sector only, and see how this energy inflow will have a role as the dark sector continues to evolve. Following this, in Part III, we will look at the reverse process, and consider how energy flowing from the dark to the visible sector will have consequences for the evolution of SM particles and their abundances, which we can physically observe and thus constrain

this interaction. Finally, in Part IV, we will consider a fully realized model of a dark sector, that could possibly contain energy transfer in both directions, as well as a complex network of interactions in the dark sector. In breaking it up this way, we identify important information along each of the various arrows within Fig. 2.5, that can be applied to more models than just those considered here.

Part II

From the Visible to the Dark

Chapter 3

Infrared Effects of Ultraviolet Operators and Dark Matter Freeze-In

3.1 Introduction

We begin our exploration of the relationship between the visible and dark sectors by considering the effects that the visible sector can have on the hidden, which we schematically depict in Fig. 3.1. In this scenario, the visible sector will directly inject energy into the dark sector, which will concurrently be interacting with itself. These dark interactions may have self-interactions or couplings between the different components of the hidden sector. The relationship and interplay between the visible sector and the interactions of the dark sector are what we wish to explore.

This relationship is most evident when the visible sector is used to directly produce dark particles, such as dark matter (DM). It has long been known that the SM does not provide a complete description of the universe, with a key missing element being DM. This is a pressing issue, as DM has been observed cosmologically to make up the majority of matter today [67]. However, very little is known about DM beyond its gravitational influence, such as its particle properties or how its density was created in the early universe [124, 142, 167]. In this chapter, we focus on the latter in our effort to explore how the visible sector can influence a dark sector, even (especially) if the coupling between the sectors is small compared to the individual sector's self-interactions[1].

Many theories of DM coupled directly to the SM rely on thermal production, with the most-studied paradigm being thermal freeze-out, as discussed in Part I [70, 168, 169]. This simple mechanism for DM production has many attractive features: it is insensitive to the state of the very early universe, and it yields the correct relic abundance (to within a couple orders of magnitude) for a generic WIMP with mass near the weak scale[170].

Despite these enticing features of thermal freeze-out, the lack of discovery in direct detection ex-

[0]This chapter is based on L. Forestell and D. E. Morrissey, *Infrared Effects of Ultraviolet Operators on Dark Matter Freeze-In*, [arXiv:1811.08905] [1].

[1]Here, I do not necessarily mean the standard definition of self-interaction in which a single particle interacts with itself, but rather all the reactions between the (possibly many) different particles that only live in one sector or the other.

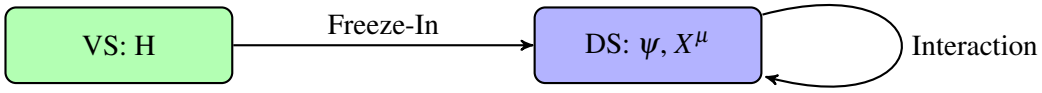

Figure 3.1: Flow of information considered in this chapter. The visible sector transfers energy and number density to the dark sector, which may go through further self-processing effects that interplay with the inflow of energy. In this chapter, the visible sector provides an interaction via the Higgs boson, while the dark sector consists of a fermionic DM candidate and a massless vector boson.

periments and collider searches for WIMPs has motivated the study of other DM production mechanisms [171, 172]. As was mentioned previously, a promising alternative is freeze-in (FI) [152], in which the DM species is assumed to interact only very feebly with the SM and to have an initial abundance well below the value it would obtain in equilibrium with the SM plasma. Transfer reactions of the form SM+SM $\rightarrow$ DM+DM then create a sub-equilibrium abundance that evolves to the DM density seen today. The feeble coupling together with this sub-equilibrium abundance means that FI is an ideal environment for studying the visible to dark sector connection, as it implies a one-way connection from visible to hidden, while the reverse is generally not true. Freeze-in can arise as a production mechanism in sterile neutrino models[173, 174], as well as the production of gravitinos[175–178], and fully understanding this method of production will be useful for many future avenues of BSM models.

Within this paradigm, there are two general classes of connectors between DM and the SM with very different cosmological behaviours, both of which are shown in Fig. 3.2. The first and most studied has DM connected to the SM through a renormalizable operator with small coupling. Production of DM for this class is dominated by temperatures near the DM mass, $T \sim m_\psi$ [152, 153, 179–188]. For this reason, it is usually categorized as infrared (IR) freeze-in. This FI mechanism retains much of the attractive insensitivity to initial conditions as WIMP freeze-out aside from the assumption of a very small initial DM density. On the flip side, the renormalizable couplings needed for IR freeze-in must be extremely feeble, which would need further explanation if one wishes to retain naturalness.

The second class of connectors leading to FI are non-renormalizable operators connecting the DM to the SM, whose interaction strength is naturally very small at low temperatures. Dominant DM production typically occurs at the highest SM temperatures attained during the radiation era, such as the reheat temperature T_{RH} post inflation[189]. Because of this early temperature dependence, this is what is called ultraviolet (UV) freeze-in [154, 189–192], with a well-known example being the gravitino in SUSY [193–196]. A less attractive property of this paradigm, is that the DM abundance depends on the state of the universe very early in its history. However, because of the natural mass suppression that arises due to the dimensionality of these operators, no further feeble (unnatural) coupling constant is required.

In this chapter we demonstrate that both UV and IR freeze-in can play a role in determining the DM relic abundance through a single, non-renormalizable connector operator. This contrasts with the standard expectation that non-renormalizable operators decouple once and for all at higher temperatures.

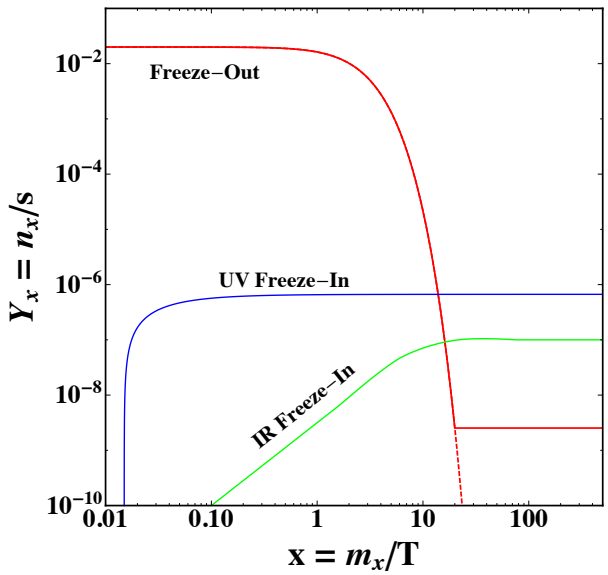

Figure 3.2: General behaviour for the yield $Y = n_x/s$ of various production mechanism for dark matter. The red curve shows the classical freeze-out behaviour (with the dotted line following equilibrium), while the blue and green curves show UV and IR freeze-in, respectively. Freeze-out occurs near $x \sim 20$, while IR freeze-in is dominant around $x \sim 1$ and UV freeze-in occurs almost completely at $x_{min} \sim x_{RH} \ll 1$.

We illustrate this feature in a concrete dark sector model consisting of a stable Dirac fermion ψ with mass m_ψ that is charged under an unbroken $U(1)_x$ gauge force with vector boson X^μ and coupling strength $\alpha_x = g_x^2/4\pi$. The only connection between the dark sector and the SM is assumed to be through the *fermionic Higgs portal* operator[197, 198],

$$-\mathscr{L} \supset \frac{1}{M}|H|^2\,\overline{\psi}\psi\,. \tag{3.1}$$

Here, M defines a very large mass scale of new physics above the energy and temperature ranges we consider. This can be done using a variety of UV completed models, as described in Refs. [199, 200]. For example, a singlet scalar S can interact with the Higgs via a renormalizable coupling. If we also include a Yukawa coupling between S and the fermionic DM, the scalar S can be integrated out to leave us with the Higgs portal. This is shown schematically in Fig. 3.3. Although the mediator creating the Higgs portal is not of interest in this work, it is still interesting to note that direct searches can be done for the mediators, such as discussed in Ref. [197, 200].

Note that we assume no gauge kinetic mixing between $U(1)_x$ and hypercharge, which can be enforced by an exact charge conjugation symmetry in the dark sector [201]. We also do not consider the pseudoscalar partner to this operator, $1/M|H^2|\bar{\psi}i\gamma_5\psi$. This is done by imposing CP symmetry. Although higher order operators could be considered, such as the dimension-6 term that comes from the four-fermion interaction, $\mathscr{L} \sim 1/M^2(\bar{Q}_L\gamma^\mu Q_L + \bar{q}_R\gamma^\mu q_R)(\bar{\psi}\gamma_\mu\psi)$, these will all be suppressed by $(m_\psi/M)^{2(d-4)}$. Because of this factor, the lowest dimension (i.e. Higgs) portal will provide the strongest effects, and thus we focus here in order to highlight the visible to hidden effects.

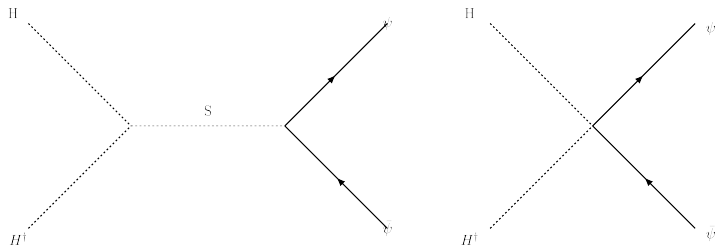

Figure 3.3: Feynman diagrams for a possible UV completion of the Higgs portal. The left diagram is the full UV model, mediated by a scalar particle. On the right, the scalar particle has been integrated out, and its propagator and couplings combine to create a new coupling, with approximate strength $\frac{1}{M}$.

The UV connector operator of Eq. (3.1) can generate both UV and IR freeze-in effects over a broad range of parameters when three plausible conditions are met. First, reheating after inflation is assumed to populate only the SM sector with visible reheating temperature T_{RH} well below the connector mass scale M. The dominant source of dark sector particles then comes from visible-to-dark transfer reactions through the connector operator (UV freeze-in). Second, for moderate to large values of the dark sector gauge coupling α_x the dark sector can self-thermalize to a temperature T_x less than the visible temperature T but greater or similar to the dark fermion mass m_ψ. And third, if the DM annihilation cross section is sufficiently large the DM abundance can track the equilibrium abundance (at temperature $T_x < T$) for long enough that transfer reactions from the non-renormalizable connector operator return as the dominant contributor to the DM abundance. This allows us to further examine the underlying behaviour of a dark sector that is directly being influenced by an inflow of energy from the visible sector, while also providing a counterexample to the standard lore that non-renormalizable operators decouple in the early universe.

The combined UV and IR freeze-in behavior we focus on in this chapter is only one of a number of "phases" of freeze-out and freeze-in possible within this dark sector model. These phases are analogous to the four phases studied in Ref. [182] for a similar dark sector consisting of a charged complex scalar DM particle connected to the SM Higgs field through the standard renormalizable Higgs portal operator, but tilted towards the UV. When the mass scale M in the fermionic connector operator of Eq. (3.1) is large relative to the weak scale and $\alpha_x \to 0$, the theory reduces to standard UV freeze-in of ψ dark matter as studied in Ref. [191] with no significant dark self-thermalization or later annihilation. In contrast, for much smaller M near the TeV scale the dark and visible sectors are thermally coupled (via the connector) throughout ψ freeze-out, and this operator can control the freeze-out process even when α_x is very small [197, 202, 203]. We focus on the scenario between these relative extremes with larger M and α_x.

This chapter is structured as follows. Following the introduction, we discuss in Sec. 3.2 the UV freeze-in transfer of number and energy density through the connector operator of Eq. (3.1) as well as dark self-thermalization. Next, in Sec. 3.3 we compute the interplay between freeze-out and IR freeze-in in determining the relic abundance ψ particles and determine the conditions under which both UV and IR freeze-in can be relevant. In Sec. 3.4, we comment briefly on the astrophysical implications of

the new dark force from DM self-interactions. Finally, Sec. 3.5 is reserved for our conclusions. Some technical details related to thermally-averaged cross sections and the calculation of freeze-in transfer rates are contained in Appendix A. This chapter is based on work published in Ref. [1] in collaboration with David Morrissey.

3.2 Populating the Dark Sector through UV Freeze-In

We begin by investigating the transfer of energy and number density to the dark sector by UV freeze-in through the connector operator of Eq. (3.1). For this, we make the standard freeze-in assumption that only the visible SM sector is populated significantly by reheating after inflation with reheating temperature $T_{RH} \ll M$ [152, 154].[2] The dark sector is then populated by transfer reactions of the form $H + H^\dagger \to \psi + \overline{\psi}$ (assuming unbroken electroweak) mediated by the operator of Eq. (3.1). Once the number density of ψ grows large enough, the dark sector may also thermalize to an effective temperature T_x through further reactions such as $\psi + \overline{\psi} \leftrightarrow X^\mu + X^\nu$. In this section we study the creation of ψ particles from SM collisions during and after reheating as well as the conditions for the self-thermalization of the dark sector.

3.2.1 Transfer without the Dark Vector

It is convenient to study first the creation of ψ fermions by SM collisions in the absence of dark vectors ($\alpha_x \to 0$) [191]. The number and energy transfer via $H + H^\dagger \to \psi + \overline{\psi}$ is described by

$$\frac{dn_\psi}{dt} = -3Hn_\psi - \langle \sigma_{tr} v(T) \rangle (n_\psi^2 - n_{\psi,eq}^2(T)) \tag{3.2}$$

$$\frac{d\rho_x}{dt} = -3H\rho_x - \langle \Delta E \cdot \sigma_{tr} v(T) \rangle (n_\psi^2 - n_{\psi,eq}^2(T)) \tag{3.3}$$

where ρ_x is the total energy density in the dark sector and ΔE is the energy transfer per collision.

Starting with number transfer, in the limit of $n_\psi \ll n_{\psi,eq}$ and $T \gg m_\psi$ the collision term is approximately

$$-\mathscr{T}(T) = -\langle \sigma_{tr} v(T) \rangle (n_\psi^2 - n_{\psi,eq}^2(T)) \simeq \frac{1}{4\pi^5} \frac{T^6}{M^2} . \tag{3.4}$$

Details of the calculation are given in Appendix A. Assuming radiation domination up to the reheating temperature $T_{RH} \gg m_\psi$, this gives the simple solution for the yield of ψ (and $\overline{\psi}$) of

$$Y_\psi(T) \simeq Y_\psi(T_{RH}) + Y_{\psi,eq}(T) \frac{\sqrt{5/2}}{2\,\zeta(2)\,\pi^4} g_*^{-1/2} \frac{M_{\rm Pl} T_{RH}}{M^2} \left[1 - \left(\frac{T_{RH}}{T} \right)^{-1} \right] . \tag{3.5}$$

This solution only holds in the limit $Y_\psi \ll Y_{\psi,eq}$, corresponding to a consistency condition of (for

[2] Obtaining such an asymmetric reheating between different sectors has been studied recently in Refs. [204, 205].

$Y_\psi(T_{RH}) \to 0$ and $T \ll T_{RH}$)[3]

$$T_{RH} \ll \frac{2\,\zeta(2)\pi^4}{\sqrt{5/2}}\, g_*^{1/2}\, \frac{M^2}{M_{\rm Pl}}\ . \tag{3.6}$$

Larger reheating temperatures imply thermalization between the dark and visible sectors at reheating with $Y_\psi(T) \to Y_{\psi,eq}(T)$ for $T \sim T_{RH}$. In this chapter we focus on the non-thermalization scenario.

Turning next to energy transfer, the transfer term is computed in Appendix A and for $m_\psi \ll T \ll M$ and $n_\psi \ll n_{\psi,eq}$ reduces to

$$-\mathscr{U}(T) = -\langle \Delta E \cdot \sigma_{tr} v(T)\rangle (n_\psi^2 - n_{\psi,eq}^2(T)) \ \simeq\ \frac{3}{2\pi^5}\frac{T^7}{M^2}\ . \tag{3.7}$$

Solving as above, we find

$$\left(\frac{\rho_x}{\rho_{\psi,eq}}\right) \ \simeq\ \left(\frac{\rho_x}{\rho_{\psi,eq}}\right)_{T_{RH}} + \frac{180\sqrt{10}}{7\pi^8}\, g_*^{-1/2}\frac{M_{\rm Pl}T_{RH}}{M^2}\left[1-\left(\frac{T_{RH}}{T}\right)^{-1}\right]\ . \tag{3.8}$$

Again, this is only valid for $Y_\psi \ll Y_{\psi,eq}$. For sufficiently large T_{RH}, $\rho_x \to \rho_{\psi,eq}(T)$ at $T \sim T_{RH}$.

Comparing Y_ψ and ρ_x found above for $Y_\psi \ll Y_{\psi,eq}$, we see that the mean momentum of the fermions produced near reheating is on the order $p \sim T_{RH}$. At later times, these momenta simply redshift as $1/a$ provided $T \gg m_\psi$. Indeed, the detailed analysis of Ref. [191] shows that (in the absence of dark vectors) the dark fermions obtain an approximate *Bose-Einstein* distribution with effective temperature $T_x \simeq (1.155)\, T_{RH}(a_{RH}/a)$.

3.2.2 Thermalization with the Dark Vector

Now that we have considered the effect that the visible sector can have on our dark particle, let us include a dark vector boson X^μ coupling to ψ with strength $\alpha_x = g_x^2/4\pi$. This interaction allows the dark fermions to scatter with each other, annihilate to vector bosons, and emit vectors as radiation, as shown in Fig. 3.4. If these reactions are strong enough, the dark fermion and vector species can thermalize with each other to yield an effective temperature $T_x \leq T$.

The self-thermalization of heavy dark particles coupled to a massless dark vector was investigated in Refs. [182, 189]. As in these works, we only make parametric estimates of the very complicated full thermalization processes. We identify self-thermalization in the dark sector with the condition

$$\Gamma_{th}(T_{th}) = H(T_{th})\ , \tag{3.9}$$

where Γ_{th} is an effective thermalization rate to be discussed below and this relation defines the visible thermalization temperature T_{th} implicitly. Note that $T_{th} \leq T_{RH}$, and we set $T_{th} = T_{RH}$ if $\Gamma_{th}(T_{RH}) \geq H(T_{RH})$.

[3]The number and energy density produced through thermal transfer prior to reheating by the operator of Eq. (3.1) is a very small fraction of that produced at reheating [191, 192].

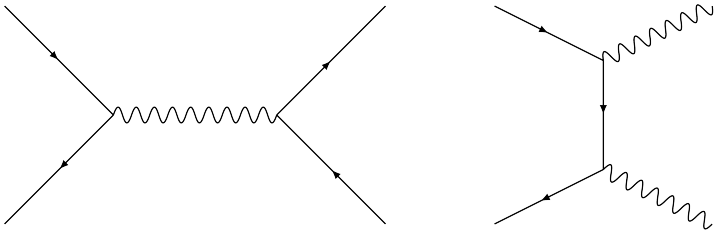

Figure 3.4: Interactions involved in the dark sector. The left hand S-channel (and the equivalent T and U channels) will contribute to the thermalization of the hidden sector. The right hand T-channel (as well as a corresponding U-channel) will contribute to thermalization as well as eventual ψ freeze-out.

It is convenient to classify the thermalization processes contributing to Γ_{th} into: i) $2 \to 2$ processes with hard momentum exchange; ii) $2 \to 3$ inelastic processes together with $2 \to 2$ with soft momentum exchange. The first class includes annihilation $\psi + \overline{\psi} \to X^{\mu} + X^{\nu}$ and hard scatterings such as $\psi + \psi \to \psi + \psi$ for which we estimate the rate to be [182]

$$\Gamma_{el}(T) \;\sim\; \frac{\pi\,\alpha_x^2}{T^2}\, n_{\psi}(T)\;, \tag{3.10}$$

where $n_{\psi}(T)$ is the number density of ψ prior to dark self-thermalization. Using Eq. (3.5) (with $Y_{\psi}(T_{RH}) \to 0$), for $T \gg m_{\psi}$ it is given by

$$n_{\psi}(T) \;\simeq\; \frac{3\sqrt{5/2}}{2\,\pi^6 g_*^{1/2}}\,\frac{M_{\rm Pl} T_{RH}}{M^2}\,T^3\;. \tag{3.11}$$

The second class of soft and inelastic processes was studied in Ref. [189] with the net result

$$\Gamma_{in}(T) \;\sim\; \min\left\{\frac{\alpha_x^3 n_{\psi}(T)}{\mu_{IR}^2},\, \alpha_x^2\sqrt{n_{\psi}/T}\right\}, \tag{3.12}$$

where μ_{IR} an effective infrared cutoff given by

$$\mu_{IR} = \max\left\{\sqrt{\alpha_x n_{\psi}/T},\, H,\, m_{\psi}\right\}. \tag{3.13}$$

We take the full thermalization rate to be the sum of the hard and inelastic rates, $\Gamma_{th} = \Gamma_{in} + \Gamma_{el}$.

If thermalization occurs with $T_{th} \gg m_{\psi}$, a smaller number of ψ and $\overline{\psi}$ fermions with typical energy T are redistributed into a larger number of ψ, $\overline{\psi}$, and X^{μ} particles in equilibrium with each other at temperature T_x. Treating the thermalization as instantaneous, the resulting dark sector temperature can be obtained from energy conservation and the result of Eq. (3.8):

$$\frac{T_x(T_{th})}{T_{th}} \;\equiv\; \xi(T_{th}) \;\simeq\; \left[\frac{180\sqrt{10}}{11\pi^8 g_*^{1/2}}\,\frac{M_{\rm Pl} T_{RH}}{M^2}\right]^{1/4}\;. \tag{3.14}$$

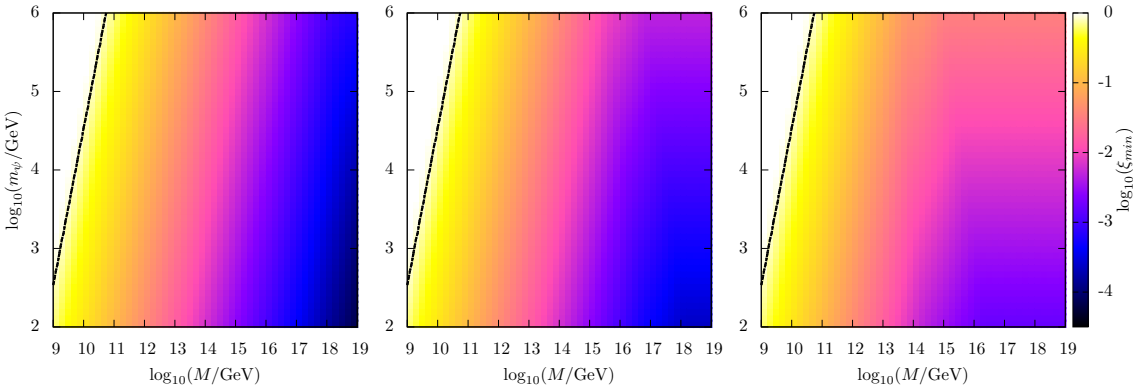

Figure 3.5: Minimum consistent values of $\xi(T_{RH})$ in the M–m_ψ plane for $\alpha_x = 10^{-1}$ (left), 10^{-2} (middle), 10^{-3} (right). The black line indicates where $\xi(T_{RH}) \to 1$ and our assumption of non-thermalization with the SM breaks down.

At later times, separate conservation of entropy in the dark and visible sectors implies

$$\xi(T) \simeq \xi(T_{th}) \left[\frac{g_{*S}(T)}{g_{*S}(T_{th})} \cdot \frac{g_{*S,x}(T_{th})}{g_{*S,x}(T)} \right]^{1/3} , \tag{3.15}$$

where $g_{*S(x)}$ refers to the number of visible (hidden) entropy degrees of freedom.

The analysis leading to the temperature ratio of Eq. (3.14) has three assumptions built into it, and their consistency implies maximal and minimal allowed values of $\xi(T_{th})$. First, the assumption of non-thermalization between the visible and dark sectors implies $\xi(T_{th}) \ll 1$. Second, the validity of the effective connector operator description of Eq. (3.1) requires $T_{RH} \ll M$ corresponding to a maximum value of $\xi(T_{th}) \lesssim (10^{-3} M_{\rm Pl}/M)^{1/4}$. And third, we have so far neglected the mass of the ψ fermion. Demanding that $T_x(T_{th}) \gtrsim m_\psi$ then leads to a lower bound on $\xi(T_{th})$ that we use to define

$$\xi_{min} \equiv \frac{m_\psi}{T_{th}} . \tag{3.16}$$

This also defines an implicit lower bound on the thermalization temperature for given values of m_ψ, M, and α_x, and correspondingly a lower limit on the reheating temperature T_{RH}.

In Fig. 3.5 we show the values of ξ_{min} in the $M-m_\psi$ plane for $\alpha_x = 10^{-1}$ (left), 10^{-2} (middle), and 10^{-3} (right). Larger M and α_x and smaller m_ψ lead to smaller ξ_{min}. The white regions in the upper left corners of the plots (bounded by black lines) have $\xi_{min} \to 1$ corresponding to thermalization between the visible and dark sectors when dark self-thermalization is achieved. As stated above, in the analysis to follow we focus on the lower right region where this does not occur.

3.3 Freeze-Out and Late Transfer in the Dark Sector

If the dark sector is populated by UV freeze-in and is self-thermalized at temperature $T_x \gtrsim m_\psi$, the dark fermion will undergo freeze-out by annihilation to dark vectors when T_x falls below m_ψ. While freeze-

out in a dark sector with $T_x \ll T$ has been studied in Refs. [189, 206–208], we identify a qualitatively new feature in the present context. Specifically, we show that the UV connector operator responsible for initially populating the dark sector at reheating can drastically change the freeze-out dynamics at much later times. This interplay between visible effects and dark sector self-interactions are precisely what we wish to study in this chapter.

3.3.1 Evolution Equations

The evolution of the ψ dark fermion number density at $T_x \lesssim m_\psi$ is described by

$$\frac{dn_\psi}{dt} + 3H n_\psi \simeq -\langle \sigma v(T_x)\rangle_{ann}(n_\psi^2 - n_{\psi,eq}^2(T_x)) + \langle \sigma_{tr} v(T)\rangle n_{\psi,eq}^2(T) \tag{3.17}$$

In writing this expression we have assumed self-thermalization in the dark sector with $T_x \ll T$ and no asymmetry between ψ and $\overline{\psi}$.

The first term on the right side of Eq. (3.17) describes annihilation $\psi + \overline{\psi} \to X^\mu + X^\nu$ with a thermal average at temperature T_x. The leading-order perturbative result for the cross section at low velocity is [209]

$$\sigma_{ann,p} v = \frac{\pi \alpha_x^2}{m_\psi^2} \,. \tag{3.18}$$

However, the full cross section receives independent non-perturbative enhancements from the Sommerfeld effect [210–212] and bound state formation [206, 213]. The full cross section can be written in the form [206, 214]

$$\sigma_{ann} v = [\mathscr{S}_{somm}(v) + \mathscr{S}_{rec}(v)]\, \sigma_{ann,p} v \,, \tag{3.19}$$

where v is the relative velocity and

$$\mathscr{S}_{som}(v) = \frac{2\pi z}{1 - e^{-2\pi z}} \,, \tag{3.20}$$

$$\mathscr{S}_{rec}(v) = \mathscr{S}_{som}(v)\, \frac{2^9}{3}\, \frac{z^4}{(1+z^2)^2}\, e^{-4z \tan^{-1}(1/z)} \,, \tag{3.21}$$

with $z = \alpha_x / v$, and which have the limits $\mathscr{S}_i(v) \to 1$ for $v \gg \alpha_x$.

The second term on the right side of Eq. (3.17) corresponds to transfer reactions of the form $H + H^\dagger \to \psi + \overline{\psi}$, and has all relevant quantities evaluated at the visible temperature T.[4] An explicit expression for this transfer term is given in Appendix A, which reduces to

$$\langle \sigma_{tr} v(T)\rangle n_{\psi,eq}^2(T) \equiv \mathscr{T}(T) \simeq \begin{cases} \frac{1}{4\pi^5}\frac{T^6}{M^2} & ; \quad T \gg m_\psi \\ \\ \frac{3}{32\pi^4}\frac{m_\psi^2 T^4}{M^2} e^{-2m_\psi/T} & ; \quad T \ll m_\psi \end{cases} . \tag{3.22}$$

[4] Since $T_x \ll T$, we can neglect the reverse reaction.

For $T_x < m_\psi$ but $T \gg m_\psi$, the standard annihilation term in Eq. (3.17) receives an exponential suppression in temperature while the transfer term is only suppressed by a power. We show below that this can allow the transfer term derived from a UV connector operator to play a significant role in the IR.

3.3.2 Analytic Estimates

It is instructive to estimate the relic density of ψ particles analytically to understand the effect of late-time transfer by the UV connector. To do so, we treat the annihilation cross section as being power-law in velocity: $\langle \sigma_{ann} v \rangle \to \sigma_0 x_x^{-n}$ where $x \equiv m_\psi / T$ and $x_x \equiv m_\psi / T_x = \xi^{-1} x$.

Freeze-Out Without the Transfer Term

Consider first the relic density of ψ with no transfer term but a definite value of $\xi \ll 1$. This can be computed by a simple generalization [206–208] of the analytic freeze-out approximation of Refs. [70, 73, 168, 169, 215]. Freeze-out occurs when the mass to dark temperature ratio is

$$x_{x,fo} \;\simeq\; \ln\left[(0.192)(n+1)(g_\psi/g_*^{1/2}) M_{\rm Pl}\, m_\psi\, \sigma_0\, \xi^2\right] - (n+\frac{1}{2})\ln(x_{x,fo})\;, \tag{3.23}$$

which can be solved iteratively for x_x^{fo}. This translates into an approximate relic density of[5]

$$\Omega_\psi h^2 \;\simeq\; (2.07\times 10^8\ {\rm GeV}^{-1})\,\frac{\xi\,(n+1)\,x_{x,fo}^{n+1}}{(g_{*S}/g_*^{1/2}) M_{\rm Pl}\,\sigma_0}\;. \tag{3.24}$$

Relative to the freeze-out of a species in thermodynamic equilibrium with the visible sector with the same mass and cross section, these relations imply

$$x_x^{fo} \;\simeq\; \tilde{x}^{fo} + (2 - 1/\tilde{x}_{fo})\ln\xi\;, \qquad \Omega_\psi h^2 \;\simeq\; \xi\left(1 + 2\ln\xi/\tilde{x}^{fo}\right)\widetilde{\Omega}_\psi h^2\;, \tag{3.25}$$

where $\tilde{x}^{fo}$ and $\widetilde{\Omega}_\psi h^2$ are the values for these quantities if the species were thermally coupled to the SM. The most important change is a reduction of the relic density by a factor of about $\xi \ll 1$.

Freeze-Out With the Transfer Term

Let us now include the transfer term from Eq. (3.17) in the evolution of the density of ψ. As T_x falls below m_ψ, annihilation is expected to dominate and keep n_ψ close to its equilibrium value at temperature T_x. However, since the corresponding annihilation rate falls exponentially in this regime, it decreases more quickly than the Hubble and transfer rates, and thus the near-equilibrium regime ends when one of these other rates catches up. We show here that late-time transfer reactions can significantly modify the final ψ relic density when the annihilation rate meets the transfer rate before reaching Hubble.

Define $T_{x,=}$ to be the value of the dark temperature T_x that solves the equation

$$\langle \sigma_{ann} v(T_x)\rangle n^2_{\psi,eq}(T_x) = \mathscr{T}(T_x/\xi)\;, \tag{3.26}$$

[5]Note that we use $M_{\rm Pl} = 2.43\times 10^{18}$ GeV, and the full DM relic density is the sum of equal ψ and $\overline{\psi}$ densities.

where $\mathscr{T}(T)$ is the transfer rate given in Eq. (3.22). If the solution has $T_= = T_{x,=}/\xi < m_\psi$, an approximate expression for it is

$$x_{x,=} \simeq \frac{1}{2}\ln\left(\frac{\pi^2}{2}\, g_\psi^2\, \sigma_0 M^2\, \xi^6\right) + \left(\frac{3-n}{2}\right)\ln(x_{x,=})\ , \tag{3.27}$$

which can be solved iteratively for $x_{x,=}$ provided it is greater than unity. When $x_{x,=}$ is greater than the freeze-out temperature without transfer, $x_{x,fo}$ given in Eq. (3.23), the transfer operator does not significantly alter the ψ relic density. In particular, the condition $x_{x,=} > x_{x,fo}$ implies that the evolution of the ψ density is dominated by Hubble dilution rather than transfer for all $x_x > x_{x,fo}$ since the expansion term decreases less quickly than the transfer term in this regime. In contrast, transfer effects are important for $x_{x,=} < x_{x,fo}$.

When $x_{x,=} < x_{x,fo}$, the transfer and annihilation terms in Eq. (3.17) can reach a balance with each other for $x_x > x_{x,=}$ until the Hubble term catches up. The number density of ψ is then approximately

$$n_{\psi,=}(T_x) \simeq \sqrt{\frac{\mathscr{T}(T_x/\xi)}{\sigma_0}}\, x_x^{n/2} \tag{3.28}$$

$$\to \frac{1}{2\pi^{5/2}}\frac{m_\psi^3}{\sqrt{\sigma_0 M^2}}\, \xi^{-3}\, x_x^{-3+n/2} \qquad \left(T_x/\xi \gg m_\psi\right) \tag{3.29}$$

where the expression in the second line only applies for $T_x/\xi \gg m_\psi$. Note that the density in this regime is always greater than the equilibrium density $n_{\psi,eq}(T_x)$, even when $T_x/\xi < m_\psi$. This follows logically from the fact that in this regime, the sourcing of new particles from the visible sector is compensating for the annihilations that are occurring, producing a net number density that is above equilibrium.

If the balance regime is achieved, $x_{x,=} < x_{x,fo}$, it ends when the Hubble term in Eq. (3.17) catches up to the annihilation and transfer terms. This later decoupling corresponds approximately to the condition

$$\langle\sigma_{ann} v(T_x)\rangle n_{\psi,=}(T_x) \simeq H(T_x/\xi)\ . \tag{3.30}$$

Defining $T_{x,dec}$ as the dark temperature that satisfies the relation above, an approximate solution for $T_{x,dec}/\xi \gg m_\psi$ is

$$x_{x,dec} \simeq \left[(0.086)\frac{m_\psi M_{\rm Pl}\sqrt{\sigma_0}}{g_*^{1/2} M}\, \xi^{-1}\right]^{1/(1+n/2)}\ . \tag{3.31}$$

The solution for $T_{x,dec}/\xi \lesssim m_\psi$ is more complicated but can be obtained similarly. The final relic density can be written in a form very similar to standard freeze-out via Eq. (3.30):

$$\Omega_\psi h^2 \simeq (2.07\times 10^8\ \mathrm{GeV}^{-1})\frac{\xi\, x_{x,dec}^{n+1}}{(g_{*S}/g_*^{1/2}) M_{\rm Pl}\, \sigma_0}\ . \tag{3.32}$$

Since $n_{\psi,=}(T_x) > n_{\psi,eq}(T_x)$ we must have $x_{x,dec} > x_{x,fo}$ whether or not $T_{x,dec}/\xi$ is larger or smaller than

m_ψ, and therefore the relic density of Eq. (3.32) is bigger than the pure freeze-out result of Eq. (3.24).

3.3.3 Numerical Results for Freeze-Out

To confirm the analytic estimates derived above and map out the parameter space of the theory, we perform a full numerical analysis of the dark matter freeze-out process. In Fig. 3.6 we show the evolution of the relevant rates in the upper panels and the ψ density in the lower panels for $\alpha_x = 0.1$, $\xi = 0.1$, $m_\psi = 10^4$ GeV, and $M = 10^{12}$ GeV (left) and 10^{15} GeV (right). The rate plots show the rates for Hubble, annihilation, and late transfer defined according to

$$\text{Hubble} = H(T)\ , \qquad \text{Annihilation} = \langle \sigma_{ann} v(T_x) \rangle\, n_\psi\ , \qquad \text{Transfer} = \mathscr{T}(T)/n_\psi\ , \tag{3.33}$$

where n_ψ is the number density obtained from solving Eq. (3.17) and $\mathscr{T}(T)$ is the transfer rate of Eq. (3.22). The value of M is smaller in the left panels of this figure, and late-time transfer becomes more important. In the ψ number density plots, we show the densities in equilibrium (dashed line), and with and without the transfer operator (upper and lower solid lines).

Late transfer by the fermionic Higgs portal operator is seen to increase significantly the final relic density in the left panels of Fig. 3.6, while its effect is negligible in the right panels. The difference corresponds to the larger transfer rate for $M = 10^{12}$ GeV in the left panels versus $M = 10^{15}$ GeV in the right. Following the rates for $M = 10^{12}$ GeV, transfer is seen to catch up to annihilation before Hubble leading to a regime of balanced rates and enhanced number density. In contrast, the Hubble rate catches up to annihilation before transfer in the right panels with $M = 10^{15}$ GeV and never plays a significant role in the evolution of n_ψ.

In Fig. 3.7 we show the enhancement of the relic density in the M–m_ψ plane for $\alpha_x = 0.1$ (left) and 0.01 (right) with $\xi = \xi_{min}$ as computed previously. The contours in both panels indicate the relic density we find to the value that would be obtained without late transfer effects, $\Omega_\psi/\Omega_\psi^{no-tr}$. Late transfer by the connector operator initially increases as M decreases and the transfer operators becomes more effective. However, as M continues to decrease we find a competing effect between the efficiency of transfer and the increasing value of ξ_{min}. As the dark and visible temperatures approach each other, transfer is more likely to occur while $T \to m_\psi$ and the effect becomes exponentially suppressed, as seen in Eq. (3.22). Transfer effects are also reduced at $\alpha_x = 0.1$ relative to $\alpha_x = 0.01$ due to the non-pertubative enhancements in the annihilation cross section at low velocities for the larger value of the gauge coupling.

Ultimately, we are interested in the parameter space where ψ can make up all the dark matter. In Fig. 3.8 we show the values of m_ψ for which this occurs as a function of M for $\alpha_x = 0.1$ (left) and 0.01 (right) for various values of ξ (solid lines). The lines in these plots are cut off at smaller M when ξ falls below ξ_{min}. As expected from the annihilation cross section, larger values of α_x coincide with larger dark matter masses. In the right part of both panels the allowed DM mass m_ψ reaches a value that is independent of M for fixed ξ. This region corresponds to late transfer being negligible for the freeze-out process, with the relic density scaling approximately as $\xi^{-1}\alpha_x^2/m_\psi^2$. Going to smaller

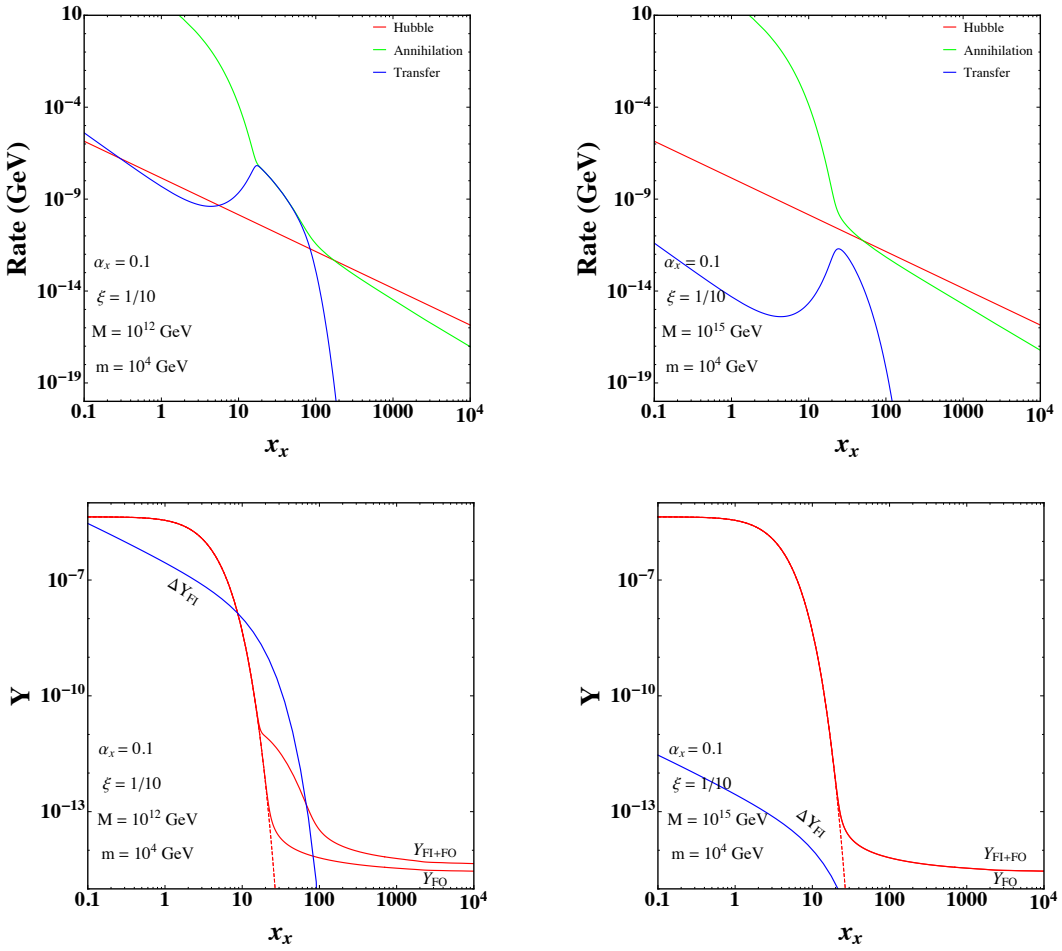

Figure 3.6: Evolution of the relevant rates in the upper panels and the ψ density in the lower panels for $\alpha_x = 0.1$, $\xi = 0.1$, $m_\psi = 10^4$ GeV, and $M = 10^{12}$ GeV (left) and 10^{15} GeV (right).

M, transfer eventually becomes important and the relic density increases. Correspondingly, the mass m_ψ that produces the correct relic density decreases. As M decreases further, the lines for different ξ values in Fig. 3.8 come together. This can be understood from Eqs. (3.31) and (3.32), where the direct dependence on ξ is seen to cancel for cross sections $\langle \sigma_{ann} v \rangle = \sigma_0 x^{-n}$ with $n \to 0$, as we have here (up to the Sommerfeld and bound state enhancements). The upper shaded region in both panels is excluded because the resulting relic density of ψ is always greater than the observed DM density for any consistent value of ξ. Going from $\alpha_x = 0.1$ to 0.01, lower ψ masses are needed to produce the correct relic density. Also shown in this figure are bounds from DM self-interactions to be discussed below.

3.4 Dark Matter Self-Interactions

Dark matter in our theory is charged under an unbroken $U(1)_x$ gauge force implying long-range self interactions among DM particles that can modify their behavior in collapsed systems. Such interactions have been suggested as a way to resolve several apparent discrepancies between simulations of DM structure formation and observations [137, 216]. However, these interactions are also constrained to not

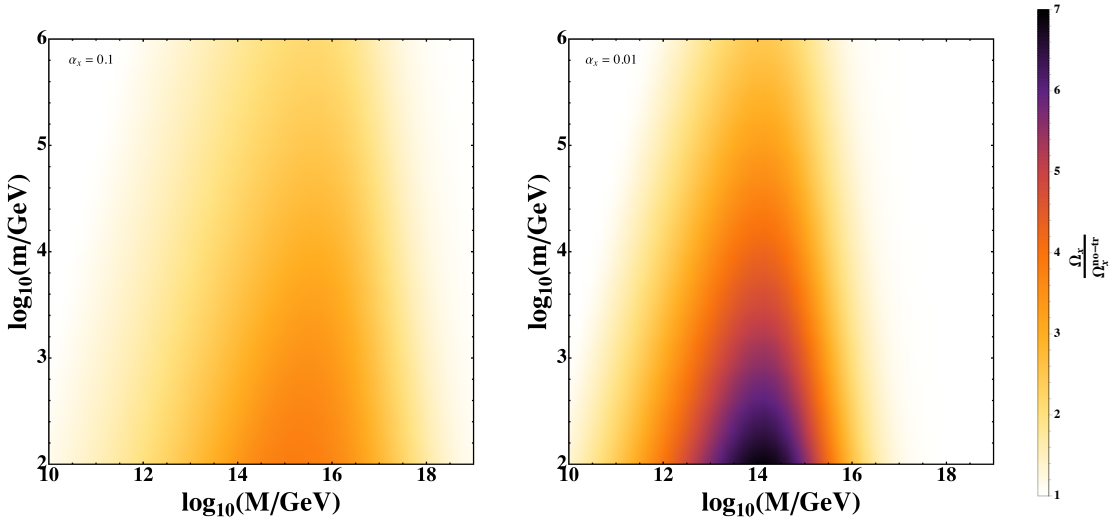

Figure 3.7: Enhancement of the ψ relic density due to late transfer effects relative to the value without this effect, $\Omega_\psi/\Omega_\psi^{no-tr}$ for $\alpha_x = 0.1$ (left) and 0.01 (right) and $\xi = \xi_{min}$.

be so large as to overly disrupt cosmic structures [217, 218].

An upper bound on DM self-interactions can be derived from the observed ellipticity of galactic halos such as NGC720 [219, 220]. For charged DM coupled to an unbroken $U(1)$, Refs. [206, 208] derived limits on the gauge coupling of the form

$$\alpha_x \lesssim \{0.35, 2.5\} \times 10^{-6} \left(\frac{m_\psi}{\mathrm{GeV}}\right)^{3/2} , \tag{3.34}$$

where the two numbers in brackets correspond to the analyses of Refs. [206] and [208], respectively. While the limit derived in Ref. [206] is considerably stronger, Ref. [208] (and Ref. [221]) argue for a weaker one based on the application of the ellipticity constraint only at larger galactic radii and a number of smaller factors. We show both upper bounds on α_x in Figs. (3.8). These favor smaller temperature ratios ξ and larger DM masses m_ψ, well above the weak scale.

The limits on α_x from the ellipticity of NGC720 correspond to an effective transfer cross section per mass below about $\sigma_T/m_\psi \lesssim 1\,\mathrm{cm}^2/\mathrm{g}$ in this system with a velocity dispersion on the order of $v \simeq 300\,\mathrm{km/s}$. Dark matter self-interactions in this regime are described by a Rutherford-like transfer cross section [206, 208, 221]:

$$\sigma_T \simeq \frac{8\pi\,\alpha_x^2}{m_\psi^2}\,\frac{1}{v^4}\,\ln\Lambda\,, \tag{3.35}$$

where $\ln\Lambda \sim 45-75$ is a collinear enhancement factor cut off by the typical interparticle spacing in the system [208]. Since this cross section has a very strong velocity dependence, the DM self-interactions in systems with lower velocity dispersions such as dwarf halos can be much stronger. Using typical

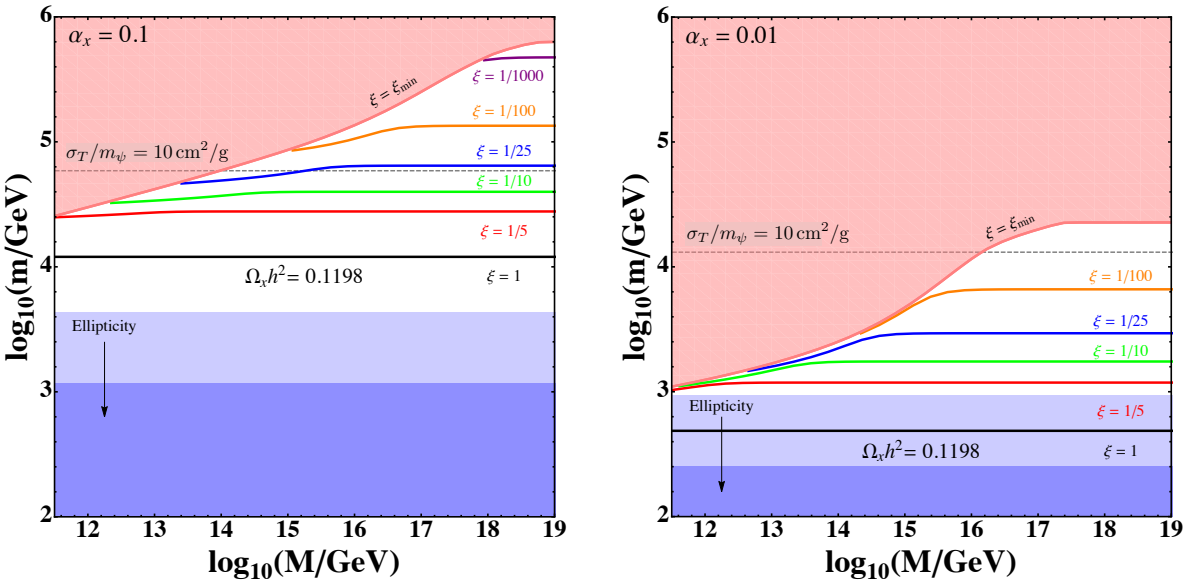

Figure 3.8: Values of m_ψ that give the correct relic density of ψ dark matter as a function of M for $\alpha_x = 0.1$ (left) and 0.01 (right) for various fixed values of ξ. Each solid line corresponds to the correct ψ relic density for the corresponding value of ξ. The red shaded upper region is excluded due to overproduction of ψ relic density for any consistent value of ξ. The lower blue shaded regions indicate exclusions from the effects of ψ dark matter self-interactions from the observed ellipticity of galactic halos, with the dark blue indicating a conservative exclusion and the light blue showing a more aggressive one. The dotted line indicates a DM self-scattering transfer cross-section per mass in dwarf halos of $\sigma_T/m_\psi = 10\,\mathrm{cm}^2/\mathrm{g}$.

velocities and densities for dwarf halos, this translates into

$$\sigma_T/m_\psi \simeq 18\,\mathrm{cm}^2/\mathrm{g}\left(\frac{\alpha_x}{0.1}\right)^2\left(\frac{5\times10^4\ \mathrm{GeV}}{m_\psi}\right)^3\left(\frac{10\,\mathrm{km/s}}{v}\right)^4\left(\frac{\ln\Lambda}{50}\right) \tag{3.36}$$

Interaction cross sections of this size are expected to lead to the formation of cores in dwarf halos, with Refs. [222, 223] suggesting a better agreement between simulations and data for $\sigma_T/m_\psi \sim 10\,\mathrm{cm}^2/\mathrm{g}$. On the other hand, it is not clear what the upper bound on σ_T/m_ψ is from these systems, with the simulations of Ref. [224] finding reasonable behavior for $\sigma_T/m_\psi = 50\,\mathrm{cm}^2/\mathrm{g}$ (the largest value studied) and Ref. [208] arguing that much larger values can work as well. Indeed, the results of Ref. [224] appear to be consistent with the approximate duality between σ_T/m_ψ and m_ψ/σ_T about Knudsen number close to unity suggested in Ref. [208] based on the analyses of Refs. [225, 226]. For reference, we also show dashed contours indicating $\sigma_T/m_\psi = 10\,\mathrm{cm}^2/\mathrm{g}$ in Figs. 3.8.

3.5 Conclusions

This chapter has focused on the interplay between a dark sector interacting with itself and small connections between the visible and dark sectors. As a first step into our exploration of the two sectors, this small connection only allowed for energy to flow from the visible to the hidden, and not

in reverse. Specifically, this was realized in a model consisting of a freeze-in transfer effect from a non-renormalizable connector operator together with a self-thermalizing hidden sector. The standard expectation for non-renormalizable operators in the early universe is that their effects are greatest at high temperatures and that they decouple at lower temperatures. For this reason, DM creation from SM collisions connecting to a secluded dark sector through a non-renormalizable operator is referred to as UV freeze-in [152, 154]. In this work we showed that such operators can also contribute importantly at lower temperatures when combined with freeze-out in a dark sector.

To illustrate the effect, we studied a concrete dark sector consisting of a massive Dirac fermion ψ DM candidate and a massless Abelian dark vector X^μ, with the only connection to the SM through the dimension-five fermionic Higgs portal operator of Eq. (3.1). At the end of reheating, the dark sector can be populated by transfer reactions $\mathrm{SM} + \mathrm{SM} \to \psi + \bar{\psi}$ mediated by the non-renormalizable portal operator to a density below the value it would have in full equilibrium with the SM. As the universe cools further, the population of dark fermions can equilibrate with the dark vectors at temperature T_x below the visible SM temperature T provided the dark gauge coupling and the initial fermion density are large enough. Freeze-out occurs in the dark sector when T_x falls below the fermion mass m_ψ. For a broad range of parameters in this theory, the relic density of ψ fermions can receive a significant additional enhancement from late transfer reactions through the non-renormalizable portal operator during the course of the freeze-out process for T down and below the fermion mass. The UV connector operator of Eq. (3.1) is therefore seen to play an important role in the IR.

The dark sector theory we have considered here also has interesting implications for DM self-interactions, which are motivated by a number of puzzles in cosmic structure [137, 216]. Such interactions were investigated for this theory in Refs. [206, 208, 221] and suggest that to be viable larger DM masses and smaller temperature ratios $\xi = T_x/T$ are required to avoid bounds from the observed ellipticity of NG720. These bounds, and the dependence of the self-interaction cross section on the DM velocity, could potentially be softened by extending the theory to include a small mass for the dark vector [218]. The calculations presented in this work can be carried over to such a massive vector scenario provided its mass is much smaller than the decoupling temperature of the dark fermion so that it provides a relativistic thermal bath during this process. Furthermore, the vector mass would also have to be small enough to avoid too much vector boson DM [227, 228].

While this work focused on a specific dark sector theory and non-renormalizable connector operator, it is expected to generalize to other connections. Specifically, a similar IR contribution from a UV operator that produces the relic density of dark-sector DM is expected to occur as well for other dark sectors or connector operators. For the effect to arise, the DM candidate in the dark sector must undergo significant annihilation to allow the power-suppressed transfer reactions (relative to reheating) of the connector operator to catch up. Other non-renormalizable connector operators can also lead to late IR transfer contributions to the DM relic density, although initial estimates suggest that the effect becomes less important as the operator dimension increases. Late-time transfer of a symmetric density could also be relevant in scenarios of secluded asymmetric DM.

Dark matter arising from a dark sector that is colder than the SM in the early universe has been

investigated in a wide range of scenarios of new physics [3, 4, 154, 187, 187, 206–208, 229–238]. In some of these works, the dark temperature T_x is taken as an input to the calculation of the DM relic density without reference to how the dark sector was populated initially. Our results show that such an assumption is not always justified, and the nature of the connector operators that mediate transfer from the SM to the dark sector can play an important role in determining the relic density of DM.

Now that we have thoroughly investigated the effect that the visible sector can have on the evolution of a dark sector, we turn to the reverse effect. In particular, we will consider how the dark sector can leave a visible imprint on the relics of BBN.

Part III

From the Dark to the Visible

Chapter 4

Limits from BBN on Light Decays and Annihilations

4.1 Introduction

In the previous chapter we explored in detail how the visible sector can play a role in the subsequent evolution of a dark sector. We now turn to the reverse scenario, and look at how dark particles can play a role in the visible. This turns out to be a very powerful technique. We can place stringent constraints on various new models of physics, because we can see the effects of this scenario explicitly through more than just gravitational potentials. The flow of energy is once again shown in Fig. 4.1. In particular, we will focus on low energy transfers that will ultimately affect the outcomes of an early universe process, Big Bang Nucleosynthesis (BBN).

BBN is one of the most powerful probes of the very early universe [112, 239–241]. Over the course of BBN, free protons and neutrons assemble into a handful of light elements [242–244]. Assuming a standard Λ cold dark matter (ΛCDM) cosmological history, the primordial abundances of these elements can be predicted using known nuclear reaction rates in terms of a single input parameter, the overall baryon density. These predictions agree well with observational determinations of primordial abundances up to plausible uncertainties in astrophysical determinations and nuclear rates [81].[1]

The success of BBN gives very strong evidence for the ΛCDM cosmological model up to radiation temperatures near the MeV scale [248–250], which extends much earlier than other known tests [67]. BBN also places stringent constraints on new physics beyond the Standard Model that injects energy into the cosmological plasma or influences the expansion rate at early times. This includes the decays of massive particles with lifetimes greater than $\tau \simeq 0.1\,\mathrm{s}$ [94, 194, 196, 251–261], dark matter (DM) annihilation with an effective cross section near the critical value for thermal freeze-out [262–265], and any new thermalized species with mass below a few MeV [10, 266–268].

Limits from BBN on the decays of long-lived massive particles have been studied in great detail [94,

[0]This chapter is based L. Forestell, D. E. Morrissey, and G. White, *Limits from BBN on Light Electromagnetic Decays*, JHEP, **1901**, (2018), 074, [arXiv:1809.01179] [2].

[1]The extrapolated densities of ^{6}Li and ^{7}Li give a particularly acute puzzle in this regard [111, 245–247].

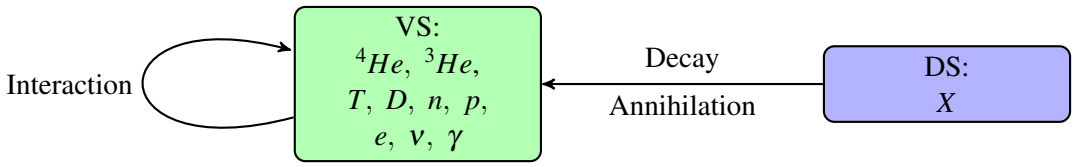

Figure 4.1: Flow of information considered in this chapter. The dark sector now transfers energy via decays and annihilations to the visible sector, which will go through further self-processing effects that interplay with the inflow of energy. In this chapter, the visible sector consists of relevant BBN particles, while the dark sector consists of a single species X.

258–261]. In the majority of this work, often motivated by new physics connected to the electroweak hierarchy puzzle or weakly-interacting massive particle (WIMP) dark matter, the energy injected by the decay has been assumed to be close to or greater than the weak scale. Thus, the decay products typically have initial energies that are much larger than the thresholds for nuclear reactions relevant to BBN which are typically on the order of several MeV. Weak-scale decay products typically also have both hadronic and electromagnetic components, if only through radiative effects.

Hadronic energy injection can modify the light element abundances at times as early as $t \sim 0.1\,\mathrm{s}$ [258, 259]. Initially, these products scatter with protons and neutrons and alter the ratio of these baryons and thus the resulting helium abundance. At later times, injected hadrons destroy and modify the abundances of helium and other light elements through hadrodissociation. Since the initial hadronic energies are usually assumed to be much larger than the MeV scale, thresholds for these reactions are easily overcome.

Electromagnetic (EM) energy – photons, electrons, and positrons – injected into the cosmological plasma does not have a significant effect on the light element abundances until much later. The main effect of electromagnetic injection on the light elements is photodissociation (unless the amount of energy deposited is enormous). However, being much lighter than hadrons, photons and electrons lose their energy very efficiently by scattering off the highly-abundant photon background. The electromagnetic cascade initiated by this scattering is strongly suppressed for energies above E_c, given by [7, 269]

$$E_c \simeq \frac{m_e^2}{22T} \simeq (2\,\mathrm{MeV})\left(\frac{6\,\mathrm{keV}}{T}\right), \tag{4.1}$$

where T is the cosmological photon temperature. As a result, even for initial energies orders of magnitude above the MeV-scale thresholds for photodissociation, the fraction of energy available for photodissociation is tiny until the background temperature falls below $T \lesssim 10\,\mathrm{keV}$, corresponding to $t \sim 10^4\,\mathrm{s}$.

While much of the focus on new sources of energy injection during BBN has been on decays or annihilations at or above the weak scale, there exist many well-motivated theories that also predict new sources well below the weak scale. Specific examples include dark photons [270, 271], dark Higgs bosons [271, 272], dark gluons and glueballs [3, 4, 235], light or strongly-interacting dark matter [273, 274], and MeV-scale neutrino decays [275, 276]. As the injection energy falls below the GeV scale, hadronic decay channels start to become kinematically unavailable and disappear entirely below the pion

threshold. This leaves electromagnetic and neutrino injection as the only remaining possibilities. Even more importantly, it was shown in Refs. [8, 277] that the development of the electromagnetic cascade at these lower energies can differ significantly relative to injection above the weak scale. Furthermore, as the injection energy falls below a few tens of MeV, photodissociation reactions begin to shut off.

In this chapter we expand upon the analysis of Refs. [8, 277] and investigate the effects of electromagnetic energy injection below 100 MeV on the primordial element abundances created during BBN. One focus of this study is the development of the electromagnetic cascade from initial photon or electron (e^+e^-) injection. For high energy injection, the resulting spectrum of photons is described very well by the so-called universal spectrum rescaled by a temperature- and energy-dependent relaxation rate. This spectrum is used widely in studies of photodissociation effects on BBN, it can be parametrized in a simple and convenient way, and has the attractive feature that it only depends on the total amount of electromagnetic energy injected. However, for lower-energy electromagnetic injection, the universal spectrum does not properly describe the resulting electromagnetic cascades.

The universal spectrum fails for lower-energy injection in two significant ways. First, the universal spectrum is based on a fast redistribution of the initial energy $E_X \gg E_c$ to a spectrum populated at $E \leq E_c$ through Compton scattering and photon-photon pair production. As shown in Refs. [8, 277], this picture does not hold for initial injection energies $E_X < E_c$, which can easily occur for smaller E_X and larger decay lifetimes. And second, as argued in Ref. [271] the Compton scattering with background photons that dominates electron interactions is qualitatively different at high energies compared to low. At higher energies, $s \sim E\,T \gg m_e^2$, electrons scatter in the Klein-Nishina limit and typically lose an order unity fraction of their energy in each scattering event. In contrast, lower energy scattering with $s \sim E\,T \ll m_e^2$ enters the Thomson regime where the fractional change in the electron energy per collision is very small and the up-scattered photon energy is much less than the initial electron energy.

To address the breakdown of the universal spectrum for lower-energy electromagnetic injection, we compute the full electromagnetic cascade for photon or electron (e^+e^-) injection with initial energies $E_X \in [1, 100]$ MeV following the methods of Ref. [7]. Our work expands upon Refs. [8, 277] that studied the photon portion of the cascade for photon injection. We compare and contrast our results to the universal spectrum, and study their implications for BBN. In addition to finding important differences from the universal spectrum at these lower energies, we also demonstrate that final-state radiation (FSR) from electron injection can have a very significant impact on the resulting photon spectrum. For very low injection energies approaching the MeV scale, we also study the interplay of the spectrum with the thresholds for the most important nuclear photodissociation reactions.

Although energy injected directly into electromagnetic cascade products will have the most drastic effect on the visible sector via the photodissociation of BBN products, there is another, more subtle method by which the dark sector can influence the visible at these low energies. This is via the alteration of N_{eff}, the effective number of neutrino species[10, 157, 278–282]. This can be done either via the presence of a new relativistic species, such as a sterile neutrino or a low mass WIMP[10, 276, 283–287], or via energy injection through particle decays and annihilations[288]. The energy injected into the visible sector can serve to alter the relative ratio of the background photon temperature to the temperature

of neutrinos. For the Standard Model with 3 generations of neutrinos, $N_{eff} = 3$. [2] The altered value of N_{eff} will in turn affect the Hubble expansion rate as the total radiation energy density increases (or decreases), relative to that obtained via a standard N_{eff}:

$$\rho_R = \rho_\gamma \left[1 + \frac{7}{8} \left(\frac{T_{\nu,0}}{T_{\gamma,0}} \right)^4 N_{eff} \right] \tag{4.2}$$

where ρ_R is the total radiative energy density contributing to the Hubble rate, ρ_γ the portion coming from photons, and the rest represented by N_{eff}, where the factors out front have been included to make $N_{eff} = 3$ for the standard 3 neutrino generations.

Both BBN and the CMB can be used to place limits on the value of N_{eff}. During BBN, increasing N_{eff} leads to a faster freeze-out of the neutron population, which will result in more ^{4}He and deuterium being produced with the extra neutron availability[81, 284, 291–293]. This is thus constrained by the same present day measurements that also place limits on the effects of photodissociation. The CMB will also provide constraints, as increasing the effective number of relativistic degrees of freedom increases the small-scale (Silk) damping of the CMB power spectrum[268, 280, 294, 295]. With precise measurements from telescopes such as the Atacama Cosmology Telescope (ACT)[296], South Pole Telescope (SPT)[297] and Planck[9], we can provide a limit on the possible values of N_{eff}. The unique thing about the N_{eff} limit is it will apply to both electromagnetic interactions, as well as neutrino effects. Although neutrinos have frozen-out and do not interact with the electromagnetic background at the time of BBN, and thus do not affect BBN directly, they are still a viable, kinematically allowed, decay/annihilation candidate at these light energies. Annihilations and their effects on N_{eff} have been broadly studied previously in the literature (see, for example, Refs. [10, 157, 268, 279–281]). However, the constraints that arise from decays have not been as thoroughly examined, so we provide a calcuation here to complete our examination of low energy constraints.

The outline of this chapter is as follows. After this introduction, we present our calculation of the electromagnetic cascade in Sec. 4.2. Next, in Sec. 4.3 we study the impact of such electromagnetic injection on the light element abundances. In Sec. 4.4 we contrast the bounds from photodissociation of light elements with other limits on late electromagnetic injection, including those derived from N_{eff}. Finally, Sec. 4.5 is reserved for our conclusions. Some technical details can be found in our paper [2], Appendix A for completeness. This chapter is based on work published in Ref. [2] in collaboration with David Morrissey and Graham White, with extended sections covering the effects on N_{eff}.

4.2 Development of the Electromagnetic Cascade

In this section we compute the electromagnetic cascade in the early universe following the injection of photons or electrons (e^+e^-) with initial energy $E_X < 100$ MeV.

[2] More precisely, the value predicted for N_{eff} is slightly above this, ~ 3.046, due to the fact that neutrinos have not completely decoupled at the time of $e^\pm$ annihilations [289, 290].

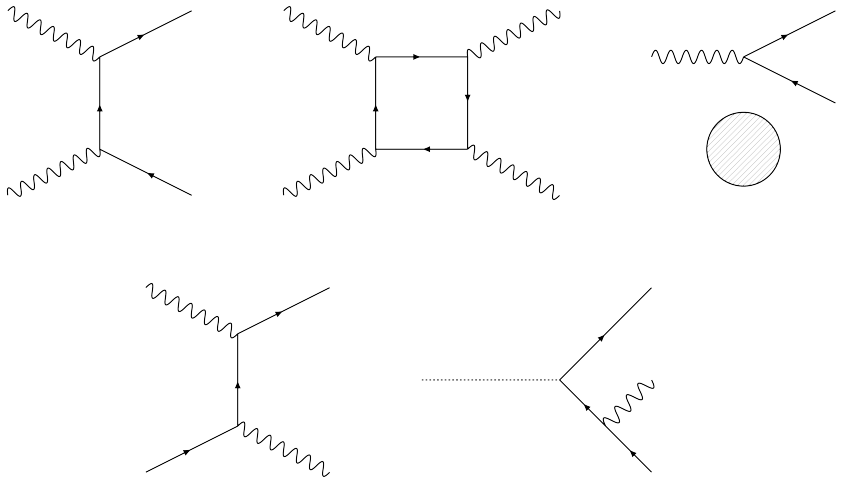

Figure 4.2: Most important reactions for the development of the electromagnetic cascade. Top row: high energy photons scatter off background photons or nuclei. Bottom row: Compton scattering for either high energy photons or $e^{\pm}$ (left), as well as final state radiation (right). The fastest processes tend to be 4P (top left) and IC (bottom left).

4.2.1 Computing the Electromagnetic Cascade

Energetic photons or electrons injected into the cosmological plasma at temperatures below the MeV scale interact with background photons and charged particles leading to electromagnetic cascades that produce spectra of photons and electrons at lower energies. Since the development of the cascade is much faster than the typical interaction time with the much more dilute light elements created in BBN, these spectra can be used as inputs for the calculation of photodissociation effects.

The most important reactions for the development of the electromagnetic cascade in the temperature range of interest $T \in [1\text{ eV}, 10\text{ keV}]$ are show in Fig. 4.2, and are given by: [7]:

- photon photon pair production (4P): $\gamma + \gamma_{BG} \to e^+ + e^-$
- photon photon scattering (PP): $\gamma + \gamma_{BG} \to \gamma + \gamma$
- pair creation on nuclei (PCN): $\gamma + N_{BG} \to N_{BG} + e^+ + e^-$
- Compton scattering (CS): $\gamma + e^-_{BG} \to \gamma + e^-$
- inverse Compton (IC): $e^{\mp} + \gamma_{BG} \to e^{\mp} + \gamma$
- final state radiation (FSR): $X \to e^+ + e^- + \gamma$

Of these processes, IC and 4P are typically the fastest provided there is enough energy for them to occur.

We define $\mathscr{N}_a = dn_a/dE$ to be the differential number densities per unit energy of photons ($a = \gamma$) and the sum of electrons and positrons ($a = e$). The Boltzmann equations for the evolution of these spectra take the form

$$\frac{d\mathscr{N}_a}{dt}(E) = -\Gamma_a(E)\mathscr{N}_a(E) + \mathscr{S}_a(E)\,, \tag{4.3}$$

where $\Gamma_a(E)$ is a relaxation rate at energy E, and $\mathscr{S}_a(E)$ describes all sources at this energy. Since the relaxation rates are typically much faster than the Hubble rate, the Hubble dilution term has been omitted. Furthermore, the relaxation rate is also much larger than the mean photodissociation rates with light nuclei, so a further quasistatic approximation can made with $d\mathscr{N}_a/dt \to 0$ [7]. This gives the solution

$$\mathscr{N}_a(E) = \frac{\mathscr{S}_a(E)}{\Gamma_a(E)} \, . \tag{4.4}$$

Note that $\mathscr{N}_a(E)$ evolves in time in this approximation through the time and temperature dependences of the sources and relaxation rates. The source terms are discussed in more detail below while explicit expressions for the contributions to the relaxation rates are given in Appendix A of Ref. [2].

Monochromatic Photon Injection

For monochromatic photon injection at energy E_X from a decay with rate per volume R, the source terms are

$$S_\gamma(E) = \xi_\gamma R \, \delta(E - E_X) + \sum_b \int_E^{E_X} dE' \, K_{\gamma b}(E,E') \, \mathscr{N}_b(E') \, , \tag{4.5}$$

$$\mathscr{S}_e(E) = 0 + \sum_b \int_E^{E_X} dE' \, K_{eb}(E,E') \, \mathscr{N}_b(E') \, , \tag{4.6}$$

where ξ_γ is the number of photons injected per decay, and the $K_{ab}(E,E')$ functions describe scattering processes that transfer energy from species b at energy E' to species a at energy $E \leq E'$. Explicit expressions for these transfer functions are given in Ref. [2]. Note that in the case of decays of species X with lifetime τ_X, the rate is $R = n_X(t)/\tau_X$. These equations can also be applied to annihilation reactions of the form $X + \bar{X} \to n\,\gamma$ with cross section $\langle \sigma v \rangle$ by setting $R = \langle \sigma v \rangle n_X n_{\bar{X}}$ and $\xi_\gamma = n$.

It is convenient to describe the cascades resulting from the initial monochromatic (delta function) injection with smooth functions that are independent of the injection rate. To this end, we define

$$\bar{f}_\gamma(E) = \frac{1}{R} \mathscr{N}_\gamma(E) - \frac{\xi_\gamma}{\Gamma_\gamma(E_X)} \, \delta(E - E_X) \tag{4.7}$$

$$\bar{f}_e(E) = \frac{1}{R} \mathscr{N}_e(E) \, . \tag{4.8}$$

Using this form in Eq. (4.4) with the sources of Eqs. (4.5,4.6), we obtain the relations

$$\Gamma_\gamma(E) \, \bar{f}_\gamma(E) = \xi_\gamma \frac{K_{\gamma\gamma}(E,E_X)}{\Gamma_\gamma(E_X)} + \sum_b \int_E^{E_X} dE' \, K_{\gamma b}(E,E') \bar{f}_b(E') \tag{4.9}$$

$$\Gamma_e(E) \, \bar{f}_e(E) = \xi_\gamma \frac{K_{e\gamma}(E,E_X)}{\Gamma_\gamma(E_X)} + \sum_b \int_E^{E_X} dE' \, K_{eb}(E,E') \bar{f}_b(E') \tag{4.10}$$

The functions $\bar{f}_\gamma$ and $\bar{f}_e$ are expected to be smooth, and can be used to reconstruct the full spectra $\mathscr{N}_\gamma(E)$

and $\mathscr{N}_e(E)$ uniquely for any given injection rate R.

Determining the electromagnetic cascade from monochromatic photon injection is therefore equivalent to solving Eqs. (4.9,4.10). We do so using the iterative method of Ref. [7], with an important modification to account for the Thomson limit of IC scattering. In this method, the spectra $\bar{f}_a(E)$ are determined on a grid of energy points E_i given by

$$E_i = E_0 \left(\frac{E_N}{E_0}\right)^{i/N} , \tag{4.11}$$

where we use $E_0 = 1$ MeV, $E_N = E_X$, $i = 0, 1, \ldots, N$, and $N \gg 1$. For the top point $i = N$, Eqs. (4.9,4.10) give

$$\bar{f}_\gamma(E_N) = \xi_\gamma K_{\gamma\gamma}(E_N, E_N)/\Gamma^2_\gamma(E_N) , \qquad \bar{f}_e(E_N) = \xi_\gamma K_{e\gamma}(E_N, E_N)/\Gamma_\gamma(E_N)\Gamma_e(E_N) . \tag{4.12}$$

To compute the spectra at lower points, we use the fact that the transfer integrals at a given energy E only depend on the spectra at energies $E' > E$. Thus, at any step i the integrals in Eqs. (4.9,4.10) can be approximated numerically (*e.g.* Simpson's rule) using the spectra already determined at points $j = i+1, \ldots, N$. Relative to Ref. [7] we also apply a finer grid to compute the top two energy points.

This approach to computing the cascades works well for $y_e = E_e T/m_e^2 \gg 1$, but becomes numerically challenging for $y_e \lesssim 0.1$. The problem comes from the contribution of inverse Compton (IC) scattering to K_{ee}. As y_e becomes small, IC scattering enters the Thomson regime in which the cross section is large but the fractional change in the electron energy per scattering is much less than unity, and thus the function $K_{ee}(E, E')$ develops a strong and narrow peak near $E' \simeq E$. To handle this we follow Refs. [269, 298] and treat the electron energy loss due to IC in the Thomson limit as a continuous process by replacing

$$-\Gamma_e(E)\bar{f}_e(E) + \int_E^{E_N} dE'\, K_{ee}(E, E')\bar{f}_e(E') \;\to\; \frac{\partial}{\partial E}\left[\dot{E}\,\bar{f}_e(E)\right] . \tag{4.13}$$

Here, $\dot{E}$ is the rate of energy loss from IC of a single electron in the photon background, given by [298]

$$\frac{\dot{E}}{E} \;=\; -\frac{4}{3}\left[\frac{3\zeta(4)}{\zeta(3)}\right]\left(\frac{ET}{m_e^2}\right)\sigma_T n_\gamma , \tag{4.14}$$

where $\sigma_T = (8\pi/3)\alpha^2/m_e^2$ is the Thomson cross section, $n_\gamma = [2\zeta(3)/\pi^2]T^3$ is the thermal photon density, and $\zeta(z)$ is the Riemann zeta function. The approximation of Eq. (4.13) is valid provided the fractional energy loss rate $\dot{E}/E$ is much smaller than the total scattering rate $\sigma_T n_\gamma$, which coincides with $y_e \ll 0.1$. In this limit, the two terms on the left-hand side of Eq. (4.13) are much larger than their difference leading to a numerical instability in the original iterative approach.

When computing the electromagnetic spectra, we use the iterative method described above with Eqs. (4.9,4.10) until $y_j = E_j T/m_e^2 < 0.05$ is reached. For lower energy bins we keep Eq. (4.9) for $\bar{f}_\gamma$ but

apply the replacement of Eq. (4.13) for $\bar{f}_e$, yielding the solution

$$\bar{f}_e(E) = \left(\frac{E_j}{E}\right)^2 \bar{f}_e(E_j) + \frac{1}{a_T E^2} \int_E^{E_j} dE'' \, \mathscr{S}'_e(E'') \; , \tag{4.15}$$

with

$$\mathscr{S}'_e(E'') = \xi_\gamma \frac{K_{e\gamma}(E'', E_N)}{\Gamma_\gamma(E_N)} + \int_{E''}^{E_X} dE' \, K_{e\gamma}(E'', E') \, \bar{f}_\gamma(E') \; , \tag{4.16}$$

and

$$a_T = \frac{\dot{E}}{E^2} = \frac{4\pi^2}{45} \, \sigma_T \, \frac{T^4}{m_e^2} \; . \tag{4.17}$$

Again, this can be evaluated iteratively, from high to low. While we use the specific value $y_e < 0.05$ to match from one method to the other, we find nearly identical results from matching within the range $y_e \in [0.001, 0.1]$.

Monochromatic Electron Injection

Monochromatic injection of electrons (and positrons) at energy E_X can be treated nearly identically to monochromatic photon injection, with the only major change being in modifying the sources to

$$S_\gamma(E) = S_\gamma^{FSR}(E) + \sum_b \int_E^{E_X} dE' \, K_{\gamma b}(E, E') \, \mathscr{N}_b(E') \; , \tag{4.18}$$

$$\mathscr{S}_e(E) = \xi_e R \, \delta(E - E_X) + \sum_b \int_E^{E_X} dE' \, K_{eb}(E, E') \, \mathscr{N}_b(E') \; , \tag{4.19}$$

where R is the decay (or annihilation) rate per unit volume, ξ_e is the number of electrons plus positrons injected per decay, and $S_\gamma^{FSR}(E)$ is a contribution to photons from final-state radiation to be discussed in more detail below. For decays of the form $X \to e^+ + e^-$ we have $R = n_X(t)/\tau_X$ and $\xi_e = 2$, while for annihilation $X + \bar{X} \to e^+ + e^-$ the rate is $R = \langle \sigma v \rangle n_X n_{\bar{X}}$ and $\xi_e = 2$.

Given these source terms, it natural to define the reduced spectra $\bar{f}_a(E)$ by

$$\bar{f}_\gamma(E) = \frac{1}{R} \mathscr{N}_\gamma(E) \tag{4.20}$$

$$\bar{f}_e(E) = \frac{1}{R} \mathscr{N}_e(E) - \frac{\xi_e}{\Gamma_e(E_X)} \, \delta(E - E_X) \tag{4.21}$$

Applying this to Eq. (4.4) with the sources of Eqs. (4.18,4.19), we obtain the relations

$$\Gamma_\gamma(E) \, \bar{f}_\gamma(E) = \frac{S_\gamma^{FSR}(E)}{R} + \xi_e \frac{K_{\gamma e}(E, E_X)}{\Gamma_e(E_X)} + \sum_b \int_E^{E_X} dE' \, K_{\gamma b}(E, E') \bar{f}_b(E') \tag{4.22}$$

$$\Gamma_e(E) \, \bar{f}_e(E) = \xi_e \frac{K_{ee}(E, E_X)}{\Gamma_e(E_X)} + \sum_b \int_E^{E_X} dE' \, K_{eb}(E, E') \bar{f}_b(E') \tag{4.23}$$

These equations can be solved using the same methods as described above for photon injection, including a matching in the Thomson limit using Eq. (4.13).

A new feature that we include for electron injection is a contribution to the photon spectrum from final-state radiation (FSR) off the injected electron; $S_\gamma^{FSR}(E)$ in Eq. (4.18). For processes of the form $X \to e^+ + e^-$ or $X + \bar{X} \to e^+ + e^-$ with X uncharged and $E_X \gg m_e$, this new source can be approximated by [299, 300]

$$S_\gamma^{FSR}(E) \simeq \frac{R}{E_X}\frac{\alpha}{\pi}\frac{1+(1-x)^2}{x}\ln\left[\frac{4E_X^2(1-x)}{m_e^2}\right]\Theta\left(1-\frac{m_e^2}{4E_X^2}-x\right), \tag{4.24}$$

where $x = E/E_X$. To be fully consistent, a corresponding subtraction should be made from the electron source. However, we find that this modifies the spectra by less than a percent. In contrast, we show below that the direct contribution to the photon spectrum from FSR can be the dominant one at higher energies when $E_X T/m_e^2 \ll 1$, when the initial electrons scatter via IC with the photon background mainly in the Thomson regime.

4.2.2 Review of the Universal Spectrum

Many studies of the effects of electromagnetic energy injection on BBN approximate the photon spectrum with the so-called universal spectrum. This is a simple parametrization of the full calculations of the photon spectrum in Refs. [7, 269]. It replaces the source terms (direct and cascade) in Eq. (4.4) with a zeroeth generation spectrum $\mathscr{S}_\gamma(E)/R \to p_\gamma(E)$ based on the assumption that 4P and IC processes instantaneously reprocess the initial injected electromagnetic energy.

The standard parametrization used for the zeroeth generation spectrum is [112, 257, 269]

$$p_\gamma(E_\gamma) \simeq \begin{cases} 0 & ; \quad E_\gamma > E_c \\ K_0\left(\frac{E_\gamma}{E_m}\right)^{-2.0} & ; \quad E_m < E_\gamma < E_c \\ K_0\left(\frac{E_\gamma}{E_m}\right)^{-1.5} & ; \quad E_\gamma < E_m \end{cases}, \tag{4.25}$$

where $E_c \simeq m_e^2/22T$ and $E_m \simeq m_e^2/80T$ are derived from Ref. [7], and K_0 is a normalization constant. For monochromatic injection of ξ photons, electrons, and positrons each with energy E_X, it is fixed by the requirement

$$\xi E_X = \int_0^{E_X} dE\, E\, p_\gamma(E), \tag{4.26}$$

implying $K_0 = \xi E_X/[E_m^2(2+\ln(E_c/E_m)]$ for $E_X > E_c$. An important feature of the spectrum is that it is proportional to the total injection energy (for either photons or electrons) provided $E_X \gg E_c$, up to an overall normalization by the total amount of energy injected.

Within the universal spectrum approximation, the final spectra are given by

$$f_\gamma(E) = \frac{p_\gamma(E)}{\Gamma_\gamma(E)}, \qquad f_e(E) = 0, \tag{4.27}$$

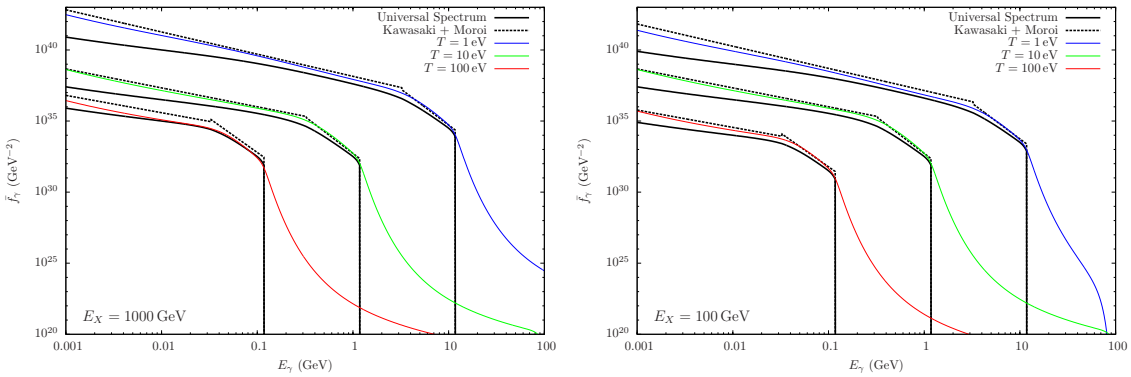

Figure 4.3: Photon spectrum $\bar{f}_\gamma(E)$ for single photon injection with energy $E_X = 1000\,\mathrm{GeV}$ (left) and $100,\mathrm{GeV}$ (right), for temperatures $T = 1, 10, 100\,\mathrm{eV}$. Also shown are the predictions of the universal spectrum (solid) and the parametrizations of Kawasaki and Moroi given in Ref. [7].

where $f_\gamma(E) = \mathcal{N}_\gamma(E)/R$, and the relaxation rate $\Gamma_\gamma(E)$ accounts for the further reprocessing of the spectrum by slower processes like Compton scattering, pair creation on nuclei, and photon-photon scattering.[3] These spectra have no residual delta-function parts since the initial injection is assumed to be fully reprocessed into the zeroeth-order spectrum by 4P and IC scatterings.

4.2.3 Results for Photon Injection

To validate our electromagnetic spectra, we compare our results to previous calculations and the universal spectrum at high injection energies. In Fig. 4.3 we show our photon spectra $\bar{f}_\gamma(E)$ for single photon injection with $E_X = 1000\,\mathrm{GeV}$ (left) and $100\,\mathrm{GeV}$ (right) at temperatures $T = 1, 10, 100\,\mathrm{eV}$. Also shown in the figure are the predictions from the universal spectrum and parametrizations of the results of Kawasaki and Moroi listed in Ref. [7]. In all cases here, $E_X \gg E_c$ and the universal spectrum is expected to be a good approximation. Our spectra agree well with the results of Ref. [7] but are somewhat larger than the universal spectrum. We have also checked that our spectra scale proportionally to the total energy injected provided $E_X \gg E_c$. In all cases shown in the figure, the electron spectra are smaller than the photon spectra by orders of magnitude due to efficient IC scattering. Also visible is the strong suppression of the photon spectra for $E > E_c$ where the 4P process is active.

In contrast to electromagnetic injection at high energies with $E_X \gg E_c$, injection at lower energies with $E_X \lesssim E_c$ has received much less attention. In Fig. 4.4 we show our computed photon spectra for single photon injection with $E_X = 100\,\mathrm{MeV}$ (left), $E_X = 30\,\mathrm{MeV}$ (middle), and $E_X = 10\,\mathrm{MeV}$ (right) for $T = 1, 10, 100\,\mathrm{eV}$. Also shown are the predictions of the universal spectrum (normalized according to Eq. (4.26)) and the prescription by Poulin and Serpico of Ref. [8]. Since $E_X < E_c$, the assumptions that go into the universal spectrum are not met and it is not expected to be accurate in this regime, as first pointed out in Ref. [8]. Our spectra agree fairly well with the results of Ref. [8], which only kept

[3] In practice, this $\Gamma_\gamma(E)$ is effectively equal to the full relaxation rate that also includes 4P scattering since this process is very strongly Boltzmann-suppressed for $E < E_c$.

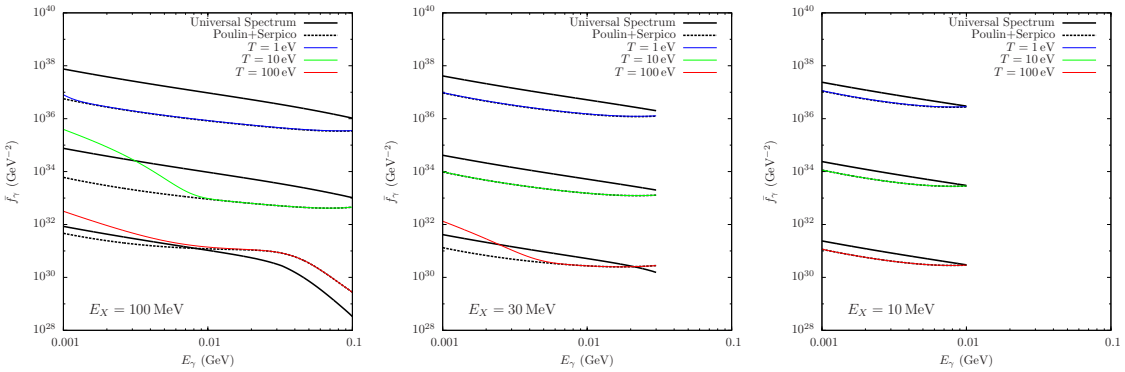

Figure 4.4: Photon spectrum $\bar{f}_\gamma(E)$ for photon injection with $E_X = 100\,\mathrm{MeV}$ (left), $E_X = 30\,\mathrm{MeV}$ (middle), and $E_X = 10\,\mathrm{MeV}$ (right), with $T = 1, 10, 100\,\mathrm{eV}$. Also shown are the predictions of the universal spectrum (solid) and the low-energy prescription of Ref. [8].

the photon part of the spectrum. Some deviations are seen at lower energies where photon regeneration by IC becomes significant. Note as well that the full cascade also contains a moderately damped delta-function part that is not shown here (and was explicitly removed in our definition of $\bar{f}_\gamma$ in Eq. (4.7)).

4.2.4 Results for Electron Injection

For electron and positron (e^+e^-) injection with energies $E_X \gg E_c$, we find the same photon (and electron) spectra as from photon injection with an equal total input energy, and thus our results agree reasonably well with Ref. [7] and the universal spectrum in this limit. However, for $E_X \lesssim E_c$ we find very significant variations from the universal spectrum as well as from pure photon injection. Photon spectra $\bar{f}_\gamma$ resulting from e^+e^- injection are shown in Fig. 4.5 for input energies $E_X = 100\,\mathrm{MeV}$ (left), $E_X = 30\,\mathrm{MeV}$ (middle), and $E_X = 10\,\mathrm{MeV}$ (right) and temperatures $T = 1, 10, 100\,\mathrm{eV}$. The solid lines show the full spectra, while the dashed lines show the corresponding result when FSR off the initial decay electrons is not taken into account. Also shown is the universal spectrum for the same total energy injection (normalized according to Eq. (4.26)). Let us also mention that the photon spectra do not have a delta function component for electron or positron injection.

The strong suppression of the photon spectrum from electron injection at lower energies in the absence of FSR was pointed out in Ref. [271]. As argued there, this suppression can be understood in terms of the behavior of IC scattering at low energy, which is the main mechanism for electrons to transfer energy to photons in this context. For smaller E_X and T, the dimensionless combination $y_e = E_e T/m_e^2 \ll 1$ is small, and IC scattering lies in the Thomson regime where each collision only slightly reduces the initial electron energy. Correspondingly, the maximal scattered photon energy E'_γ in the Thomson limit is $E'_\gamma \leq 4(E_e/m_e)E_\gamma$, where E_γ is the energy of the initial photon. Since the initial photon comes from the CMB, $E_\gamma \sim T$ is expected so that

$$\begin{aligned} E'_\gamma &\lesssim 4(E_e/m_e)^2 T \\ &\sim 15\,\mathrm{MeV}\left(\frac{E_e}{100\,\mathrm{MeV}}\right)^2\left(\frac{T}{100\,\mathrm{eV}}\right). \end{aligned} \tag{4.28}$$

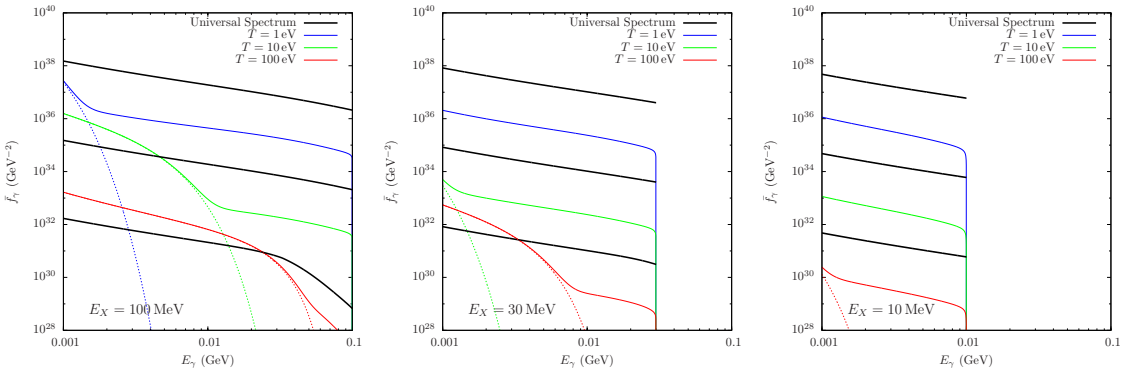

Figure 4.5: Photon spectrum $\bar{f}_\gamma(E)$ for electron plus positron (e^+e^-) injection with energies $E_X =$ 100 MeV (left), 30 MeV (middle), and 10 MeV (right), with $T = 1, 10, 100$ eV. The solid lines show the full spectrum, while the dashed lines show the result when FSR is not taken into account. Also shown is the universal spectrum for the same total injected energy.

Higher scattered photon energies are possible, but they come at the cost of an exponential Boltzmann suppression.

In this regime, FSR from the injected electrons and positrons can be the dominant contribution to the photon spectrum, as illustrated in Fig. 4.5. Relative to the rest of the cascade, the distribution of photons from FSR is hard, falling off roughly as $1/E$ instead of as $1/E^2$. Despite the suppression of FSR by $(\alpha/\pi) \times \log$ (with $\log \sim$ few), it can easily overcome the exponential suppression of IC for photon energies above the bound of Eq. (4.28). We show below that this has a very important implication for the effects of lower-energy electron injection on the primordial light element abundances. Note, however, that FSR has only a very minor effect on the spectra for photon injection or when $E_X \gg E_c$.

4.3 Effects of Electromagnetic Injection on BBN

Having computed the electromagnetic cascades from lower-energy injection, we turn next to investigate the effects of such injection on the primordial element abundances from BBN.

4.3.1 Photodissociation of Light Elements

Photodissociation of light element begins when the temperature of the cosmological plasma falls low enough for MeV photons to populate the electromagnetic cascade. From Eq. (4.1), this does not begin until temperatures fall below about 10 keV (corresponding to $t \sim 10^4$ s). By this time element creation by BBN has effectively turned off, and thus we can compute the effects of photodissociation as a post-processing of the outputs of standard BBN [241, 257].

The effects of photodissociation on the light element abundances can be described by a set of coupled Boltzmann equations of the form

$$\frac{dY_A}{dt} = \sum_i Y_i \int_0^\infty dE_\gamma \mathcal{N}_\gamma(E_\gamma)\, \sigma_{\gamma+i\to A}(E_\gamma) - Y_A \sum_f \int_0^\infty dE_\gamma \mathcal{N}_\gamma(E_\gamma)\, \sigma_{\gamma+A\to f}(E_\gamma)\ , \tag{4.29}$$

Process	Threshold (MeV)	Peak value (mb)
$\mathrm{D}+\gamma \to p+n$ [301]	2.220	2.47
$^3\mathrm{He}+\gamma \to \mathrm{D}+p$ [302]	5.490	1.18
$^3\mathrm{He}+\gamma \to p+p+n$ [302]	7.718	1.02
$\mathrm{T}+\gamma \to n+\mathrm{D}$ [303, 304]	6.260	0.818
$\mathrm{T}+\gamma \to n+n+p$ [304]	8.480	0.878
$^4\mathrm{He}+\gamma \to \mathrm{T}+p$ [305]	19.81	1.31
$^4\mathrm{He}+\gamma \to {}^3\mathrm{He}+n$ [306, 307]	20.58	1.28
$^4\mathrm{He}+\gamma \to \mathrm{D}+\mathrm{D}$ [257]	23.85	0.0051
$^4\mathrm{He}+\gamma \to n+p+\mathrm{D}$ [305]	26.07	0.182

Table 4.1: Processes included in our calculation of photodissociation effects from electromagnetic injections, as well as their threshold energies and peak cross sections.

where $\mathscr{N}_\gamma(E_\gamma)$ are the photon spectra calculated above, A and the sums run over the relevant isotopes, and Y_A are number densities normalized to the entropy density,

$$Y_A = \frac{n_A}{s} \,. \tag{4.30}$$

Note that we do not include reactions initiated by electrons because the electron spectra are always strongly suppressed by IC scattering.

In our analysis we include the nuclear species hydrogen (H), deuterium ($\mathrm{D} = {}^2\mathrm{H}$), tritium ($\mathrm{T} = {}^3\mathrm{H}$), helium-3 (^{3}He), and helium ($\mathrm{He} = {}^4\mathrm{He}$). Heavier species including lithium isotopes could also be included, but these have much smaller abundances and they would not alter the results for the lighter elements we consider. The nuclear cross sections included in our study are listed in Table 4.1, for which we use the simple parametrizations of Ref. [257]. All these cross sections have the same general shape as a function of energy, with a sharp rise at the threshold up to a peak followed by a smooth fall off. We list the threshold energies and peak values of the cross sections in the table to give an intuitive picture of their relevant strengths and ranges of importance. Of the nine cross sections listed, it is helpful to group them into processes that destroy helium and create deuterium and helium-3 with thresholds above 20 MeV, and processes that destroy the lighter isotopes with significantly lower thresholds.

It is straightforward to solve the evolution equations of Eq. (4.29) numerically following the standard convention of converting the dependent variable from time to redshift. For standard BBN values of the primordial abundances, we use the predictions of `PArthENoPE` [308, 309]:

$$Y_p = 0.247 \,, \qquad \frac{n_\mathrm{D}}{n_\mathrm{H}} = 2.45\times 10^{-5} \,, \qquad \frac{n_{^3\mathrm{He}}}{n_\mathrm{H}} = 0.998\times 10^{-5} \,. \tag{4.31}$$

In the analysis to follow, we compare the computed output densities to the following observed values, quoted with effective 1σ uncertainties into which we have combined theoretical and experimental

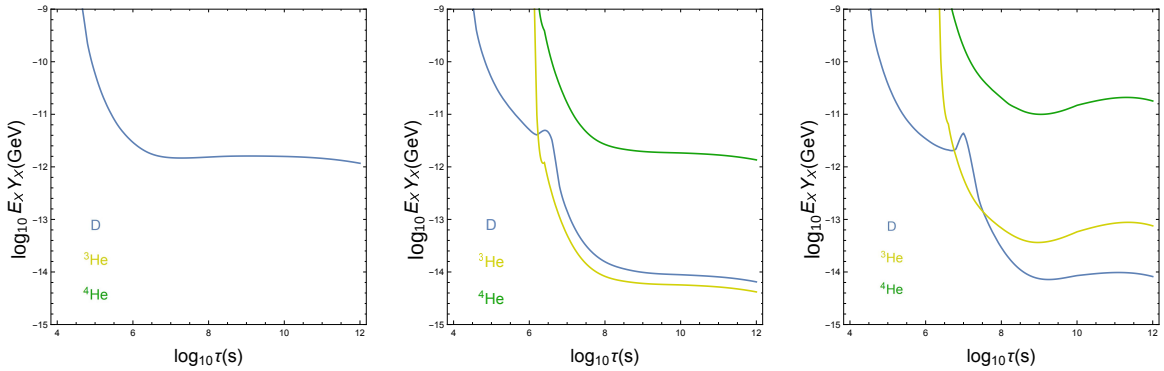

Figure 4.6: Limits on $E_X Y_X$ from BBN on the monochromatic photon decay of species X as a function of the lifetime τ_X for photon injection energies $E_X = 10$ MeV (left), 30 MeV (middle), and 100 MeV (right). Bounds are given for the effects on the nuclear species D, ^{3}He, and ^{4}He.

uncertainties in quadrature:

$$Y_p = 0.245 \pm 0.004 \quad \text{(Ref. [101])} \tag{4.32}$$

$$\frac{n_{\rm D}}{n_{\rm H}} = (2.53 \pm 0.05) \times 10^{-5} \quad \text{(Ref. [91])} \tag{4.33}$$

$$\frac{n_{^3{\rm He}}}{n_{\rm H}} = (1.0 \pm 0.5) \times 10^{-5} \quad \text{(Ref. [310])} \, . \tag{4.34}$$

For the helium mass fraction Y_p, the value we use is consistent with Ref. [104] and previous determinations but significantly lower than the determination of Ref. [102]. The quoted uncertainty on the ratio $n_{\rm D}/n_{\rm H}$ is dominated by a theory uncertainty on the rate of photon capture on deuterium from Ref. [311]. For $n_{^3{\rm He}}/n_{\rm H}$, we use the determination of $(n_{\rm D} + n_{^3{\rm He}})/n_{\rm H}$ of Ref. [310] together with the value of $n_{\rm D}/n_{\rm H}$ from Ref. [91]; the resulting upper bound (with uncertainties) is similar to but slightly stronger than what is used in Ref. [94]. The uncertainties quoted here are generous, and in the analysis to follow we implement exclusions at the 2σ level.

4.3.2 BBN Constraints on Photon Injection

Following the methods described above and the electromagnetic cascades computed previously, we derive BBN bounds on monochromatic photon injection from late decays with lifetime τ_X and initial injection energy E_X. In Fig. 4.6 we show the resulting limits on the combination $E_X Y_X$, where Y_X is the predecay yield of the decaying species X (assumed to produce one photon per decay) for injection energies $E_X = 10$, 30, 100 MeV. The bounds coming from D, ^{3}He, and ^{4}He are shown individually, and correspond to 2σ exclusions. Early on, when E_c is small, the dominant effect is destruction of D since it has the lowest photodissociation threshold. Later on, as E_c increases, it becomes possible to create excess D and ^{3}He through the destruction of ^{4}He provided the injection energy is larger than the ^{4}He threshold of about 20 MeV. Destruction of D is the dominant effect at all times for E_X below the helium threshold, as can be seen in the leftmost panel of Fig. 4.6.

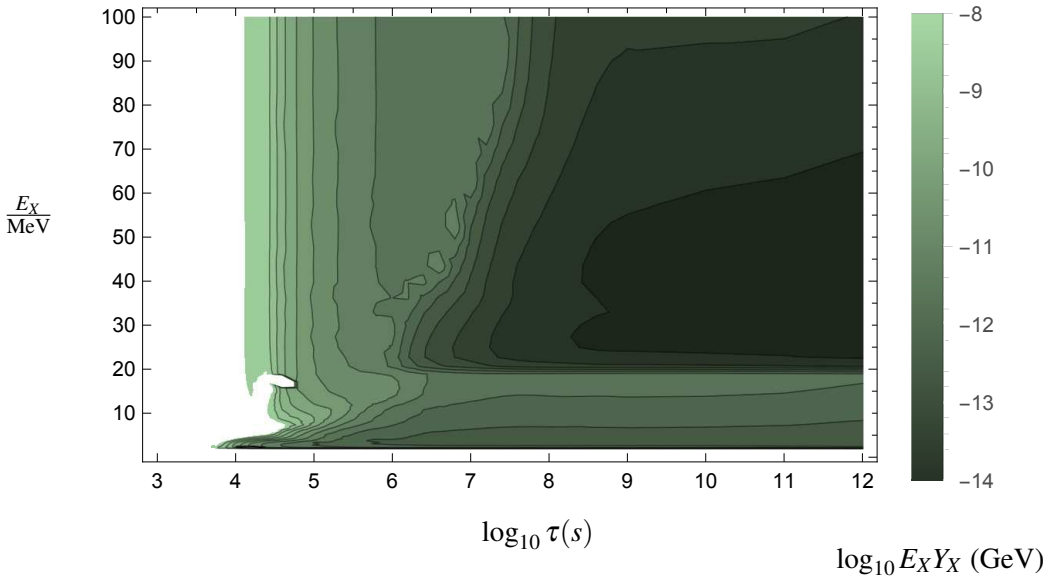

Figure 4.7: Combined limits on $E_X Y_X$ as a function of τ_X and E_X for the decay of a species X with lifetime τ_X injecting a single photon with energy E_X.

In Fig. 4.7 we show maximal values of $E_X Y_X$ from monochromatic photon injection at energy E_X from the decay of species X as a function of τ_X and E_X. The combined exclusion is based on the union of 2σ exclusions of the individual species. Clear features are visible in this figure at $\tau_X \simeq 10^6\,\text{s}$ and $E_X \simeq 20\,\text{MeV}$. These coincide with the structure of the exclusions shown in Fig. 4.6, with both corresponding to where the photodissociation of ^{4}He turns off, either because E_c or E_X is too small.

4.3.3 BBN Constraints on Electron Injection

In Fig. 4.8 we show the limits for $e + e^-$ injection from the decay of a species X with lifetime τ_X on $E_X Y_X$, where Y_X is the predecay yield of the decaying species X (assumed to produce one e^+e^- pair per decay) for injection energies for each electron of $E_X = 10, 30, 100\,\text{MeV}$ (from left to right). The bounds coming from D, ^{3}He, and ^{4}He are shown individually, and correspond to 2σ exclusions. The electromagnetic spectra used in this calculation include FSR from the injected e^+e^- pair. The resulting bounds are somewhat weaker than for photon injection and follow a similar pattern, and remain quite strong even down to $E_X = 10\,\text{MeV}$. For comparison, we show the corresponding results when FSR effects are not included in Fig. 4.9. As expected, the exclusions are significantly weaker, particularly for larger τ_X and lower E_X where the relevant IC scattering is deep in the Thomson regime.

In Fig. 4.10 we show maximal values of $E_X Y_X$ from monochromatic e^+e^- injection at energy E_X from the decay of species X as a function of τ_X and E_X, with FSR effects included in the electromagnetic cascade. The combined exclusion is based on the union of 2σ exclusions of the individual species. Again, the exclusions become weaker for $\tau_X \lesssim 10^6\,\text{s}$ or $E_X \lesssim 20\,\text{MeV}$ where the photodissociation of ^{4}He turns off. The bounds on e^+e^- injection are also typically weaker than for photon injection, but not drastically so when FSR is taken into account.

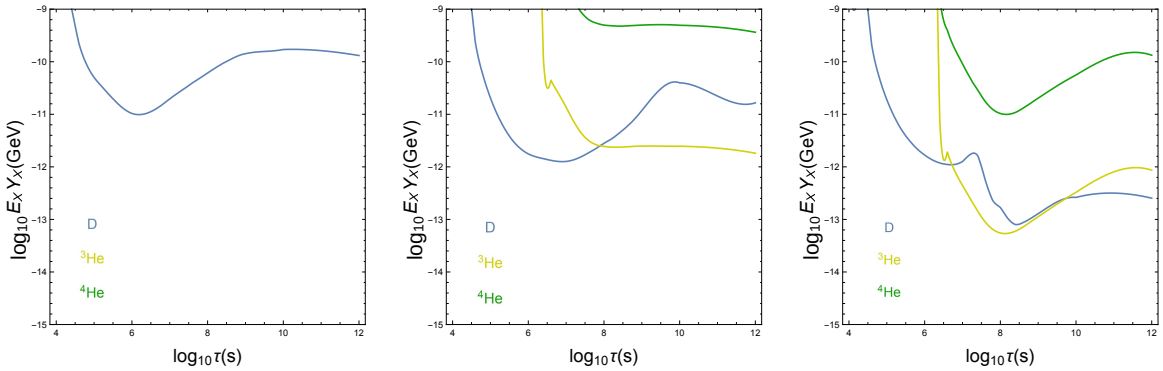

Figure 4.8: Limits on $E_X Y_X$ from BBN on the monochromatic e^+e^- decay of species X as a function of the lifetime τ_X for individual electron injection energies $E_X = 10\,\text{MeV}$ (left), 30 MeV (middle), and 100 MeV (right). Bounds are given for the effects on the nuclear species D, ^{3}He, and ^{4}He, and contributions to the electromagnetic cascades from FSR are included.

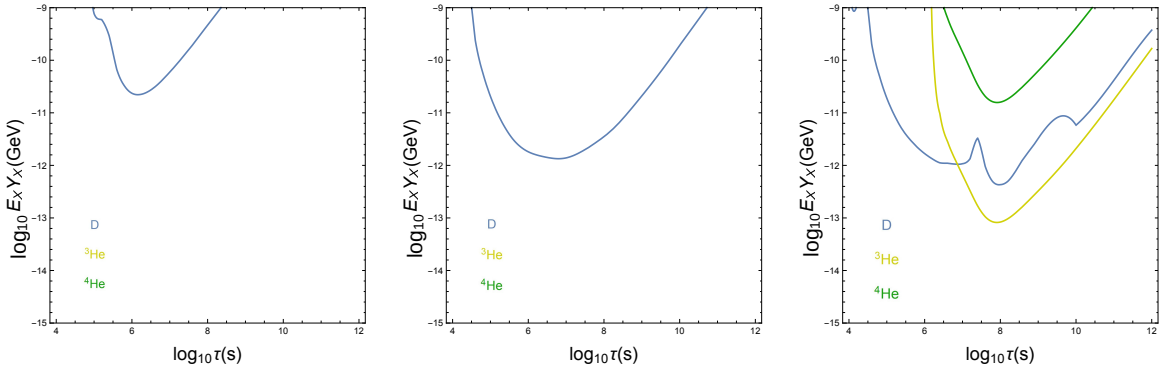

Figure 4.9: Same as Fig. 4.8 but without FSR effects.

4.4 Other Constraints on Low Energy Decays

In addition to directly modifying the primordial light element abundances, energy injection in the early universe can produce other deviations from the standard cosmology. Electromagnetic decays near or after recombination at $t_{rec} \simeq 1.2 \times 10^{13}\,\text{s}$ can modify the the temperature and polarization power spectra of the CMB [123, 312–314]. Since current CMB observations are found to constrain such decays much more strongly than BBN [80, 315], we focus here on decays prior to recombination. The best limits in this case, aside from BBN, come from alterations to N_{eff} and modifications to the CMB frequency spectrum. N_{eff} can be constrained both before the beginning of BBN, as while as much later due to its effect on the CMB as well. Early alterations of N_{eff} will alter the radiation energy density, in turn leading to an altered neutron abundance available for the main BBN processes. N_{eff} will also be constrained by the CMB as it increases the amount of small-scale Silk damping present in the CMB power spectrum[268, 280, 294, 295]. In this section we estimate these other limits on late energy injection and compare them to our results for BBN.

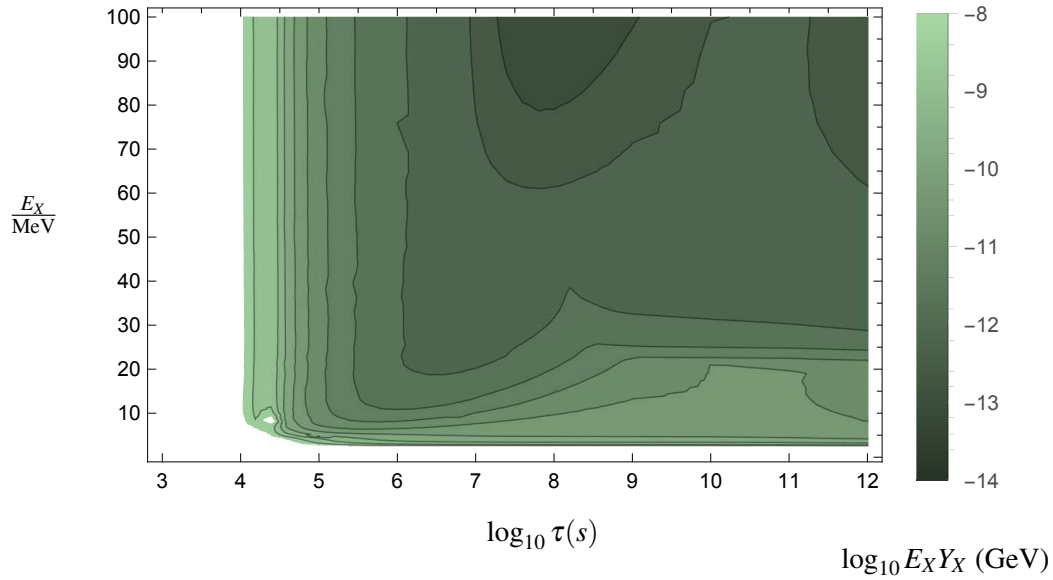

Figure 4.10: Combined limits on $E_X Y_X$ as a function of τ_X and E_X for the decay of a species X with lifetime τ_X injecting an electron-positron pair each with energy E_X, with FSR effects included.

4.4.1 Constraints from N_{eff}

Recall that we have defined N_{eff} to be a proxy for the total contribution of radiative species to the radiation energy density that are not photons, as shown in Eq. (4.2). This includes standard model neutrinos, such that without the presence of new physics, $N_{eff} = N_\nu = 3.046$, which is slightly larger than 3 due to reheating during the non-instantaneous decoupling of electron-positron annihilations. The $T_{\nu,0}/T_{\gamma,0}$ factor is the temperature ratio of neutrinos to photons assuming no new physics. It accounts for the fact that neutrinos have a different temperature from photons after $e^\pm$ annihilation, and is given by [70, 71]:

$$\frac{T_{\nu,0}}{T_{\gamma,0}} = \begin{cases} 1 & T \gg m_e \\ (4/11)^{1/3} & T \ll m_e \end{cases} \tag{4.35}$$

As was dicussed in Ch. 2. If we allow for particles to decay either electromagnetically, or into neutrinos, we inject extra energy into the visible sector. This energy will effectively heat up all particles that are in thermal equilibrium with the decay products. As such, we can also write out the total radiation energy density during times of interest as:

$$\rho_R = \rho_\gamma + \rho_\nu + \rho_X \tag{4.36}$$

Note that here, we do not include $e^\pm$ as radiative species, as we will typically be concerned only with temperatures below their mass. In theory, the decaying X particles could contribute to the radiation density as well, if they are light enough and have a thermal temperature $T_x \gg m_x$. This type of effect has

been well studied for particles in thermal equilibrium with standard model particles [10, 268, 279, 280]. Instead, we focus on the case of a cold dark particle, that will not itself contribute to the radiation energy density, and thus $\rho_X = 0$, and it instead contributes indirectly via the alteration of either ρ_γ or ρ_ν.

Comparing Eqs. (4.2) and (4.36), and using Eq. (2.24), with g_i = 2 (6) for photons (neutrinos), we see that a working definition of N_{eff} is given by:

$$\frac{N_{eff}}{N_\nu} = \left(\frac{T_{\gamma,0}}{T_{\nu,0}} \times \frac{T_\nu}{T_\gamma}\right)^4 \tag{4.37}$$

To calculate changes to N_{eff}, we consider conservation of both energy and entropy. We begin by assuming that the decay will happen instantaneously, when the Hubble rate has dropped to match the decay rate, $1/\tau$. This occurs at a decay temperature, T_d of:

$$T_d = \left(\frac{M_{\rm Pl}}{\tau}\right)^{1/2} \left(g_*(T_d)\frac{\pi^2}{90}\right)^{-1/4} \tag{4.38}$$

with g_* defined as in Eq. (2.30). This not only allows us to produce analytic estimates, but it will be accurate to within a few percent. If the decay occurs to electromagnetic species, the photon temperature will increase, and N_{eff} will be reduced. However, if the the decay occurs to neutrinos, then N_{eff} increases. Note that in both cases, we assume explicitly that the decay is occurring after the neutrinos have decoupled, at temperature $T \sim 2$ MeV. Otherwise, any energy introduced into the visible sector is equilibriated between both photons and neutrinos, and both T_ν and T_γ will change by the same amount.

In particular, we assume that the decaying particle has some steady comoving number density before it decays. If the decaying particle has an initial mass weighted yield, $m_x Y_x$, then the energy density of the particle right before it decays is:

$$\rho_X = m_x n_x = m_x Y_x s(T_d) \tag{4.39}$$

with s the relativistic entropy density, given in Eq. (2.34). We can use this to calculate the energy that is transferred to either ρ_γ or ρ_ν. In particular, we find that for decays to electromagnetic species, this results in an N_{eff} of:

$$\frac{N_{eff}}{N_\nu} = \begin{cases} 1 & T > T_d \\ \left[1 + \frac{2}{3} g_{*s}(T_d)\left(\frac{m_x Y_x}{T_d}\right)\right]^{-1} & T < T_d \end{cases} \tag{4.40}$$

while for decays to neutrinos, we find:

$$\frac{N_{eff}}{N_\nu} = \begin{cases} 1 & T > T_d \\ \left[1 + \frac{16}{63} g_{*s}(T_d)\left(\frac{T_{\gamma,d}}{T_{\nu,d}}\right)^4 \left(\frac{m_x Y_x}{T_d}\right)\right] & T < T_d \end{cases} \tag{4.41}$$

Note that the factor $T_{\gamma,d}/T_{\nu,d}$ is 1 for decays before $e^\pm$ annihilations, and $(11/4)^{1/3}$ otherwise.

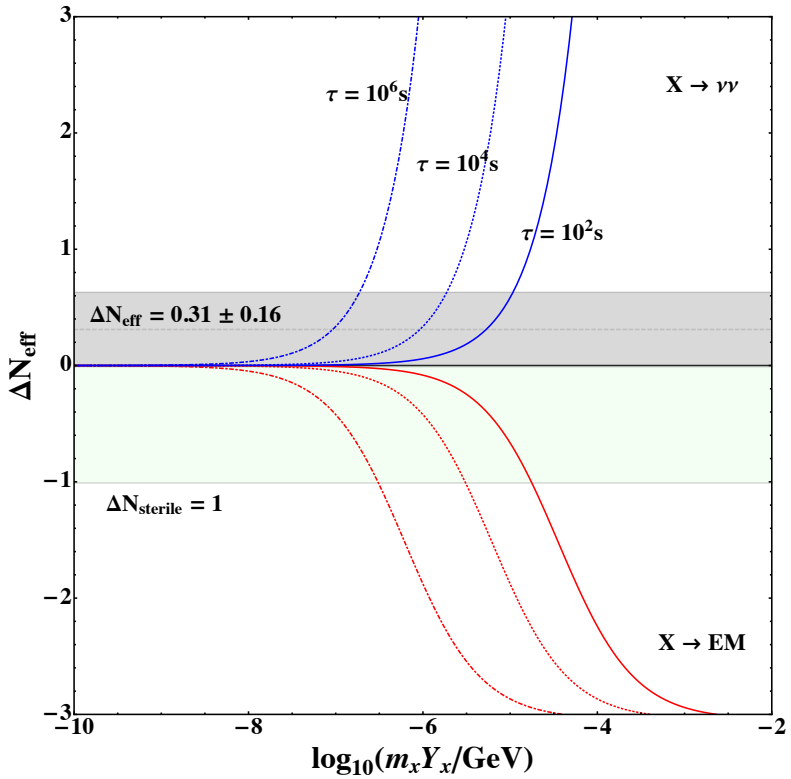

Figure 4.11: Effects of low energy decays on N_{eff} for decays to neutrinos (top, blue), and electromagnetic species (bottom, red). Shown are effects for various particle lifetimes. The central grey band corresponds to the conservative estimate given in Eq. (4.42), in agreement with Planck and BBN estimates[9, 10]. The enlarged green region shows the extra phase space that could be allowed if a sterile neutrino with $\Delta N_{eff} = 1$ is included.

The results for decays to light visible species are given in Fig. 4.11. The blue, increasing lines correspond to decays to neutrinos, while the red, falling lines correspond to decays to γ and $e^{\pm}$, as we expect. We also include a grey band to show the region that is consistent with present day observations. Currently, the 2018 Planck results constrain N_{eff} to a central value of 3.27 ± 0.15, when considered in conjunction with other astrophysical observations [67]. Furthermore, if we consider BBN constraints, then $N_{eff} = 3.56 \pm 0.23$ is favoured [10]. This gives us combined results of:

$$\Delta N_{eff} = N_{eff} - 3.046 = 0.31 \pm 0.16 \tag{4.42}$$

which implies that cosmological observations favour a slightly larger value of N_{eff} than is present in the SM. In Fig. 4.11, we use 95% confidence intervals to estimate a conservative region that is consistent with observations.

It's also interesting to note that the decay to EM species has an interesting caveat. If there is a fully thermalized sterile neutrino, this would correspond to a $\Delta N_{eff} = 1$. As such, decays to EM species can be compensated by the presence of a sterile neutrino, thus allowing slightly larger decays to remain consistent with current observations [316]. This is given by the extended green band in Fig. 4.11.

4.4.2 Constraints from the CMB

Late decays releasing electromagnetic energy can also distort the frequency spectrum of the CMB [317, 318], which is observed to be a nearly-perfect blackbody [319]. The effect depends on the decay time τ_X relative to the times $\tau_{dC} \simeq 6.1 \times 10^6\,\mathrm{s}$ when double-Compton scattering freezes out and $\tau_C \simeq 8.8 \times 10^9\,\mathrm{s}$ when Compton scattering turns off [317, 318]. Decays with $\tau_{dC} < \tau_X < \tau_C$ yield products that thermalize through Compton scattering and generate an effective photon chemical potential μ given by [317, 318, 320]

$$\mu \;\simeq\; 5.6 \times 10^{-4} \left(\frac{\Delta E\, Y_X}{10^{-10}\,\mathrm{GeV}}\right) \left(\frac{\tau}{10^6\,\mathrm{s}}\right)^{1/2} e^{-(\tau_{dC}/\tau)^{5/4}} \,. \tag{4.43}$$

For $\tau_X > \tau_C$, electromagnetic injection produces a distortion that can be described by the Compton parameter $y = \Delta\rho_\gamma/4\rho_\gamma$, with the approximate result [317, 318, 320]

$$y \;\simeq\; 5.7 \times 10^{-5} \left(\frac{\Delta E\, Y_X}{10^{-10}\,\mathrm{GeV}}\right) \left(\frac{\tau}{10^6\,\mathrm{s}}\right)^{1/2} \mathscr{C}(\tau) \,, \tag{4.44}$$

where $\mathscr{C}(\tau) = 1$ for $\tau < t_{eq}$ and $\mathscr{C}(\tau) \simeq (\tau/t_{eq})^{1/6}$ for $\tau > t_{eq}$. The current limits on μ and y are [319]

$$\mu < 9 \times 10^{-5}, \quad |y| < 1.5 \times 10^{-5} \,, \tag{4.45}$$

while the proposed PIXIE satellite is to have sensitivity to constrain [321]

$$\mu < 1 \times 10^{-8}, \quad |y| < 2 \times 10^{-9} \,. \tag{4.46}$$

In the left and right panels of Fig. 4.12 we show the limits from N_{eff} and CMB spectral distortions. The solid (dashed) red line shows $N_{eff} = 0.31 \pm 0.16$ for decays to EM (neutrinos), with a conservative 95% estimate included. Note that the constraint arising from EM decays is much stronger, due to the fact that these decays lower N_{eff}, while cosmologically evidence preferentially raises it. This constraint can be mediated by the presence of sterile neutrinos, as discussed above. For CMB spectral distortions we show bounds on the μ and y parameters in blue based on the approximate estimates above based on measurements by COBE/FIRAS (solid) and the projected sensitivity of PIXIE (dotted). For comparison, we show in green the limits derived above for monochromatic photon injection (left) and monochromatic e^+e^- injection (right). In both panels, the dotted, dashed, and solid lines correspond to injection with $E_X = 10, 30, 100\,\mathrm{MeV}$. Even for low injection energies, BBN constraints currently dominate for $\tau \gtrsim 10^4\,\mathrm{s}$ until being replaced by bounds from either CMB frequency or power spectrum variations. Even with the vast improvement expected from PIXIE, BBN will continue to provide the strongest limit on electromagnetic decays in the early universe with lifetimes $10^4\,\mathrm{s} \lesssim \tau_X \lesssim 10^6\,\mathrm{s}$ and energy injections above a few MeV.

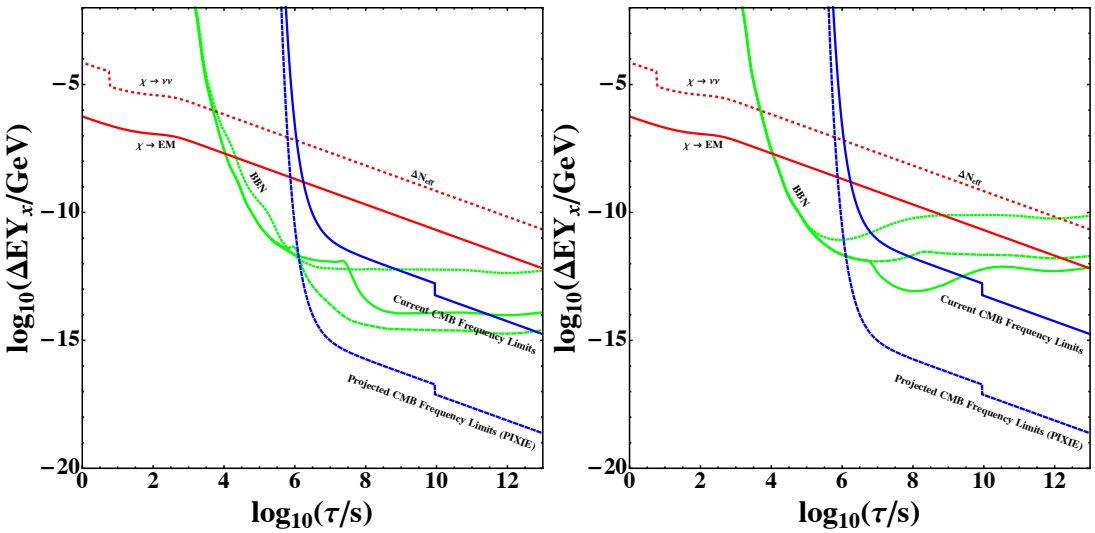

Figure 4.12: Other bounds on electromagnetic decays in the early universe as a function of the lifetime τ_X and the total electromagnetic injection $\Delta E Y_X$ relative to limits derived from BBN. In both panels, the red line shows $\Delta N_{eff} = 0.31 \pm 0.16$, while the solid (dotted) blue lines show the current and projected CMB frequency bounds from COBE/FIRAS (PIXIE). The left panel also indicates the limits derived from BBN for photon injection with energy $E_X = 10, 30, 100$ MeV with green dotted, dashed, and solid lines. The right panel shows the corresponding BBN bounds from monochromatic e^+e^- injection.

4.5 Conclusions

In this chapter, we have focused on the interplay between the dark sector and the visible sector from the perspective of decaying dark species. As in the previous chapter, we have focused specifically on a one-way energy flow, as indicated in Fig. 4.1. In this section, the energy flow was from the dark to the visible, so that we can isolate the effect that dark decays and annihilations may have on various SM particles and how we can observe this influential effect. Also similar to the previous chapter, we focus on 'small' interactions. In Ch. 3, we focus on small interactions via a feeble coupling, such that the two sectors never fully thermalize. In this chapter, however, we focus on 'small' in the sense that we consider low energy transfers, typically below 100 MeV. Although early, well motivated theories tended to focus on new physics at or above the weak energy scale, new models can still be well motivated much below this, and these low energy ranges have not yet been fully explored. We are able to place stringent constraints on new physics, simply by modelling how the visible sector, which is full of well-understood and strongly coupled particles, responds to the energy inflow. This response can be compared to present day observations to identify models and parameter spaces that are in conflict.

To set the stage for dark energy deposition, we have investigated the electromagnetic cascades induced by electromagnetic energy injection in the range $E_X = 1 - 100$ MeV and we have studied its effects on the light elements abundances created during BBN. As in Ref. [8], we find significant deviations from the universal photon spectrum for monochromatic initial photon injection with energy $E_X \lesssim E_c = m_e^2/22T$. Our study also expands on previous work by computing the full electromagnetic

cascade including electrons.

Photon and electron injection produce very similar electromagnetic cascades for $E_X \gg E_c$ but differ in important ways for $E_X \lesssim E_c$. Initial hard photons induce a smooth population of lower-energy photons through Compton and photon-photon scattering. In contrast, electrons injected with $E_X \lesssim m_e^2/10T$ interact mainly through inverse Compton (IC) scattering off the CMB, which lies in the Thomson regime at such energies. The upscattered photons from Thomson scattering have much lower energy than the initial electron, and can easily fall below the MeV scales needed to induce photodissociation. However, in this regime we find that photons radiated off the initial hard electrons can populate and dominate the induced photon spectrum up to near the initial electron energy. To our knowledge, the contribution of FSR to the photon spectrum has not been considered before in this context since its effects are very small at the higher initial injection energies that have been investigated in the greatest detail.

We also study how this impacts BBN, both directly through photodissociation of the light elements, and indirectly through changes to N_{eff}. For either photon or electron injection, we find that BBN provides the strongest constraint on late-decaying particles with lifetimes between $10^4\,\mathrm{s} \lesssim \tau \lesssim 10^{13}\,\mathrm{s}$ for electromagnetic energies nearly all the way down to the photodissociation threshold of deuterium near $E_{th} \simeq 2.22$, MeV. For earlier lifetimes, the indirect effects obtained via N_{eff} provide the strongest constraints. When considering N_{eff}, we gain the ability to consider decays to the other kinematically allowed species, neutrinos. While decays to neutrinos typically raise their temperature and thus increase N_{eff}, decays to EM species do the opposite. Because current observations favour a slight increase in N_{eff}, the EM decays are thus more constrained (although they do allow for the possibility of a sterile neutrino to compensate for the N_{eff} reduction).

While this work has concentrated on decays, our results for electromagnetic cascades are also applicable to annihilation in the early universe. Our results could also be used to investigate potential solutions to the apparent anomalies in the lithium abundances, which was studied in Refs. [276, 322] using the universal spectrum.

At this point, we have studied elementary models that move energy from either the visible sector to the dark, or the dark sector to the visible. In both cases, we have considered dark sectors that have minimal interactions, and focused on understanding how the two sectors might interact with each other. Let us now turn to a more concrete and complex model of a hidden sector, in which we can apply the tools we have learned to study it in greater detail.

Part IV

A Complete Dark Model

Chapter 5

Non-Abelian Dark Forces and the Relic Densities of Dark Glueballs

5.1 Introduction

Up to this point, we have split the dark and visible sectors of the Universe, in an effort to understand how the two sectors may interact and play roles in the evolution of each other. In doing this, we have utilized fairly simple models of the dark sector, so that the inter-sector interactions would be highlighted and not masked by effects in the hidden sector. In the next few chapters we will focus on a more concrete realization of a dark sector, in which we can find a rich spectrum of interactions. To begin, we will focus explicitly on the dark sector isolated by itself, and attempt to understand how the self-interactions of this sector play a role in its own evolution, as shown in Fig. 5.1. In the following chapter, we will incorporate Standard Model connections, thus creating a full, rich, and connected dark sector that will incorporate what we have learned in the previous chapters.

To motivate the dark sector we will consider, we note that gauge invariance under the $SU(3)_c \times SU(2)_L \times U(1)_Y$ group of the Standard Model provides a remarkable description of the non-gravitational forces of Nature. Yet, our knowledge of the Universe is incomplete and new gauge forces beyond those of the SM may be crucial to describing the laws of physics. The existence of such forces is highly constrained if they couple significantly to SM matter unless they have an associated mass scale (such as from confinement or the Higgs mechanism) well above a TeV [323, 324]. In contrast new *dark* gauge forces, with only feeble connections to the SM, can exist at energy scales much less than the TeV scale (or even be in a massless phase) and still be fully consistent with existing experimental bounds [325–327]. Such dark forces may also be related to the cosmological dark matter [146, 209, 213].

Abelian dark forces have been studied in great detail and have the novel property that they can connect to the SM at the renormalizable level through gauge kinetic mixing [328, 329]. Limits on the existence of such a kinetically-mixed *dark photon* have been obtained from existing experimental

[0]This chapter is based on L. Forestell, D. E. Morrissey, and K. Sigurdson, *Non-Abelian Dark Forces and the Relic Densities of Dark Glueballs*, Phys. Rev. D, **95**, (2016), 015032, [arXiv:1605.08048] [3]

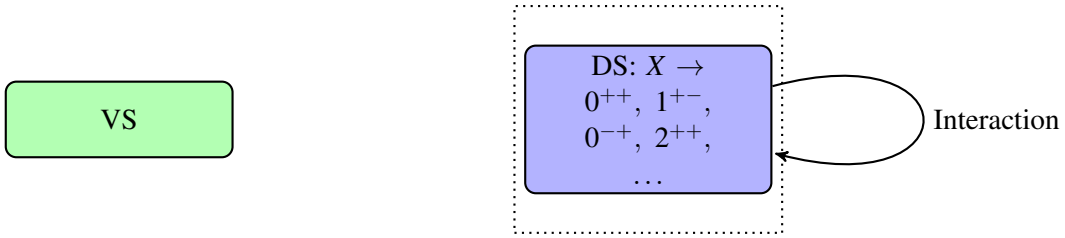

Figure 5.1: Flow of information considered in this chapter. We start our inspection of a non-Abelian dark force with a completely hidden sector, entirely isolated from the visible. However, even though isolated, the dark sector will still have a complex set of interactions, with many stable glueball states that can be involved in self-interactions, annihilations, and so on.

searches and astrophysical and cosmological observations for a range of dark photon masses spanning many orders of magnitude [325–327]. An exciting dedicated experimental program to search for dark photons is also underway [326, 327].

Non-Abelian dark forces have received somewhat less attention. As gauge invariance forbids the simple kinetic-mixing interaction with the SM, it is less clear how they might connect to the SM. Even so, non-Abelian dark forces are well motivated and arise in many contexts including string theory constructions [330], in models of dark matter [229, 231, 232, 235, 331–338], baryogenesis [339–341], theories of neutral naturalness [54, 342], and within the *hidden valley* paradigm [11, 12, 343]. Non-Abelian dark forces can also lead to very different phenomenological effects compared to their Abelian counterparts owing to the requisite self-interactions among the corresponding gauge bosons and their potential for a confining phase transition at low energies.

The minimal realization of a non-Abelian dark force is a pure Yang-Mills theory with simple gauge group G_x. Such a theory is expected to confine at the characteristic energy scale Λ_x, with the elementary dark gluons binding into a spectrum of colour-neutral dark glueballs (GBs) of mass $m \sim \Lambda_x$ [344]. These dark states may have significant cosmological effects even when their connection to the SM is too small to be detected in laboratory experiments. For very small values of Λ_x, dark gluons can act as self-interacting dark radiation [345–348], and can be consistent with existing constraints provided their effective temperature is somewhat lower than the SM plasma. With larger Λ_x, the glueballs will contribute to the density of dark matter if they are long-lived [229, 231, 232, 235, 336], or they may lead to observable astrophysical or cosmological signals if they decay at late times [229, 235, 336].

Assessing the cosmological impact of massive dark glueballs requires a precise knowledge of their relic abundances. The primary goal of this chapter is to compute these abundances and map out the ranges of parameters where one or more dark glueball states might constitute all or some of the observed dark matter. We focus mainly on $G_x = SU(3)$, but we also comment on how our results can be applied to other non-Abelian gauge groups. In the next chapter we will describe in detail the cosmological effects of both stable and unstable primordial glueball populations and use them to constrain the existence of non-Abelian dark forces.

Starting from an early Universe containing a thermal plasma of dark gluons with temperature $T_x > \Lambda_x$, typically different than the temperature of the SM plasma, dark glueballs will be formed in a phase

transition as the temperature of the dark sector falls below the confinement scale, $T_x \lesssim \Lambda_x$. Since glueball number is not conserved, the number densities of the glueball states will then track their equilibrium values so long as their $2 \to 2$ and $n \to 2$ interaction rates are fast relative to the Hubble expansion rate. The key difference compared to standard freeze-out is that without direct annihilation or rapid decays to SM or lighter hidden states, the overall chemical equilibrium of the dark glueballs will be maintained primarily by $3 \leftrightarrow 2$ number-changing reactions [147, 349, 350]. Moreover, if the hidden glueballs do not have a kinetic equilibration with the SM or a bath of relativistic hidden states, the energy released by the $3 \to 2$ annihilations will cause the remaining glueballs to cool much more slowly than they would otherwise [349]. Together, these two effects produce freeze-out yields with a much different dependence on the underlying parameters of the theory than the typical freeze-out paradigm of annihilation into light relativistic particles.

Previous works have studied the effects of $3 \to 2$ annihilation and self-heating in general massive self-coupled sectors [147, 349, 350]. The specific application of these processes to dark glueballs has also been studied in Refs. [231, 232, 235]. We expand upon these works in two ways. First, we investigate possible effects of the confining phase transition on the final glueball yields.[1] And second, we compute the freeze-out abundances of the heavier glueball states in addition to the lightest mode. We also comment on the importance of including some of the heavier states, as when the glueballs are connected to the SM, the heavier relic glueball states can sometimes have a greater observational effect than the lightest mode.

Following this introduction, we discuss the general properties of dark glueballs in Section 5.2. Next, we study the freeze-out of the lightest glueball in Section 5.3 and investigate the effects of the confining phase transition. In Section 5.4 we extend our freeze-out analysis to include the heavier glueball states. The possibility of dark glueball dark matter is studied in Section 5.5, as well as a brief introduction to additional constraints that may be placed on general dark forces when a connection to the SM is added. We give brief concluding remarks in Section 5.6. This chapter is based on work published in Ref. [3] in collaboration with David Morrissey and Kris Sigurdson.

5.2 Glueball Spectrum and Interactions

The spectrum of glueballs in pure $SU(N)$ gauge theories has been studied extensively using both analytic models and lattice calculations [352]. Stable glueballs are classified according to their masses and their quantum numbers under angular momentum (J), parity (P), and charge conjugation (C). The lightest state is found to have $J^{PC} = 0^{++}$ [6, 353, 354], as expected based on general grounds [355], but a number of stable states with other J^{PC} values are seen as well. In this section we summarize briefly the expected spectrum of glueballs and we estimate how they interact with each other.

[1] These effects were studied in a slightly different context in Ref. [351].

J^{PC}	$m\,r_0\,(N=2)$	$m\,r_0\,(N=3)$
0^{++}	4.5(3)	4.21(11)
2^{++}	6.7(4)	5.85(2)
3^{++}	10.7(8)	8.99(4)
0^{-+}	7.8(7)	6.33(7)
2^{-+}	9.0(7)	7.55(3)
1^{+-}	–	7.18(3)
3^{+-}	–	8.66(4)
2^{+-}	–	10.10(7)
0^{+-}	–	11.57(12)
1^{--}	–	9.50(4)
2^{--}	–	9.59(4)
3^{--}	–	10.06(21)

Table 5.1: Masses of known stable glueballs in $SU(2)$ [5] and $SU(3)$ [6].

5.2.1 Glueball Masses

Much of what is known about the spectrum of glueballs in $SU(N)$ gauge theories comes from lattice calculations. It is conventional to express these masses in terms of a length scale r_0 corresponding to where the gauge potential transitions from Coulombic to linear [356, 357], or in terms of the confining string tension $\sqrt{\sigma}$. Both of these quantities can be related to the energy scale $\Lambda_{\overline{MS}}$ where the running gauge coupling becomes strong [358]. For $SU(3)$ (with zero flavors), they are given by $r_0\Lambda_{\overline{MS}} = 0.614(2)(5)$ [358] and $r_0\sqrt{\sigma} = 1.197(11)$ [5, 357]. To facilitate connections with modern lattice calculations, we will express the glueball masses in terms of $1/r_0$ and define the strong coupling scale as the mass of the lightest 0^{++} glueball, $\Lambda_x \equiv m_0^{++}$.

Assuming conserved P and C in the dark sector, the dark glueballs will have definite J^{PC} quantum numbers. In Table 5.1 we list the spectra of $SU(N)$ glueballs for $N = 2$ and $N = 3$ determined in lattice studies in units of r_0. The $N = 3$ glueballs in the table correspond to all the known stable states, with the masses listed taken from Ref. [6]. Listings for the $N = 2$ case are based on Ref. [5], have significantly larger fractional uncertainties, and may not give a complete accounting of all the stable states. Note that the absence of C-odd states is expected for $SU(2)$ and other Lie groups with a vanishing $d^{abc} = tr(t^a\{t^b,t^c\})$ symbol (where t^a is the generator of the fundamental representation) [11, 352, 359].

Glueball spectra for $SU(N > 3)$ have also been investigated on the lattice [360, 361]. The (lowest-lying) glueball masses are found to scale with N according to

$$r_0\, m(N) \simeq P + Q/N^2\,, \tag{5.1}$$

with P and Q on the order of unity. These corrections are found to be numerically modest for $N > 3$, and the glueball spectrum for larger N appears to be similar to $N = 3$. Extrapolations to large N also find that $r_0\sqrt{\sigma} \simeq 1.2$ remains nearly constant [5], while the strong-coupling scale decreases smoothly to $r_0\Lambda_{\overline{MS}} \simeq 0.45$ [362]. A further variation on $SU(N)$ theories is the addition of a non-zero topological

theta term. This violates P and T explicitly, shifts the string tension $\sqrt{\sigma}$ and glueball masses [363], and induces mixing between glueball states with different P quantum numbers [363, 364].

The glueballs for other non-Abelian gauge groups have not been studied in as much detail on the lattice, but a few specific features are expected based on general arguments. As mentioned above, there are no C-odd states for $SU(2)$, $SO(2N+1)$, or $Sp(2N)$ due to their vanishing d^{abc} coefficient [11, 352, 359]. For $SO(2N)$, $SO(4) \cong SU(2) \times SU(2)$ and $SO(6) \cong SU(4)$ reduce to previous cases, while for $2N > 6$ the C-odd states are expected to be significantly heavier than the lowest C-even glueballs [11]. This follows from the fact that the minimal gluon operators giving rise to the C-odd states for the groups have mass dimension $2N$ [359], and higher-dimension gluon operators are generally expected to lead to heavier glueball states [6, 11, 359].

In this study we concentrate on $SU(N)$ glueballs with P and C conservation in the dark sector. However, other non-Abelian gauge groups could be realized in nature [330], and we comment on these more general scenarios when they lead to important phenomenological distinctions.

5.2.2 Glueball Couplings

Dark glueball freeze-out in the early Universe depends on the cross sections for $2 \to 2$ and $3 \to 2$ glueball reactions. Glueball self-couplings and transition matrix elements are thus needed to compute their cosmological evolution. These quantities have not been studied in as much detail on the lattice as the glueball mass spectrum. Here, we collect the relevant existing lattice results, and we use naive dimensional analysis (NDA) [365–367] and large-N scaling [368, 369] to make estimates when no lattice data is available.

Glueball interactions are expected to be perturbative in the limit of large N (for an underlying $SU(N)$ gauge group), and this motivates writing an effective Lagrangian in terms of glueball fields. Combining the N scaling of gluon n-point functions with dimensional analysis suggests the form

$$\mathscr{L}_{eff} = \left(\frac{N}{4\pi}\right)^2 m_x^4 F(\phi/m_x, \partial/m_x) \,, \tag{5.2}$$

where ϕ represents a glueball field interpolated by a single-trace gluon operator, m_x is a characteristic glueball mass scale, and $F(x,y)$ is a smooth function that is finite as $N \to \infty$. Expanding this function in a power series and rescaling to obtain a canonical kinetic operator, the effective Lagrangian becomes

$$\mathscr{L}_{eff} = \frac{1}{2}(\partial\phi)^2 - \sum_n \frac{a_n}{n!} m_x^{4-n} \left(\frac{4\pi}{N}\right)^{n-2} \phi^n + \ldots \tag{5.3}$$

where the coefficients a_n are expected to be of order unity. This form matches the NDA scaling of Ref. [231] as well as the $1/N$ counting of Ref. [235]. Note that shifting the gluon field to remove the linear term does not alter this general form. In the analysis to follow, we identify $m_x = m_0$ with the mass of the lightest glueball.

This gives rise to diagrams such as those shown in Fig. 5.2, which allows for both $2 \to 2$ as well as $3 \to 2$ interactions. Applying this form to $2 \to 2$ elastic scatterings of the 0^{++} state with mass m_x, we

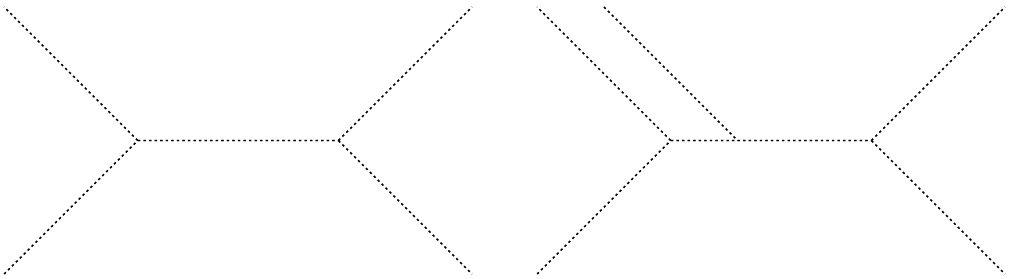

Figure 5.2: Feynman diagrams for the scalar 0^{++} glueball state, which include a typical self-interaction (left), as well as a number changing interaction (right).

estimate

$$\sigma_{2\to 2} v \simeq \frac{A}{4\pi}\left(\frac{4\pi}{N}\right)^4 \frac{\beta}{s}\,, \tag{5.4}$$

where A is dimensionless and close to unity, s is the square of the center-of-mass energy, and $\beta = \sqrt{1-4m_x^2/s}$. The same arguments applied to $3\to 2$ processes at low momentum give

$$\sigma_{3\to 2} v^2 \simeq \frac{B}{(4\pi)^3}\left(\frac{4\pi}{N}\right)^6 \frac{1}{m_x^5}\,, \tag{5.5}$$

with B also close to unity. These cross sections are at the limit of perturbative unitarity for small N but become moderate for $N \gtrsim 4\pi$, reflecting the expected transition to weak coupling in this regime [369]. In the analysis to follow we set $A = B = 1$, and we generalize the cross section estimate for $2\to 2$ interactions to more general processes involving other glueball states using the same NDA and large-N arguments.

5.3 Freeze-out of the Lightest Glueball

Having reviewed the properties of glueballs, we turn next to investigate their freeze-out dynamics in the early Universe. In this section we study the thermodynamic decoupling of the lightest 0^{++} glueball in a simplified single-state model. We also discuss the confining transition in which the glueballs are formed and investigate how it might modify the glueball relic density. The freeze-out of heavier glueballs will be studied in the section to follow.

Throughout our analysis, we assume that the dark glueballs are thermally decoupled from the SM during the freeze-out process but maintain a kinetic equilibrium among themselves. This implies that the entropy of the dark sector is conserved separately from the visible sector, up to a possible increase during a first-order confining phase transition. This motivates the definition

$$R \equiv \frac{s_x}{s} = \text{constant}\,, \tag{5.6}$$

where s_x is the entropy density of the dark sector *after the confining transition* and s is that of the

visible. The value of R is an input to our calculation, and may be regarded as an initial condition set by the relative reheating of the dark and visible sectors after inflation if they were never in thermal contact [204, 231], or by the thermal decoupling of the sectors if they once were [350]. Since inflation can potentially reheat the dark and visible sectors very asymmetrically, we consider a broad range of $R \in [10^{-12}, 10^{-3}]$. For $T_x \gg T_c$ and $G_x = SU(N)$, the entropy ratio is related to the temperatures in the two sectors by

$$R = \frac{2(N^2-1)}{g_{*S}} \left(\frac{T_x}{T}\right)^3 , \tag{5.7}$$

where g_{*S} is an effective number of degrees of freedom in the visible sector at temperature T. This ratio will be maintained through the confining transition provided it is not too strongly first order [351].

5.3.1 Single-State Model

Consider first a dark sector consisting of a single real scalar ϕ_x with mass m_x, $2 \to 2$ and $3 \to 2$ self-interaction cross sections given by Eqs. (5.4,5.5), and no direct connection to the SM. We show below that this is often an accurate simplified model for the freeze-out of the lightest 0^{++} glueball, even when the heavier glueballs are included.

The freeze-out dynamics of this model coincide with the general scenario of Ref. [349]. Chemical equilibrium of the ϕ_x scalar is maintained by $3 \to 2$ transitions. These transitions also transfer energy to the remaining ϕ_x particles in the non-relativistic plasma causing them to cool more slowly than they would if there was a relativistic bath to absorb the input heat [349, 350]. Freeze-out occurs when the $3 \to 2$ transition rate becomes too slow to keep up with the Hubble expansion. While this happens, kinetic equilibrium is maintained by $2 \to 2$ elastic scattering of glueballs, which is parametrically much faster than the $3 \to 2$ processes at dark-sector temperatures below the scalar mass.

Kinetic equilibrium implies that the number density of ϕ_x particles takes the form

$$n_x = \int \frac{d^3p}{(2\pi)^3} \left[e^{(E_x-\mu_x)/T_x} - 1\right]^{-1} , \tag{5.8}$$

where $E = \sqrt{\vec{p}^2 + m_x^2}$, and T_x and μ_x refer to the temperature and chemical potential of the ϕ_x plasma. Analogous to our derivation of the $2 \to 2$ Boltzmann equation in chapter 2, this number density evolves in time according to [147, 349]

$$\dot{n}_x + 3Hn_x = -\langle \sigma_{32} v^2 \rangle (n_x^3 - n_x^2 \bar{n}_x) , \tag{5.9}$$

where H is the Hubble rate (sourced by both the visible and dark sectors), $\bar{n}_x = n_x(\mu_x \to 0)$ is the number

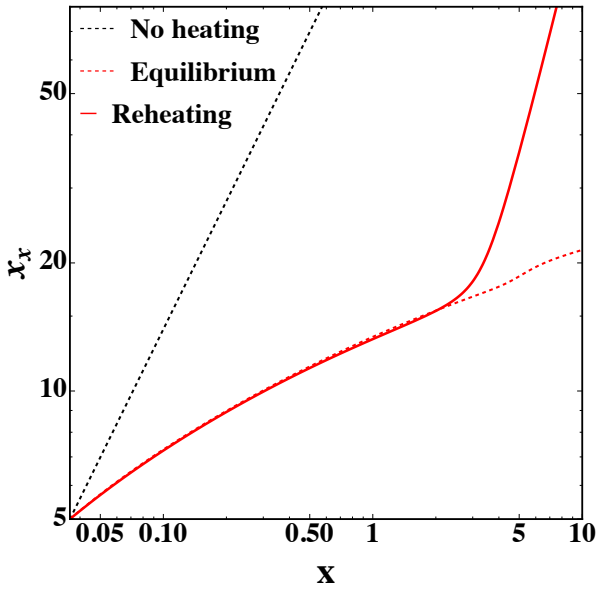

Figure 5.3: Temperature evolution of the hidden sector while the 0^{++} is freezing-out. Shown are the inverse of the dark and visible sector temperatures ($x_x(x) = m_x/T_x(T)$). Before freeze-out, the temperature drops (x_x rises) much slower than the visible sector, as the glueballs reheat themselves through the $3 \to 2$ process (dashed red line). After freeze-out, the dark temperature scales as $T_x \propto a^{-2}$ (solid red line). The dashed black line shows the comparison with how the temperatures would evolve if there was no reheating.

density in the limit of zero chemical potential, and the thermally-averaged cross section is

$$\begin{aligned} \langle \sigma_{32} v^2 \rangle &= \frac{1}{\bar{n}_x^3} \int d\Pi_1 d\Pi_2 d\Pi_3 \, e^{-(E_1+E_2+E_3)/T_x} \, \sigma_{32} v^2 \\ &\simeq \frac{1}{(4\pi)^3} \left(\frac{4\pi}{N}\right)^6 \frac{1}{m_x^5} \,, \end{aligned} \tag{5.10}$$

where $d\Pi_i = g_i d^3 p_i/(2\pi)^3 2E_i$ and we have used Eq. (5.5) in going to the second line. The dark-sector entropy is

$$T_x s_x = \rho_x + p_x - \mu_x n_x \,, \tag{5.11}$$

with the energy density ρ_x and pressure p_x determined by the same distribution function as n_x in Eq. (5.8). Together, Eqs. (5.6,5.9) provide two equations for the two unknowns $T_x(t)$ and $\mu_x(t)$ that can be solved in conjunction with the Friedmann equation for $H(t)$ [70]. Prior to freeze-out of the 0^{++} mode (and after dark confinement), the dark temperature falls as $T_x \propto 1/\ln(a)$ due to the energy injected by $3 \to 2$ annihilations [349]. After 0^{++} freeze-out, the dark temperature falls as $T_x \propto a^{-2}$. This effect is illustrated in Fig. 5.3.

While the results we present below are based on the numerical evaluation of Eqs. (5.6,5.9), it is instructive to derive an approximate solution for the non-relativistic freeze-out process [349]. For $m_x \gg$

T_x, μ_x, the dark-sector entropy density is

$$s_x \simeq \left(\frac{m_x}{T_x}\right) n_x \,. \tag{5.12}$$

This relation is maintained with zero chemical potential until freeze-out occurs, after which the number density just dilutes with the expansion of spacetime. Matching these limits and applying Eq. (5.6), the freeze-out yield is

$$Y_x = \frac{n_x}{s} \simeq \frac{R}{x_x^{fo}} \,, \tag{5.13}$$

where $x_x^{fo} = m_x/T_x^{fo}$ and T_x^{fo} is the dark temperature at which chemical equilibrium is lost. To determine x_x^{fo}, we follow Ref. [349] and identify freeze-out with the point at which the equilibrium $3 \to 2$ rate falls below the fractional rate of change of $n_x a^3$, which gives

$$3H \simeq x_x^{fo} \langle \sigma_{32} v^2 \rangle \bar{n}_x^2 \,. \tag{5.14}$$

Assuming visible radiation dominates the total energy density during freeze-out, this implies a visible-sector freeze-out temperature of

$$T^{fo} \simeq \bar{n}_x \left(\frac{x_x^{fo} M_{\rm Pl} \langle \sigma_{32} v^2 \rangle}{\sqrt{g_*^{fo} \pi^2/10}} \right)^{1/2} \,, \tag{5.15}$$

where $M_{\rm Pl}$ is the reduced Planck mass and g_*^{fo} is the number of effective energy degrees of freedom in the visible sector [70] at glueball freeze-out. Combining this with the entropy relation of Eq. (5.6) and the explicit form of $\bar{n}_x$ in the non-relativistic regime, we find

$$(x_x^{fo})^{5/2} e^{2x_x^{fo}} = \frac{g_{*S}^{fo}}{180\pi} R \left(\frac{m_x^4 M_{\rm Pl} \langle \sigma_{32} v^2 \rangle}{\sqrt{g_*^{fo} \pi^2/10}} \right)^{3/2} \,, \tag{5.16}$$

with g_{*S}^{fo} the number of effective entropy degrees of freedom in the visible sector [70] at glueball freeze-out. This relation can be solved iteratively for x_x^{fo}. Numerically, we find $x_x^{fo} \in [5, 20]$ for $R \in [10^{-12}, 0.1]$ and $m_0 \in [10^{-3}, 10^9]$ GeV.

In Fig. 5.4 we show the mass-weighted relic yield $m_x Y_x$ of ϕ_x with $N = 3$ as a function of the mass of the lightest glueball $\Lambda_x = m_x$ and the dark-to-visible entropy ratio R. If the lightest glueball is stable, the mass-weighted yield is related directly to the relic density by

$$\Omega_x h^2 = (0.1186) \times \left(\frac{m_x Y_x}{4.322 \times 10^{-10}\ \text{GeV}} \right) \,. \tag{5.17}$$

We also indicate on the plot where the relic yield coincides with the observed dark matter relic density,

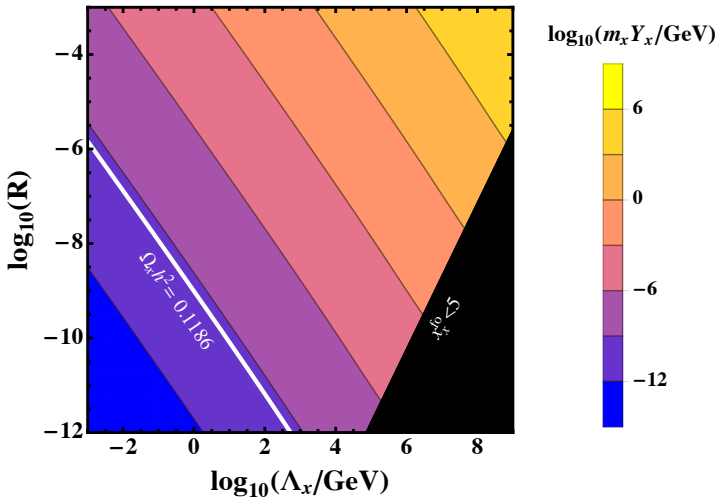

Figure 5.4: Mass-weighted relic yields in the single-state simplified model discussed in the text with $N = 3$ as a function of the mass $\Lambda_x = m_x$ and entropy ratio R. The solid white line indicates where the glueball density saturates the observed dark matter abundance $\Omega_x h^2 = 0.1186$ [9]. The dark masked region at the lower right indicates where freeze-out occurs for $x_x^{fo} < 5$ and our freeze-out calculation is not applicable due to the unknown dynamics of the confining phase transition.

$\Omega_x h^2 = 0.1186$ [9]. The dark shaded region at the lower right corresponds to $x_x^{fo} < 5$. As will be discussed below, there is an additional uncertainty in the relic abundance in this region when this simplified model is applied to dark glueballs, and the present calculation might not be applicable here.

5.3.2 Dynamics of the Confining Transition

Dark glueballs are first formed in the early Universe in a confining phase transition. At dark temperatures much larger than the confinement scale, $T_x \gg \Lambda_x$, the dark sector can be described as a thermal bath of weakly interacting dark gluons with $g_* = 2(N^2-1)$ degrees of freedom. As T_x cools below Λ_x a phase transition occurs with the gluons binding to form glueballs. Depending on the nature of the transition and the interaction rate of the resulting glueballs, this transition can affect the glueball relic density.

The nature of the confining transition in pure $SU(N)$ gauge theories has been studied in detail on the lattice [370–379] and in a number of semi-analytic models (*e.g.* Refs. [380–385]). The transition is found to be second order for $N = 2$, weakly first order for $N = 3$, and increasingly first order for $N \geq 4$ [372, 373]. The dark-sector critical temperature T_c for $N = 2-8$ is fit well by the relation [378]

$$T_c/\sqrt{\sigma} = 0.5949(17) + 0.458(18)/N^2 \,, \tag{5.18}$$

where $\sqrt{\sigma} \simeq 1.2/r_0$ [357] (or $\sqrt{\sigma} \simeq 2.5\Lambda_{\overline{MS}}$ [358, 362]). Note that this is about a factor of five smaller than the mass of the lightest glueball in Tab. 5.1. For $N > 2$ where the transition is found to be first-order,

the latent heat L_h scales according to [376]

$$\frac{L_h}{(N^2-1)T_c^4} = 0.388(3) - 1.61(4)/N^2 \,, \tag{5.19}$$

while the interface tension between the phases is consistent with [373]

$$\frac{\sigma_{cd}}{T_c^3} = 0.0138(3)N^2 - 0.104(3) \,. \tag{5.20}$$

In the confined phase just below the critical temperature, $0.7\,T_c \lesssim T_x < T_c$, the entropy and pressure are significantly larger than what is predicted from the known glueball states [377, 386]. Interestingly, this discrepancy can be explained by additional glueball states with a Hagedorn spectrum corresponding to the excitations of a bosonic closed string [386–388], in agreement with the model of Ref. [389]. The lattice studies of Refs. [390, 391] also suggest that the lowest-lying glueball pole masses persist nearly unchanged up to T_c (although see Ref. [392] for a different conclusion).

Much less is known about the non-equilibrium properties of the $SU(N)$ confining transition such as the nucleation temperature and rate. An estimate of the nucleation rate in the early Universe for $SU(3)$, valid in the limit of small supercooling, is given in Ref. [351]. For supercooling by an amount $T_x = (1-\delta)T_c$, they find a decay per unit volume of

$$\Gamma/V \simeq T_x^4 e^{-\Delta F_c/T_x} \tag{5.21}$$

with

$$\frac{\Delta F_c}{T_x} \simeq \frac{16\pi}{3}\frac{\sigma_{cd}^3}{L_h^2 T_c}\delta^{-2} \tag{5.22}$$

$$\simeq 2.92\times 10^{-4}\delta^{-2}N^2\frac{\left(1-7.54/N^2\right)^3}{\left(1-4.15/N^2\right)^2} \,, \tag{5.23}$$

where ΔF_c is the difference between the free energies of the two phases, and in the second line we have generalized the result of Ref. [351] to $SU(N\geq 3)$ using the central lattice values of L_h and σ_{cd} listed above. For moderate N, this suggests that nucleation occurs at T_x extremely close to T_c (provided $T_x/T \sim R^{1/3}$ is not too small) with only a very small injection of entropy. For very large N, the nucleation rate becomes small and the assumption of small supercooling made above breaks down. This suggests that significant supercooling can occur at large N, although a full non-perturbative calculation of the nucleation rate would be needed to verify this.

To apply these results to the calculation of relic glueball abundances, we assume that the phase transition completes with $T_x = T_c \simeq m_{0^{++}}/5$ [393] and that the mass spectrum of stable glueballs just after the transition is the same as at $T_x \to 0$. The simplified model discussed above can then be used with initial conditions at $x_x = x_x^c \equiv m_x/T_c$, which can be specified completely in terms of $R = s_x/s$ and $\mu_x(x_x^c)$. If the $3\to 2$ depletion process is fast relative to the Hubble rate at $x_x = x_x^c$, the initial chemical potential relaxes quickly to zero and the final relic density is specified completely by the choice of R. However,

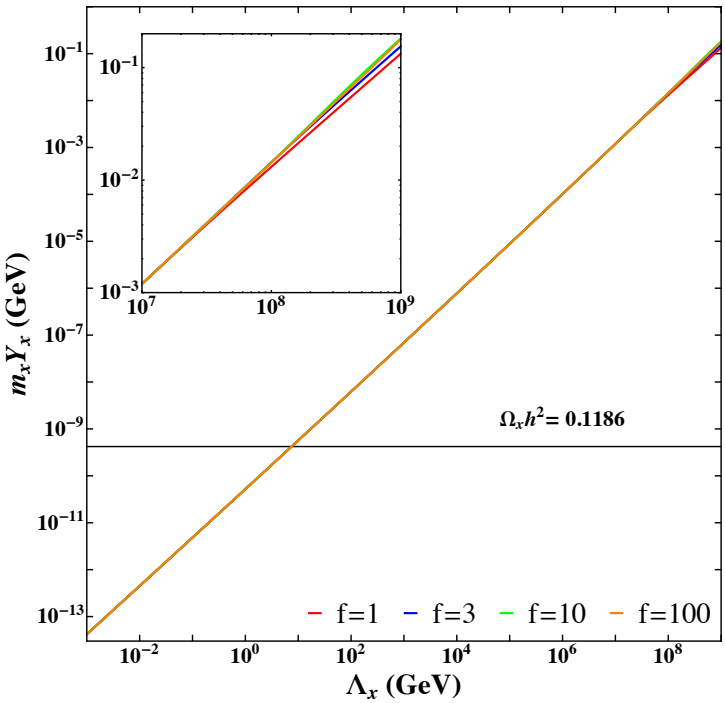

Figure 5.5: Mass-weighted relic yields in the single-state simplified model with the initial density set by $f = Y_x(x_x^c)/Y_x(x_x^c, \mu_x = 0)$ at $T_x = \Lambda_x/5$ with $R = 10^{-9}$ and $N = 3$.

if full chemical equilibration does not occur at $x_x = x_x^c$, a range of $\mu(x_x^c)$ values can be consistent with the equilibration rate relative to Hubble, and there is an additional uncertainty in the final glueball relic density for a given value of the entropy ratio R.

To investigate the potential dependence of the relic yield on the initial glueball density following the phase transition, we repeat the freeze-out calculation described in the previous section for $G_x = SU(3)$ with different initial glueball densities at $T_x = T_c$ defined by the ratio $f = Y_x(x_x^c)/Y_x(x_x^c, \mu_x = 0)$. Our results are shown for a range of values of Λ_x with $R = 10^{-9}$ and $N = 3$ in Fig. 5.5. For most of the range of Λ_x and R of interest, dark freeze-out occurs with $x_x^{fo} > x_x^c \simeq 5$ and the final glueball relic density is insensitive to the initial value after the phase transition. Even when $x_x^{fo} < x_x^c$, some residual annihilation (or creation) typically occurs, and the final density tends to be similar to $f = 1$. The region in the Λ_x–R plane in which this additional uncertainty is present is indicated by the shaded area in Fig. 5.4.

5.4 Freeze-Out with Multiple Glueballs

We turn next to the heavier glueballs above the lightest state. Recall from Section 5.2 that multiple stable glueballs are expected in a confining Yang-Mills theory, with the spectra found for $SU(2)$ and $SU(3)$ groups listed in Table 5.1. These heavier states lead to new annihilation channels involving the lightest glueball, and their relic densities can be of cosmological interest.

The freeze-out of the full glueball spectrum involves many states and a network with numerous reaction channels. Despite this complexity, we find that the glueball relic densities follow a relatively

i	J^{PC}	$m_i/m_{0^{++}}$
1	0^{++}	1.00
2	2^{++}	1.39
3	3^{++}	2.13
4	0^{-+}	1.50
5	2^{-+}	1.79
6	1^{+-}	1.70
7	3^{+-}	2.05
8	2^{+-}	2.40
9	0^{+-}	2.74
10	1^{--}	2.23
11	2^{--}	2.27
12	3^{--}	2.39

Table 5.2: List of stable glueball states and mass ratios for $SU(3)$, from Ref. [6].

simple pattern with three main features. First, the relic density of the lightest glueball is described very well by the simplified one-state model presented above provided it freezes out while it is significantly non-relativistic. Second, the relic densities of the heavier C-even states are typically extremely small relative to the lightest glueball. And third, the total relic density of C-odd states (for $SU(N \geq 3)$ gauge groups) is dominated by the lightest C-odd mode and is much smaller than the lightest 0^{++} state but typically larger than all the other C-even states. This significant difference arises from the conserved C number in the dark sector, which allows coannihilation of the heavier C-even states with the lightest glueball but forbids it for C-odd states.

In this section we investigate the relic densities of the full set of glueballs for the dark gauge group $SU(3)$. We begin by determining which $2 \to 2$ glueball reactions are allowed by J^{PC} conservation in the dark sector, and we estimate their rates. Next, we study a simplified reaction network of C-even states that we argue captures the most important features of the full dynamics. Finally, we perform a similar analysis for the C-odd states.

5.4.1 Glueball Reactions

To discuss glueball reactions for $G_x = SU(3)$, it will be convenient to label the modes in the spectrum by $i = 1, 2, \ldots, 12$ as in Table 5.2. This table also lists their relative masses and J^{PC} quantum numbers.

The specific interactions between glueballs are not known, but all possible processes consistent with dark-sector J, P, and C conservation are expected to be present. For a $2 \to 2$ glueball reaction of the form $i + j \to k + l$, conservation of C requires

$$C_i C_j = C_k C_l \ . \tag{5.24}$$

This is trivial to apply and rules out a number of reactions. Conservation of P implies

$$P_i P_j = (-1)^L P_k P_l \ , \tag{5.25}$$

where L is the relative orbital angular momentum of the reaction channel. When identical particles are present, they must also be symmetrized. In general, it can be shown that there always exists a value of L such that both parity and total angular momentum are conserved unless either $J_i = J_j = 0$ or $J_k = J_l = 0$.

If the process $i + j \leftrightarrow k + l$ is allowed, it contributes to the collision term in the Boltzmann equation for glueball i according to

$$\Delta \dot{n}_i \ = \ - \langle \sigma v \rangle_{ijkl} n_i n_j + \langle \sigma v \rangle_{klij} n_k n_l \ , \tag{5.26}$$

where $\langle \sigma v \rangle_{ijkl}$ is the thermally-averaged cross section and n_i refers to the number density of the i-th species. Assuming kinetic equilibrium is maintained among the glueballs, we have

$$n_i \ = \ g_i \, e^{\mu_i / T_x} (4\pi) m_i^2 T_x K_2(m_i/T_x) \tag{5.27}$$

$$\simeq \ g_i \left(\frac{m_i T_x}{2\pi} \right)^{3/2} e^{-(m_i - \mu_i)/T_x} \ , \tag{5.28}$$

where T_x is the temperature of the glueball bath and g_i, m_i, and μ_i are the number of degrees of freedom, mass, and chemical potential of the type-i glueball. The thermally-averaged cross-section is given by

$$\langle \sigma v \rangle_{ijkl} \ = \ \frac{1}{n_i n_j} \int \frac{d^3 p_i}{(2\pi)^3} \int \frac{d^3 p_j}{(2\pi)^3} \, g_i \, e^{(\mu_i - E_i)/T_x} g_j \, e^{(\mu_j - E_j)/T_x} (\sigma v)_{ijkl} \tag{5.29}$$

$$= \ \frac{g_i g_j}{\bar{n}_i \bar{n}_j} \int \frac{d^3 p_i}{(2\pi)^3} \int \frac{d^3 p_j}{(2\pi)^3} \, e^{-(E_i + E_j)/T_x} \, (\sigma v)_{ijkl} \ , \tag{5.30}$$

where $E_i = \sqrt{m_i^2 + \vec{p}_i^{\,2}}$ and $\bar{n}_i = n_i(\mu_i = 0)$. Note that the chemical potentials cancel in this expression.

The reaction $i + j \to k + l$ is either exothermic ($m_i + m_j \geq m_k + m_l$) or endothermic ($m_i + m_j < m_k + m_l$). Equilibration of this process implies $\mu_i + \mu_j = \mu_k + \mu_l$. Combined with detailed balance, we must have

$$\langle \sigma v \rangle_{ijkl} \, \bar{n}_i \bar{n}_j = \langle \sigma v \rangle_{klij} \, \bar{n}_k \bar{n}_l \ . \tag{5.31}$$

Using these relations, the thermally-averaged rates of endothermic reactions can be estimated based on those of exothermic reactions.

Thermal averaging of cross sections was studied in detail in Refs. [73, 215]. Generalizing their results slightly and using the large-N and NDA estimates of interaction strengths, we estimate the thermally-averaged cross section of an exothermic process $i + j \to k + l$ that proceeds at lowest orbital

angular momentum level L by

$$\langle\sigma v\rangle_{ijkl} \;\simeq\; \frac{(4\pi)^3}{N^4}\,\frac{\beta_{ijkl}}{s_{ij}}\;c_L\!\left(\frac{2}{x_i+x_j}\right)^{L}\,, \tag{5.32}$$

where $x_i = m_i/T$,

$$s_{ij} = \left(1+\frac{3}{x_i+x_j}\right)(m_i+m_j)^2\,, \tag{5.33}$$

along with

$$\begin{aligned}\beta_{ijkl} &= \frac{2p'_{kl}}{\sqrt{s_{ij}}} \\ &= \frac{1}{s_{ij}}\left(s_{ij}^2+m_k^4+m_l^4-2s_{ij}m_k^2-2s_{ij}m_l^2-2m_l^2m_k^2\right)^{1/2}\,,\end{aligned} \tag{5.34}$$

and the coefficients c_L are [73]

$$c_0 = 1,\;\; c_1 = 3/2,\;\; c_2 = 15/8,\;\; c_3 = 35/16,\;\; c_4 = 315/128\,. \tag{5.35}$$

The first factor in Eq. (5.32) contains the couplings, the second factor describes the kinematics near threshold in the non-relativistic limit, while the third is the velocity suppression for a process that goes at the L-th partial wave.

The cross-section estimates of Eq. (5.32) can be used to judge which reactions are most significant during freeze-out. The relative effect of the process $i+j\to k+l$ (with $j,k,l\neq i$) on the number density of glueball species i is

$$\frac{|\Delta\dot{n}_i|}{n_i} = \langle\sigma v\rangle_{ijkl}\,n_j\,. \tag{5.36}$$

In general, this reaction is cosmologically active for $|\Delta\dot{n}_i|/n_i > H$. Scanning over all possible $2\to 2$ reactions of $SU(N=3)$ glueballs, we find that in full equilibrium with $x_x > 5$ and for every glueball species $i > 1$ there exist multiple number-changing $2\to 2$ reactions down to lighter states with $|\Delta\dot{n}_i|/n_i$ significantly larger than the corresponding quantity for $3\to 2$ annihilation of the lightest glueball. This implies that *relative chemical equilibrium* is maintained among the glueballs during and for some time after $3\to 2$ freeze-out, with

$$\frac{n_i}{n_j} = \frac{\bar{n}_i}{\bar{n}_j} \simeq \frac{g_i}{g_j}\left(\frac{m_i}{m_j}\right)^{3/2} e^{-(m_i-m_j)/T_x}\,. \tag{5.37}$$

Equivalently, the number densities of all species immediately after $3\to 2$ freeze-out are given by their equilibrium values with a common chemical potential.

Relative chemical equilibrium after $3\to 2$ freeze-out implies further that the relative importance of different $2\to 2$ reactions on the subsequent freeze-out of the heavier glueballs can be estimated using

their equilibrium number densities. This allows us to greatly simplify the set of reaction networks by keeping only the dominant processes and concentrating exclusively on a few key states. It turns out to be consistent and convenient to study the C-even and C-odd states independently, and this is the approach we take below.

5.4.2 Relic Densities of C-Even States

The lightest C-even glueballs above the lowest mode have $J^{PC} = 2^{++}, 0^{-+}, 2^{-+}$ and correspond to $i = 2, 4, 5$, in our labelling scheme. Scanning over all possible reactions for these states and estimating their relative effects on the number densities as above, the dominant interactions near relative equilibrium are found to form a minimal closed system. The reaction network for the system is described by

$$\begin{aligned}
\dot{n}_1 + 3H n_1 &= -\langle \sigma_{32} v^2 \rangle n_1^2 (n_1 - \bar{n}_1) \\
&\quad -\frac{1}{2}\langle \sigma v \rangle_{2111} \left[\left(\frac{\bar{n}_2}{\bar{n}_1} \right) n_1 n_2 - n_2^2 \right] \\
&\quad -\langle \sigma v \rangle_{2211} \left[\left(\frac{\bar{n}_2}{\bar{n}_1} \right)^2 n_1^2 - n_2^2 \right] \\
&\quad -\frac{1}{2}\langle \sigma v \rangle_{2214} \left[\left(\frac{\bar{n}_2^2}{\bar{n}_1 \bar{n}_4} \right) n_1 n_4 - n_2^2 \right] \\
&\quad -\frac{1}{2}\langle \sigma v \rangle_{2415} \left[\left(\frac{\bar{n}_2 \bar{n}_4}{\bar{n}_1 \bar{n}_5} \right) n_1 n_5 - n_2 n_4 \right]
\end{aligned} \tag{5.38}$$

$$\begin{aligned}
\dot{n}_2 + 3H n_2 &= +\frac{1}{2}\langle \sigma v \rangle_{2111} \left[\left(\frac{\bar{n}_2}{\bar{n}_1} \right) n_1 n_2 - n_2^2 \right] \\
&\quad +\langle \sigma v \rangle_{2211} \left[\left(\frac{\bar{n}_2}{\bar{n}_1} \right)^2 n_1^2 - n_2^2 \right] \\
&\quad +\langle \sigma v \rangle_{2214} \left[\left(\frac{\bar{n}_2^2}{\bar{n}_1 \bar{n}_4} \right) n_1 n_4 - n_2^2 \right] \\
&\quad +\frac{1}{2}\langle \sigma v \rangle_{2415} \left[\left(\frac{\bar{n}_2 \bar{n}_4}{\bar{n}_1 \bar{n}_5} \right) n_1 n_5 - n_2 n_4 \right] \\
&\quad -\frac{1}{2}\langle \sigma v \rangle_{1512} \left[\left(\frac{\bar{n}_1 \bar{n}_5}{\bar{n}_1 \bar{n}_2} \right) n_1 n_2 - n_1 n_5 \right]
\end{aligned} \tag{5.39}$$

$$\begin{aligned}
\dot{n}_4 + 3H n_4 &= -\frac{1}{2}\langle \sigma v \rangle_{2214} \left[\left(\frac{\bar{n}_2^2}{\bar{n}_1 \bar{n}_4} \right) n_1 n_4 - n_2^2 \right] \\
&\quad +\frac{1}{2}\langle \sigma v \rangle_{2415} \left[\left(\frac{\bar{n}_2 \bar{n}_4}{\bar{n}_1 \bar{n}_5} \right) n_1 n_5 - n_2 n_4 \right]
\end{aligned} \tag{5.40}$$

$$\begin{aligned}
\dot{n}_5 + 3H n_5 &= -\frac{1}{2}\langle \sigma v \rangle_{2415} \left[\left(\frac{\bar{n}_2 \bar{n}_4}{\bar{n}_1 \bar{n}_5} \right) n_1 n_5 - n_2 n_4 \right] \\
&\quad +\frac{1}{2}\langle \sigma v \rangle_{1512} \left[\left(\frac{\bar{n}_1 \bar{n}_5}{\bar{n}_1 \bar{n}_2} \right) n_1 n_2 - n_1 n_5 \right]
\end{aligned} \tag{5.41}$$

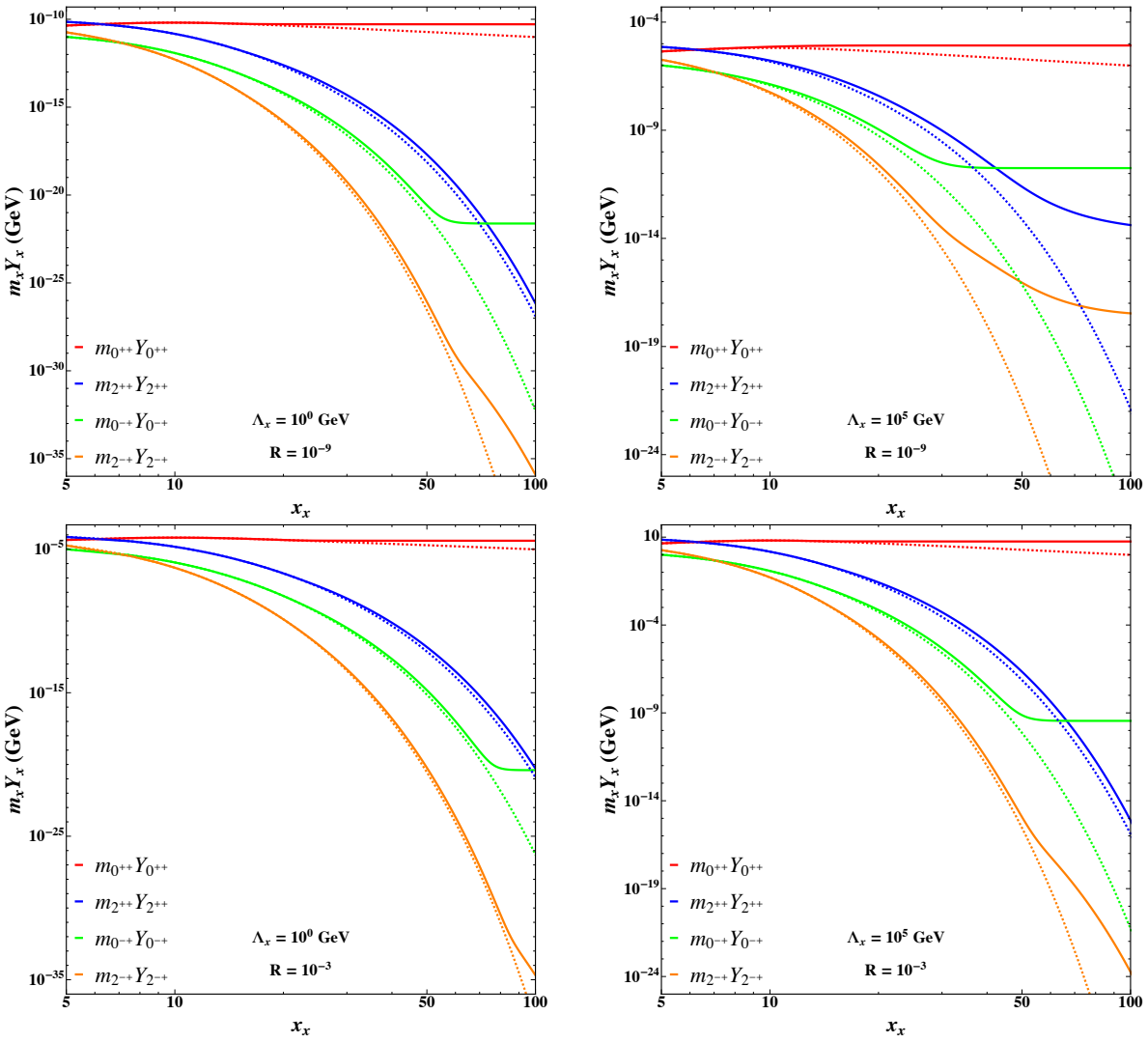

Figure 5.6: Mass-weighted relic yields of the four lightest C-even glueballs in $SU(3)$, $J^{PC} = 0^{++}, 2^{++}, 0^{-+}, 2^{-+}$, as a function of the dark glueball temperature variable $x_x = m_x/T_x$ computed using the simplified reaction network discussed in the text. The solid lines show the yields derived from the reaction network while the dashed lines indicate the yields expected if the states were to continue following equilibrium with $\mu_i = 0$. Top left: $(\Lambda_x/\,\mathrm{GeV}, R) = (1, 10^{-9})$. Top right: $(\Lambda_x/\,\mathrm{GeV}, R) = (10^5, 10^{-9})$. Bottom left: $(\Lambda_x/\,\mathrm{GeV}, R) = (1, 10^{-3})$. Bottom right: $(\Lambda_x/\,\mathrm{GeV}, R) = (10^5, 10^{-3})$.

The factors of $1/2$ appearing here are symmetry factors for initial states that are not included in the standard definition of the thermally-averaged cross section [215]. They ensure that the summed number density $n_1 + n_2 + n_4 + n_5$ is conserved in the absence of $3 \to 2$ reactions. In addition to these evolution equations, the ratio of entropies $R = s_x/s$ is conserved after the confining transition at $T_x^c \simeq m_x/5$, with the dark sector entropy now extended to include all (relevant) glueball modes.

Numerical solutions of this system of equations for $SU(3)$ dark glueballs are shown in Fig. 5.6 for

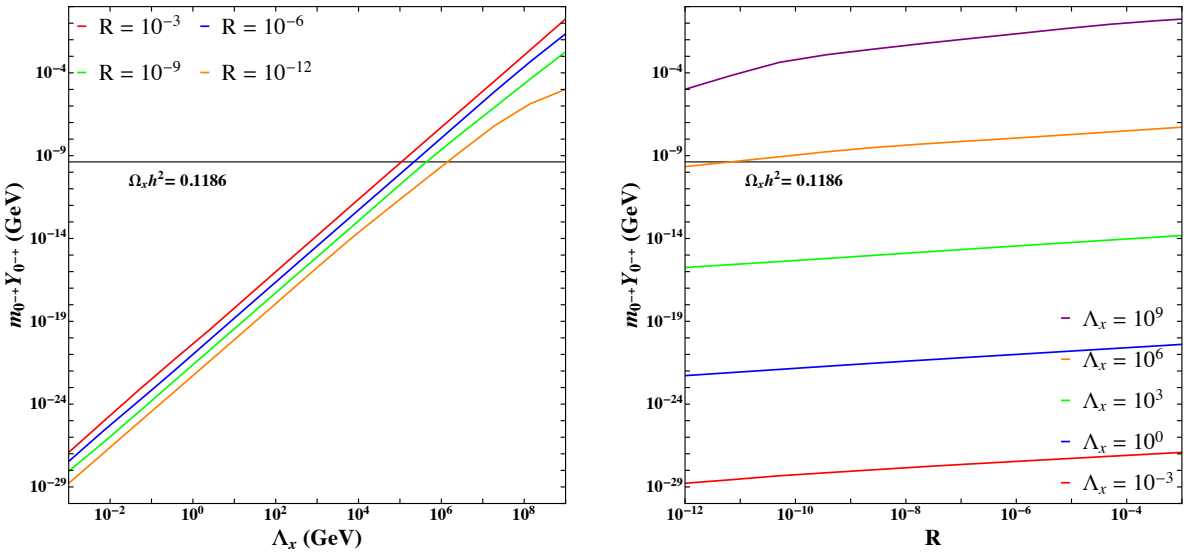

Figure 5.7: Mass-weighted relic yields of the 0^{-+} dark glueball in $SU(3)$ as functions of $\Lambda_x = m_x$ and R, computed using the simplified C-even reaction network discussed in the text. For reference, we also indicate the yield corresponding to the observed dark matter density. Note that the yield of the 0^{++} state is much larger.

the parameter values $(\Lambda_x/\,\mathrm{GeV}, R) = (1, 10^{-9}), (10^5, 10^{-9}), (1, 10^{-3}), (10^5, 10^{-3})$. In each panel, the evolution of the mass-weighted yields $m_i Y_x$ with $x_x = m_x/T_x$ are given by the solid lines, while the dashed lines show the mass-weighted yield of each species with $\mu_i = 0$. In all four panels, the lightest 0^{++} mode is seen to dominate the total glueball relic abundance for $x_x \gtrsim 10$. This abundance is found to match closely with the value determined by the one-glueball simplified model discussed above. The much smaller relic abundances of the heavier glueball modes is due to the efficient coannihilation reactions they experience. Since these $2 \to 2$ processes are parametrically faster than the $3 \to 2$ annihilations setting the 0^{++} density, relative chemical equilibrium is maintained to large values of x_x. This implies a strong exponential suppression of the heavier glueball densities as in Eq. (5.37).

Let us also point out that the 0^{-+} state freezes out (of relative chemical equilibrium) well before the 2^{++} and 2^{-+} modes, even though it is heavier than the 2^{++}. This can be understood by examining the relative rates of the depletion reactions for the 0^{-+} state; for $x_x \gtrsim 20$ it is found to be $0^{-+} + 0^{++} \to 2^{++} + 2^{++}$. Comparing masses, this reaction is found to be endothermic and thus it receives an additional rate suppression as discussed in Ref. [394]. The dependence of the 0^{-+} $(i = 4)$ glueball relic density on $\Lambda_x = m_x$ and R is also shown in Fig. 5.7.

5.4.3 Relic Densities of C-Odd States

Freeze-out of the C-odd glueballs is qualitatively different from that of the C-even modes due to the conservation of C number in the dark sector. This forbids coannihilation reactions of the C-odd states with the relatively abundant lightest 0^{++} glueball into final states with only C-even modes, and can lead

to a significant relic density for the lightest C-odd 1^{+-} state.

To see how this comes about, let us split up the labels of the state indices defined in Table 5.2 according to

$$i, j = 1,2,3,4,5 = C\text{-even} , \quad a, b = 6,7,\ldots 12 = C\text{-odd} , \tag{5.42}$$

and let us also define the net C-odd density by

$$n_- = \sum_{a=6}^{12} n_a . \tag{5.43}$$

The net collision term in the Boltzmann equation for n_- is

$$\begin{aligned} \Delta\dot{n}_- &= \sum_a \Delta\dot{n}_a & (5.44)\\ &= -\sum_{ab,ij} \langle\sigma v\rangle_{abij} n_a n_b + \sum_{ij,ab} \langle\sigma v\rangle_{ijab} n_i n_j . & (5.45) \end{aligned}$$

The key feature of this expression is that all processes contributing to the rate of change of $\dot{n}_-$ have two C-odd particles either in the initial or the final state [215]. Using detailed balance, we can rewrite Eq. (5.45) in the form

$$\begin{aligned} \Delta\dot{n}_- &= -\langle\sigma v\rangle_{6611} n_-^2 \left[\sum_{abij}\left(\frac{\langle\sigma v\rangle_{abij}}{\langle\sigma v\rangle_{6611}}\frac{n_a n_b}{n_-^2}\Theta_+ + \frac{\langle\sigma v\rangle_{ijab}}{\langle\sigma v\rangle_{6611}}\frac{n_a n_b}{n_-^2}\frac{\bar{n}_i\bar{n}_j}{\bar{n}_a\bar{n}_b}\Theta_-\right)\right] \\ &\quad + \langle\sigma v\rangle_{6611} n_1^2 \left(\frac{\bar{n}_-}{\bar{n}_1}\right)^2 \left[\sum_{abij}\left(\frac{\langle\sigma v\rangle_{abij}}{\langle\sigma v\rangle_{6611}}\frac{\bar{n}_a\bar{n}_b}{n_-^2}\frac{n_i n_j}{\bar{n}_i\bar{n}_j}\frac{\bar{n}_1^2}{n_1^2}\Theta_+ + \frac{\langle\sigma v\rangle_{ijab}}{\langle\sigma v\rangle_{6611}}\frac{n_i n_j}{n_-^2}\frac{\bar{n}_1^2}{n_1^2}\Theta_-\right)\right] , \end{aligned} \tag{5.46}$$

where $\Theta_+ = \Theta(m_a + m_b - m_i - m_j)$ and $\Theta_- = \Theta(m_i + m_j - m_a - m_b)$ are step functions to select out exothermic reactions as appropriate.

Consider the relative sizes of the individual terms in Eq. (5.46) when relative equilibrium is maintained. In the first line, the first term is on the order of unity for $a = b = 6$ but has an exponential suppression otherwise from the factor of $n_a n_b / n_-^2$, while the second term has an additional exponential suppression from the factor $\bar{n}_i\bar{n}_j/\bar{n}_a\bar{n}_b$ ($m_i + m_j > m_a + m_b$). Similar arguments also apply to the terms in the second line of Eq. (5.46), noting that $\bar{n}_i\bar{n}_j n_1^2 = n_i n_j \bar{n}_1^2$ in relative equilibrium, and only the $a = b = 6$ portion of the first term avoids an exponential suppression. Indeed, a numerical evaluation of these contributions, assuming relative equilibrium and moderate $x_x \gtrsim 10$, confirms that the $a = b = 6$ terms of the Θ_+ pieces dominate the collision term.

The total C-odd density begins to deviate appreciably from the relative equilibrium value for $\langle\sigma v\rangle_{6611}\, \bar{n}_-^2 (n_1/\bar{n}_1)^2 \sim H$. This occurs well before the C-even states freeze out, and also well before C-odd transfer reactions, such as $7+1 \leftrightarrow 2+6$, turn off. The latter result implies that the relative densities of C-odd states are maintained among themselves (but not the C-even states) even after the net C-odd density has frozen out. Therefore we also expect $n_6/n_- \to 1$ and $n_{a>6}/n_- \to 0$ provided these processes

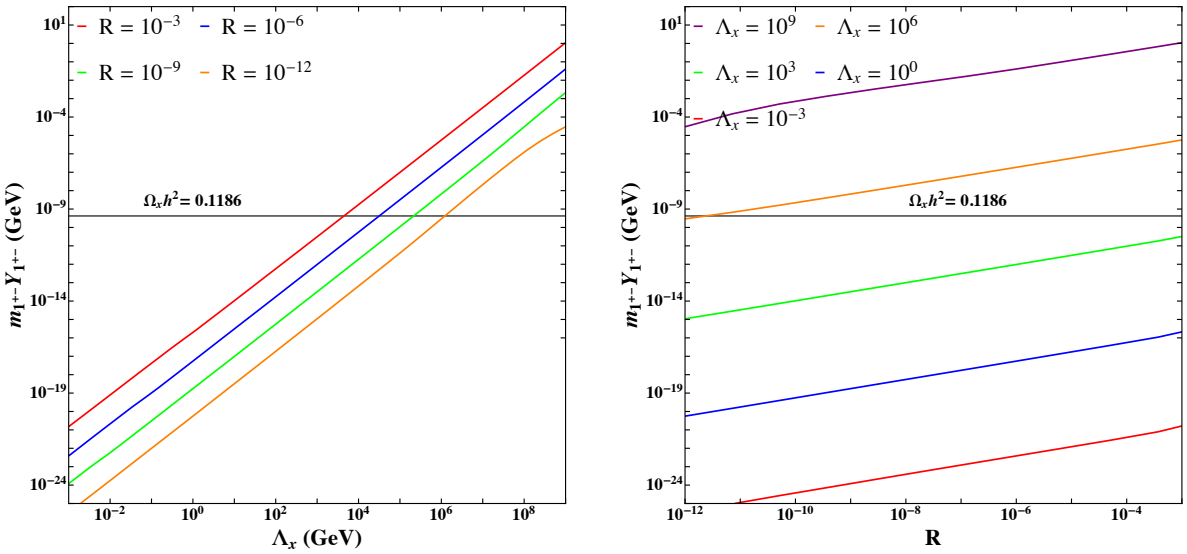

Figure 5.8: Mass-weighted relic yields of the 1^{+-} dark glueball in $SU(3)$ as a function of $\Lambda_x = m_x$ and R, computed in the simplified two-state network discussed in the text. For reference, we also indicate the yield corresponding to the observed dark matter density. Note that the yield of the 0^{++} state is much larger.

turn off at moderate $x_x \gtrsim 10$.

The net result of this analysis is that it is generally a good approximation to compute the freeze-out of the C-odd density using a simplified two-state system consisting only of the $i = 1, 6$ (0^{++} and 1^{+-}) glueballs. Correspondingly, the system of Boltzmann equations is

$$\begin{aligned} \dot{n}_1 + 3Hn_1 &= -\langle\sigma_{32}v^2\rangle n_1^2(n_1 - \bar{n}_1) \\ &\quad + \langle\sigma v\rangle_{6611}\left[n_6^2 - \left(\frac{n_1}{\bar{n}_1}\right)^2 \bar{n}_6^2\right] \end{aligned} \tag{5.47}$$

$$\dot{n}_6 + 3Hn_6 = -\langle\sigma v\rangle_{6611}\left[n_6^2 - \left(\frac{n_1}{\bar{n}_1}\right)^2 \bar{n}_6^2\right] . \tag{5.48}$$

Corrections to this estimate are expected to be of order unity, which is well within the uncertainties on the cross sections.

The mass-weighted yields of the lightest 1^{+-} C-odd $SU(3)$ glueball based on this analysis are shown in Fig. 5.8. Like for the C-even states, the inclusion of additional heavier C-odd glueballs generally has a negligible effect on the final abundance of the lightest 0^{++} mode relative to the one-state model discussed previously. Furthermore, the 0^{++} state dominates the total glueball density, and the relic abundance of the 1^{+-} state is smaller by several orders of magnitude. However, the 1^{+-} density can be considerably larger than any of the C-even states, even though it is heavier than the 2^{++} and 0^{-+} glueballs. As discussed above, this can be understood by the absence of relevant coannihilation reactions

involving the much more abundant 0^{++} glueball. Let us also point out that C-odd dark glueballs provide an explicit realization of the scenario discussed in Ref. [395] consisting of a stable dark matter state freezing out in the background of a massive bath.

5.5 Dark Matter Scenarios and Connections to the SM

Stable dark glueballs will contribute to the dark matter (DM) density of the Universe. However, if the dark sector has a connection to the SM, some or all of the dark glueballs will be able to decay [229]. Possible SM connections include heavy matter charged under both the dark and SM gauge groups [11, 12], a Higgs portal [337], or a Yukawa connection [12]. In all of the above scenarios, the decay rates of glueballs through the various operators can span an enormous range. For lifetimes beyond the age of the Universe the glueballs will contribute to the DM density and the considerations discussed above apply here as well. In addition, for lifetimes $\tau \lesssim 10^{26}\,\mathrm{s}$ there will also be constraints from energy injection into the CMB near recombination [123, 270, 396], x-ray and gamma-ray fluxes [235, 397], and energy release during primordial nucleosynthesis [258–260, 270], such as that discussed in Part III. Given the parametrically similar decay rates and the much larger relic density of the lightest 0^{++} glueball relative to the others, these bounds apply primarily to this state, although it is possible for the 1^{+-} (and to a lesser extent, the 0^{-+}) to also contribute to the constraints if certain symmetry conditions are met. These will be discussed in detail in the following chapter.

These SM operators can also be relevant for the glueball freeze-out abundances. At high temperatures they can lead to the thermalization of the dark and visible sectors, although the specific details depend on the reheating history after primordial inflation. They may also help to further populate the dark sector through inverse decays [270], or induce decays before freeze-out occurs, although this typically requires relatively larger values of Λ_x/M. This is a modification of the scenario discussed in Part II, and so we must keep in mind the connection between the two sectors when moving forward.

With no connection to the SM, all the states in the glueball spectrum discussed in Section 5.2 will be stable and contribute to the net DM density[2]. As reported in Sections 5.3 and 5.4, the total glueball contribution will be dominated by the lightest 0^{++} state. The DM scenario in this case coincides with the glueball scenarios considered in Refs. [231, 232, 235] in which only the lightest glueball was considered. Avoiding overclosure by the glueball relic density bounds Λ_x and R from above, as can be seen in Fig. 5.4. If the lightest glueball makes up all the DM, Λ_x is bounded from below by the requirement that its self-interaction cross section not be too large, $\sigma_{2\to2}/m \lesssim 10\,\mathrm{cm}^2/\mathrm{g}$, which translates into [231, 232, 235]

$$\Lambda_x \gtrsim 100\,\mathrm{MeV}\left(\frac{3}{N}\right)^{4/3}. \tag{5.49}$$

Smaller Λ_x can also interfere with cosmic structure formation [207, 235, 398].

[2]Decays to gravitons are possible, but the corresponding lifetime is much longer than the age of the Universe for $\Lambda_x \lesssim 10^7$ GeV [235].

5.6 Conclusions

In this chapter we have investigated the freeze-out dynamics of $SU(3)$ dark glueballs in the early Universe. This is our first step towards creating a complex hidden sector (that will eventually have SM connections). Such glueballs arise from confinement in theories with a new non-Abelian gauge force decoupled from the SM and all charged matter significantly heavier than the confinement scale. Our results expand upon previous studies of the cosmological history of dark glueballs in two key ways [231, 232, 235]. First, we studied potential new effects on the glueball relic density due to the confining phase transition itself. And second, we performed a detailed analysis of the freeze-out dynamics of the heavier glueballs in the spectrum. We also briefly discussed connections to the SM as well as some of the implications of the heavier glueballs on dark matter, astrophysics, and cosmology, with a more detailed study of these effects to follow in the next chapter.

When the glueballs are unable to decay efficiently through connectors to the SM (or other lighter states), we find that the lightest 0^{++} state dominates the total glueball relic abundance, and the abundance we calculate is in agreement with previous studies that only considered the lightest state [232, 235]. The relative relic densities of heavier glueballs in the spectrum are orders of magnitude smaller, with the largest contributions coming from the 0^{-+} and 1^{+-} modes (for $SU(3)$). Even though the abundances of these states are much smaller than the lightest 0^{++}, they can also be parametrically long-lived compared to the 0^{++}. This opens the possibility of the 0^{++} mode decaying away early, and the heavier modes making up the DM density today or leading to the most stringent constraints on dark Yang-Mills theories. A detailed study of these effects based on the results determined here for the freeze-out relic abundances will be the focus of the next chapter.

Our results are also be applicable to other non-Abelian gauge groups with some straightforward modifications. The lightest glueball, which is generically expected to have $J^{PC} = 0^{++}$ [355], will have the largest relic yield. This yield can be computed reliably in the single-state model of Section 5.3, provided $3 \to 2$ annihilation processes are active after the confining transition. The relic yields of the heavier glueballs will depend on their specific masses and quantum numbers, but can be computed following the general methods of Section 5.4. For a given confinement scale, their masses will be similar to those of $SU(3)$ for general $SU(N)$ groups, while the C-odd states are expected to be considerably heavier for $SO(2N)$ groups and absent for $SU(2)$, $SO(2N+1)$, and $Sp(2N)$ groups with a vanishing d^{abc} symbol. The different properties of the more massive glueballs will only be relevant to cosmology when they have lifetimes that are parametrically much longer than the lightest 0^{++} mode.

Now that we have developed a solid foundational understanding of how glueballs will interact and evolve when treated independently from external influences, we relax that assertion. As has been alluded to already, in the next chapter we build up our non-Abelian gauge force to include SM connections. This will entail incorporating all of the previous chapters. For example, we will need to be careful to work in regimes that will not be affected by the presence of extra freeze-in transfer (or include those effects if necessary), as we found in Ch. 3. After building up the model, we will identify the implications that the glueballs will have on astrophysics and cosmology, using constraints very closely related to those derived in Ch. 4. As such, the next chapter will be a culmination of everything we have studied thus far.

Chapter 6

Cosmological Bounds on Non-Abelian Dark Forces

6.1 Introduction

In previous chapters, we have explored the many different facets of SM interactions with a dark sector. To begin, we started with only SM influence on a dark sector, and learned about how the evolution of the dark sector may change, even in the presence of UV operators. Next, we considered low-energy decays in the context of BBN constraints, which explicitly considers how energy injected from a hidden sector can alter the abundances of the products of BBN. Finally, we moved away from simple dark sectors to a more complex model, motivated by many different areas of study. This new model, a non-Abelian gauge force, gives rise to a full spectrum of stable glueballs. We studied this glueball spectrum in an isolated environment, and learned how the various states will interact, ultimately leading to solutions for the relic yields of the different glueballs. Now, we put all of this information to use, and consider how this more complex model will interact with the Standard Model. Although we focus more explicitly on the effect that glueball decays will have on the visible sector, we still make mention of the role that SM connectors might have on their production, before moving on to constraining the full theory. Schematically, we depict this wholistic view of the two sectors in Fig. 6.1.

As we motivated previously, new gauge forces may be realized in nature beyond the $SU(3)_c \times SU(2)_L \times U(1)_Y$ structure of the Standard Model (SM). If a new gauge force connects directly to SM matter, it must have a characteristic mass scale above about a TeV to be consistent with experimental tests of the SM [399–401]. On the other hand, new *dark* gauge forces that couple only very weakly to the SM can be significantly lighter [325–327]. Such dark forces can be very challenging to probe directly in experiments, and in many scenarios the strongest bounds on them come from astrophysical and cosmological observations [270–272, 402].

In this chapter we investigate the cosmological evolution and constraints on new non-Abelian dark

[0]This chapter is based on L. Forestell, D. E. Morrissey, and K. Sigurdson, *Cosmological Bounds on Non-Abelian Dark Forces*, Phys. Rev. D, **97**, (2018), 075029, [arXiv:1710.06447] [4]

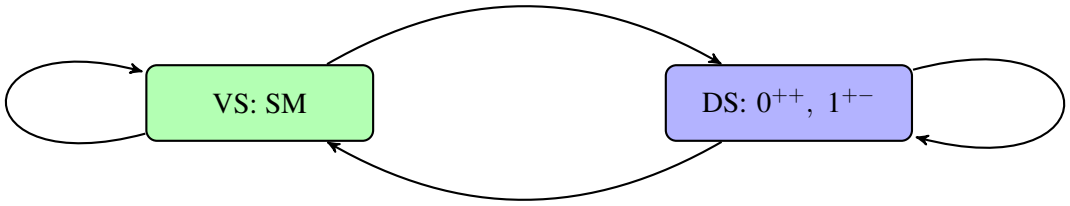

Figure 6.1: Flow of information considered in this chapter. We now have a fully realized dark sector, with complex interactions. The dark sector may also transfer energy to the visible sector via decays, while the visible sector may influence the production of dark glueballs.

forces. The requirement of gauge invariance in theories of non-Abelian dark forces implies that the new gauge vector bosons can only couple to the SM through non-renormalizable operators [11, 12]. This stands in contrast to Abelian dark forces that can connect to the SM at the renormalizable level through kinetic mixing with hypercharge. As a result, direct low-energy searches for non-Abelian dark forces are very difficult, and cosmological observations usually provide the most powerful tests of them [231, 232, 235–237, 336–338, 351, 403–407].

The particle spectrum in theories of non-Abelian forces is diverse and complicated, and depends on both the gauge group and the representations of the matter fields charged under it. We continue to focus on the minimal realization of a non-Abelian dark force consisting of a pure Yang-Mills theory with a simple gauge group G_x. If the visible and dark sectors do not interact, they evolve independently with distinct temperatures T and T_x. This was thoroughly investigated in the previous chapter. After confinement at $T_x = T_c$, the dark glueballs undergo a complicated freeze-out process. The energy density of the dark sector is dominated by the lightest glueball state, which on general grounds is expected to have $J^{PC} = 0^{++}$ [355]. The lightest 0^{++} number density changes mainly through $(3 \to 2)$ self-annihilation processes [235], as we demonstrated explicitly in the previous chapter. While these reactions are active, the dark temperature changes very slowly, only falling off as the logarithm of the cosmological scale factor [349, 408]. As a result, the lightest glueballs form a massive thermal bath in which the other heavier glueballs annihilate through $2 \to 2$ processes and eventually freeze out [395, 409]. In the end, a collection of relic glueball densities is left over, dominated by the 0^{++} with exponentially smaller yields for the heavier states [409].

The process of glueball freeze-out can change drastically if there are operators that connect the visible and dark sectors. Such operators are always expected at some level; quantum gravitational effects are thought to induce gauge-invariant operators involving both SM and dark sector fields suppressed by powers of the Planck mass [410–413]. Even stronger connections can arise if there exist new matter fields that couple directly to both the visible and dark sectors [11, 12]. As long as the new physics generating these operators is much larger than the confinement scale, their effects can be parametrized in terms of a set of non-renormalizable connector operators.

With connectors, energy can now be transferred between the dark and visible sectors [229, 235–237]. After confinement, connector operators can also modify the glueball freeze-out dynamics and induce decays of some or all of the dark glueballs to the SM. If one of the glueballs is long-lived or stable, it will

contribute to the density of dark matter (DM) [231]. However, glueball lifetimes that are not exceedingly long will inject energy into the cosmological plasma and modify the standard predictions for big bang nucleosynthesis (BBN) [259, 260] and the cosmic microwave background (CMB) [123, 312], as well as act as astrophysical sources of cosmic and gamma rays [402].

The aim of this chapter is to estimate the bounds on pure non-Abelian dark forces in the presence of connector operators from cosmology and astrophysics. We focus mainly on the dark gauge group $G_x = SU(3)$ with glueball masses above $m_0 \geq 100\,\text{MeV}$, and we study the leading connector operators between the dark vector bosons and the SM with characteristic mass scale $M \gg m_0$. As an initial condition, we assume inflation (or something like it) followed by preferential reheating to the visible sector to a temperature above the confinement scale but below that of the connectors. With these assumptions, we find very strong limits on non-Abelian dark forces.

Cosmological effects of dark gluons and glueballs were studied previously in Refs. [229, 231, 232, 235–237, 336, 351, 402, 406], including the detailed analysis of the relic yield we presented in Ch. 5. We extend these earlier works with a more detailed analysis of the leading (2-body) connector operators and their effects on energy transfer between the visible and dark sectors. We also investigate the effects of heavier glueballs in the spectrum beyond the lightest mode, and we show that the lightest C-odd glueball can play an important role in some cases and even make up the observed DM density when it is long lived or stable.

Following this introduction, we discuss and review the general properties of glueballs relevant to this analysis in Sec. 6.2. Next, we present the leading connector operators to the SM and investigate their implications for glueball decays in Sec. 6.3. In Sec. 6.4 we study the cosmological evolution of the dark gauge theory and we compute glueball yields both with and without connector operators. These results are then applied to derive cosmological constraints on dark glueballs in Sec. 6.5. Finally, Sec. 6.6 is reserved for our conclusions. Some technical details about gluon thermalization are collected in Appendix B. This chapter is based on work published in Ref. [4] in collaboration with David Morrissey and Kris Sigurdson.

6.2 Glueball Properties

Glueballs have been studied using a variety of methods for a wide range of non-Abelian gauge groups [352, 359]. In this section we review and derive some general results for $SU(N)$ glueballs that will be essential for the analysis to follow. The basic properties, such as masses and self-interaction strengths can be found in Ch. 5, while extra connections relevant to the standard model will be given here.

6.2.1 Glueball Matrix Elements

In Ch. 5, we described the glueball self-interactions. However, we will also need glueball matrix elements in the analysis to follow. Specific glueball states can be identified with gauge invariant gluon operators, in the sense that the operators can create one-particle glueball states from the vacuum. For

example [11],

$$\begin{array}{rcll} S & = & tr(X_{\mu\nu}X^{\mu\nu}) & \to \quad 0^{++} \\ P & = & tr(X_{\mu\nu}\widetilde{X}^{\mu\nu}) & \to \quad 0^{-+} \\ T_{\mu\nu} & = & \frac{1}{2}tr(X_{\mu\alpha}X_{\nu}{}^{\alpha}) - \frac{1}{4}\eta_{\mu\nu}S & \to \quad 2^{++}, 1^{-+}, 0^{++} \\ \Omega^{(1)}_{\mu\nu} & = & tr(X_{\mu\nu}X_{\alpha\beta}X^{\alpha\beta}) & \to \quad 1^{--}, 1^{+-} \\ \Omega^{(2)}_{\mu\nu} & = & tr(X_{\mu}{}^{\alpha}X_{\alpha}{}^{\beta}X_{\beta\nu}) & \to \quad 1^{--}, 1^{+-} \end{array} \tag{6.1}$$

Here, $X_{\mu\nu} = X^a_{\mu\nu}t^a$ is the dark gluon field strength contracted with the generators of the fundamental representation of the group normalized to $tr(t^a t^b) = \delta^{ab}/2$.

The two matrix elements of greatest interest to us are

$$\alpha_x F^S_{0^{++}} \quad \equiv \quad \alpha_x \langle 0|tr(X_{\mu\nu}X^{\mu\nu})|0^{++}\rangle \sim m_x^3 \tag{6.2}$$

$$\alpha_x^{3/2} M_{1^{+-}0^{++}} \quad \equiv \quad \alpha_x^{3/2}\langle 0^{++}|\big(\Omega^{(1)}_{\mu\nu} - \frac{5}{14}\Omega^{(2)}_{\mu\nu}\big)|1^{+-}\rangle \sim \sqrt{\frac{4\pi}{N}}\, m_x^3 \,, \tag{6.3}$$

where the estimates on the right hand sides are based on large-N and NDA, and $\alpha_x = g_x^2/4\pi$ is the dark gauge coupling. In the second line, we have also suppressed the Lorentz structure of the matrix element, $\varepsilon_{\mu\nu\alpha\beta}\, p^\alpha \varepsilon^\beta$, where p^α is the outgoing momentum and ε^β is the polarization of the initial state [11]. The first of these matrix elements, $F^S_{0^{++}}$, has been computed on the lattice for $N = 3$ with the result [354, 414]

$$4\pi\alpha_x F^S_{0^{++}} = 2.3(5)\, m_x^3 \,, \tag{6.4}$$

which agrees reasonably well with our large-N and NDA estimate and is scale independent. In contrast, the second matrix element has not been calculated on the lattice. We use the lattice value of $F^S_{0^{++}}$ and the NDA estimate $\alpha_x^{3/2} M_{1^{+-}0^{++}} = \sqrt{4\pi/N}\, m_x^3$ in the analysis to follow.

6.3 Connections to the SM and Glueball Decays

With the SM uncharged under the dark gauge group G_x, gauge invariance forbids a direct renormalizable connection of the dark gluons to the SM. However, massive mediator states that couple to both sectors can generate non-renormalizable operators connecting them. If the characteristic mass scale of the mediators is $M \gg \Lambda_x$, the leading operators have mass dimension of eight and six, and take the form [11, 12]

$$\mathcal{O}^{(8a)} \quad \sim \quad \frac{1}{M^4} tr(F_{SM}F_{SM})\, tr(XX) \,, \tag{6.5}$$

$$\mathcal{O}^{(8b)} \quad \sim \quad \frac{1}{M^4} B_{\mu\nu}\, tr(XXX)^{\mu\nu} \,, \tag{6.6}$$

$$\mathcal{O}^{(6)} \quad \sim \quad \frac{1}{M^2} H^\dagger H\, tr(XX) \,, \tag{6.7}$$

where X and F_{SM} refer to the dark gluon and SM field strengths. If present, these operators allow some or all of the glueballs to decay to the SM. In this section we illustrate mediator scenarios that generate

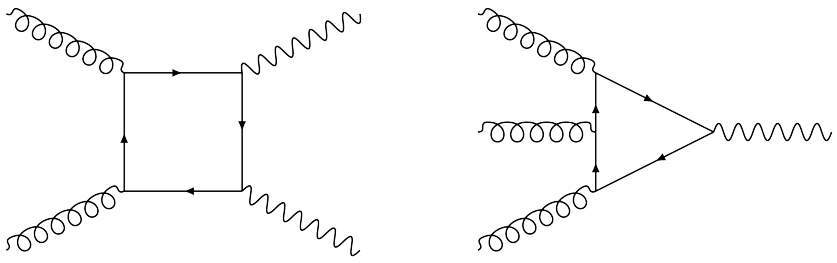

Figure 6.2: Diagrams that contribute to the effective Lagrangian of Eqs. (6.9) and (6.10). Effective operators are created via integration of loops of the heavy mediator fermions[11]. The left hand diagram will loosely correspond to decays of 0^{++} (Eq. (6.9)), while the right hand diagram will also contain terms that describe 1^{+-} decays (Eq. (6.10)).

these operators, and we compute the glueball decay rates they induce. This is an explicit realization of the unstable glueball scenarios hinted at in Ch. 5.

6.3.1 Dimension-8 Operators

Dimension-8 operators of the form of Eqs. (6.5,6.6) lead to glueball decays with characteristic rate

$$\Gamma_8 \sim \frac{m_x^9}{M^8} . \tag{6.8}$$

Here, we present an explicit scenario of mediator fermions that generates these operators and we compute the glueball decay rates they induce.

Before proceeding, it is helpful to organize the dimension-8 operators according to a dark charge conjugation operation C_x under which $X_\mu^a \to -\eta(a) X_\mu^a$, where $\eta(a)$ is the sign change of the fundamental generator t^a under charge conjugation [415], with the SM vector bosons being invariant. The operators of Eq. (6.5) are even under C_x and those of Eq. (6.6) are odd. Furthermore, C_x coincides with the C_x-number assignments of the glueball states. Correspondingly, the operators of Eq. (6.5) only allow direct decays of C_x-even glueballs to the SM, or glueball transitions from even to even or odd to odd. In particular, at $d = 8$ the operator of Eq. (6.6) is required for the lightest C_x-odd 1^{+-} glueball to decay.

Consider now a set of massive vector-like fermions with masses $M_r \sim M \gg \Lambda_x$, each transforming as a fundamental or antifundamental under $G_x = SU(N)$ and the representation r of the SM gauge group (defined with respect to the left-handed component of the fermion). Direct collider and precision electroweak limits on such fermions imply $M_r \gtrsim 100\,\text{GeV}$ if they only have electroweak charges, and $M_r \gtrsim 1000\,\text{GeV}$ if they are charged under QCD [11, 12, 416]. The diagrams that will be relevant for the effective operators are shown in Fig. 6.2. The effective Lagrangian generated by integrating the

fermions out is [11]:

$$\begin{aligned}\mathscr{L}_{eff} \supset\ & \frac{\alpha_x}{M^4}\left(\alpha_1\chi_1 B_{\mu\nu}B_{\alpha\beta}+\alpha_2\chi_2 W^c_{\mu\nu}W^c_{\alpha\beta}+\alpha_3\chi_3 G^a_{\mu\nu}G^a_{\alpha\beta}\right)\\ & \times\left(\frac{1}{60}S\eta^{\mu\nu}\eta^{\alpha\beta}+\frac{1}{45}P\varepsilon^{\mu\nu\alpha\beta}+\ldots\right) \qquad (6.9)\\ & +\ \frac{\alpha_x^{3/2}\alpha_1^{1/2}}{M^4}\chi_Y B_{\mu\nu}\frac{14}{45}\left(\Omega^{(1)}_{\mu\nu}-\frac{5}{14}\Omega^{(2)}_{\mu\nu}\right)\ . \qquad (6.10)\end{aligned}$$

Here, the dark gluon operators S, P, and $\Omega^{(1,2)}_{\mu\nu}$ correspond to Eq. (6.1), and the coefficients χ_i are given by

$$\begin{aligned}\chi_i &= \sum_r d(r_i)T_2(r_i)/\rho_r^4 \qquad (6.11)\\ \chi_Y &= \sum_r d(r_i)Y_r/\rho_r^4\ , \qquad (6.12)\end{aligned}$$

where the sums run over the SM representations r of the fermions, and $\rho_r = M_r/M$. For each such representation, we define sub-representations $r=(r_1,r_2,r_3)$ with respect to the SM gauge factors $G_i = U(1)_Y, SU(2)_L, SU(3)_c$. The quantity $d(r_i)$ is the number of copies of the i-th sub-representation within r, and $T_2(r_i)$ is the trace invariant for that factor (normalized to $1/2$ for the N of $SU(N)$ and Y^2 for $U(1)_Y$).[1]

Generic representations of mediator fermions break the dark charge conjugation number C_x explicitly and generate both operator types of Eqs. (6.5,6.6). This is explicit in Eq. (6.9), with both even ($\chi_i \neq 0$) and odd operators ($\chi_Y \neq 0$). However, there exist mediator fermion combinations that preserve C_x [201] and yield $\chi_Y = 0$. From Eq. (6.12), we see that this requires a specific combination of fermion charges as well as masses. The presence of masses also implies that C_x can be broken softly. In contrast, the χ_i coefficients of Eq. (6.11) are positive semi-definite and not subject to cancellation.

The C_x-preserving operator of Eq. (6.9) allows direct decays of the 0^{++} glueball to pairs of SM vector bosons. The corresponding decay widths are [11]

$$\begin{aligned}\Gamma(0^{++}\to gg) &= (N_c^2-1)\frac{\alpha_3^2}{16\pi}\left(\frac{2}{60}\right)^2\chi_3^2\frac{m_0^3(\alpha_x F^S_{0^{++}})^2}{M^8}\ , \qquad (6.13)\\ \frac{\Gamma(0^{++}\to\gamma\gamma)}{\Gamma(0^{++}\to gg)} &= \frac{1}{(N_c^2-1)}\left(\frac{\alpha\chi_\gamma}{\alpha_3\chi_3}\right)^2 \qquad (6.14)\\ \frac{\Gamma(0^{++}\to ZZ)}{\Gamma(0^{++}\to gg)} &= \frac{1}{(N_c^2-1)}\left(\frac{\alpha_2\chi_Z}{\alpha_3\chi_3}\right)^2\left(1-4\frac{m_Z^2}{m_0^2}\right)^{1/2}\left(1-4\frac{m_Z^2}{m_0^2}+6\frac{m_Z^4}{m_0^4}\right) \qquad (6.15)\\ \frac{\Gamma(0^{++}\to W^+W^-)}{\Gamma(0^{++}\to gg)} &= \frac{2}{(N_c^2-1)}\left(\frac{\alpha_2\chi_2}{\alpha_3\chi_3}\right)^2\left(1-4\frac{m_W^2}{m_0^2}\right)^{1/2}\left(1-4\frac{m_W^2}{m_0^2}+6\frac{m_W^4}{m_0^4}\right) \qquad (6.16)\\ \frac{\Gamma(0^{++}\to\gamma Z)}{\Gamma(0^{++}\to gg)} &= \frac{2}{(N_c^2-1)}\left(\frac{\sqrt{\alpha\alpha_2}\chi_{\gamma Z}}{\alpha_3\chi_3}\right)^2\left(1-\frac{m_Z^2}{m_0^2}\right)^3 \qquad (6.17)\end{aligned}$$

[1] Note that due to our normalizations, our $\chi_{2,3}$ are smaller by a factor of $1/2$ than the corresponding terms in Ref. [11].

where $m_0 = m_x$ is the 0^{++} glueball mass, $F^S_{0^{++}}$ is given by Eq. (6.2), $N_c^2 - 1 = 8$, the χ_i are defined in Eq. (6.11), $\chi_\gamma = \chi_1 + \chi_2$, $\chi_Z = (s_W^4 \chi_1 + c_W^4 \chi_2)/c_W^2$, and $\chi_{\gamma Z} = (c_W^2 \chi_2 - s_W^2 \chi_1)/c_W$, with s_W being the sine of the weak mixing angle. Note that the decay width to gluons in Eq. (6.13) only applies for $m_0 \gg 1\,\text{GeV}$; at lower masses the final states consist of hadrons. We do not attempt to model this hadronization, and instead we apply a factor of $\sqrt{1-(2m_\pi/m_0)^2}$ to the decay width. In evaluating the width of Eq. (6.13), we take α_3 at scale m_0 since the corresponding gluon operator is renormalized (at one-loop) in the same way as the standard field strength operator.

Decays of the lightest 1^{+-} glueball occur through the C_x-odd operator term in Eq. (6.9), with the leading decay channels expected to be $1^{+-} \to 0^{++} + \{\gamma, Z\}$. The widths are [11]

$$\Gamma(1^{+-} \to 0^{++}\gamma) = \frac{\alpha}{24\pi}\chi_Y^2 \left(1 - \frac{m_x^2}{m_1^2}\right)^3 \frac{m_1^3 (\alpha_x^{3/2} M_{1^{+-}0^{++}})^2}{M^8} \tag{6.18}$$

$$\Gamma(1^{+-} \to 0^{++}Z) = \frac{\alpha}{24\pi} t_W^2 \chi_Y^2 \left[\left(1 + \frac{m_x^2}{m_1^2} - \frac{m_Z^2}{m_1^2}\right)^2 - 4\frac{m_x^2}{m_1^2}\right]^{3/2} \frac{m_1^3 (\alpha_x^{3/2} M_{1^{+-}0^{++}})^2}{M^8} \tag{6.19}$$

with $m_1 = m_{1^{+-}}$, and $M_{1^{+-}0^{++}}$ defined in Eq. (6.3).

The total decay lifetimes $\tau = 1/\Gamma$ of the 0^{++} and 1^{+-} glueball states from the dimension-8 operators above with $\chi_i = \chi_Y = 1$ and $G_x = SU(3)$ are shown in the left and right panels of Fig. 6.3. In the upper left of both plots, we mask out the regions with $m_0 > M/10$ where our treatment in terms of effective operators breaks down. The dotted, solid, and dashed lines indicate reference lifetimes of $\tau = 1/\Gamma = 0.1\,\text{s},\ 5\times 10^{17}\,\text{s}, 10^{26}\,\text{s}$. These lifetimes correspond to decays that occur early in the history of the Universe, at the present day, and long lived glueballs, respectively. Both decay rates follow the approximate scaling of Eq. (6.8). All other known ($SU(3)$) glueballs can decay through these dimension-8 operators as well with parametrically similar rates, although there can be numerically significant differences due to coupling factors and phase space [11].

6.3.2 Dimension-6 Operators

Glueball decays through the dimension-6 operator of Eq. (6.7) proceed with characteristic rate

$$\Gamma_6 \sim \frac{m_0^5}{M^4}\,. \tag{6.20}$$

We present here two mediator scenarios that generate the operator of Eq. (6.7) and we compute the decay rates they induce.

Our first mediator scenario follows Ref. [12] and consists of mediator fermions with Yukawa couplings to the SM Higgs boson, as shown in Fig. 6.4. A minimal realization contains a vector-like $SU(2)_L$ doublet P with gauge quantum numbers $(r_x, 1, 2, -1/2)$, and a vector-like singlet N with quantum numbers $(r_x, 1, 1, 0)$ together with the interactions [12, 416]

$$-\mathscr{L} \supset M_P \bar{P} P + M_N \bar{N} N + \lambda \bar{P} H N + (h.c.)\,. \tag{6.21}$$

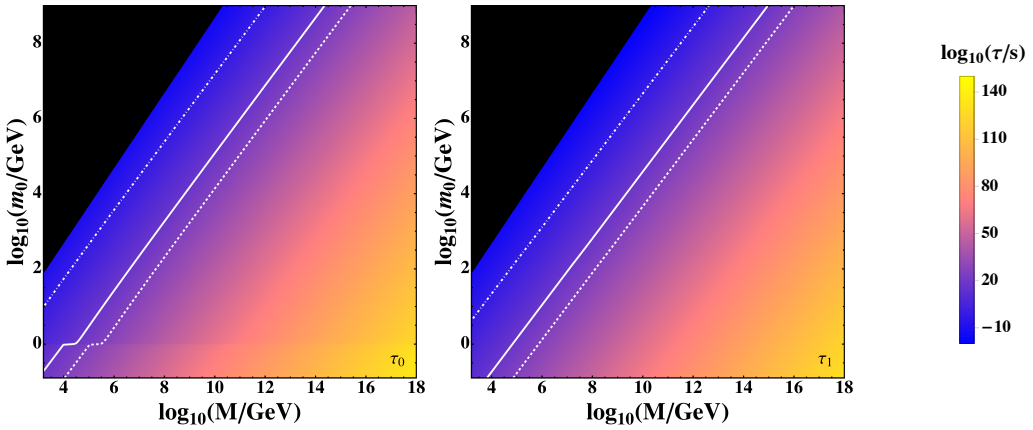

Figure 6.3: Decay lifetimes $\tau = 1/\Gamma$ of the 0^{++} (left) and 1^{+-} (right) glueball states due to the dimension-8 operators as a function of M and m_0 for $\chi_i = \chi_Y = 1$ and $G_x = SU(3)$. The masked regions at the upper left show where $m_0 > M/10$ and our treatment in terms of effective operators breaks down, while the white dotted, solid, and dashed lines indicate reference lifetimes of $\tau = 0.1\,\mathrm{s},\ 5\times10^{17}\,\mathrm{s},\ 10^{26}\,\mathrm{s}$.

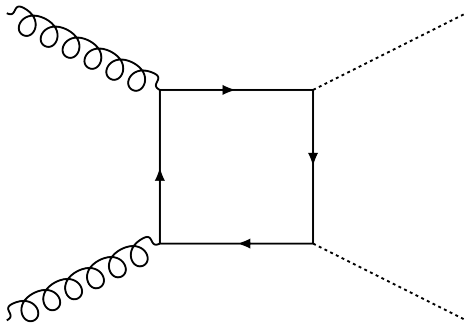

Figure 6.4: Diagram that contributes to the effective Lagrangian of Eq. (6.22). Effective operators are created via integration of loops of the heavy mediator fermions[12].

For $M_N, M_P \gg m_h$, the leading glueball effective operator from integrating out the fermions can be obtained using the low-energy Higgs theorem [417],

$$\mathscr{L}_{eff} \supset \frac{\alpha_x}{6\pi} T_2(r) \frac{\lambda^2}{M^2} H^\dagger H X^a_{\mu\nu} X^{a\,\mu\nu} \,, \tag{6.22}$$

where $M^2 \simeq M_P M_N$ and $T_2(r_x) = 1/2$ is the trace invariant of the fermion representation r_x under the dark gauge group G_x. In addition to the dimension-6 operator above, the massive fermions also generate dimension-8 operators of the form of Eq. (6.9).

A second mediator scenario consists of a complex scalar Φ_x charged under the dark gauge group with a Higgs-portal coupling,

$$-\mathscr{L} \supset M_\Phi^2 |\Phi_x|^2 + \kappa |\Phi_x|^2 |H|^2 \tag{6.23}$$

Applying the low-energy Higgs theorem to this state (for $M_\Phi \gg m_h$), we find

$$-\mathscr{L}_{eff} \supset -\frac{\alpha_x}{48\pi} T_2(r) \frac{\kappa}{M_\Phi^2} H^\dagger H X^a_{\mu\nu} X^{a\mu\nu} \,. \tag{6.24}$$

In passing, we note that the Higgs portal coupling of Eq. (6.23) respects dark C_x number.

The operator generated in either mediator scenario can be written in the form

$$-\mathscr{L}_{eff} \supset \frac{\alpha_x y_{eff}^2}{6\pi M^2} H^\dagger H X^a_{\mu\nu} X^{a\mu\nu} \,, \tag{6.25}$$

with the dimensionless coefficient y_{eff}. Since this operator is even under C_x, it only allows direct decays of C_x-even glueballs to the SM, or even-to-even or odd-to-odd glueball transitions. It was shown in Ref. [12] that this is sufficient to allow all known $SU(3)$ glueballs to decay, except for the 1^{+-} and 0^{-+} modes. The absence of a 1^{+-} decay follows from C_x considerations, while the conclusion for 0^{-+} is a result of spin and parity, rather than C_x. This mode can decay at the dimension-6 level if a topological dark gluon term is added to the UV Lagrangian or by extending to a two-Higgs doublet model [12].

Using the parametrization of Eq. (6.25), the direct decay of the 0^{++} glueball to the SM has rate [12]

$$\Gamma(0^{++} \to SM) = \left(\frac{y_{eff}^2}{3\pi}\right)^2 \frac{(\sqrt{2}\langle H\rangle)^2 (\alpha_x F_{0^{++}}^S)^2}{M^4 \left[(m_0^2 - m_h^2)^2 + (m_h \Gamma_h)^2\right]} \Gamma_h(m_h \to m_0) \,, \tag{6.26}$$

where $\sqrt{2}\langle H\rangle = 246\,\text{GeV}$ is the electroweak vacuum expectation value, $F_{0^{++}}^S$ is defined in Eq. (6.2), $m_h = 125\,\text{GeV}$ is the Higgs mass, $\Gamma_h = 4.1\,\text{MeV}$ is the Higgs width, and $\Gamma_h(m_h \to m_0)$ is the total width the SM Higgs would have if its mass were m_0 (and includes decays to Higgs final states for $m_0 > 2m_h$). We evaluate this width using the expressions of Refs. [418, 419].

In Fig. 6.5 we show the decay lifetime $\tau = 1/\Gamma$ of the 0^{++} glueball from the dimension-6 (and dimension-8) operators above with $y_{eff} = 1$ and $G_x = SU(3)$. The upper region of the plot is masked out since it corresponds to $m_0 > M/10$ where our treatment in terms of effective operators breaks down. The dotted, solid, and dashed lines indicate lifetimes of $\tau = 0.1\,\text{s},\ 5\times10^{17}\,\text{s}, 10^{26}\,\text{s}$. For $m_0 \gg m_h$, the 0^{++} lifetime scales according to Eq. (6.20), while for $m_0 < m_h$ there is an additional suppression from small Yukawa couplings. Comparing to the 1^{+-} lifetime in Fig. 6.3, we see that it is parametrically long-lived compared to the 0^{++} when both dimension-6 and dimension-8 operators are present.

6.3.3 Decay Scenarios

Based on the discussion above, we present four glueball decay scenarios organized by the dimensions of the relevant decay operators and the dark conjugation charge C_x:

1. **Dimension-8 decays with broken C_x**

   In this scenario glueballs decay exclusively through the dimension-8 operators of the form of Eq. (6.9). All glueballs are able to decay with parametrically similar rates. To realize this scenario, we use the effective interactions in Eq. (6.9) with $\chi_i = \chi_Y = 1$.

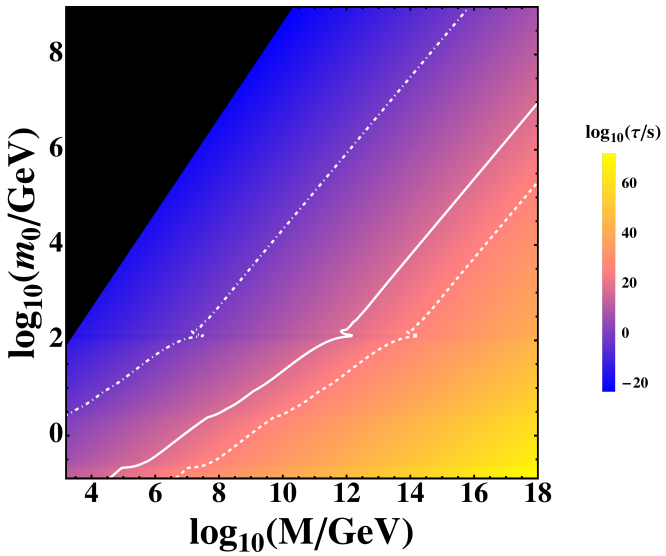

Figure 6.5: Decay lifetime $\tau = 1/\Gamma$ of the 0^{++} glueball due to the combined dimension-6 and dimension-8 operators as a function of M and m_0 for $\chi_i = \chi_Y = 1$, $y_{eff} = 1$, and $G_x = SU(3)$. The masked region at the upper left shows where $m_0 > M/10$ and our treatment in terms of effective operators breaks down, while the dotted, solid, and dashed white lines indicate lifetimes of $\tau = 0.1\,\mathrm{s},\ 5\times10^{17}\,\mathrm{s},\ 10^{26}\,\mathrm{s}$.

2. **Dimension-8 decays with exact C_x**

   This scenario is similar to the first, but now with $\chi_Y = 0$. Conservation of C_x implies that the lightest 1^{+-} glueball is stable. The other glueballs are all able to decay with parametrically similar rates.

3. **Dimension-6 decays with broken C_x**

   Glueball decays occur through the dimension-6 operator of Eq. (6.25) and the dimension-8 operators of Eq. (6.9). We realize the scenario by setting $y_{eff} = 1$ together with $\chi_i = \chi_Y = 1$. With the exception of the 1^{+-} mode (and possibly the 0^{-+}), glueballs decay primarily through the dimension-6 operator. In contrast, the 1^{+-} glueball only decays through the C_x-breaking dimension-8 operator with a parametrically suppressed rate, making it much longer-lived than the other glueballs, which in turn leads to different cosmological scenarios when considering the constraints we can place on this model.

4. **Dimension-6 decays with exact C_x**

   Decays occur through the dimension-6 operator of Eq. (6.25) and the C_x-conserving terms in Eq. (6.9). We realize the scenario by taking $y_{eff} = 1$, $\chi_i = 1$, and $\chi_Y = 0$. The 1^{+-} glueball is stable, while the other glueballs decay mainly through the dimension-6 operator.

We study the cosmological implications of these four decay scenarios in the analysis to follow.

6.4 Glueball Densities in the Early Universe

Glueballs are formed in the early universe in a confining transition as the dark sector temperature T_x falls below a critical temperature $T_c \sim m_0$. After they are created, the glueballs undergo a complicated freeze-out process involving a range of $2 \to 2$ and $3 \to 2$ reactions. These dynamics become even more complicated when the dark sector connects to the SM through the operators discussed above, with new effects such as energy transfer between the visible and dark sectors and glueball decays. In this section we briefly review the formation and freeze-out of glueballs in the absence of connectors to the SM, as was studied in detail in Ch. 5, and we investigate how this picture changes when connectors are present.

6.4.1 Glueball Formation and Freeze-Out without Connectors

This section is a review of Ch. 5, and serves to emphasize the key points and parameters that are used in estimating glueball yields. This will be important when we move on to consider the effects of the decay scenarios discussed previously. Although parts of this are repetitions of the previous chapter, we include it to highlight the key differences and results that will be important in further analysis.

In the absence of operators that connect to the SM, the visible and dark sectors do not thermalize with each other. We assume that enough energy is liberated by reheating following primordial inflation (or something similar) that both sectors are able to thermalize independently with temperatures T and T_x [204], and furthermore that $T_x \geq T_c$ at this point.[2] Following the recipe for glueball formation provided in Ch. 5, entropy is conserved independently in both sectors while kinetic equilibrium is maintained. This implies that the ratio of entropy densities s and s_x in the two sectors remains constant, and can be parametrized by a single value, R. We again take R as an input to our calculation. However, we do assume $R < 1$ corresponding to preferential reheating to the visible sector.

Once formed, dark glueballs interact with each other and undergo a freeze-out process in which they depart from thermodynamic equilibrium and develop stable relic densities. This process is what we studied in detail in Ch. 5. In the last chapter, the evolution of glueball numbers was computed numerically using a network of Boltzmann equations containing the most important $2 \to 2$ and $3 \to 2$ reactions, with thermally averaged cross sections estimated using the glueball effective Lagrangian of Eq. (5.3). There, we considered various different subsets of glueballs, in which we discovered that the 0^{++} relic yield is predominately determined by the $3 \to 2$ reaction, and including other glueballs was largely irrelevant to the overall yield. However, because some of our decay scenarios explicitly allow for stable 1^{+-} states, we consider the two-state model of Sec. 5.4.3 for the rest of this chapter so that we can track both the 0^{++} and 1^{+-} yields for further analysis.

In Fig. 6.6 we show the relic yields of 0^{++} (left) and 1^{+-} (right) glueballs in the absence of connectors to the SM in the m_0–R plane for $G_x = SU(3)$. The white lines in both panels indicate where the relic density of that species coincides with the observed DM density, $\Omega_{DM}h^2 = 0.1188(10)$ [9]. The shaded regions at the lower right of both panels show where $x_x^{fo} < 5$ implying the glueball densities are set by the non-perturbative dynamics of the confining phase transition. As expected, the 1^{+-} yield is always

[2] If not, the glueball relic density is set by the details of inflationary reheating.

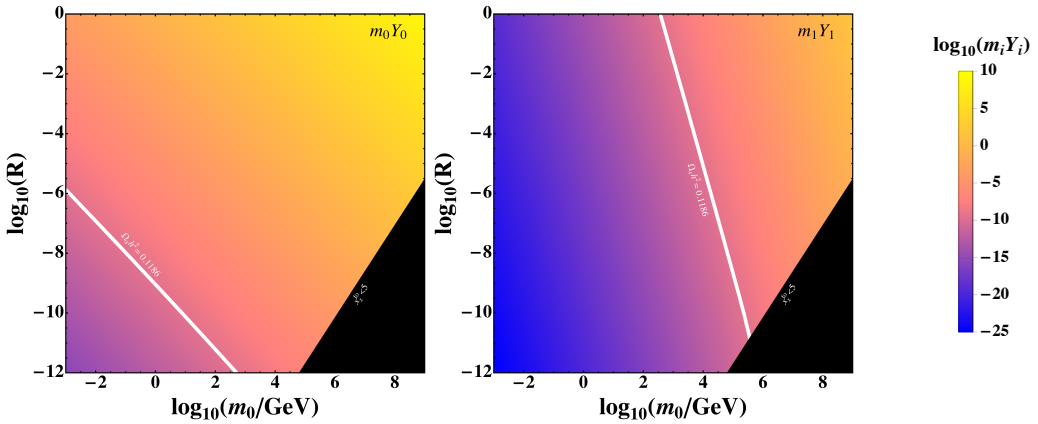

Figure 6.6: Mass-weighted relic yields of the 0^{++} (left) and 1^{+-} (right) glueballs in the m_0–R plane in the absence of connectors for $G_x = SU(3)$. The solid white lines in each panel indicate where the relic density saturates the observed dark matter abundance. The dark masked region at the lower right of both panels shows where 0^{++} freeze-out occurs for $x_x^{fo} < 5$ and our freeze-out calculation is not applicable due to the unknown dynamics of the confining phase transition.

much lower than the 0^{++} yield.

Going beyond the two-state model, our arguments regarding the exponential suppression of the 1^{+-} density relative to the 0^{++} also apply to the other heavier glueball modes, as we showed in Ch. 5. The total glueball relic density is strongly dominated by the 0^{++} density, while $2 \to 2$ annihilation reactions push the heavier glueball densities to much smaller values. In fact, these reactions tend to be much more efficient for the other heavier glueballs than the 1^{+-} due to coannihilation with the 0^{++}. As a result, the 1^{+-} state generally develops the second largest relic density, with the densities of the other dark glueballs being much smaller. This, combined with the unique decay properties of the 1^{+-} glueball when connectors are included, is the reason why we only consider the effects of the 0^{++} and 1^{+-} glueballs in our analysis of glueball cosmology.

6.4.2 Glueball Freeze-Out with Connectors

Connector operators can modify the freeze-out of glueballs in a number of ways. As we explicitly examined in Ch. 3, we realize that it is important to fully understand these connector operators before moving forward with our models. Scattering and decay reactions mediated by such operators transfer energy between the visible and dark sectors, and may allow them to thermalize. Decays through the connector operators after confinement also deplete glueballs, and can occur before or after the freeze-out of the various $(3 \to 2)$ and $(2 \to 2)$ reactions. We investigate these effects here, both before and after confinement, with a focus on the 0^{++} and 1^{+-} glueballs. Our goal is to compute the yields of these species prior to their decay.

As in the freeze-out analysis without connectors, we take as an initial condition primordial inflation (or something like it) with preferential reheating to the visible sector characterized by a temperature T_{RH} that is larger than the confinement transition temperature $T_c \simeq m_0/5.5$. With connectors, we also

assume $T_{RH} \ll M$. Reheating above the connector scale M is likely to thermalize the dark and visible sectors at T_{RH}, and can produce a relic abundance of the connector particles themselves. These can have interesting cosmological effects in their own right, acting as *quirks* if they carry G_x charge [342, 420, 421], and potentially creating dark glueballs non-thermally [406, 407, 422, 423]. By taking $T_{RH} \ll M$, the production of connector particles in the early universe is strongly suppressed allowing us to focus on the effects of the glueballs.

Energy Transfer before Confinement

Consider first the transfer of energy at temperatures T well above the confinement temperature T_c. In the absence of connectors, preferential reheating to the visible sector produces $T_x \ll T$. Connector operators allow reactions of the form $\mathrm{SM}+\mathrm{SM} \leftrightarrow X+X$ that transfer energy from the visible sector to the dark sector. For $T_x > T_c$, the evolution equation for the energy density of the dark sector is [424, 425]

$$\frac{d\rho_x}{dt} + 4H\rho_x \;=\; -\langle \Delta E \cdot \sigma v \rangle \left(n_x^2 - \widetilde{n}_x^2\right) \;, \tag{6.27}$$

where $\langle \Delta E \cdot \sigma v \rangle$ is the thermally averaged energy transfer cross section for $X+X \to \mathrm{SM}+\mathrm{SM}$, n_x is the dark gluon number density, and $\widetilde{n}_x = \tilde{g}_x(\zeta(3)/\pi^2)T^3$ is the value it would have in full equilibrium with the visible sector with $\tilde{g}_x$ dark gluon degrees of freedom (equal to $\tilde{g}_x = 2(N^2-1)$ for $G_x = SU(N)$).[3] For $T_x \ll T$, the $\widetilde{n}_x^2$ term on the right side above dominates and leads to a net energy transfer to the dark sector. This transfer saturates and ceases when $T_x \to T$ and $n_x \to \widetilde{n}_x$.

For visible radiation domination with constant g_*, Eq. (6.27) can be rewritten as

$$\frac{d}{dT}\left(\frac{\rho_x}{T^4}\right) = \frac{1}{HT^5}\langle \Delta E \cdot \sigma v \rangle \left(n_x^2 - \widetilde{n}_x^2\right) \;. \tag{6.28}$$

With the connector operators of Eqs. (6.5,6.7) and $T \gg T_x$, the right side of Eq. (6.28) takes the parametric form

$$\Delta\mathscr{C} \;\equiv\; \langle \Delta E \cdot \sigma v \rangle \left(n_x^2 - \widetilde{n}_x^2\right) \tag{6.29}$$

$$\sim\; -D_n \frac{M_{\rm Pl}\, T^{n-2}}{M^n} \;, \tag{6.30}$$

where $n = 4, 8$. Integrating from temperature T to the reheating temperature T_{RH}, the approximate solution is

$$\left(\frac{\rho_x}{T^4}\right) - \left(\frac{\rho_x}{T^4}\right)_{RH} \;\sim\; \frac{D_n}{(n-1)} \frac{M_{\rm Pl} T_{RH}^{n-1}}{M^n} \left[1 - \left(\frac{T}{T_{RH}}\right)^{n-1}\right] \;, \tag{6.31}$$

This expression is dominated by the contribution near the reheating temperature, and represents the contribution to the dark energy density from transfer reactions.

[3] Implicit in Eq. (6.27) is the assumption of self-thermalization of the energy injected into the dark sector to a temperature $T_x > T_c$. Thermalization of non-Abelian gauge theories tends to be efficient [426], and we expect this assumption to be valid provided the total energy transfer is not exceedingly small.

The approximate forms of Eqs. (6.30,6.31) are only valid for $T < T_{RH}$ and $T > T_x \geq T_c$. The first of these conditions corresponds to the upper limit on the era of radiation domination. An even higher radiation temperature can be achieved prior to reheating, but for standard perturbative reheating and $n < 29/3 \simeq 9.67$ we find that the energy transfer before the radiation era is also dominated by reactions near $T \sim T_{RH}$. The second condition $T > T_x \geq T_c$ is needed to justify our neglect of the n_x^2 term on the right side of Eq. (6.28) and our assumption of a deconfined phase. As T_x approaches T due to the energy transfer, this term becomes important and the net energy transfer goes to zero, corresponding to the thermalization of the two sectors.

Motivated by these considerations, let us define

$$\Delta\left(\frac{\rho_x}{T^4}\right) \equiv \int_{\cdot}^{T} dT' \left(\frac{\Delta\mathscr{C}}{HT'^5}\right) \tag{6.32}$$

$$\sim \frac{D_n}{(n-1)} \frac{M_{\rm Pl} T^{n-1}}{M^n} \,. \tag{6.33}$$

This represents the contribution to the dark sector energy from thermal transfer in the vicinity of temperature T. Thermalization occurs when

$$\Delta\left(\frac{\rho_x}{T^4}\right) \geq \frac{\pi^2}{30}\tilde{g}_x \,, \tag{6.34}$$

where $\tilde{g}_x$ is the number of dark gluon degrees of freedom. Let T_{th} be the temperature that solves Eq. (6.34) as an equality. If $T_{th} < T_c$, the visible and dark sectors remain thermalized at least until confinement. Conversely, if $T_{th} > T_c$ thermalization is lost at $T = T_{th}$ and the dark and visible sectors evolve independently thereafter with separately conserved entropies.

The dark to visible entropy ratio R is constant for $T < T_{th}$ and depends on reheating. If $T_{th} < T_{RH}$, thermalization occurs after reheating and is maintained until $T = T_{th}$. The entropy ratio R (for $T_{th} > T_c$) after thermalization ceases is then

$$R = R_{max} \equiv \frac{\tilde{g}_x}{g_{*S}(T_{th})} \,. \tag{6.35}$$

Thermalization need never have occurred after reheating if $T_{RH} < T_{th}$. In this case, (for $T_{th} > T_c$) we can define

$$T_{xRH} = T_{RH} \left[\frac{30}{\pi^2 \tilde{g}_x} \Delta\left(\frac{\rho_x}{T^4}\right)_{RH}\right]^{1/4} \,. \tag{6.36}$$

This implies a lower bound on the entropy ratio of

$$R \geq \frac{\tilde{g}_x}{g_{*S}(T_{RH})} \left(\frac{T_{xRH}}{T_{RH}}\right)^3 \,. \tag{6.37}$$

In general, lower reheating temperatures allow for smaller values of R. We define R_{min} to be the value of

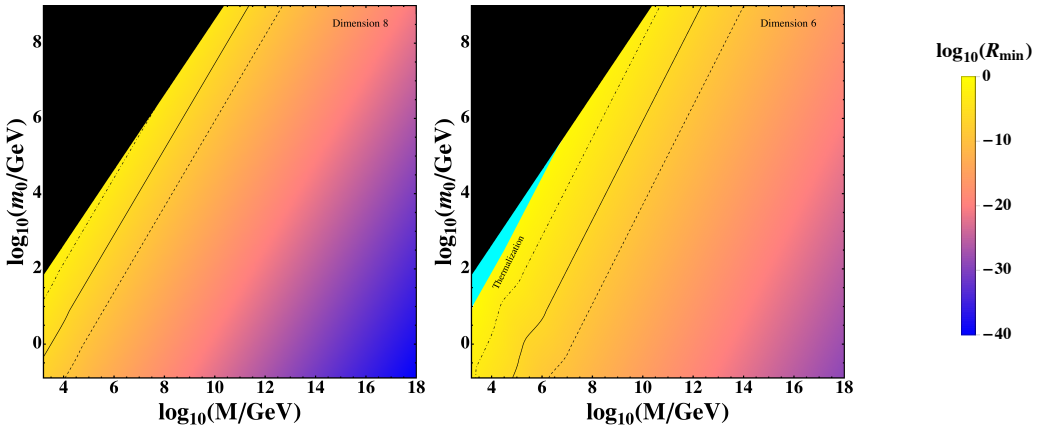

Figure 6.7: Values of the minimal entropy ratio R_{min} in the M–m_0 plane for energy transfer via dimension-8 (left) and dimension-6 (right) operators for $G_x = SU(3)$. The black shaded region at the upper left indicates where our treatment in terms of effective operators breaks down. The diagonal black dotted, solid, and dashed lines show reference values of $R_{min} = 10^{-3}, 10^{-6}, 10^{-9}$. In the cyan region in the right panel, thermalization between the visible and dark sectors is maintained at least until confinement.

R such that $T_{xRH} = T_c$, the lowest possible reheating temperature given our assumption of $T_{xRH} \geq T_c$.[4] When $T_{th} > T_c$, the range of R values is therefore $R_{min} \leq R \leq R_{max}$.

In Appendix B we present explicit expressions for the collision term $\Delta\mathscr{C}$ needed to compute the energy transfer $\Delta(\rho_x/T^4)$ via Eq. (6.32). The results obtained for R_{min} are shown in Fig. 6.7 in the m_0–M plane for energy transfer via dimension-8 (left) and dimension-6 (right) operators for $G_x = SU(3)$. The shaded region at the upper left has $m_0 > M/10$ and indicates where our treatment in terms of effective operators breaks down. The black dotted, solid, and dashed lines show reference values of $R_{min} = 10^{-3}, 10^{-6}, 10^{-9}$. In the cyan region in the right panel, thermalization between the visible and dark sectors is maintained at least until confinement, corresponding to $T_{th} < T_c$.

Evolution of the 0^{++} Density

Glueballs form at $T_x = T_c$ and undergo freeze-out, transfer, and decay reactions. In the absence of connectors, the dominant glueball species is the lightest 0^{++} mode. To track its evolution with connector operators, it is convenient to organize the analysis according to the thermalization temperature T_{th}, computed above in the unconfined phase, relative to the confinement temperature.

$T_{th} < T_c$: This condition implies that thermalization is maintained at least until confinement, and thus we expect $T = T_x = T_c$ as an initial condition for the glueball evolution. To compute the 0^{++} density and thermal transfer after confinement we adapt the analysis of Refs. [350, 428] based on Refs. [424, 425, 429], which is applicable here since T, $T_x \leq T_c \simeq m_0/5.5$. If thermal equilibrium is maintained

[4] Even lower values of R are possible for $T_{xRH} < T_c$, but this also implies that reheating can interfere with the freeze-out process [427], and goes beyond the scope of this work.

independently within both the dark and visible sectors, the dark temperature evolves as [350, 428]

$$\frac{dT_x}{dt} \simeq -2HT_x + \frac{2}{3n_0}(\mathscr{C}_\rho - m_0\mathscr{C}_n) \tag{6.38}$$

where $\mathscr{C}_\rho$ and $\mathscr{C}_n$ are the collision terms appearing in the evolution equations for the 0^{++} energy and number densities. The Hubble term in Eq. (6.38) gives the usual $1/a^2$ redshifting of the effective temperature of an independent massive species, while the second term describes energy transfer from scattering and decay processes.

The explicit forms of the collision terms are

$$\mathscr{C}_n \simeq -\langle\sigma_{32}v^2\rangle n_0^2(n_0-\bar{n}_0) - \Gamma_0\left[n_0(1-3T_x/2m_0) - \widetilde{n}_0(1-3T/2m_0)\right] , \tag{6.39}$$

where $\bar{n}_0 = n_0(T_x)$ and $\widetilde{n}_0 = n_0(T)$, as well as

$$\mathscr{C}_\rho \simeq n_0 n_{SM}\langle\sigma_{el}v\cdot\Delta E\rangle - m_0\Gamma_0(n_0-\widetilde{n}_0) . \tag{6.40}$$

The only new piece in these expressions is the elastic scattering term $n_0 n_{SM}\langle\sigma_{el}v\cdot\Delta E\rangle$ in Eq. (6.40). It corresponds to reactions of the form $\mathrm{SM}+0^{++}\to\mathrm{SM}+0^{++}$, and was studied in detail in Refs. [424, 425].

Combined in Eq. (6.38), the $(3\to 2)$ scattering term from Eq. (6.39) tends to heat the dark glueballs, and the elastic scattering and decay terms tend to drive $T_x\to T$. Applied to the 0^{++} glueball with either the dimension-8 or dimension-6 connector operators, we find that thermalization below confinement implies $\Gamma_0 > H(T=m_0)$. Thus, the 0^{++} density simply tracks the equilibrium value with temperature T following confinement.[5]

$\mathbf{T_{th} > T_c}$: With $T_{th} > T_c$, the visible and dark sectors are not thermally connected at confinement, and thus $T \geq T_x$ at this point with a well-defined entropy ratio in the range $R_{min} \leq R \leq R_{max}$. Using the scaling arguments applied above, it can be shown that $R \geq R_{min}$ implies $T \leq m_0$ when the 0^{++} decays set in at $\Gamma_0 \simeq H(T)$.[6] The evolution equations for the 0^{++} number density and temperature can thus be written as (to leading order in T_x/m_0)

$$\frac{dn_0}{dt} = -3Hn_0 - \langle\sigma_{32}v^2\rangle n_0^2(n_0-\bar{n}_0) - \Gamma_0(n_0-\widetilde{n}_0) \tag{6.41}$$

$$\frac{dT_x}{dt} = -2HT_x + \frac{2}{3}m_0\langle\sigma_{32}v^2\rangle n_0(n_0-\bar{n}_0) + \Gamma_0 T_x\left(1-\frac{\widetilde{n}_0}{n_0}\frac{T}{T_x}\right) \tag{6.42}$$

where again $\bar{n}_0$ is the equilibrium value at temperature T_x and $\widetilde{n}_0$ is the equilibrium value at temperature T. Note that we have neglected the elastic scattering term because it can be shown to be parametrically small relative to the Hubble term for $T < T_{th}$ and $R \geq R_{min}$.

[5] In the absence of decays, massive glueballs with connectors would give an explicit realization of the SIMP [147] or ELDER [350, 428] DM scenarios.

[6] Our numerical analysis confirms this as well.

When the decay terms are neglected, the evolution equations of Eqs. (6.41, 6.42) are equivalent to those we used previously with no connector operators (to leading order in T_x/m_0). Glueball decays only become significant when $\Gamma_0 \simeq H(T)$, and quickly drive $T_x \to T$ and $n_0 \to \widetilde{n}_0$. It follows that our previous analysis without connectors can be applied to compute the 0^{++} relic yield prior to decay (which may occur before freeze-out). The only significant effect of energy transfer on this calculation is to limit the range of the initial entropy ratio to $R_{min} \leq R \leq R_{max}$.

Evolution of the 1^{+-} Density

Even though the lightest 0^{++} glueball dominates the total glueball density and controls the dark temperature prior (and even after) its decay, the heavier 1^{+-} glueball can also be relevant for cosmology due to its longer lifetime. Recall that the 1^{+-} is parametrically long-lived relative the 0^{++} in the decay scenarios **2–4** listed in Sec. 6.3.3, where the 0^{++} decays through a dimension-6 operator while the 1^{+-} is stable or only decays at dimension-8. Even in decay scenario **1**, where both states decay at dimension-8, the 0^{++} decay rate tends to be larger than the 1^{+-} by a factor of $(N_c^2-1)\alpha_3/\alpha$.

The evolution of the 1^{+-} density is sensitive to the 0^{++} density in several ways. Prior to decay, the 0^{++} density acts as a massive thermal bath that cools very slowly relative to the visible temperature, thereby delaying the freeze-out of the 1^{+-} state. This thermal bath collapses and disappears when the 0^{++} decays, which can hasten 1^{+-} freeze-out. If the 0^{++} density is large when it decays, the entropy transferred to the visible sector can also dilute the densities of the remaining 1^{+-} glueballs. We investigate these effects here, dividing the analysis into $T_{th} < T_c$ and $T_{th} > T_c$ cases.

$\mathbf{T_{th} < T_c}$: Recall that this case is only realized for dimension-6 transfer operators, and implies that the 0^{++} decay rate is larger than Hubble following confinement. This means the 0^{++} density tracks its equilibrium value with effective temperature $T_x = T$, and there is no longer a separately conserved entropy in the dark sector. The evolution of the 1^{+-} number density in this context is

$$\frac{dn_1}{dt} + 3Hn_1 = -\langle \sigma_{22} v \rangle \left(n_1^2 - \widetilde{n}_1^2\right) - \Gamma_1 (n_1 - \widetilde{n}_1) \,, \tag{6.43}$$

where $\widetilde{n}_1$ denotes the equilibrium density of the 1^{+-} at temperature T. Note that Eq. (6.43) assumes the 1^{+-} mode also thermalizes with the visible sector. This is expected prior to freeze-out since the equilibrium density of the 1^{+-} is smaller than that of the 0^{++}, and elastic scattering between these two species is at least as efficient as the annihilation reaction.

$\mathbf{T_{th} > T_c}$: This second case implies $T_x \leq T$ at confinement, with 0^{++} decays inactive ($\Gamma_0 < H$) until $T < m_0$. To compute the resulting 1^{+-} relic density, we treat the 0^{++} decay as instantaneous and match the density evolution immediately before and after it occurs. Prior to the decay, the dark and visible entropies are conserved independently with ratio R, and the glueball densities evolve according to Eqs. (5.47,5.48). Decays of the 0^{++} are implemented at $\Gamma_0 = H$, where the Hubble rate includes contributions from both the visible and dark energy densities. If $T_i < m_0$ is the visible temperature prior

to the decay, the visible temperature afterwards is obtained from local energy conservation,

$$\rho(T_f) = \rho(T_i) + \rho_x(T_i) \,, \tag{6.44}$$

where we have neglected the exponentially subleading contribution of the 1^{+-} mode to the energy density. Note that $T_f > T_i$ is always smaller than m_0 as well. The evolution of the 1^{+-} number density after the 0^{++} decays is given by Eq. (6.43). Since the 1^{+-} number density is not changed by the decays, $n_1(T_f) = n_1(T_i)$ is used as the initial condition at $T = T_f$.

The interplay of glueball annihilation, transfer, and decays leads to many different qualitative behaviours. These were investigated in Ref. [395, 409] for a simplified model consisting of an unstable massive bath particle and a heavier DM state. Dark glueballs provide an explicit realization of this scenario, with the 0^{++} making up the massive bath and the 1^{+-} acting as (metastable) dark matter. Compared to the simple model studied in Ref. [395, 409], the 0^{++} massive bath particle always freezes out (or decays) before the would-be 1^{+-} dark matter, corresponding to the *chemical* or *decay* scenarios discussed there. A potential further behavior that we have not captured in our approximations is the late production of 1^{+-} glueballs through transfer reactions while $T > m_1$ but after 1^{+-} freeze-out has occurred in the dark sector. We estimate that this is potentially relevant in a very limited corner of the parameter space, and will only increase the limits we find.

6.4.3 Comments on Theoretical Uncertainties

Before applying our results for dark glueball lifetimes and densities to derive cosmological and astrophysical constraints on them, it is worth taking stock of the theoretical uncertainties in our calculations. It is also useful to identify how some of these uncertainties might be reduced with improved lattice calculations.

The glueball lifetimes computed in Sec. 6.3 rely on glueball masses and transition matrix elements. Masses for $G_x = SU(3)$ have been obtained to a precision greater than 5% in Refs. [6, 354], while the matrix element relevant for 0^{++} decay was determined to about 20% in Refs. [354, 414]. Thus, we expect our determination of the 0^{++} decay width to be reasonably accurate. The situation is less clear for the 1^{+-} width, which relies on a $1^{+-} \to 0^{++}$ transition matrix element that we were only able to estimate using NDA. In the absence of lattice calculations for this matrix element, we estimate that our 1^{+-} width is only reliable to within a factor of a few.

Turning next to the cosmological evolution of the dark gluons and glueballs, we implicitly treated their interactions as being perturbative. This is a good approximation at temperatures well above the confinement scale, but significant deviations can arise as the temperature falls to near confinement [377]. For the range of entropy ratios R due to energy transfer computed above, this implies that values of R_{max} with $T_{th} \gg T_c$ are reliable, but the specific values of R_{min} and R_{max} for $T_{RH} \sim T_c$ could receive large corrections. Similarly, the glueball interactions used to compute the $(3 \to 2)$ and $(2 \to 2)$ cross sections are quite strong for $N = 3$. It is difficult to quantify how this affects the pre-decay glueball relic densities, but we do note that the densities typically depend roughly linearly on R and the annihilation

cross sections. Our naive estimate is that the pre-decay glueball densities we find are accurate to within about an order of magnitude.

6.5 Cosmological Constraints

In the analysis above we showed that dark glueballs can have a wide range of decay rates and a variety of formation histories in the early universe. Very long-lived dark glueballs can potentially make up the cosmological dark matter. On the other hand, shorter-lived glueballs are strongly constrained by the modifications they can induce in the standard predictions for big bang nucleosynthesis (BBN) [94, 259, 260], the cosmic microwave background (CMB) [123, 430] and the spectrum of cosmic rays [402]. We investigate the bounds from cosmology and astrophysics on dark glueballs in this section for the four decay scenarios discussed in Sec. 6.3. Throughout the analysis, we focus on $G_x = SU(N=3)$, and we assume reheating such that $T_{RH} \ll M$ and $T_{xRH} \geq T_c$. Details of how we implement the bounds from BBN, the CMB, and cosmic rays are collected in the following section.

6.5.1 Decay Constraints from BBN

Particle decays during or after big bang nucleosynthesis (BBN) can modify the primordial abundances of light elements including tritium, deuterium, helium, and lithium [81, 112, 259, 260]. The observed abundances of these light elements (with the exception of lithium) agree well with the predictions of standard BBN when the baryon density deduced from the CMB is used as an input [81]. If there was non-standard physics present during the era of BBN, such as the decays of dark glueballs to SM fields, the predictions the elemental abundance would be altered. Thus, constraints can be placed upon decays of glueballs after the onset of BBN.

Hadronic decays of a long-lived relic after $t \simeq 0.05\,\mathrm{s}$ can modify the neutron (n) to proton (p) ratio and increase the helium fraction through charge exchange reactions such as $\pi^- + p \to \pi^0 + n$, or destroy light elements through spallation reactions like $n + {}^4\mathrm{He} \to \mathrm{D} + p + 2n$ [81, 112]. Electromagnetic decays are only constrained at later times, after about $t \sim 10^4\,\mathrm{s}$, since energetic electromagnetic decay products emitted before this thermalize with the photon-electron plasma before can they can destroy light elements by photodissociation [7, 81, 112].

The combined effects of hadronic and electromagnetic decays on BBN have been studied in a number of works, including Refs. [94, 259, 260]. We apply the exclusions derived in Ref. [94] to place limits on decaying glueballs, using an interpolation to generalize their results to arbitrary relic mass values between the range $30\,\mathrm{GeV} \leq m_x \leq 10^6\,\mathrm{GeV}$ they studied, and matching to the appropriate set of final states. For masses outside these ranges, we apply the constraint for the nearest mass boundary.

6.5.2 Decay Constraints from the CMB

Particle decays during or after recombination at $t \simeq 1.2 \times 10^{13}\,\mathrm{s}$ can modify the temperature and polarization spectra of the CMB. They do so by injecting energy that increases the ionization fraction and temperature of the cosmological plasma. In turn, this broadens the last scattering surface and alters the

correlations among the temperature and polarization fluctuations [123].

Detailed studies of the impact of such energy injection on the CMB have been performed in Refs. [80, 313–315, 430–432]. Corresponding limits on particle decays based on the CMB measurements of Planck [9] were extracted in Refs. [80, 430]. Given the theoretical uncertainties in our calculation of the pre-decay glueball yields, we apply a very simple parametrization of the results of Ref. [430]:

$$m_i Y_i \;<\; (4.32\times 10^{-10}\,\mathrm{GeV})\left(\frac{\tau}{10^{24}\,\mathrm{s}}\right)\mathscr{F}(\tau)\,, \tag{6.45}$$

where $\mathscr{F}(\tau)$ accounts for the effects of early decays. It is obtained by fitting to the curve of Fig. 4 of Ref. [430], and is normalized to unity for $\tau \gg 1.2\times 10^{13}\,\mathrm{s}$. The form of Eq. (6.45) neglects mild dependences on the mass of the decaying glueball and the specific final state, but these effects are smaller than the uncertainties in the calculation of the pre-decay yield. We also apply this limit to relic masses well above the largest value of $m_x \sim 10$ TeV studied in Ref. [430] (and elsewhere). Such large masses lead to injections of highly energetic photons and electrons that deposit their energy very efficiently in the cosmological plasma [315]. As a result, we do not expect any major loss of sensitivity for glueball masses well above 10 TeV.

Bounds on glueball decays can also be obtained from their effects on the CMB frequency spectrum [318, 433]. We find that these are subleading compared to those derived from BBN and the CMB power spectra.

6.5.3 Decay Constraints from Gamma Rays

Glueballs with lifetimes greater than the age of the universe $t_0 \simeq 4.3\times 10^{17}\,\mathrm{s}$ can produce observable signals in gamma ray and cosmic ray telescopes, even if their density is only a small fraction of the total DM value. Limits on the lifetimes of decaying DM were derived in Ref. [402] for dimension-6 glueball decays and other final states over a broad range of masses using galactic gamma ray data from *Fermi* [434]. With the theoretical uncertainty on glueball yields in mind, we use the following parametrization of the limits on the glueball yield:

$$m_i Y_i \;<\; (4.32\times 10^{-10}\,\mathrm{GeV})\left(\frac{\tau}{5\times 10^{27}\,\mathrm{s}}\right) e^{t_0/\tau}\, e^{(10\,\mathrm{GeV}/m_i)}\,, \tag{6.46}$$

where the last two factors account for the depletion of the signal if the decay occurs before the present time and the loss of sensitivity of *Fermi* at lower masses [435]. This limit is fairly conservative and can be applied safely to all dominant 0^{++} decays, which occur on their own or shortly after being created in a 1^{+-} decay.

6.5.4 Application to Glueballs

In this next section we apply the constraints collected above to the specific decay scenarios presented in section 6.3.3.

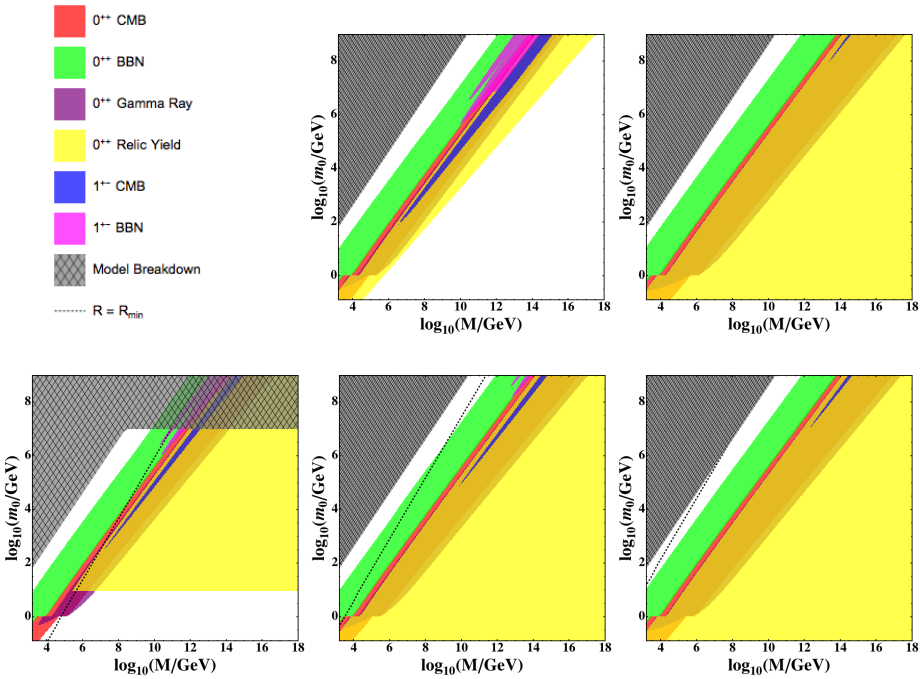

Figure 6.8: Cosmological constraints on dark glueballs in the M–m_0 plane for decay scenario **1** with dominant dimension-8 operators and broken C_x. The upper two panels have $R = R_{min}, R_{max}$, while the lower three panels have fixed $R = 10^{-9}, 10^{-6}, 10^{-3}$. The grey shaded region in each panel indicates where our theoretical assumptions fail, while $R < R_{min}$ to the left of the dashed line.

Decay Scenario 1: Dimension-8 Decays with Broken C_x

This scenario has all the dimension-8 operators of Eq.(6.9) with $\chi_i = \chi_Y = 1$. Both the 0^{++} and 1^{+-} glueballs decay with parametrically similar rates, as shown in Fig. 6.3.

The cosmological constraints on this scenario are shown in Fig. 6.8 in the M-m_0 plane for various values of the entropy ratio R. The upper two panels have $R = R_{min}, R_{max}$ respectively,[7] and the lower three panels show $R = 10^{-9}, 10^{-6}, 10^{-3}$. The grey shaded regions indicate where our theoretical assumptions break down. The rising diagonal portion of the gray shaded region corresponds to $m_0 > M/10$; we demand smaller values of m_0 to justify our treatment in terms effective operators suppressed by powers of M. The upper part of the grey shaded region indicates $T_{xfo} > T_c$, corresponding to glueball densities set by the non-perturbative dynamics of the confining phase transition. To the left of the diagonal dotted lines in the lower three panels, the given fixed value of R is less than R_{min} and is inconsistent with minimal energy transfer by the connector operators for $T_{xRH} > T_c$.

We see from Fig. 6.8 that dark glueballs are strongly constrained by cosmological and astrophysical observations. When the 0^{++} is long-lived, corresponding to small m_0/M, its relic density tends to be too large unless the entropy ratio R is much less than unity. With sufficiently small R the 0^{++} can make up all the dark matter corresponding to the white line in the left panel of Fig. 6.6. Such a DM candidate

[7] Recall from Eq. (6.35) that R_{max} corresponds to thermalization after reheating, while from Eq. (6.37) R_{min} is the lowest possible entropy ratio consistent with energy transfer and $T_{xRH} > T_c$.

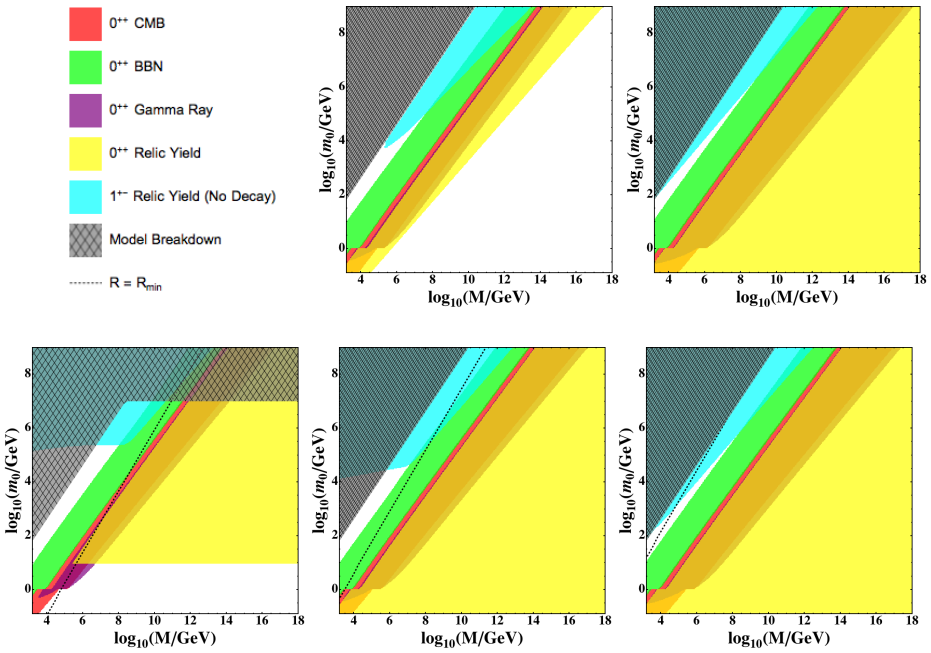

Figure 6.9: Cosmological constraints on dark glueballs in the M–m_0 plane for decay scenario **2** with dominant dimension-8 operators and conserved C_x. The upper two panels have $R = R_{min}, R_{max}$, and the lower three panels have fixed $R = 10^{-9}, 10^{-6}, 10^{-3}$. The grey shaded region indicates where our theoretical assumptions fail, while to the left of the dashed line we find $R < R_{min}$.

would be very difficult to probe, with the most promising avenues being high energy gamma rays and modifications to cosmic structure from glueball self interactions. Using large-N and NDA, the $2 \to 2$ self-interaction cross section of 0^{++} glueballs is [231, 235]

$$\sigma_{2\to 2}/m_0 \simeq (10\,\mathrm{cm}^2/\mathrm{g}) \left(\frac{3}{N}\right)^4 \left(\frac{100\,\mathrm{MeV}}{m_0}\right)^3 . \tag{6.47}$$

This is at (or slightly above) the current limit for $N \geq 3$ and $m_0 \geq 100$ MeV and could have observable effects close to these values [137], but falls off very quickly with higher mass or if the 0^{++} glueball is only a small fraction of the full DM density. For larger m_0/M ratios, the 0^{++} and 1^{+-} glueballs both decay quickly enough to alter BBN or the CMB or create high energy gamma rays. Not surprisingly, the bounds from glueball decays in this scenario come primarily from the 0^{++} which has a much larger relic yield prior to decay.

Decay Scenario 2: Dimension-8 Decays with Exact C_x

Our second decay scenario has dominant dimension-8 operators with $\chi_i = 1$ and a conserved C_x charge that implies $\chi_Y = 0$ and a stable 1^{+-} glueball. The cosmological bounds on this scenario are shown in Fig. 6.9 for various values of the entropy ratio R. The upper two panels have $R = R_{min}, R_{max}$ respectively, and the lower three panels show $R = 10^{-9}, 10^{-6}, 10^{-3}$. As above, the grey shaded regions indicate

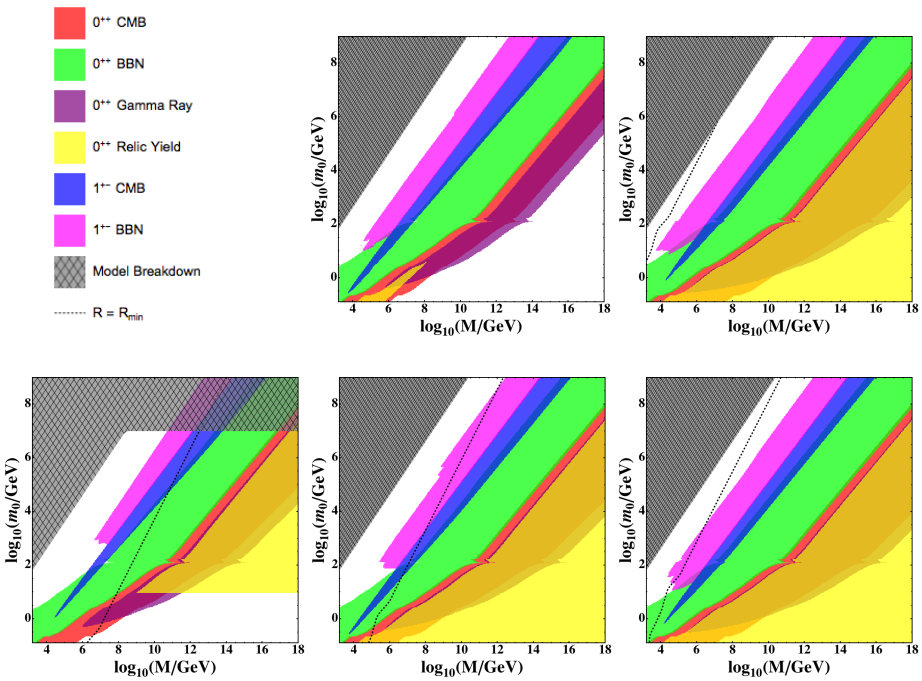

Figure 6.10: Cosmological constraints on dark glueballs in the M–m_0 plane for decay scenario **3** with dominant dimension-6 operators and broken C_x. The upper two panels have $R = R_{min}, R_{max}$, and the lower three panels have fixed $R = 10^{-9}, 10^{-6}, 10^{-3}$. The black shaded region indicates where our theoretical assumptions fail, while to the left of the dashed line we find $R < R_{min}$.

where our theoretical assumptions are not satisfied, and the diagonal dashed lines have $R < R_{min}$ to their left.

The cosmological exclusions on this scenario are nearly identical to those on scenario **1** except for the new bounds from the 1^{+-} relic density. At the lower edge of the cyan excluded region, the 1^{+-} glueball can make up all the dark matter. This occurs primarily when the 0^{++} decays relatively quickly, since otherwise it tends to dilute the 1^{+-} relic density too strongly. Note as well that the 1^{+-} glueball can make up the dark matter for a wide range of values of the entropy ratio R, and for masses well above the weak scale, between about 10^2 GeV $\lesssim 10^5$ GeV. For smaller values of m_0/M, the 0^{++} is long-lived and remains the dominant species as in scenario **1**.

Decay Scenario 3: Dimension-6 Decays with Broken C_x

The third decay scenario **3** has both dimension-6 and dimension-8 operators with $y_{eff} = 1$ and $\chi_i = \chi_Y = 1$, and broken C_x. This leads to 0^{++} decays dominated by the dimension-6 operator, but decays of the 1^{+-} only through the dimension-8 operators. As a result, the 1^{+-} glueball is parametrically long-lived relative to the 0^{++} (and the other glueball states).

We show the cosmological and astrophysical bounds on this scenario in Fig. 6.10 for various values of the entropy ratio R. The upper two panels have $R = R_{min}, R_{max}$ respectively, and the lower three panels show $R = 10^{-9}, 10^{-6}, 10^{-3}$. As above, the grey shaded regions indicate where our theoretical

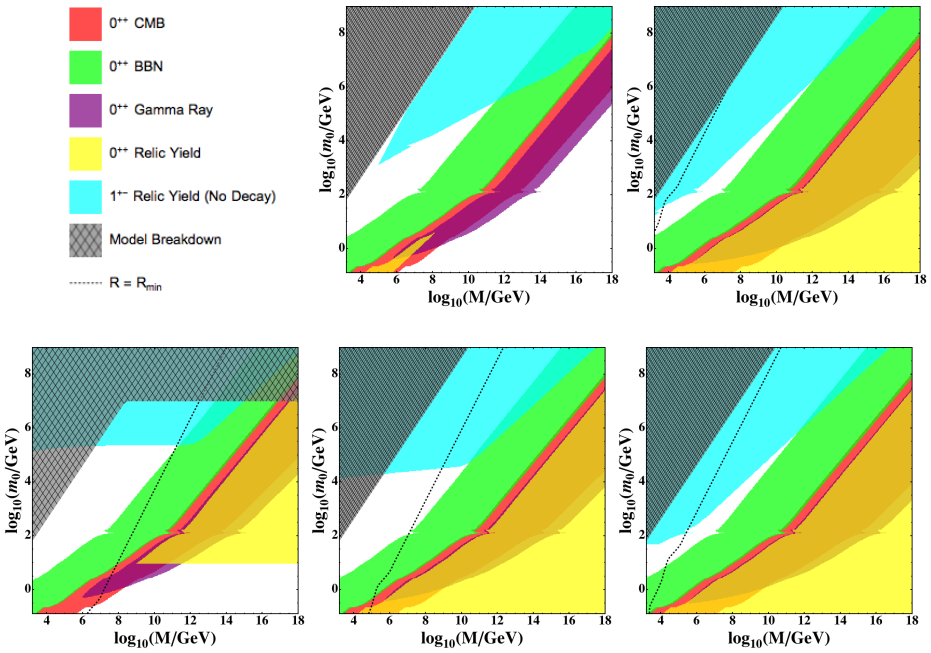

Figure 6.11: Cosmological constraints on dark glueballs in the M–m_0 plane for decay scenario **4** with dominant dimension-8 operators and conserved C_x. The upper two panels have $R = R_{min}, R_{max}$, and the lower three panels have fixed $R = 10^{-9}, 10^{-6}, 10^{-3}$. The black shaded region indicates where our theoretical assumptions fail, while to the left of the dashed line we find $R < R_{min}$.

assumptions are not satisfied, and the diagonal dashed lines have $R < R_{min}$ to their left, except in the $R = R_{max}$ panel. Here, thermalization is maintained all the way to confinement (and beyond) to the left of the line.

Decays of both the 0^{++} and 1^{+-} glueballs lead to relevant exclusions in this scenario. The 0^{++} relic density tends to be much larger than the 1^{+-} prior to decay, and produces the strongest constraints for small values of m_0/M when it is long-lived. For very long lifetimes and small R, it can make up all the DM as before. However, larger values of m_0/M lead to relatively short-lived 0^{++} glueballs that decay before the start of BBN. In this case, the longer-lived 1^{+-} can decay late enough to disrupt nucleosynthesis or the CMB in an unacceptable way. Note as well that the region in which the 1^{+-} relic density is potentially large, it decays too quickly to make up the dark matter.

Decay Scenario 4: Dimension-6 Decays with Exact C_x

Our final decay scenario **4** has has both dimension-6 and dimension-8 operators with $y_{eff} = 1$ and $\chi_i = 1$, together with conserved C_x (and $\chi_Y = 0$). The 0^{++} mode decays as in the previous scenario, but now the 1^{+-} is stable.

The cosmological bounds on this scenario are shown in Fig. 6.11 for various values of the entropy ratio R. The upper two panels have $R = R_{min}, R_{max}$ respectively, and the lower three panels show $R = 10^{-9}, 10^{-6}, 10^{-3}$. As above, the grey shaded regions indicate where our theoretical assumptions are not satisfied, and the diagonal dashed lines have $R < R_{min}$ to their left, except in the $R = R_{max}$ panel. Here,

thermalization is maintained all the way to confinement (and beyond) to the left of the line.

The exclusions on this scenario from the 0^{++} are identical to those on scenario **3**. However, the constraints from the 1^{+-} are now from its relic density rather than the effects of its decays on BBN and the CMB. This state can make up the dark matter for a range of values of its mass and the entropy ratio R. Compared to the analogous scenario **2**, the relic density of the 1^{+-} tends to be larger here because it experiences less dilution from the more rapid decay of the 0^{++}.

6.6 Conclusions

In this chapter we culminated all of the individual pieces that were considered in previous chapters. We have investigated the cosmological constraints on non-Abelian dark forces with connector operators to the SM. We have focused on the minimal realization of such a dark force in the form of a pure Yang-Mills theory. In the early universe, the dark gluons of such theories confine to form a set of dark glueballs. Connector operators allow the transfer of energy between the visible (SM) and dark sectors, modify the freeze-out dynamics of the glueballs, and induce some or all of the dark glueballs to decay. Late decays of glueballs can modify the standard predictions for BBN, the CMB, and cosmic ray spectra, while very long-lived or stable glueballs must not produce too much dark matter. Using these considerations, we have derived strong constraints on the existence of new non-Abelian dark forces.

A significant new feature of our work compared to previous studies [229, 231, 232, 235–237, 336, 351, 406] is the inclusion of the heavier 1^{+-} glueball species. This state can be parametrically long-lived or stable relative to the other glueballs. It freezes out in conjunction with the 0^{++}, with the 0^{++} density forming a massive thermal bath, leading to a rich array of freeze-out and decay dynamics [395, 409]. In general, the (pre-decay) relic density of the 1^{+-} mode is much smaller than the 0^{++}. Even so, the 1^{+-} can sometimes yield the strongest cosmological bounds due to its longer lifetime. Specifically, the 0^{++} could decay before impacting standard cosmological processes such as BBN, while the 1^{+-} decays late enough to directly interfere. In some cases, the 1^{+-} glueball could even make up the observed DM density.

Our study also concentrated on the dark gauge group $G_x = SU(N=3)$ with a lightest 0^{++} glueball mass above $m_0 \geq 100\,\text{MeV}$. The constraints found here could also be generalized to other dark gauge groups and lower masses. A very similar glueball spectrum is expected for $SU(N>3)$ [5], but the confining phase transition will be more strongly first-order and its effect on glueball freeze-out deserves further study [351, 378]. For $G_x = SU(2), SO(2N+1), Sp(2N)$ there are no C_x-odd glueballs [11, 359], but otherwise we expect the constraints based on the 0^{++} glueballs to be applicable here. In the case of $SO(2N>6)$, the C_x-odd states are expected to be significantly heavier than the 0^{++}, and thus the additional constraints on the lightest C_x-odd mode would typically be weakened.

Thus, we have now completed a comprehensive overview of how the visible and dark sectors of the Universe may interact with one another. We have used our knowledge and intuitions, built up over the previous chapters, to create a fully realized hidden sector in the form of a non-Abelian dark gauge field. The sectors own self-interactions were studied extensively, before allowing for SM connections, completing the energy transfer circle we first outlined in Fig. 2.5, and made explicit in Fig. 6.1.

Part V

Conclusions

Chapter 7

Conclusions and Future Outlook

In this thesis we have investigated how new physics beyond the Standard Model may interact with that which we understand already. This was depicted in Fig. 2.5. In particular, we have focused on how a dark sector may be influenced by, or influence, the visible sector that we know and understand. This has involved studying and constraining new physics in different epochs in the Universe, ranging from Big Bang Nucleosynthesis to how new physics could alter galactic formation. These are effects that the dark sector could have on the hidden. However, it is also possible to affect the dark sector directly via the visible sector, and so we have also studied how energy transfer in this direction can play a factor as well.

In Chapter 3, we started our overview of the visible-dark dynamic by looking specifically at the visible to hidden energy transfer, in a modified freeze-in scenario. We wished to understand how ultraviolet freeze-in may continue to play an important role in the relic abundance of dark matter, well after it is typically considered complete. Specifically, we realized this scenario by including a freeze-in transfer effect from a non-renormalizable, UV operator, coupled with a self-thermalizing hidden sector. To be concrete, we focused on the dimension-five fermionic Higgs portal operator to connect the two sectors, but note that this effect should extend to any UV operator. The freeze-in transfer serves to initially minimally populate the hidden sector (although we leave open the possibility that during reheating, some other mechanism could have also produced hidden sector particles, but to a temperature less than the visible sector). Within the hidden sector there is contained a candidate dark matter fermion, as well as a massless Abelian dark vector that couples to the dark matter. This typically results in what would be a standard, hidden freeze-out scenario as the Universe continues to expand and cool in both sectors. However, the extra freeze-in coupling serves to halt the freeze-out process. Instead, the dark matter candidate reaches a new pseudo-equilibrium state, where the freeze-out rate becomes balanced by the freeze-in rate, even well after the freeze-in rate should have become negligible. Thus, we find that the UV connector operator continues to play an important role, even into the IR.

While this effect is suppressed if there is no dark sector annihilation subsequent to the initial transfer, it is nevertheless expected to generalize to any other connection. Thus, we expect IR contributions from any UV operators that produce relic abundances of dark-sector DM, as long as there is some form of annihilation that continues to occur in the hidden-sector. This can lead to a significant additional en-

hancement of the relic density over a broad range of parameters in the theory. As we continue to expand our searches for new physics, dark-sector scenarios grow more complicated, and it is thus important to keep in mind this visible energy transfer dynamic. An interesting extension would be to consider a massive vector boson in the hidden sector, and consider the interplay between the freeze-in energy transfer and subsequent evolutionary dynamics. Other more complicated hidden sectors could be considered as well; any model of new physics that maintains a hidden annihilation will have to keep this effect in mind. As our direct detection experiments continue to probe smaller DM-nucleon cross-sections (with no evidence for WIMP-like DM), we need to build up a robust understanding of more production mechanisms than just standard freeze-out, and as such it becomes important to understand how these feeble interactions can have an effect on the evolution of hidden sector fields. Furthermore, as these interactions may never be directly probe-able with various experiments, it becomes crucial to understand those parts of new theories that will have long-lasting evolutionary effects, as observations of the DM relic density may be one of the only mechanisms by which we may study BSM physics.

Following this study of the visible energy transfer, we moved on to a study of how dark sector energy may affect the visible in Chapter 4. In particular, we have focused on decaying dark species with SM by-products, in an effort to understand how this energy injection can alter the outcomes of Big Bang Nucleosynthesis. Although this has been studied in the literature before, it had not yet been done for the lowest range of masses that may affect the outputs of BBN. Specifically, we have focused on the 1-100 MeV range. This range has received less attention as the earliest, well-motivated BSM models were typically at the weak scale, $\sim$ TeV range. However, new models can still be motivated below this, and as these low energy ranges have not yet been fully explored, we wished to fill this gap in our understanding. Even at these low energy transfers, we are still able to place stringent constraints on new physics, by modelling how the SM responds to the energy inflow.

Because we constrain ourselves to such low energy ranges, nearly all of the energy must be transferred via electromagnetic energy injection, as the threshold for hadronic energy injection lies at the pion mass ($\sim$ 134 MeV). Because of this, we model the electromagnetic cascades induced by EM energy in this range. This leads to a photon spectrum that is different from the historical universal photon spectrum that is typically adopted for photon injection. The spectrum is altered due to the inclusion of Thomson scattering for low energy electrons, as well as including final state radiation in the decay of the dark sector particle to electron-positron pairs.

The photon spectrum determined from electromagnetic decays of the dark sector particles is then used to determine photodissociation rates of light elements in the epoch following their production. For energies below the threshold photodissociation energy of ^{4}He, the most stringent constraint comes from destruction of Deuterium below the levels we observe today. For energies above the ^{4}He threshold, there is instead an interplay between the destruction of ^{4}He and the overproduction of deuterium, as it gets produced as a by-product of ^{4}He dissociation. Because our present-day limits on ^{3}He are much more uncertain than the other two elements, this is typically a weaker limit than the other two, although there are still some regions of parameter space where it may provide the limiting constraint. Future studies may wish to also include the Lithium observations, and perhaps attempt to explain (or contribute to) the

Lithium puzzle that has still not been solved.

While direct energy injection can be used to directly dissociate the light elements, we also look at indirect effects on BBN. This was done by identifying the effect that energy injections may have on N_{eff}, which is a measure of the radiation energy density in the early Universe. Decays to electrons, photons, and even neutrinos can affect N_{eff}, either increasing or decreasing the energy density, which in turn effects when BBN occurs, altering the ratio of all the final elements present at the end of BBN. These indirect effects are the dominant constraint on particles with lifetimes $< 10^4$s, while lifetimes up to 10^{13}s are most strongly constrained by the direct EM injections and photodissociation of the light elements. For later lifetimes, constraints from the CMB and gamma-rays today become more relevant. Nevertheless, this chapter has provided a unique look into how low-energy transfers from a hidden sector can affect the elements that we know and understand.

Now that we have developed a complete understanding of the constraints that may be placed on new physics that is active during the epoch of BBN, we may begin to apply these constraints to specific realizations of new physics. Although many early, well motivated theories of new physics typically involved much higher energy scales, the lack of evidence from direct detection and collider experiments has pushed our studies to expand and look in different energy regimes. Moving forward, as new models develop that are continually pushing to lower energies, we can apply this BBN constraint to supplement our bounds on such new physics. For example, various light vector bosons often appear in new models. These could include dark photons, B-L symmetry theories, and even the dark glueballs considered here[270, 436]. Thus the future outlook for cosmological probes is bright, across many different energy scales.

After studying cases of energy injected into either the hidden-sector or into the visible-sector, we moved on to a more complicated hidden-sector in Part IV. Here, we investigated the dynamics associated with a hidden SU(3) sector of dark glueballs that would have formed and evolved in the early Universe. These glueballs arise from confinement in non-Abelian gauge sectors, and typically have masses near, or slightly above, the confinement scale.

In Chapter 5, we began with a focused study of isolated glueballs, with no transfer allowed between the glueballs and the visible sector. The primary focus was to perform a detailed analysis of the freeze-out dynamics associated with a complex dark sector. In particular, we modelled the $3 \to 2$ interaction that dominates the freeze-out of the lightest 0^{++} state, while also determining what effects the heavier glueballs may have on the overall density. The heavier glueball states are included in the analysis via an expanded set of Boltzmann equations, that include the most dominant and relevant $2 \to 2$ interactions. We found that the heavy C-even states do not have a large effect on the lightest state, although their individual yields are in fact affected by the presence of other glueballs, through effects such as coannihilation. However, when the glueballs are unable to decay efficiently through SM connectors, these yields are always subdominant to the lightest 0^{++} state, and have a negligible effect on the relic abundance constraint associated with the glueball spectrum making up the cosmological dark matter. The C-odd states have a similar effect. However, these are modelled separately, as dark-sector symmetries could stabilize the lightest C-odd states while the C-even states decay to SM particles, making the

lightest C-odd state, the 1^{+-} state, of cosmological interest as well.

This was studied explicitly in Chapter 6, in which we relaxed the assertion that these glueballs were entirely isolated. We considered the two most relevant non-renormalizable decay operators that might connect the hidden SU(3) sector to the Standard Model. These are dimension-6 operators, which only allow for C-even (and so, in particular, the 0^{++} state) decays, as well as dimension-8 operators, which allow all glueball modes to decay (although even here, only some of the vector portals allow for decay of the 1^{+-} state). This leads to a broad host of cosmologically interesting constraints, including bounds from BBN, the CMB, and gamma-ray constraints for lifetimes close to the age of the Universe. When the dimension-6 operator is not present, the 0^{++} and 1^{+-} states have parametrically similar decay rates, and so the larger yield associated with the 0^{++} state causes this to have the strongest constraints over all epochs. If we consider still only the dimension-8 operator, but stabilize the 1^{+-} state via a dark C symmetry, then we gain constraints on the yield of 1^{+-} being larger than the cosmological dark matter abundance today. Including the dimension-6 operator lifts the parametric similarities of the 0^{++} and 1^{+-} decay rates: the 0^{++} will now decay earlier. This causes the decays of both states to contribute to the overall constraint picture, allowing us to rule out vast portions of the parameter space, regardless of the type of transfer operator being considered.

Thus, we have now seen a comprehensive overview of how the visible and dark sectors of the Universe may interact, and explored a rich and diverse hidden sector in the form of a full non-Abelian gauge force that is realized as a massive glueball spectrum. We have explored both visible and dark sector energy injections in detail, while addressing how these energy injections can lead to constraints on new physics. Moving forward, these new constraints and insights should prove invaluable to future studies, and can be expanded upon by building more complex models, and updating the bounds as our cosmological measurements grow ever-more precise.

The outlook for the future is certainly bright. Although we are currently in an era of physics where we are not sure what the future holds or where BSM physics could be hiding, we have developed an extraordinary set of tools to guide our analyses moving forward. As the LHC goes through upgrades to come back at higher luminosities, cosmological surveys probe further into the past history of the Universe with evermore precision, and new technologies such as gravitational wave detectors are produced, theoretical models and constraints stand ready to be applied to whatever new signals lurk around the corner. And if no signal presents itself immediately, we can still close the doors on, or at least narrow the windows for, many new models of physics by simply continuing to develop our understanding of the cosmological evolution of known and unknown fields based on the immense amount of data we have amassed and continue to cultivate. We are truly developing theories in an era of data, which is an exciting experience and hopefully one that will lead to answers to some of our puzzles as the data continues to grow.

Bibliography

[1] L. Forestell and D. E. Morrissey (2018), 1811.08905. → pages v, 52, 56

[2] L. Forestell, D. E. Morrissey, and G. White, JHEP **01**, 074 (2019), 1809.01179. → pages v, 70, 73, 75

[3] L. Forestell, D. E. Morrissey, and K. Sigurdson, Phys. Rev. **D95**, 015032 (2017), 1605.08048. → pages v, 68, 71, 93, 95

[4] L. Forestell, D. E. Morrissey, and K. Sigurdson, Phys. Rev. **D97**, 075029 (2018), 1710.06447. → pages v, 68, 71, 115, 117

[5] M. J. Teper (1998), hep-th/9812187. → pages x, 13, 96, 139

[6] C. J. Morningstar and M. J. Peardon, Phys. Rev. **D60**, 034509 (1999), hep-lat/9901004. → pages x, 13, 95, 96, 97, 105, 132

[7] M. Kawasaki and T. Moroi, Astrophys. J. **452**, 506 (1995), astro-ph/9412055. → pages xii, 38, 71, 72, 74, 75, 76, 78, 79, 80, 133

[8] V. Poulin and P. D. Serpico, Phys. Rev. **D91**, 103007 (2015), 1503.04852. → pages xii, 72, 79, 80, 90

[9] P. A. R. Ade et al. (Planck), Astron. Astrophys. **594**, A13 (2016), 1502.01589. → pages xiii, xiv, 32, 73, 88, 102, 125, 134

[10] K. M. Nollett and G. Steigman, Phys. Rev. **D89**, 083508 (2014), 1312.5725. → pages xiii, 70, 72, 73, 87, 88

[11] J. E. Juknevich, D. Melnikov, and M. J. Strassler, JHEP **07**, 055 (2009), 0903.0883. → pages xv, 94, 96, 97, 113, 116, 118, 119, 120, 121, 139

[12] J. E. Juknevich, JHEP **08**, 121 (2010), 0911.5616. → pages xv, 94, 113, 116, 118, 119, 121, 122, 123

[13] G. Aad et al. (ATLAS), Phys. Lett. **B716**, 1 (2012), 1207.7214. → page 2

[14] S. Chatrchyan et al. (CMS), Phys. Lett. **B716**, 30 (2012), 1207.7235.

[15] G. Arnison et al. (UA1), Phys. Lett. **B122**, 103 (1983), [,611(1983)]. → page 2

[16] M. E. Peskin and D. V. Schroeder, *An Introduction to quantum field theory* (Addison-Wesley, Reading, USA, 1995), ISBN 9780201503975, 0201503972, URL http://www.slac.stanford.edu/~mpeskin/QFT.html. → pages 2, 12, 16

[17] C. P. Burgess and G. D. Moore, *The standard model: A primer* (Cambridge University Press, 2006), ISBN 9780511254857, 9781107404267, 9780521860369.

[18] M. Srednicki, *Quantum field theory* (Cambridge University Press, 2007), ISBN 9780521864497, 9780511267208.

[19] L. H. Ryder, *QUANTUM FIELD THEORY* (Cambridge University Press, 1996), ISBN 9780521478144, 9781139632393, 9780521237642.

[20] P. Langacker, in *Proceedings of Theoretical Advanced Study Institute in Elementary Particle Physics on The dawn of the LHC era (TASI 2008): Boulder, USA, June 2-27, 2008* (2010), pp. 3–48, 0901.0241. → pages 2, 14

[21] H. Georgi, Front. Phys. **54**, 1 (1999). → page 3

[22] R. Slansky, Phys. Rept. **79**, 1 (1981). → page 3

[23] S. Pokorski, *GAUGE FIELD THEORIES* (Cambridge University Press, 2005), ISBN 9780511037801, 9780521478168, URL http://www.cambridge.org/uk/catalogue/catalogue.asp?isbn=0521265371. → page 3

[24] H. K. Dreiner, H. E. Haber, and S. P. Martin, Phys. Rept. **494**, 1 (2010), 0812.1594. → page 4

[25] P. B. Pal, Am. J. Phys. **79**, 485 (2011), 1006.1718. → page 4

[26] M. Tanabashi et al. (Particle Data Group), Phys. Rev. **D98**, 030001 (2018). → pages 7, 9, 39, 48

[27] P. W. Higgs, Phys. Rev. Lett. **13**, 508 (1964), [,160(1964)]. → page 7

[28] F. Englert and R. Brout, Phys. Rev. Lett. **13**, 321 (1964), [,157(1964)].

[29] G. S. Guralnik, C. R. Hagen, and T. W. B. Kibble, Phys. Rev. Lett. **13**, 585 (1964), [,162(1964)]. → page 7

[30] Y. Nambu, Phys. Rev. **117**, 648 (1960), [,132(1960)]. → page 8

[31] J. Goldstone, Nuovo Cim. **19**, 154 (1961).

[32] J. Goldstone, A. Salam, and S. Weinberg, Phys. Rev. **127**, 965 (1962). → page 8

[33] N. Cabibbo, Phys. Rev. Lett. **10**, 531 (1963), [,648(1963)]. → page 11

[34] M. Kobayashi and T. Maskawa, Prog. Theor. Phys. **49**, 652 (1973). → page 11

[35] K. G. Wilson, Phys. Rev. **D10**, 2445 (1974), [,319(1974)]. → page 12

[36] T. DeGrand and C. E. Detar, *Lattice methods for quantum chromodynamics* (2006). → page 12

[37] R. Machleidt and D. R. Entem, Phys. Rept. **503**, 1 (2011), 1105.2919. → page 13

[38] L. Alvarez-Gaume and M. A. Vazquez-Mozo, in *High-energy physics. Proceedings, 3rd Latin American CERN-CLAF School, Malargue, Argentina, February 27-March 12, 2005* (2014), pp. 1–80, [,1(2015)], hep-th/0510040. → page 14

[39] C. Csáki, S. Lombardo, and O. Telem, in *Proceedings, Theoretical Advanced Study Institute in Elementary Particle Physics : Anticipating the Next Discoveries in Particle Physics (TASI 2016): Boulder, CO, USA, June 6-July 1, 2016*, WSP (WSP, 2018), pp. 501–570, 1811.04279, URL http://webtheory.sns.it/ggilectures2018/csaki/notes.pdf. → page 14

[40] Y. Fukuda et al. (Super-Kamiokande), Phys. Rev. Lett. **81**, 1562 (1998), hep-ex/9807003. → page 14

[41] Q. R. Ahmad et al. (SNO), Phys. Rev. Lett. **87**, 071301 (2001), nucl-ex/0106015. → page 14

[42] A. de Gouvea, in *Physics in D ¿= 4. Proceedings, Theoretical Advanced Study Institute in elementary particle physics, TASI 2004, Boulder, USA, June 6-July 2, 2004* (2004), pp. 197–258, hep-ph/0411274. → page 14

[43] Z. Maki, M. Nakagawa, and S. Sakata, in *High-energy physics. Proceedings, 11th International Conference, ICHEP'62, Geneva, Switzerland, Jul 4-11, 1962* (1962), pp. 663–666. → page 14

[44] B. Pontecorvo, Sov. Phys. JETP **7**, 172 (1958), [Zh. Eksp. Teor. Fiz.34,247(1957)]. → page 14

[45] A. J. Cuesta, V. Niro, and L. Verde, Phys. Dark Univ. **13**, 77 (2016), 1511.05983. → page 14

[46] M. Gell-Mann, P. Ramond, and R. Slansky, Conf. Proc. **C790927**, 315 (1979), 1306.4669. → page 14

[47] A. Aguilar-Arevalo et al. (LSND), Phys. Rev. **D64**, 112007 (2001), hep-ex/0104049. → page 15

[48] A. A. Aguilar-Arevalo et al. (MiniBooNE), Phys. Rev. Lett. **121**, 221801 (2018), 1805.12028. → page 15

[49] J. C. Ward, Phys. Rev. **78**, 182 (1950). → page 16

[50] R. Harnik, G. D. Kribs, and G. Perez, Phys. Rev. **D74**, 035006 (2006), hep-ph/0604027. → page 17

[51] S. P. Martin, pp. 1–98 (1997), [Adv. Ser. Direct. High Energy Phys.18,1(1998)], hep-ph/9709356. → page 17

[52] N. Arkani-Hamed, A. G. Cohen, E. Katz, and A. E. Nelson, JHEP **07**, 034 (2002), hep-ph/0206021. → page 17

[53] M. Perelstein, Prog. Part. Nucl. Phys. **58**, 247 (2007), hep-ph/0512128.

[54] Z. Chacko, H.-S. Goh, and R. Harnik, Phys. Rev. Lett. **96**, 231802 (2006), hep-ph/0506256. → page 94

[55] M. Schmaltz, JHEP **08**, 056 (2004), hep-ph/0407143.

[56] M. Schmaltz and D. Tucker-Smith, Ann. Rev. Nucl. Part. Sci. **55**, 229 (2005), hep-ph/0502182.

[57] C. T. Hill and E. H. Simmons, Phys. Rept. **381**, 235 (2003), [Erratum: Phys. Rept.390,553(2004)], hep-ph/0203079. → page 17

[58] A. Hook (2018), 1812.02669. → page 17

[59] M. Dine, in *Flavor physics for the millennium. Proceedings, Theoretical Advanced Study Institute in elementary particle physics, TASI 2000, Boulder, USA, June 4-30, 2000* (2000), pp. 349–369, hep-ph/0011376.

[60] R. D. Peccei, Lect. Notes Phys. **741**, 3 (2008), [,3(2006)], hep-ph/0607268.

[61] J. E. Kim and G. Carosi, Rev. Mod. Phys. **82**, 557 (2010), 0807.3125. → page 17

[62] P. Fileviez Perez and H. H. Patel, Phys. Lett. **B732**, 241 (2014), 1402.6340. → page 18

[63] R. J. Crewther, P. Di Vecchia, G. Veneziano, and E. Witten, Phys. Lett. **88B**, 123 (1979), [Erratum: Phys. Lett.91B,487(1980)]. → page 18

[64] J. M. Pendlebury et al., Phys. Rev. **D92**, 092003 (2015), 1509.04411. → page 18

[65] R. D. Peccei and H. R. Quinn, Phys. Rev. Lett. **38**, 1440 (1977), [,328(1977)]. → page 18

[66] J. Kawamura, S. Okawa, Y. Omura, and Y. Tang (2018), 1812.07004. → page 18

[67] N. Aghanim et al. (Planck) (2018), 1807.06209. → pages 20, 23, 37, 43, 52, 70, 88

[68] R. V. Wagoner, W. A. Fowler, and F. Hoyle, Astrophys. J. **148**, 3 (1967). → page 20

[69] D. N. Schramm and M. S. Turner, Rev. Mod. Phys. **70**, 303 (1998), astro-ph/9706069. → page 20

[70] E. W. Kolb and M. S. Turner, Front. Phys. **69**, 1 (1990). → pages 20, 32, 45, 52, 61, 86, 100, 101

[71] S. Dodelson, *Modern Cosmology* (Academic Press, Amsterdam, 2003), ISBN 9780122191411, URL http://www.slac.stanford.edu/spires/find/books/www?cl=QB981:D62:2003. → pages 27, 40, 41, 86

[72] J. Bernstein, *KINETIC THEORY IN THE EXPANDING UNIVERSE*, Cambridge Monographs on Mathematical Physics (Cambridge University Press, Cambridge, U.K., 1988), ISBN 9780511564185. → pages 20, 27

[73] P. Gondolo and G. Gelmini, Nucl. Phys. **B360**, 145 (1991). → pages 25, 61, 106, 107, 166, 168

[74] D. J. Fixsen, Astrophys. J. **707**, 916 (2009), 0911.1955. → page 27

[75] J. M. Cline (2018), 1807.08749. → pages 31, 32

[76] J. Rubio, Front. Astron. Space Sci. **5**, 50 (2019), 1807.02376. → page 31

[77] B. Ryden, *Introduction to cosmology* (Cambridge University Press, 2016), ISBN 9781107154834, 9781316889848, URL http://www.cambridge.org/de/academic/subjects/astronomy/cosmology-and-relativity/introduction-cosmology-2nd-edition-1?format=HB. → page 31

[78] A. D. Sakharov, Pisma Zh. Eksp. Teor. Fiz. **5**, 32 (1967), [Usp. Fiz. Nauk161,no.5,61(1991)]. → page 32

[79] M.-C. Chen, in *Proceedings of Theoretical Advanced Study Institute in Elementary Particle Physics : Exploring New Frontiers Using Colliders and Neutrinos (TASI 2006): Boulder, Colorado, June 4-30, 2006* (2007), pp. 123–176, hep-ph/0703087, URL http://lss.fnal.gov/cgi-bin/find_paper.pl?pub-07-059. → page 32

[80] J. M. Cline and P. Scott, JCAP **1303**, 044 (2013), [Erratum: JCAP1305,E01(2013)], 1301.5908. → pages 32, 85, 134

[81] R. H. Cyburt, B. D. Fields, K. A. Olive, and T.-H. Yeh, Rev. Mod. Phys. **88**, 015004 (2016), 1505.01076. → pages 33, 70, 73, 133

[82] M. Pettini and R. Cooke, Mon. Not. Roy. Astron. Soc. **425**, 2477 (2012), 1205.3785. → page 34

[83] D. Romano, M. Tosi, C. Chiappini, and F. Matteucci, Mon. Not. Roy. Astron. Soc. **369**, 295 (2006), astro-ph/0603190. → page 34

[84] T. Prodanovic, G. Steigman, and B. D. Fields, Mon. Not. Roy. Astron. Soc. **406**, 1108 (2010), 0910.4961. → page 34

[85] R. I. Epstein, J. M. Lattimer, and D. N. Schramm, Nature **263**, 198 (1976). → page 34

[86] T. Prodanovic and B. D. Fields, Astrophys. J. **597**, 48 (2003), astro-ph/0307183. → page 34

[87] R. Cooke, M. Pettini, C. C. Steidel, G. C. Rudie, and P. E. Nissen, Mon. Not. Roy. Astron. Soc. **417**, 1534 (2011), 1106.2805. → page 34

[88] R. Cooke, M. Pettini, R. A. Jorgenson, M. T. Murphy, and C. C. Steidel, Astrophys. J. **781**, 31 (2014), 1308.3240.

[89] R. J. Cooke, M. Pettini, K. M. Nollett, and R. Jorgenson, Astrophys. J. **830**, 148 (2016), 1607.03900.

[90] R. Cooke, M. Pettini, and C. C. Steidel, Mon. Not. Roy. Astron. Soc. **467**, 802 (2017), 1701.03103.

[91] R. J. Cooke, M. Pettini, and C. C. Steidel, Astrophys. J. **855**, 102 (2018), 1710.11129. → pages 34, 83

[92] E. O. Zavarygin, J. K. Webb, S. Riemer-Sørensen, and V. Dumont, J. Phys. Conf. Ser. **1038**, 012012 (2018), 1801.04704. → page 35

[93] G. Steigman, Ann. Rev. Nucl. Part. Sci. **57**, 463 (2007), 0712.1100. → page 35

[94] M. Kawasaki, K. Kohri, T. Moroi, and Y. Takaesu, Phys. Rev. **D97**, 023502 (2018), 1709.01211. → pages 35, 36, 70, 83, 133

[95] G. Sigl, K. Jedamzik, D. N. Schramm, and V. S. Berezinsky, Phys. Rev. **D52**, 6682 (1995), astro-ph/9503094. → page 35

[96] J. Geiss and G. Gloeckler, Space Science Reviews **106**, 3 (2003). → pages 35, 36

[97] T. M. Bania, R. T. Rood, and D. S. Balser, Nature **415**, 54 (2002). → page 35

[98] P. Mahaffy, T. Donahue, S. Atreya, T. Owen, and H. Neimann, Space Science Reviews **84**, 251 (1998). → page 35

[99] M. Peimbert, Curr. Sci. **95**, 1165 (2008), 0811.2980. → page 36

[100] E. Aver, K. A. Olive, R. L. Porter, and E. D. Skillman, JCAP **1311**, 017 (2013), 1309.0047. → page 36

[101] E. Aver, K. A. Olive, and E. D. Skillman, JCAP **1507**, 011 (2015), 1503.08146. → pages 36, 83

[102] Y. I. Izotov, T. X. Thuan, and N. G. Guseva, Mon. Not. Roy. Astron. Soc. **445**, 778 (2014), 1408.6953. → pages 36, 83

[103] R. L. Porter, G. J. Ferland, P. J. Storey, and M. J. Detisch, Mon. Not. Roy. Astron. Soc. **425**, 28 (2012), [Erratum: Mon. Not. Roy. Astron. Soc.433,89(2013)], 1303.5115. → page 36

[104] A. Peimbert, M. Peimbert, and V. Luridiana, Rev. Mex. Astron. Astrofis. **52**, 419 (2016), 1608.02062. → pages 36, 83

[105] M. Spite and F. Spite, Nature **297**, 483 (1982). → page 37

[106] E. Vangioni-Flam, M. Casse, R. Cayrel, J. Audouze, M. Spite, and F. Spite, New Astron. **4**, 245 (1999), astro-ph/9811327. → page 37

[107] P. Bonifacio and P. Molaro, Mon. Not. Roy. Astron. Soc. **285**, 847 (1997), astro-ph/9611043. → page 37

[108] P. Bonifacio et al., Astron. Astrophys. **390**, 91 (2002), astro-ph/0204332.

[109] J. Melendez, L. Casagrande, I. Ramirez, M. Asplund, and W. Schuster, Astron. Astrophys. **515**, L3 (2010), 1005.2944. → page 37

[110] P. Bonifacio et al., Astron. Astrophys. **462**, 851 (2007), astro-ph/0610245. → page 37

[111] L. Sbordone et al., Astron. Astrophys. **522**, A26 (2010), 1003.4510. → pages 37, 70

[112] M. Pospelov and J. Pradler, Ann. Rev. Nucl. Part. Sci. **60**, 539 (2010), 1011.1054. → pages 37, 38, 70, 78, 133

[113] S. Cole et al. (2dFGRS), Mon. Not. Roy. Astron. Soc. **362**, 505 (2005), astro-ph/0501174. → page 38

[114] D. Scott and G. F. Smoot (2010), 1005.0555. → page 39

[115] G. F. Smoot et al. (COBE), Astrophys. J. **396**, L1 (1992). → page 40

[116] C. L. Bennett et al. (WMAP), Astrophys. J. Suppl. **148**, 1 (2003), astro-ph/0302207.

[117] P. A. R. Ade et al. (Planck), Astron. Astrophys. **571**, A16 (2014), 1303.5076. → page 40

[118] E. V. Linder, Phys. Rev. **D72**, 043529 (2005), astro-ph/0507263. → page 41

[119] M. Kunz, S. Nesseris, and I. Sawicki, Phys. Rev. **D94**, 023510 (2016), 1604.05701. → page 41

[120] S. C. Trager, S. M. Faber, and A. Dressler, Mon. Not. Roy. Astron. Soc. **386**, 715 (2008), 0803.0464. → page 41

[121] R. A. E. Fosbury et al., Astrophys. J. **596**, 797 (2003), astro-ph/0307162. → page 41

[122] P. A. Oesch et al., American Astronomical Society **819**, 129 (2016), 1603.00461. → page 41

[123] X.-L. Chen and M. Kamionkowski, Phys. Rev. **D70**, 043502 (2004), astro-ph/0310473. → pages 41, 85, 113, 117, 133, 134

[124] G. Bertone, D. Hooper, and J. Silk, Phys. Rept. **405**, 279 (2005), hep-ph/0404175. → pages 42, 52

[125] J. Silk et al., *Particle Dark Matter: Observations, Models and Searches* (Cambridge Univ. Press, Cambridge, 2010), ISBN 9781107653924, URL http://www.cambridge.org/uk/catalogue/catalogue.asp?isbn=9780521763684. → page 44

[126] D. B. Cline, ed., *Sources of Dark Matter in the Universe: Proceedings, 1st International Symposium, February 16-18, 1994, Bel Air, CA*, World Scientific (World Scientific, Singapore, 1995).

[127] A. Del Popolo, Int. J. Mod. Phys. **D23**, 1430005 (2014), 1305.0456. → page 42

[128] F. Zwicky, Helv. Phys. Acta **6**, 110 (1933), [Gen. Rel. Grav.41,207(2009)]. → page 42

[129] V. C. Rubin and W. K. Ford, Jr., Astrophys. J. **159**, 379 (1970). → page 42

[130] A. Bosma, Astron. J. **86**, 1825 (1981).

[131] K. G. Begeman, Astron. Astrophys. **223**, 47 (1989). → page 42

[132] D. Clowe, M. Bradac, A. H. Gonzalez, M. Markevitch, S. W. Randall, C. Jones, and D. Zaritsky, Astrophys. J. **648**, L109 (2006), astro-ph/0608407. → page 43

[133] A. M. Nierenberg, T. Treu, N. Menci, Y. Lu, P. Torrey, and M. Vogelsberger, Mon. Not. Roy. Astron. Soc. **462**, 4473 (2016), 1603.01614. → page 44

[134] D. H. Weinberg, J. S. Bullock, F. Governato, R. Kuzio de Naray, and A. H. G. Peter, Proc. Nat. Acad. Sci. **112**, 12249 (2015), 1306.0913. → page 44

[135] L. E. Strigari, J. S. Bullock, M. Kaplinghat, J. Diemand, M. Kuhlen, and P. Madau, Astrophys. J. **669**, 676 (2007), 0704.1817. → page 44

[136] W. J. G. de Blok, Adv. Astron. **2010**, 789293 (2010), 0910.3538. → page 44

[137] S. Tulin and H.-B. Yu, Phys. Rept. **730**, 1 (2018), 1705.02358. → pages 44, 64, 67, 136

[138] M. Boylan-Kolchin, J. S. Bullock, and M. Kaplinghat, Mon. Not. Roy. Astron. Soc. **415**, L40 (2011), 1103.0007. → page 44

[139] F. Governato, A. Zolotov, A. Pontzen, C. Christensen, S. H. Oh, A. M. Brooks, T. Quinn, S. Shen, and J. Wadsley, Mon. Not. Roy. Astron. Soc. **422**, 1231 (2012), 1202.0554. → page 44

[140] G. Despali, M. Sparre, S. Vegetti, M. Vogelsberger, J. Zavala, and F. Marinacci, Mon. Not. Roy. Astron. Soc. **484**, 4563 (2019), 1811.02569. → page 44

[141] F. D. Steffen, Eur. Phys. J. **C59**, 557 (2009), 0811.3347. → page 44

[142] G. Jungman, M. Kamionkowski, and K. Griest, Phys. Rept. **267**, 195 (1996), hep-ph/9506380. → pages 44, 52

[143] A. Boyarsky, M. Drewes, T. Lasserre, S. Mertens, and O. Ruchayskiy, Prog. Part. Nucl. Phys. **104**, 1 (2019), 1807.07938. → page 44

[144] A. Kusenko, Phys. Rept. **481**, 1 (2009), 0906.2968. → page 44

[145] K. Griest and D. Seckel, Phys. Rev. **D43**, 3191 (1991). → page 46

[146] N. Arkani-Hamed, D. P. Finkbeiner, T. R. Slatyer, and N. Weiner, Phys. Rev. **D79**, 015014 (2009), 0810.0713. → pages 46, 93

[147] Y. Hochberg, E. Kuflik, T. Volansky, and J. G. Wacker, Phys. Rev. Lett. **113**, 171301 (2014), 1402.5143. → pages 46, 95, 99, 130

[148] E. W. Kolb, D. J. H. Chung, and A. Riotto, AIP Conf. Proc. **484**, 91 (1999), [,592(1999)], hep-ph/9810361. → page 46

[149] J. L. Feng, A. Rajaraman, and F. Takayama, Phys. Rev. Lett. **91**, 011302 (2003), hep-ph/0302215. → page 47

[150] G. Gelmini, P. Gondolo, A. Soldatenko, and C. E. Yaguna, Phys. Rev. **D74**, 083514 (2006), hep-ph/0605016. → page 47

[151] D. E. Kaplan, M. A. Luty, and K. M. Zurek, Phys. Rev. **D79**, 115016 (2009), 0901.4117. → page 47

[152] L. J. Hall, K. Jedamzik, J. March-Russell, and S. M. West, JHEP **03**, 080 (2010), 0911.1120. → pages 47, 53, 56, 67

[153] N. Bernal, M. Heikinheimo, T. Tenkanen, K. Tuominen, and V. Vaskonen, Int. J. Mod. Phys. **A32**, 1730023 (2017), 1706.07442. → pages 47, 53

[154] F. Elahi, C. Kolda, and J. Unwin, JHEP **03**, 048 (2015), 1410.6157. → pages 47, 53, 56, 67, 68

[155] R. Bernabei et al., Universe **4**, 116 (2018), [At. Energ.19,307(2018)], 1805.10486. → page 48

[156] R. Agnese et al. (CDMS), Phys. Rev. Lett. **111**, 251301 (2013), 1304.4279. → page 48

[157] S. Knapen, T. Lin, and K. M. Zurek, Phys. Rev. **D96**, 115021 (2017), 1709.07882. → pages 48, 72, 73

[158] J. Bramante, B. Broerman, J. Kumar, R. F. Lang, M. Pospelov, and N. Raj (2018), 1812.09325. → page 48

[159] L. Goodenough and D. Hooper (2009), 0910.2998. → page 48

[160] T. E. Jeltema and S. Profumo, Mon. Not. Roy. Astron. Soc. **450**, 2143 (2015), 1408.1699. → page 48

[161] M.-Y. Cui, Q. Yuan, Y.-L. S. Tsai, and Y.-Z. Fan, Phys. Rev. Lett. **118**, 191101 (2017), 1610.03840. → page 48

[162] O. Adriani et al. (PAMELA), Nature **458**, 607 (2009), 0810.4995. → page 48

[163] D. Hooper (2018), 1812.02029. → page 48

[164] A. Albert et al. (2017), 1703.05703. → page 48

[165] A. Soffer, PoS **FPCP2015**, 025 (2015), 1507.02330.

[166] A. Choudhury, K. Kowalska, L. Roszkowski, E. M. Sessolo, and A. J. Williams, JHEP **04**, 182 (2016), 1509.05771. → page 48

[167] M. Lisanti, in *Proceedings, Theoretical Advanced Study Institute in Elementary Particle Physics: New Frontiers in Fields and Strings (TASI 2015): Boulder, CO, USA, June 1-26, 2015* (2017), pp. 399–446, 1603.03797. → page 52

[168] S. Wolfram, Phys. Lett. **82B**, 65 (1979). → pages 52, 61

[169] R. J. Scherrer and M. S. Turner, Phys. Rev. **D33**, 1585 (1986), [Erratum: Phys. Rev.D34,3263(1986)]. → pages 52, 61

[170] G. Steigman and M. S. Turner, Nucl. Phys. **B253**, 375 (1985). → page 52

[171] P. S. Bhupal Dev, A. Mazumdar, and S. Qutub, Front.in Phys. **2**, 26 (2014), 1311.5297. → page 53

[172] H. Baer, K.-Y. Choi, J. E. Kim, and L. Roszkowski, Phys. Rept. **555**, 1 (2015), 1407.0017. → page 53

[173] M. Chianese and S. F. King, JCAP **1809**, 027 (2018), 1806.10606. → page 53

[174] B. Shakya, Mod. Phys. Lett. **A31**, 1630005 (2016), 1512.02751. → page 53

[175] J. R. Ellis, J. E. Kim, and D. V. Nanopoulos, Phys. Lett. **145B**, 181 (1984). → page 53

[176] G. F. Giudice, A. Riotto, and I. Tkachev, JHEP **11**, 036 (1999), hep-ph/9911302.

[177] R. Kallosh, L. Kofman, A. D. Linde, and A. Van Proeyen, Phys. Rev. **D61**, 103503 (2000), hep-th/9907124.

[178] K. Choi, K. Hwang, H. B. Kim, and T. Lee, Phys. Lett. **B467**, 211 (1999), hep-ph/9902291. → page 53

[179] J. McDonald, Phys. Rev. Lett. **88**, 091304 (2002), hep-ph/0106249. → page 53

[180] C. Cheung, G. Elor, L. J. Hall, and P. Kumar, JHEP **03**, 042 (2011), 1010.0022.

[181] C. Cheung, G. Elor, L. J. Hall, and P. Kumar, JHEP **03**, 085 (2011), 1010.0024.

[182] X. Chu, T. Hambye, and M. H. G. Tytgat, JCAP **1205**, 034 (2012), 1112.0493. → pages 55, 57, 58

[183] C. E. Yaguna, JHEP **08**, 060 (2011), 1105.1654.

[184] C. E. Yaguna, JCAP **1202**, 006 (2012), 1111.6831.

[185] M. Blennow, E. Fernandez-Martinez, and B. Zaldivar, JCAP **1401**, 003 (2014), 1309.7348.

[186] M. Heikinheimo, T. Tenkanen, K. Tuominen, and V. Vaskonen, Phys. Rev. **D94**, 063506 (2016), [Erratum: Phys. Rev.D96,no.10,109902(2017)], 1604.02401.

[187] G. Krnjaic, JHEP **10**, 136 (2018), 1711.11038. → page 68

[188] M. J. Baker, M. Breitbach, J. Kopp, and L. Mittnacht, JHEP **03**, 114 (2018), 1712.03962. → page 53

[189] M. Garny, A. Palessandro, M. Sandora, and M. S. Sloth (2018), 1810.01428. → pages 53, 57, 58, 60

[190] S. B. Roland, B. Shakya, and J. D. Wells, Phys. Rev. **D92**, 113009 (2015), 1412.4791.

[191] J. McDonald, JCAP **1608**, 035 (2016), 1512.06422. → pages 55, 56, 57

[192] S.-L. Chen and Z. Kang, JCAP **1805**, 036 (2018), 1711.02556. → pages 53, 57

[193] H. Pagels and J. R. Primack, Phys. Rev. Lett. **48**, 223 (1982). → page 53

[194] J. R. Ellis, D. V. Nanopoulos, and S. Sarkar, Nucl. Phys. **B259**, 175 (1985). → page 70

[195] V. S. Berezinsky, Phys. Lett. **B261**, 71 (1991).

[196] T. Moroi, H. Murayama, and M. Yamaguchi, Phys. Lett. **B303**, 289 (1993). → pages 53, 70

[197] M. A. Fedderke, J.-Y. Chen, E. W. Kolb, and L.-T. Wang, JHEP **08**, 122 (2014), 1404.2283. → pages 54, 55

[198] Y. G. Kim and K. Y. Lee, Phys. Rev. **D75**, 115012 (2007), hep-ph/0611069. → page 54

[199] A. Freitas, S. Westhoff, and J. Zupan, JHEP **09**, 015 (2015), 1506.04149. → page 54

[200] M. A. Fedderke, T. Lin, and L.-T. Wang, JHEP **04**, 160 (2016), 1506.05465. → page 54

[201] A. DiFranzo, P. J. Fox, and T. M. P. Tait, JHEP **04**, 135 (2016), 1512.06853. → pages 54, 120

[202] L. Lopez-Honorez, T. Schwetz, and J. Zupan, Phys. Lett. **B716**, 179 (2012), 1203.2064. → page 55

[203] A. De Simone, G. F. Giudice, and A. Strumia, JHEP **06**, 081 (2014), 1402.6287. → page 55

[204] P. Adshead, Y. Cui, and J. Shelton, JHEP **06**, 016 (2016), 1604.02458. → pages 56, 99, 125

[205] E. Hardy and J. Unwin, JHEP **09**, 113 (2017), 1703.07642. → page 56

[206] J. L. Feng, H. Tu, and H.-B. Yu, JCAP **0810**, 043 (2008), 0808.2318. → pages 60, 61, 65, 67, 68

[207] S. Das and K. Sigurdson, Phys. Rev. **D85**, 063510 (2012), 1012.4458. → page 113

[208] P. Agrawal, F.-Y. Cyr-Racine, L. Randall, and J. Scholtz, JCAP **1705**, 022 (2017), 1610.04611. → pages 60, 61, 65, 66, 67, 68

[209] M. Pospelov, A. Ritz, and M. B. Voloshin, Phys. Lett. **B662**, 53 (2008), 0711.4866. → pages 60, 93

[210] J. Hisano, S. Matsumoto, and M. M. Nojiri, Phys. Rev. Lett. **92**, 031303 (2004), hep-ph/0307216. → page 60

[211] J. Hisano, S. Matsumoto, M. M. Nojiri, and O. Saito, Phys. Rev. **D71**, 063528 (2005), hep-ph/0412403.

[212] M. Cirelli, A. Strumia, and M. Tamburini, Nucl. Phys. **B787**, 152 (2007), 0706.4071. → page 60

[213] M. Pospelov and A. Ritz, Phys. Lett. **B671**, 391 (2009), 0810.1502. → pages 60, 93

[214] B. von Harling and K. Petraki, JCAP **1412**, 033 (2014), 1407.7874. → page 60

[215] J. Edsjo and P. Gondolo, Phys. Rev. **D56**, 1879 (1997), hep-ph/9704361. → pages 61, 106, 109, 111, 166, 168

[216] D. N. Spergel and P. J. Steinhardt, Phys. Rev. Lett. **84**, 3760 (2000), astro-ph/9909386. → pages 64, 67

[217] L. Ackerman, M. R. Buckley, S. M. Carroll, and M. Kamionkowski, Phys. Rev. **D79**, 023519 (2009), [,277(2008)], 0810.5126. → page 65

[218] S. Tulin, H.-B. Yu, and K. M. Zurek, Phys. Rev. **D87**, 115007 (2013), 1302.3898. → pages 65, 67

[219] D. A. Buote, T. E. Jeltema, C. R. Canizares, and G. P. Garmire, Astrophys. J. **577**, 183 (2002), astro-ph/0205469. → page 65

[220] P. J. Humphrey, D. A. Buote, C. R. Canizares, A. C. Fabian, and J. M. Miller, Astrophys. J. **729**, 53 (2011), 1010.6078. → page 65

[221] F. Kahlhoefer, K. Schmidt-Hoberg, M. T. Frandsen, and S. Sarkar, Mon. Not. Roy. Astron. Soc. **437**, 2865 (2014), 1308.3419. → pages 65, 67

[222] M. Vogelsberger, J. Zavala, and A. Loeb, Mon. Not. Roy. Astron. Soc. **423**, 3740 (2012), 1201.5892. → page 66

[223] J. Zavala, M. Vogelsberger, and M. G. Walker, Mon. Not. Roy. Astron. Soc. **431**, L20 (2013), 1211.6426. → page 66

[224] O. D. Elbert, J. S. Bullock, S. Garrison-Kimmel, M. Rocha, J. Oñorbe, and A. H. G. Peter, Mon. Not. Roy. Astron. Soc. **453**, 29 (2015), 1412.1477. → page 66

[225] K. Ahn and P. R. Shapiro, J. Korean Astron. Soc. **36**, 89 (2003), astro-ph/0212575. → page 66

[226] K.-J. Ahn and P. R. Shapiro, Mon. Not. Roy. Astron. Soc. **363**, 1092 (2005), astro-ph/0412169. → page 66

[227] E. Ma, Phys. Lett. **B772**, 442 (2017), 1704.04666. → page 67

[228] M. Duerr, K. Schmidt-Hoberg, and S. Wild, JCAP **1809**, 033 (2018), 1804.10385. → page 67

[229] A. E. Faraggi and M. Pospelov, Astropart. Phys. **16**, 451 (2002), hep-ph/0008223. → pages 68, 94, 113, 116, 117, 139

[230] F.-Y. Cyr-Racine and K. Sigurdson, Phys. Rev. **D87**, 103515 (2013), 1209.5752.

[231] K. K. Boddy, J. L. Feng, M. Kaplinghat, and T. M. P. Tait, Phys. Rev. **D89**, 115017 (2014), 1402.3629. → pages 94, 95, 97, 99, 113, 114, 116, 117, 136, 139

[232] K. K. Boddy, J. L. Feng, M. Kaplinghat, Y. Shadmi, and T. M. P. Tait, Phys. Rev. **D90**, 095016 (2014), 1408.6532. → pages 94, 95, 113, 114, 116, 117, 139

[233] A. Berlin, D. Hooper, and G. Krnjaic, Phys. Lett. **B760**, 106 (2016), 1602.08490.

[234] A. Berlin, D. Hooper, and G. Krnjaic, Phys. Rev. **D94**, 095019 (2016), 1609.02555.

[235] A. Soni and Y. Zhang, Phys. Rev. **D93**, 115025 (2016), 1602.00714. → pages 71, 94, 95, 97, 113, 114, 116, 117, 136, 139

[236] J. Halverson, B. D. Nelson, and F. Ruehle, Phys. Rev. **D95**, 043527 (2017), 1609.02151.

[237] B. S. Acharya, M. Fairbairn, and E. Hardy, JHEP **07**, 100 (2017), 1704.01804. → pages 116, 117, 139

[238] N. Bernal, M. Dutra, Y. Mambrini, K. Olive, M. Peloso, and M. Pierre, Phys. Rev. **D97**, 115020 (2018), 1803.01866. → page 68

[239] S. Sarkar, Rept. Prog. Phys. **59**, 1493 (1996), hep-ph/9602260. → page 70

[240] F. Iocco, G. Mangano, G. Miele, O. Pisanti, and P. D. Serpico, Phys. Rept. **472**, 1 (2009), 0809.0631.

[241] K. Jedamzik and M. Pospelov, New J. Phys. **11**, 105028 (2009), 0906.2087. → pages 70, 81

[242] D. N. Schramm and R. V. Wagoner, Ann. Rev. Nucl. Part. Sci. **27**, 37 (1977). → page 70

[243] J. Bernstein, L. S. Brown, and G. Feinberg, Rev. Mod. Phys. **61**, 25 (1989).

[244] T. P. Walker, G. Steigman, D. N. Schramm, K. A. Olive, and H.-S. Kang, Astrophys. J. **376**, 51 (1991), [,43(1991)]. → page 70

[245] M. Asplund, D. L. Lambert, P. E. Nissen, F. Primas, and V. V. Smith, Astrophys. J. **644**, 229 (2006), astro-ph/0510636. → page 70

[246] R. H. Cyburt, B. D. Fields, and K. A. Olive, JCAP **0811**, 012 (2008), 0808.2818.

[247] B. D. Fields, Ann. Rev. Nucl. Part. Sci. **61**, 47 (2011), 1203.3551. → page 70

[248] M. Kawasaki, K. Kohri, and N. Sugiyama, Phys. Rev. Lett. **82**, 4168 (1999), astro-ph/9811437. → page 70

[249] M. Kawasaki, K. Kohri, and N. Sugiyama, Phys. Rev. **D62**, 023506 (2000), astro-ph/0002127.

[250] S. Hannestad, Phys. Rev. **D70**, 043506 (2004), astro-ph/0403291. → page 70

[251] R. Juszkiewicz, J. Silk, and A. Stebbins, Phys. Lett. **158B**, 463 (1985). → page 70

[252] S. Dimopoulos, R. Esmailzadeh, L. J. Hall, and G. D. Starkman, Astrophys. J. **330**, 545 (1988).

[253] M. H. Reno and D. Seckel, Phys. Rev. **D37**, 3441 (1988).

[254] S. Dimopoulos, R. Esmailzadeh, L. J. Hall, and G. D. Starkman, Nucl. Phys. **B311**, 699 (1989).

[255] J. R. Ellis, G. B. Gelmini, J. L. Lopez, D. V. Nanopoulos, and S. Sarkar, Nucl. Phys. **B373**, 399 (1992).

[256] M. Kawasaki and T. Moroi, Prog. Theor. Phys. **93**, 879 (1995), hep-ph/9403364.

[257] R. H. Cyburt, J. R. Ellis, B. D. Fields, and K. A. Olive, Phys. Rev. **D67**, 103521 (2003), astro-ph/0211258. → pages 78, 81, 82

[258] K. Jedamzik, Phys. Rev. **D70**, 063524 (2004), astro-ph/0402344. → pages 71, 113

[259] M. Kawasaki, K. Kohri, and T. Moroi, Phys. Rev. **D71**, 083502 (2005), astro-ph/0408426. → pages 71, 117, 133

[260] K. Jedamzik, Phys. Rev. **D74**, 103509 (2006), hep-ph/0604251. → pages 113, 117, 133

[261] M. Kawasaki, K. Kohri, T. Moroi, and A. Yotsuyanagi, Phys. Rev. **D78**, 065011 (2008), 0804.3745. → pages 70, 71

[262] J. A. Frieman, E. W. Kolb, and M. S. Turner, Phys. Rev. **D41**, 3080 (1990). → page 70

[263] J. Hisano, M. Kawasaki, K. Kohri, and K. Nakayama, Phys. Rev. **D79**, 063514 (2009), [Erratum: Phys. Rev.D80,029907(2009)], 0810.1892.

[264] J. Hisano, M. Kawasaki, K. Kohri, T. Moroi, and K. Nakayama, Phys. Rev. **D79**, 083522 (2009), 0901.3582.

[265] M. Kawasaki, K. Kohri, T. Moroi, and Y. Takaesu, Phys. Lett. **B751**, 246 (2015), 1509.03665. → page 70

[266] R. H. Cyburt, B. D. Fields, K. A. Olive, and E. Skillman, Astropart. Phys. **23**, 313 (2005), astro-ph/0408033. → page 70

[267] C. M. Ho and R. J. Scherrer, Phys. Rev. **D87**, 023505 (2013), 1208.4347.

[268] C. Boehm, M. J. Dolan, and C. McCabe, JCAP **1308**, 041 (2013), 1303.6270. → pages 70, 73, 85, 87

[269] R. J. Protheroe, T. Stanev, and V. S. Berezinsky, Phys. Rev. **D51**, 4134 (1995), astro-ph/9409004. → pages 71, 76, 78

[270] A. Fradette, M. Pospelov, J. Pradler, and A. Ritz, Phys. Rev. **D90**, 035022 (2014), 1407.0993. → pages 71, 113, 115, 143

[271] J. Berger, K. Jedamzik, and D. G. E. Walker, JCAP **1611**, 032 (2016), 1605.07195. → pages 71, 72, 80

[272] A. Fradette and M. Pospelov, Phys. Rev. **D96**, 075033 (2017), 1706.01920. → pages 71, 115

[273] B. Henning and H. Murayama (2012), 1205.6479. → page 71

[274] Y. Hochberg, E. Kuflik, R. Mcgehee, H. Murayama, and K. Schutz (2018), 1806.10139. → page 71

[275] S. Sarkar and A. M. Cooper-Sarkar, Phys. Lett. **148B**, 347 (1984), [,I.362(1984)]. → page 71

[276] H. Ishida, M. Kusakabe, and H. Okada, Phys. Rev. **D90**, 083519 (2014), 1403.5995. → pages 71, 72, 91

[277] V. Poulin and P. D. Serpico, Phys. Rev. Lett. **114**, 091101 (2015), 1502.01250. → page 72

[278] M. Kaplinghat and M. S. Turner, Phys. Rev. Lett. **86**, 385 (2001), astro-ph/0007454. → page 72

[279] C. Boehm, M. J. Dolan, and C. McCabe, JCAP **1212**, 027 (2012), 1207.0497. → pages 73, 87

[280] K. M. Nollett and G. Steigman, Phys. Rev. **D91**, 083505 (2015), 1411.6005. → pages 73, 85, 87

[281] A. Berlin and N. Blinov, Phys. Rev. Lett. **120**, 021801 (2018), 1706.07046. → page 73

[282] G. Steigman, Phys. Rev. **D87**, 103517 (2013), 1303.0049. → page 72

[283] A. D. Dolgov and F. L. Villante, Nucl. Phys. **B679**, 261 (2004), hep-ph/0308083. → page 72

[284] P. D. Serpico and G. G. Raffelt, Phys. Rev. **D70**, 043526 (2004), astro-ph/0403417. → page 73

[285] P. Hernandez, M. Kekic, and J. Lopez-Pavon, Phys. Rev. **D89**, 073009 (2014), 1311.2614.

[286] P. Hernandez, M. Kekic, and J. Lopez-Pavon, Phys. Rev. **D90**, 065033 (2014), 1406.2961.

[287] K. Nakayama, F. Takahashi, and T. T. Yanagida, Phys. Lett. **B697**, 275 (2011), 1010.5693. → page 72

[288] J. H. Heo and C. S. Kim, J. Korean Phys. Soc. **68**, 715 (2016), 1504.00773. → page 72

[289] G. Mangano, G. Miele, S. Pastor, and M. Peloso, Phys. Lett. **B534**, 8 (2002), astro-ph/0111408. → page 73

[290] G. Mangano, G. Miele, S. Pastor, T. Pinto, O. Pisanti, and P. D. Serpico, Nucl. Phys. **B729**, 221 (2005), hep-ph/0506164. → page 73

[291] E. W. Kolb, M. S. Turner, and T. P. Walker, Phys. Rev. **D34**, 2197 (1986). → page 73

[292] G. Steigman, in *Fourth NO-VE International Workshop on Neutrino Oscillations in Venice : Ten years after the neutrino oscillations!! : Venezia, April 15-18, 2008, Istituto Veneto di Scienze, Lettere ed Arti, Campo Santo Stefano* (2008), pp. 241–256, 0807.3004.

[293] G. Mangano and P. D. Serpico, Phys. Lett. **B701**, 296 (2011), 1103.1261. → page 73

[294] J. Silk, Astrophys. J. **151**, 459 (1968). → pages 73, 85

[295] Z. Hou, R. Keisler, L. Knox, M. Millea, and C. Reichardt, Phys. Rev. **D87**, 083008 (2013), 1104.2333. → pages 73, 85

[296] J. Dunkley et al., Astrophys. J. **739**, 52 (2011), 1009.0866. → page 73

[297] R. Keisler et al., Astrophys. J. **743**, 28 (2011), 1105.3182. → page 73

[298] G. R. Blumenthal and R. J. Gould, Rev. Mod. Phys. **42**, 237 (1970). → page 76

[299] A. Birkedal, K. T. Matchev, M. Perelstein, and A. Spray (2005), hep-ph/0507194. → page 78

[300] J. Mardon, Y. Nomura, D. Stolarski, and J. Thaler, JCAP **0905**, 016 (2009), 0901.2926. → page 78

[301] R. Evans, *The Atomic Nucleus* (Krieger Publishing Company, 2003), ISBN 9780758184115, URL https://books.google.ca/books?id=mWTFPQAACAAJ. → page 82

[302] A. N. Gorbunov and A. T. Varfolomeev, Phys. Lett. **11**, 137 (1964). → page 82

[303] R. Pfeiffer, Z. Phys. **208**, 129 (1968). → page 82

[304] D. D. Faul, B. L. Berman, P. Meyer, and D. L. Olson, Phys. Rev. Lett. **44**, 129 (1980). → page 82

[305] Yu. M. Arkatov, P. I. Vatset, V. I. Voloshchuk, V. N. Gurev, and A. F. Khodyachikh, Ukr. Fiz. Zh.(Russ. Ed.) **23**, 1818 (1978). → page 82

[306] J. D. Irish, R. G. Johnson, B. L. Berman, B. J. Thomas, K. G. McNeill, and J. W. Jury, Can. J. Phys. **53**, 802 (1975). → page 82

[307] C. K. Malcom, D. V. Webb, Y. M. Shin, and D. M. Skopik, Phys. Lett. **47B**, 433 (1973). → page 82

[308] O. Pisanti, A. Cirillo, S. Esposito, F. Iocco, G. Mangano, G. Miele, and P. D. Serpico, Comput. Phys. Commun. **178**, 956 (2008), 0705.0290. → page 82

[309] R. Consiglio, P. F. de Salas, G. Mangano, G. Miele, S. Pastor, and O. Pisanti, Comput. Phys. Commun. **233**, 237 (2018), 1712.04378. → page 82

[310] J. Geiss and G. Gloeckler, Space Science Reviews **106**, 3 (2003). → page 83

[311] L. E. Marcucci, G. Mangano, A. Kievsky, and M. Viviani, Phys. Rev. Lett. **116**, 102501 (2016), [Erratum: Phys. Rev. Lett.117,no.4,049901(2016)], 1510.07877. → page 83

[312] J. A. Adams, S. Sarkar, and D. W. Sciama, Mon. Not. Roy. Astron. Soc. **301**, 210 (1998), astro-ph/9805108. → pages 85, 117

[313] N. Padmanabhan and D. P. Finkbeiner, Phys. Rev. **D72**, 023508 (2005), astro-ph/0503486. → page 134

[314] L. Zhang, X. Chen, M. Kamionkowski, Z.-g. Si, and Z. Zheng, Phys. Rev. **D76**, 061301 (2007), 0704.2444. → page 85

[315] T. R. Slatyer, N. Padmanabhan, and D. P. Finkbeiner, Phys. Rev. **D80**, 043526 (2009), 0906.1197. → pages 85, 134

[316] C. M. Ho and R. J. Scherrer, Phys. Rev. **D87**, 065016 (2013), 1212.1689. → page 88

[317] W. Hu and J. Silk, Phys. Rev. **D48**, 485 (1993). → page 89

[318] W. Hu and J. Silk, Phys. Rev. Lett. **70**, 2661 (1993). → pages 89, 134

[319] D. J. Fixsen, E. S. Cheng, J. M. Gales, J. C. Mather, R. A. Shafer, and E. L. Wright, Astrophys. J. **473**, 576 (1996), astro-ph/9605054. → page 89

[320] J. Chluba and R. A. Sunyaev, Mon. Not. Roy. Astron. Soc. **419**, 1294 (2012), 1109.6552. → page 89

[321] A. Kogut et al., JCAP **1107**, 025 (2011), 1105.2044. → page 89

[322] M. Kusakabe, A. B. Balantekin, T. Kajino, and Y. Pehlivan, Phys. Rev. **D87**, 085045 (2013), 1303.2291. → page 91

[323] V. Khachatryan et al. (CMS), JHEP **04**, 025 (2015), 1412.6302. → page 93

[324] G. Aad et al. (ATLAS), Phys. Lett. **B755**, 285 (2016), 1512.05099. → page 93

[325] M. Pospelov, Phys. Rev. **D80**, 095002 (2009), 0811.1030. → pages 93, 94, 115

[326] J. D. Bjorken, R. Essig, P. Schuster, and N. Toro, Phys. Rev. **D80**, 075018 (2009), 0906.0580. → page 94

[327] R. Essig et al., in *Proceedings, 2013 Community Summer Study on the Future of U.S. Particle Physics: Snowmass on the Mississippi (CSS2013): Minneapolis, MN, USA, July 29-August 6, 2013* (2013), 1311.0029, URL http://www.slac.stanford.edu/econf/C1307292/docs/IntensityFrontier/NewLight-17.pdf. → pages 93, 94, 115

[328] L. B. Okun, Sov. Phys. JETP **56**, 502 (1982), [Zh. Eksp. Teor. Fiz.83,892(1982)]. → page 93

[329] B. Holdom, Phys. Lett. **166B**, 196 (1986). → page 93

[330] R. Blumenhagen, M. Cvetic, P. Langacker, and G. Shiu, Ann. Rev. Nucl. Part. Sci. **55**, 71 (2005), hep-th/0502005. → pages 94, 97

[331] S. Nussinov, Phys. Lett. **165B**, 55 (1985). → page 94

[332] S. M. Barr, R. S. Chivukula, and E. Farhi, Phys. Lett. **B241**, 387 (1990).

[333] S. B. Gudnason, C. Kouvaris, and F. Sannino, Phys. Rev. **D73**, 115003 (2006), hep-ph/0603014.

[334] M. Baumgart, C. Cheung, J. T. Ruderman, L.-T. Wang, and I. Yavin, JHEP **04**, 014 (2009), 0901.0283.

[335] G. D. Kribs, T. S. Roy, J. Terning, and K. M. Zurek, Phys. Rev. **D81**, 095001 (2010), 0909.2034.

[336] J. L. Feng and Y. Shadmi, Phys. Rev. **D83**, 095011 (2011), 1102.0282. → pages 94, 116, 117, 139

[337] J. M. Cline, Z. Liu, G. Moore, and W. Xue, Phys. Rev. **D90**, 015023 (2014), 1312.3325. → page 113

[338] N. Yamanaka, S. Fujibayashi, S. Gongyo, and H. Iida (2014), 1411.2172. → pages 94, 116

[339] H. An, S.-L. Chen, R. N. Mohapatra, and Y. Zhang, JHEP **03**, 124 (2010), 0911.4463. → page 94

[340] M. T. Frandsen, S. Sarkar, and K. Schmidt-Hoberg, Phys. Rev. **D84**, 051703 (2011), 1103.4350.

[341] S. M. Barr and R. J. Scherrer, JCAP **1605**, 065 (2016), 1508.07469. → page 94

[342] G. Burdman, Z. Chacko, H.-S. Goh, and R. Harnik, JHEP **02**, 009 (2007), hep-ph/0609152. → pages 94, 127

[343] M. J. Strassler and K. M. Zurek, Phys. Lett. **B651**, 374 (2007), hep-ph/0604261. → page 94

[344] R. L. Jaffe and K. Johnson, Phys. Lett. **60B**, 201 (1976). → page 94

[345] K. S. Jeong and F. Takahashi, Phys. Lett. **B725**, 134 (2013), 1305.6521. → page 94

[346] N. Blinov, J. Kozaczuk, A. Menon, and D. E. Morrissey, Phys. Rev. **D91**, 035026 (2015), 1409.1222.

[347] M. A. Buen-Abad, G. Marques-Tavares, and M. Schmaltz, Phys. Rev. **D92**, 023531 (2015), 1505.03542.

[348] M. Reece and T. Roxlo, JHEP **09**, 096 (2016), 1511.06768. → page 94

[349] E. D. Carlson, M. E. Machacek, and L. J. Hall, Astrophys. J. **398**, 43 (1992). → pages 95, 99, 100, 101, 116

[350] E. Kuflik, M. Perelstein, N. R.-L. Lorier, and Y.-D. Tsai, Phys. Rev. Lett. **116**, 221302 (2016), 1512.04545. → pages 95, 99, 129, 130

[351] I. Garcia Garcia, R. Lasenby, and J. March-Russell, Phys. Rev. **D92**, 055034 (2015), 1505.07109. → pages 95, 99, 103, 116, 117, 139

[352] V. Mathieu, N. Kochelev, and V. Vento, Int. J. Mod. Phys. **E18**, 1 (2009), 0810.4453. → pages 95, 96, 97, 117

[353] H. B. Meyer, Ph.D. thesis, Oxford U. (2004), hep-lat/0508002. → page 95

[354] Y. Chen et al., Phys. Rev. **D73**, 014516 (2006), hep-lat/0510074. → pages 95, 118, 132

[355] G. B. West, Phys. Rev. Lett. **77**, 2622 (1996), hep-ph/9603316. → pages 95, 114, 116

[356] R. Sommer, Nucl. Phys. **B411**, 839 (1994), hep-lat/9310022. → page 96

[357] M. Guagnelli, R. Sommer, and H. Wittig (ALPHA), Nucl. Phys. **B535**, 389 (1998), hep-lat/9806005. → pages 96, 102

[358] M. Gockeler, R. Horsley, A. C. Irving, D. Pleiter, P. E. L. Rakow, G. Schierholz, and H. Stuben, Phys. Rev. **D73**, 014513 (2006), hep-ph/0502212. → pages 96, 102

[359] R. L. Jaffe, K. Johnson, and Z. Ryzak, Annals Phys. **168**, 344 (1986). → pages 96, 97, 117, 139

[360] B. Lucini, M. Teper, and U. Wenger, JHEP **06**, 012 (2004), hep-lat/0404008. → page 96

[361] B. Lucini, A. Rago, and E. Rinaldi, JHEP **08**, 119 (2010), 1007.3879. → page 96

[362] B. Lucini and G. Moraitis, Phys. Lett. **B668**, 226 (2008), 0805.2913. → pages 96, 102

[363] E. Vicari and H. Panagopoulos, Phys. Rept. **470**, 93 (2009), 0803.1593. → page 97

[364] G. Gabadadze and A. Iglesias, Phys. Lett. **B609**, 167 (2005), hep-th/0411278. → page 97

[365] A. Manohar and H. Georgi, Nucl. Phys. **B234**, 189 (1984). → page 97

[366] A. G. Cohen, D. B. Kaplan, and A. E. Nelson, Phys. Lett. **B412**, 301 (1997), hep-ph/9706275.

[367] R. Nishio, T. Watari, T. T. Yanagida, and K. Yonekura, Phys. Rev. **D86**, 016010 (2012), 1205.2949. → page 97

[368] G. 't Hooft, Nucl. Phys. **B72**, 461 (1974). → page 97

[369] E. Witten, Nucl. Phys. **B160**, 57 (1979). → pages 97, 98

[370] G. Boyd, J. Engels, F. Karsch, E. Laermann, C. Legeland, M. Lutgemeier, and B. Petersson, Nucl. Phys. **B469**, 419 (1996), hep-lat/9602007. → page 102

[371] B. Beinlich, F. Karsch, and A. Peikert, Phys. Lett. **B390**, 268 (1997), hep-lat/9608141.

[372] B. Lucini, M. Teper, and U. Wenger, JHEP **01**, 061 (2004), hep-lat/0307017. → page 102

[373] B. Lucini, M. Teper, and U. Wenger, JHEP **02**, 033 (2005), hep-lat/0502003. → pages 102, 103

[374] T. Umeda, S. Ejiri, S. Aoki, T. Hatsuda, K. Kanaya, Y. Maezawa, and H. Ohno, Phys. Rev. **D79**, 051501 (2009), 0809.2842.

[375] M. Panero, Phys. Rev. Lett. **103**, 232001 (2009), 0907.3719.

[376] S. Datta and S. Gupta, Phys. Rev. **D82**, 114505 (2010), 1006.0938. → page 103

[377] S. Borsanyi, G. Endrodi, Z. Fodor, S. D. Katz, and K. K. Szabo, JHEP **07**, 056 (2012), 1204.6184. → pages 103, 132

[378] B. Lucini, A. Rago, and E. Rinaldi, Phys. Lett. **B712**, 279 (2012), 1202.6684. → pages 102, 139

[379] A. Francis, O. Kaczmarek, M. Laine, T. Neuhaus, and H. Ohno, Phys. Rev. **D91**, 096002 (2015), 1503.05652. → page 102

[380] P. Levai and U. W. Heinz, Phys. Rev. **C57**, 1879 (1998), hep-ph/9710463. → page 102

[381] P. N. Meisinger, T. R. Miller, and M. C. Ogilvie, Phys. Rev. **D65**, 034009 (2002), hep-ph/0108009.

[382] R. D. Pisarski, Phys. Rev. **D74**, 121703 (2006), hep-ph/0608242.

[383] S. S. Gubser, A. Nellore, S. S. Pufu, and F. D. Rocha, Phys. Rev. Lett. **101**, 131601 (2008), 0804.1950.

[384] U. Gursoy, E. Kiritsis, L. Mazzanti, and F. Nitti, JHEP **05**, 033 (2009), 0812.0792.

[385] A. Dumitru, Y. Guo, Y. Hidaka, C. P. K. Altes, and R. D. Pisarski, Phys. Rev. **D86**, 105017 (2012), 1205.0137. → page 102

[386] H. B. Meyer, Phys. Rev. **D80**, 051502 (2009), 0905.4229. → page 103

[387] F. Buisseret and G. Lacroix, Phys. Lett. **B705**, 405 (2011), 1105.1092.

[388] M. Caselle, A. Nada, and M. Panero, JHEP **07**, 143 (2015), [Erratum: JHEP11,016(2017)], 1505.01106. → page 103

[389] N. Isgur and J. E. Paton, Phys. Rev. **D31**, 2910 (1985). → page 103

[390] N. Ishii, H. Suganuma, and H. Matsufuru, Phys. Rev. **D66**, 094506 (2002), hep-lat/0206020. → page 103

[391] X.-F. Meng, G. Li, Y. Chen, C. Liu, Y.-B. Liu, J.-P. Ma, and J.-B. Zhang, Phys. Rev. **D80**, 114502 (2009), 0903.1991. → page 103

[392] M. Caselle and R. Pellegrini, Phys. Rev. Lett. **111**, 132001 (2013), 1304.4757. → page 103

[393] A. Megevand and A. D. Sanchez, Phys. Rev. **D77**, 063519 (2008), 0712.1031. → page 103

[394] R. T. D'Agnolo and J. T. Ruderman, Phys. Rev. Lett. **115**, 061301 (2015), 1505.07107. → page 110

[395] D. Pappadopulo, J. T. Ruderman, and G. Trevisan, Phys. Rev. **D94**, 035005 (2016), 1602.04219. → pages 113, 116, 132, 139

[396] Y. Yang, Phys. Rev. **D91**, 083517 (2015), 1504.01195. → page 113

[397] M. Cirelli, E. Moulin, P. Panci, P. D. Serpico, and A. Viana, Phys. Rev. **D86**, 083506 (2012), 1205.5283. → page 113

[398] A. A. de Laix, R. J. Scherrer, and R. K. Schaefer, Astrophys. J. **452**, 495 (1995), astro-ph/9502087. → page 113

[399] P. Langacker, Rev. Mod. Phys. **81**, 1199 (2009), 0801.1345. → page 115

[400] V. Khachatryan et al. (CMS), Phys. Lett. **B768**, 57 (2017), 1609.05391.

[401] M. Aaboud et al. (ATLAS) (2017), 1707.02424. → page 115

[402] T. Cohen, K. Murase, N. L. Rodd, B. R. Safdi, and Y. Soreq, Phys. Rev. Lett. **119**, 021102 (2017), 1612.05638. → pages 115, 117, 133, 134

[403] J. Kopp, J. Liu, T. R. Slatyer, X.-P. Wang, and W. Xue, JHEP **12**, 033 (2016), 1609.02147. → page 116

[404] P. Ko and Y. Tang, Phys. Lett. **B768**, 12 (2017), 1609.02307.

[405] K. R. Dienes, F. Huang, S. Su, and B. Thomas, Phys. Rev. **D95**, 043526 (2017), 1610.04112.

[406] A. Soni, H. Xiao, and Y. Zhang (2017), 1704.02347. → pages 117, 127, 139

[407] A. Mitridate, M. Redi, J. Smirnov, and A. Strumia (2017), 1707.05380. → pages 116, 127

[408] A. D. Dolgov (2017), 1705.03689. → page 116

[409] M. Farina, D. Pappadopulo, J. T. Ruderman, and G. Trevisan, JHEP **12**, 039 (2016), 1607.03108. → pages 116, 132, 139

[410] S. B. Giddings and A. Strominger, Nucl. Phys. **B307**, 854 (1988). → page 116

[411] L. F. Abbott and M. B. Wise, Nucl. Phys. **B325**, 687 (1989).

[412] R. Kallosh, A. D. Linde, D. A. Linde, and L. Susskind, Phys. Rev. **D52**, 912 (1995), hep-th/9502069.

[413] T. Banks and N. Seiberg, Phys. Rev. **D83**, 084019 (2011), 1011.5120. → page 116

[414] H. B. Meyer, JHEP **01**, 071 (2009), 0808.3151. → pages 118, 132

[415] R. D. Peccei, Lect. Notes Phys. **521**, 1 (1999), hep-ph/9807516. → page 119

[416] Q. Lu, D. E. Morrissey, and A. M. Wijangco, JHEP **06**, 138 (2017), 1705.08896. → pages 119, 121

[417] M. A. Shifman, A. I. Vainshtein, M. B. Voloshin, and V. I. Zakharov, Sov. J. Nucl. Phys. **30**, 711 (1979), [Yad. Fiz.30,1368(1979)]. → page 122

[418] J. F. Gunion, H. E. Haber, G. L. Kane, and S. Dawson, Front. Phys. **80**, 1 (2000). → page 123

[419] J. F. Gunion, H. E. Haber, G. L. Kane, and S. Dawson (1992), hep-ph/9302272. → page 123

[420] L. B. Okun, JETP Lett. **31**, 144 (1980), [Pisma Zh. Eksp. Teor. Fiz.31,156(1979)]. → page 127

[421] L. B. Okun, Phys. Usp. **50**, 380 (2007), hep-ph/0606202. → page 127

[422] J. Kang, M. A. Luty, and S. Nasri, JHEP **09**, 086 (2008), hep-ph/0611322. → page 127

[423] C. Jacoby and S. Nussinov (2007), 0712.2681. → page 127

[424] E. Bertschinger, Phys. Rev. **D74**, 063509 (2006), astro-ph/0607319. → pages 127, 129, 130

[425] T. Bringmann and S. Hofmann, JCAP **0704**, 016 (2007), [Erratum: JCAP1603,no.03,E02(2016)], hep-ph/0612238. → pages 127, 129, 130

[426] A. Kurkela and G. D. Moore, JHEP **12**, 044 (2011), 1107.5050. → page 127

[427] T. Moroi and L. Randall, Nucl. Phys. **B570**, 455 (2000), hep-ph/9906527. → page 129

[428] E. Kuflik, M. Perelstein, N. R.-L. Lorier, and Y.-D. Tsai, JHEP **08**, 078 (2017), 1706.05381. → pages 129, 130

[429] P. Gondolo, J. Hisano, and K. Kadota, Phys. Rev. **D86**, 083523 (2012), 1205.1914. → page 129

[430] T. R. Slatyer and C.-L. Wu, Phys. Rev. **D95**, 023010 (2017), 1610.06933. → pages 133, 134

[431] D. P. Finkbeiner, S. Galli, T. Lin, and T. R. Slatyer, Phys. Rev. **D85**, 043522 (2012), 1109.6322.

[432] T. R. Slatyer, Phys. Rev. **D87**, 123513 (2013), 1211.0283. → page 134

[433] J. L. Feng, A. Rajaraman, and F. Takayama, Phys. Rev. **D68**, 063504 (2003), hep-ph/0306024. → page 134

[434] W. B. Atwood et al. (Fermi-LAT), Astrophys. J. **697**, 1071 (2009), 0902.1089. → page 134

[435] A. Massari, E. Izaguirre, R. Essig, A. Albert, E. Bloom, and G. A. Gómez-Vargas, Phys. Rev. **D91**, 083539 (2015), 1503.07169. → page 134

[436] J. Heeck, Phys. Lett. **B739**, 256 (2014), 1408.6845. → page 143

Appendix A

Calculation of Transfer Rates during Freeze-In

In this appendix we calculate the effective transfer rates of number and energy density from the visible sector to the dark sector through the operator of Eq. (3.1), used in chapter 3. The squared matrix element for $\psi + \bar{\psi} \to H + H^\dagger$ derived from this interaction and summed over both initial and final degrees of freedom is

$$\widetilde{|\mathscr{M}|^2} = \frac{4}{M^2}(s - 4m_\psi^2) \,, \tag{A.1}$$

with $s = (p_1 + p_2)^2$. Note that we assume implicitly that the Higgs is in the electroweak unbroken phase and can be treated as a massless $SU(2)_L$ scalar doublet.

Number Transfer

The relevant number transfer term via $\psi(1) + \overline{\psi}(2) \to H(3) + H^\dagger(4)$ is

$$\begin{aligned} \mathscr{T}(T) &\equiv \langle \sigma_{tr} v(T) \rangle (n_\psi^2 - n_{\psi,eq}^2(T)) \\ &\equiv \int d\Pi_1 \int d\Pi_2 \int d\Pi_3 \int d\Pi_4 \, (2\pi)^4 \delta^{(4)}(p_i) \widetilde{|\mathscr{M}|^2} (f_1 f_2 - f_3 f_4) \,, \end{aligned} \tag{A.2}$$

where $d\Pi_i = d^3 p_i / 2E_i (2\pi)^3$. To make the calculation tractable, we approximate the distribution functions by the Maxwell-Boltzmann form $f_i = \zeta_i e^{-E_i/T}$, where ζ_i is the rescaling needed to get the correct number densities relative to equilibrium at temperature T. We expect that the Maxwell-Boltzmann approximation used here is correct up to factors very close to unity.

For $n_\psi \ll n_{\psi,eq}(T)$ we have $f_1 = f_2 \simeq 0$, while Higgs fields in full thermodynamic equilibrium with the SM (in the electroweak unbroken phase) imply $f_3 = f_4 = 1$. The transfer term then reduces to

$$\mathscr{T}(T) = \int d\Pi_1 \int d\Pi_2 \, \left(4 g_\psi^2 E_1 E_2 \sigma_{tr} v\right) e^{-(E_1 + E_2)/T} \,, \tag{A.3}$$

with $g_\psi = 2$ being the number of fermion spin states. Note that the combination in brackets is Lorentz invariant and can depend only on the variable s. It is given by

$$\begin{aligned}\left(4g_\psi^2 E_1 E_2 \sigma_{tr} v\right) &= \int d\Pi_3 \int d\Pi_4 \, (2\pi)^4 \delta^{(4)}(p_i) \widetilde{|\mathscr{M}|^2} \\ &= \frac{1}{8\pi}\left(\frac{1}{4\pi}\int d\Omega \, \widetilde{|\mathscr{M}|^2}\right)_{CM} \\ &= \frac{1}{2\pi}\frac{1}{M^2}(s-4m_\psi^2) \, .\end{aligned} \tag{A.4}$$

To integrate this over the initial states, we follow Refs. [73, 215] and use the fact that the integrand depends only on s and $E_+ = (E_1 + E_2)$ to write

$$\int d\Pi_1 \int d\Pi_2 = \frac{1}{4(2\pi)^4}\int_{4m_\psi^2}^\infty ds \int_{\sqrt{s}}^\infty dE_+ \sqrt{1-4m_\psi^2/s}\sqrt{E_+^2 - s} \, . \tag{A.5}$$

Since the only E_+ dependence of the integrand is in the Boltzmann exponential, integrating using a Bessel function identity[1] gives

$$\begin{aligned}\mathscr{T}(T) &= \frac{1}{4(2\pi)^4}\int_{4m_\psi^2}^\infty ds \, (4g_1 g_2 E_1 E_2 \sigma_{tr} v) \sqrt{1-4m_\psi^2/s} \\ &= \frac{1}{2(2\pi)^5}\frac{T^6}{M^2}\mathscr{F}(x) \, ,\end{aligned} \tag{A.6}$$

where $x = m_\psi/T$ and

$$\begin{aligned}\mathscr{F}(x) &= \int_{2x}^\infty du \, u (u^2 - 4x^2)^{3/2} K_1(u) \\ &\simeq \begin{cases} 16 & ; \quad x \ll 1 \\ 6\pi x^2 e^{-2x} & ; \quad x \gg 1 \end{cases}\end{aligned} \tag{A.7}$$

Energy Transfer

We are also interested in the net rate of energy transfer between the visible and dark sectors. The relevant energy collision term for $\psi + \overline{\psi} \to H + H^\dagger$ is identical to Eq. (A.2) but with an additional factor

[1] $K_\nu(z) = \frac{\sqrt{\pi} z^\nu}{2^\nu \Gamma(\nu+1/2)} \int_1^\infty dt \, (t^2-1)^{\nu-1/2} e^{-zt}$.

of $\Delta E = (E_1 + E_2) = E_+$ in the integrand. The result is[2]

$$\begin{aligned}
\mathscr{U}(T) &\equiv \langle \Delta E \cdot \sigma_{tr} v(T) \rangle (n_\psi^2 - n_{\psi,eq}^2(T)) \\
&\equiv \frac{T}{4(2\pi)^4} \int_{4m_\psi^2}^{\infty} ds\, (4 g_1 g_2 E_1 E_2 \sigma_{tr} v) \sqrt{s - 4m_\psi^2}\, \sqrt{s} K_2(\sqrt{s}/T) \\
&= \frac{1}{2(2\pi)^5} \frac{T^7}{M^2} \mathscr{G}(x)
\end{aligned} \tag{A.8}$$

with $x = m_\psi / T$ and

$$\begin{aligned}
\mathscr{G}(x) &= \int_{2x}^{\infty} du\, u^2 \, (u^2 - 4x^2)^{3/2} K_2(u) \\
&\simeq \begin{cases} 96 & ; \quad x \ll 1 \\ 12\pi x^3 e^{-2x} & ; \quad x \gg 1 \end{cases}
\end{aligned} \tag{A.9}$$

[2] $\int_1^\infty dt\, t\sqrt{t^2-1}\, e^{-zt} = -\frac{d}{dz}[K_1(z)/z] = K_2(z)/z.$

Appendix B

Thermalization Rates for Glueballs

In this appendix we calculate expressions for the collision term, $\Delta\mathscr{C}$ needed to compute the energy transfer $\Delta(\rho_x/T^4)$, in Eq. 6.27.

The collision term relevant for thermalization corresponds to the process $X+X \to \mathrm{SM}+\mathrm{SM}$, and is given by

$$\begin{aligned} \Delta\mathscr{C} &= \langle \sigma v \cdot \Delta E \rangle \widetilde{n}_x^2 \\ &= \int d\Pi_1 \int d\Pi_2 \, f_1 f_2 \, W(s) \, \Delta E \ , \end{aligned} \tag{B.1}$$

where E_1 and E_2 are the initial-state energies, $\Delta E = (E_1+E_2)$ is to be evaluated in the comoving frame, $d\Pi_i = g_i d^3p_i/(2\pi)^3 2E_i$, f_i are the equilibrium distribution functions at temperature T, and the *scattering kernel* is defined by [73, 215]

$$\begin{aligned} W(s) &= 4E_1E_2\sigma v \\ &= \frac{\mathscr{S}}{g_1 g_2} \int \frac{d^3p_3}{(2\pi)^3 2E_3} \int \frac{d^3p_4}{(2\pi)^3 2E_4} (2\pi)^4 \delta^{(4)}(p_1+p_2-p_3-p_4) \sum_{\{int\}} |\mathscr{M}|^2 \ . \end{aligned} \tag{B.2}$$

Here, $\mathscr{S}$ is the symmetry factor for identical particles, g_i are the numbers of degrees of freedom of the initial-state particles, the sum runs over all internal degrees of freedom, and $|\mathscr{M}|^2$ is the squared matrix element for the reaction. Note that this quantity is Lorentz invariant, and can therefore only depend on $s=(p_1+p_2)^2$.

Following Refs. [73, 215], the expression of Eq. (B.1) can be reduced to a single integral if we approximate the distribution functions by Maxwell-Boltzmann forms, $f_i = \exp(-E_i/T)$:

$$\begin{aligned} \Delta\mathscr{C} &= \frac{g_1 g_2 T^2}{32\pi^4} \int_{(m_1+m_2)^2}^{\infty} ds \, p_{12} \, \mathscr{F}(\sqrt{s}/T) \, W(s) \\ &= \frac{g_1 g_2}{32\pi^4} T^5 \int_{x_+}^{\infty} dx \, \sqrt{\left(x^2-x_+^2\right)\left(x^2-x_-^2\right)} \, \mathscr{F}(x) \, W(s=x^2T^2) \ , \end{aligned} \tag{B.3}$$

where $\mathscr{F}(x) = \left(K_1(x) + \frac{x}{2}\left[K_0(x)+K_2(x)\right]\right) = \left[2K_1(x)+xK_0(x)\right]$ and $x_\pm = (m_1 \pm m_2)/T$.

Cross Sections for Dimension-8 Operators

The relevant operator has the general form

$$\mathscr{O}_8 = \frac{A}{M^4} X^a_{\alpha\beta} X^{a\,\alpha\beta} F^C_{\mu\nu} F^{C\,\mu\nu} \ , \tag{B.4}$$

where $F^C_{\mu\nu}$ is a SM field strength. This operator generates $XX \to AA$ transfer reactions for $T \gg m_A, m_0$, as well as $XA \to XA$ elastic scattering. Concentrating on $XX \to AA$, the corresponding matrix element for $(p_1,a)+(p_2,b) \to (p_3,C)+(p_4,D)$ is

$$\mathscr{M} = 4A \frac{s^2}{M^4} \delta^{ab} \delta^{CD} (\varepsilon_1^* \cdot \varepsilon_2^*)(\varepsilon_3 \cdot \varepsilon_4) \ , \tag{B.5}$$

where a,b,C,D are "colours" and ε_i are polarization vectors. From this expression, we find (neglecting possible masses)

$$W(s) = \frac{1}{\pi} \left(\frac{\tilde{g}_A}{\tilde{g}_x} \right) A^2 \, \frac{s^4}{M^8} \ , \tag{B.6}$$

where $\tilde{g}_x$ and $\tilde{g}_A = 2(N_A^2 - 1)$ are the dark and visible numbers of degrees of freedom. The energy-transfer collision term is then

$$\Delta\mathscr{C} \quad = \quad \frac{\tilde{g}_x \tilde{g}_A}{32\pi^5} A^2 \left[\int_0^\infty dx \, x^{10} \mathscr{F}(x) \right] \frac{T^{13}}{M^8} \ . \tag{B.7}$$

The integral is dominated by $x = \sqrt{s}/T \sim 10$, corresponding to scattering at the high end of the thermal distribution.

The coupling A can be obtained by matching to our previous results for dark gluon connector operators. While there are several operators that can contribute, we keep only the S component corresponding to the operator listed above, which yields

$$A_i = \frac{\alpha_i \alpha_x}{120} \chi_i \ , \tag{B.8}$$

with $A_i = Y, 2, 3$ for each of the SM gauge factors. For $\chi_i \to 1$, the gluon contribution dominates with $\tilde{g}_A = 2(N_c^2 - 1)$, and we focus on it exclusively. Note that since we are considering $T \gtrsim m_0 \gtrsim 100\,\mathrm{MeV}$ and the integration is dominated by $\sqrt{s} \sim 10T$, we should always be safely above the QCD confinement scale.

Cross Sections for Dimension-6 Operators

The operator of interest is now

$$\mathscr{O}_6 = \frac{B}{M^2} |H|^2 X^a_{\alpha\beta} X^{a\,\alpha\beta} \ , \tag{B.9}$$

with

$$B = \frac{\alpha_x y_{eff}^2}{6\pi} \ . \tag{B.10}$$

To treat scattering through this operator, we should distinguish between temperatures above and below the electroweak phase transition at $T_{EWPT} \simeq 100\,\mathrm{GeV}$. Above the transition, all the SM states are massless and we can treat the Higgs field as a complex scalar doublet. Below the transition, we must account for masses.

For $T > T_{EWPT}$, the dominant transfer reaction is $X + X \to H + H^\dagger$, for which the scattering kernel is

$$W(s) = \frac{1}{\pi}\frac{1}{\tilde{g}_x}\frac{B^2}{M^4}s^2 \ . \tag{B.11}$$

This yields the collision term

$$\Delta\mathscr{C} = \frac{\tilde{g}_x}{32\pi^5}B^2\left[\int_0^\infty dx x^6 \mathscr{F}(x)\right]\frac{T^9}{M^4} \ , \tag{B.12}$$

where now the integral is dominated by $\sqrt{s} \sim 6T$.

Below the transition temperature, we have $f\bar{f}$, hh, W^+W^-, and ZZ final states at leading order. Their contributions to the scattering kernels are

$$W_f(s) = \frac{N_c^{(f)}}{\pi}\frac{1}{\tilde{g}_x}\frac{B^2}{M^4}s^2\left(\frac{m_f^2}{s}\right)\left(\frac{s}{s-m_h^2}\right)^2\left(1-\frac{4m_f^2}{s}\right)^{3/2} \tag{B.13}$$

$$W_h(s) = \frac{1}{4\pi}\frac{1}{\tilde{g}_x}\frac{B^2}{M^4}s^2\left(1-\frac{4m_h^2}{s}\right)^{1/2} \tag{B.14}$$

$$W_Z(s) = \frac{1}{4\pi}\frac{1}{\tilde{g}_x}\frac{B^2}{M^4}s^2\left(\frac{s}{s-m_h^2}\right)^2\left(1-\frac{2m_Z^2}{s}+\frac{12m_Z^4}{s^2}\right)\left(1-\frac{4m_Z^2}{s}\right)^{1/2} \tag{B.15}$$

$$W_W(s) = \frac{1}{2\pi}\frac{1}{\tilde{g}_x}\frac{B^2}{M^4}s^2\left(\frac{s}{s-m_h^2}\right)^2\left(1-\frac{2m_W^2}{s}+\frac{12m_W^4}{s^2}\right)\left(1-\frac{4m_W^2}{s}\right)^{1/2} \tag{B.16}$$

These results only apply for $\sqrt{s} > 2m_i$; they are zero otherwise. Note that for $\sqrt{s} \gg 2m_h, 2m_f$, the sum of these kernels is equal to the result of Eq. (B.11).